SHEARING AND VOLUMETRIC STRAINING RESPONSE OF
KIZILIRMAK SAND

A THESIS SUBMITTED TO
THE GRADUATE SCHOOL OF NATURAL AND APPLIED SCIENCES
OF
MIDDLE EAST TECHNICAL UNIVERSITY

BY

ELİFE ÇAKIR

IN PARTIAL FULFILLMENT OF THE REQUIREMENTS
FOR
THE DEGREE OF MASTER OF SCIENCE
IN
CIVIL ENGINEERING

SEPTEMBER 2020

Approval of the thesis:

SHEARING AND VOLUMETRIC STRAINING RESPONSE OF KIZILIRMAK SAND

submitted by **ELİFE ÇAKIR** in partial fulfillment of the requirements for the degree of **Master of Science** in **Civil Engineering, Middle East Technical University** by,

Prof. Dr. Halil Kalıpçılar

Dean, Graduate School of **Natural and Applied Sciences**

Prof. Dr. Ahmet Türer

Head of the Department, **Civil Engineering**

Prof. Dr. Kemal Önder Çetin

Supervisor, **Civil Engineering, METU**

Examining Committee Members:

Prof. Dr. Erdal Çokça

Civil Engineering, METU

Prof. Dr. Kemal Önder Çetin

Civil Engineering, METU

Prof. Dr. Zeynep Gülerce

Civil Engineering, METU

Prof. Dr. Nihat Sinan Işık

Civil Engineering., Gazi Uni.

Assoc. Prof. Dr. Nabi Kartal Toker

Civil Engineering, METU

Date: 14.09.2020

I hereby declare that all information in this document has been obtained and presented in accordance with academic rules and ethical conduct. I also declare that, as required by these rules and conduct, I have fully cited and referenced all material and results that are not original to this work.

Name, Last name : Elife Çakır

Signature :

ABSTRACT

**SHEAR AND VOLUMETRIC STRAINING RESPONSE OF
KIZILIRMAK SAND**

Çakır, Elife
Master of Science, Civil Engineering
Supervisor : Prof. Dr. Kemal Önder Çetin

September 2020, 217 pages

The response of sandy soils under monotonic loading depends on size, shape and mineralogy of particles, fabric, stress, and density states of mixtures. Researchers around the world have studied their local sands and calibrated their responses (e.g., Toyoura sand-Japan, Ottawa sand-Canada, Sacramento sand-US, Sydney sand-Australia, etc.). However, there are not many studies that have focused on regional sands from Turkey. This research study aims to introduce a local sand, Kızılırmak sand, to literature as a "standard sand" from Turkey. For this purpose, shear and volumetric straining responses of Kızılırmak sand samples were investigated by a series of consolidated undrained monotonic triaxial and oedometer tests. Specimens with relative densities of 35-45-60-75 and 80 %, were prepared by wet tamping method and consolidated under 50 kPa, 100 kPa, 200 kPa and 400 kPa cell pressures, followed by undrained shearing. Test results were presented by four-way plots, which enable the individual variations of axial load, cell pressure, pore water pressure, and axial deformation along with the progress of the stress paths relative to failure envelopes. On the basis of test results, linear and nonlinear elastic-perfectly plastic constitutive modeling parameters, including but not limited to stress and relative-density dependent modulus and effective stress based angles of shearing

resistance, were estimated. Due to its angular nature, Kızılırmak sands' angles of shearing resistance values of 35.4°-42.8° were observed, which are closer to the upper limits of available literature. Triaxial modulus values fall in the range of ~10 and ~160 MPa and are concluded to be in conformance with available literature.

Similarly, samples with varying relative densities, prepared by air pluviation method, were tested in a conventional oedometer device under stresses starting from ~17 kPa increasing up to ~33.5 MPa. During tests, unloading and reloading cycles were performed. Based on these test results, particle crushing-induced yield stresses of Kızılırmak sands along with their C_c, C_α values were estimated as ~2.1-4.0 MPa, ~2×10^{-3}-1×10^{-2}, and ~1×10^{-5}–1×10^{-3}, respectively. It was concluded that Kızılırmak sand exhibited Type B volumetric compression response as defined by Mesri and Vardhanabhuti (2009). Additionally, test results were also assessed within critical state framework. Critical state framework soil parameters of angle of steady state shearing resistances, λ and Γ values were estimated as 39.4°, 0.070, and 0.975. Initial dividing line, defining the boundary between strain hardening and softening responses, is determined specific for Kızılırmak sand.

Keywords: Triaxial test, One-dimensional volumetric compression, Angle of shearing resistance, Particle crushing, Kızılırmak sand

ÖZ

KIZILIRMAK KUMUNUN KAYMA VE HACİMSEL BİRİM DEFORMASYON DAVRANIŞI

Çakır, Elife
Yüksek Lisans, İnşaat Mühendisliği
Tez Yöneticisi: Prof. Dr. Kemal Önder Çetin

Eylül 2020, 217 sayfa

Kumlu zeminlerin statik yükleme altındaki davranışı dane boyutu, şekli, mineralojisi, dokusu, gerilme ve sıkılık durumları gibi bir çok etken tarafından kontrol edilmektedir. Araştırmacılar kendi yerel bölgelerinde bulunan kumları çalışarak kalibre etmiş ve standart kumlar olarak literatüre sunmuşlardır (örneğin; Toyoura kumu- Japonya, Ottawa kumu- Kanada, Sacramento kumu- ABD, Sydney kumu- Avusturalya, vb.). Ancak Türkiye'de yerel kumlar üzerinde standart bir kum geliştirmeye odaklı fazla sayıda çalışma bulunmamaktadır.

Bu çalışma yerel Kızılırmak kumunu literatüre standart bir kum olarak sunmayı amaçlamaktadır. Bu amaca yönelik olarak Kızılırmak kumunun kayma ve hacimsel birim deformasyon davranışı konsolidasyonlu-drenajsız statik üç eksenli ve odometre deneyleri ile incelenmiştir. Bağıl yoğunlukları % 35-45-60-75 ve 80 olan, nemli sıkıştırma yöntemi ile hazırlanmış, ve 50 kPa, 100 kPa, 200 kPa ve 400 kPa hücre basınçları altında konsolide edilen numuneler, drenajsız yükler altında test edilmiştir. Sonuçlar, deney süresince numunenin eksenel yükleme, birim deformasyon, boşluk suyu basınç birikiminin izlenmesine imkan veren ve gerilme izini yenilme zarfı ile ilişkilendirebilen 4 yönlü grafikler kullanılarak sunulmuştur.

Bu veriler esas alınarak, doğrusal ve doğrusal olmayan elastik-mükemmel plastik bünye modeli parametreleri belirlenmiş, bu parametrelerden modül ve efektif kayma direnci açısı gerilme ve bağıl sıkılık ile değişecek şekilde modellenmiştir. Kızılırmak kumunun köşeli dane yapısı nedeni ile kayma direnci açısının 35.4°-42.8° aralığında olduğu belirlenmiş, bu değerin literatürdeki değerlerin üst sınırına yaklaştığı görülmüştür. Üç eksenli modül değerileri ise 10 ve 170 MPa aralığında değişmekte olup, literatürde verilen değerlerle uyum göstermektedir.

Benzer olarak, farklı bağıl sıkılıklarda, yağmurlama yöntemi ile hazırlanan numuneler odometre düzeneğinde 17 kPa'dan başlayıp 33.5 MPa'a kadar artan düşey yükler altında test edilmiştir. Deney sırasında yükleme ve boşaltma tekrarları uygulanmıştır. Kızılırmak kumunun, danelerin kırılmaya başladığı yenilme gerilmelerinin ve C_c, C_α indis değerlerinin sırası ile ~2.1 ve ~4.0 MPa, ~2×10^{-3} ve ~1×10^{-2}, ~1×10^{-5} ve ~1×10^{-3}, mertebelerinde olduğu belirlenmiştir. Kızılırmak kumunun hacimsel birim deformasyon davranışının, Mesri and Vardhanabhuti (2009) tarafından tanımlanan, Tip B davranış grubuna dahil olduğu sonucuna varılmıştır. Ek olarak, deney sonuçları kritik durum zemin mekaniği çerçevesinden de irdelenmiştir. Kritik durum zemin mekaniği parametrelerinden durağan-durum kayma direnci açısı, λ ve Γ değerleri sırasıyla 39.4°, 0.070, ve 0.975 olarak belirlenmiştir. Birim deformasyon pekleşmesi ve yumuşaması davranışlarını ayıran başlangıç sınır doğrusu Kızılırmak kumuna özel tariflenmiştir.

Anahtar Kelimeler: Üç eksenli deney, Bir-boyutlu hacimsel sıkışma, Kayma direnci açısı, Dane kırılması, Kızılırmak kumu)

To my family…

ACKNOWLEDGMENTS

TABLE OF CONTENTS

LIST OF TABLES

LIST OF FIGURES

FIGURES

xvi

xviii

LIST OF ABBREVIATIONS

ABBREVIATIONS

2-D	Two-Dimensional
3-D	Three-Dimensional
ASTM	American Society for Testing and Materials
CSL	Critical State Locus, Critical State Line
CU	Consolidated Undrained
EOP	End of Primary Compression
GSD	Grain Size Distribution
ICL	Isotropic Compression Line
IDL	Initial Dividing Line
LVDT	Linear Variable Displacement Transducer
METU	Middle East Technical University
QSS	Quasi-Steady State
QSSL	Quasi-Steady State Line
SEM	Scanning Electron Microscope
SP	Poorly Graded Sand
SS	Steady State
SSL	Steady State Line
USCS	Unified Soil Classification System

LIST OF SYMBOLS

SYMBOLS

A_0	Initial area of the specimen
A_c	Area of specimen after consolidation stage
B	Bulk modulus / Pore water pressure ratio coefficient
B_{15}	Breakage measurement suggested by Lee and Farhoomand, 1967
B_p	Breakage potential
B_r	Relative breakage
B_t	Total breakage
c'	Cohesion
C_c	Coefficient of curvature
C_c	Compression index
$C_{c,max}$	Maximum compression index
CO_2	Carbon dioxide
C_r	Recompression index
C_u	Coefficient of uniformity
C_α	Secondary compression index
d_0	Initial deformation reading in ach loading stage
d_a	Apparatus deformation in each loading stage
d_{eop}	Deformation reading in each loading stage at the end of primary compression

$d\varepsilon_a$	Rate of axial strain
$d\varepsilon_v$	Rate of volumetric strain
D_{10}	Diameter of the 10% of the sample to be finer
D_{15}	Diameter of the 15% of the sample to be finer
D_{30}	Diameter of the 30% of the sample to be finer
D_{50}	Mean grain size
D_{60}	Diameter of the 60% of the sample to be finer
D_R , D_r	Relative density
e	Void ratio
e_0	Initial void ratio
e_c	Void ratio after consolidation stage
e_{max}	Maximum void ratio
e_{min}	Minimum void ratio
e_s	Void ratio on quasi-steady state curve
E	Young's modulus
E_0, E_i	Maximum Young's modulus
E_{TRX}	Stiffness estimated from triaxial test
F	Elongation
F	Deviatoric force
g	Gravitational acceleration
G	Shear modulus
G_0 , G_{max}	Maximum shear modulus
G_s	Specific gravity

H_0	Initial height of the specimen
H_c	Height of specimen after consolidation stage
H_s	Height of solids
I_D	Relative density
I_R	Roundness
I_R	Relative dilatancy index
I_s	State index
I_{sph}	Sphericity
K	Modulus number
M	Frictional constant in critical soil mechanics
M_a	Mass of top cap
M_{max}	Tangent constrained modulus at the first inflection point of σ_{0v} versus ε_v or p' versus ε_v
M_{min}	Tangent constrained modulus at the second inflection point of σ_{0v} versus ε_v or p' versus ε_v
n	Modulus exponent
p'	Mean effective stress
p'_0	Initial mean effective stress
p_{atm}	Atmospheric pressure
p'_{crit}	Mean effective stress at failure
p'_{ref}	Reference mean effective stress
P	Load on specimen
q	Deviatoric stress / Half of deviatoric stress (shear stress)

q_f	Deviatoric stress / Half of deviatoric stress (shear stress) at failure
q/p'	Effective stress ratio
(q/p')$_f$	Effective stress ratio at failure
r_{max-in}	Maximum circle radius which fits inside the grain
$r_{min-cir}$	Minimum circle radius which encircled the grain
R	Roundness
R_f	Stress ratio
R_q	Surface texture
RD	Relative density
S	Sphericity
t	Time
u	Pore water pressure
U_{exc}	Excess pore water pressure
v	Specific volume
V_0	Initial volume of the specimen
V_s	Volume of solids
V_s	Shear wave velocity
$\dot{W}$	Rate of work
W_{soil}	Weight of specimen
γ	Shear strain
$\dot{\gamma}$	Rate of shear strain
Γ	Specific volume at a reference stress

Δe	Change in void ratio
Δu	Change in pore water pressure
ΔH	Change in height
ΔV	Change in volume
$\Delta \varepsilon_a$	Change in axial strain
$\Delta \sigma_3$	Change in cell pressure
$\Delta \sigma'_v$	Change in vertical effective stress
$\Delta \phi$	Change in friciotn angle
ε_1	Major principal strain
$\dot{\varepsilon}_1$	Major principal strain
ε_3	Minor principal strain
$\dot{\varepsilon}_3$	Minor principal strain
ε_a	Axial strain
$\varepsilon_{a,failure}$	Axial strain at failure
ε_r	Reference strain
ε_v	Volumetric strain
$\dot{\varepsilon}_v$	Rate of volumetric strain
λ	Slope of the critical state line
ν	Poisson's ratio
ρ_w	Density of water
σ'_1	Major principal effective stress
σ'_3	Minor principal effective stress / Effective confining pressure

σ_a	Axial stress
σ'_c	Effective consolidation pressure
σ_{cell}	Cell pressure
σ_d	Deviatoric stress
$(\sigma_1 - \sigma_3)_{ult}$	Asymptotic stress
σ_n'	Normal effective stress
σ'_v	Vertical effective stress
$\sigma'_v(M_{Max})$	Effective vertical stress at the yield point defined at the first inflection point of e versus σ_{0v}
$\sigma'_v(M_{Min})$	Effective vertical stress at the second inflection point of e versus σ_{0v} defining the end of the second stage of compression
$\sigma'_v (C_{c_{max}})$	Effective vertical stress at the maximum compression index
σ'_{yield}	Yield stress
τ	Shear strength
ϕ'	Angle of shearing resistance
ϕ_0	value of friciton angle at confining stress equals to atmospheric pressure
ϕ_{cv}	Constant volume angle of shearing resistance
ϕ'_{crit}	Critical state angle of shearing resistance
ϕ_d	Drained angle of shearing resistance
ϕ_{dc}	Frictional component due to density (dilation) state
ϕ_{max}	Maximum angle of shearing resistance

ϕ'_p	Peak angle of shearing resistance
ϕ'_u	Undrained effective stress angle of shearing resistance
ϕ_μ	Fundamental angle of friction for grain-to-grain contact
ψ	Dilation angle
$\Sigma r_i / N$	Average radius of the circles which fit the grain's protrusion

CHAPTER 1

INTRODUCTION

1.1   Research Statement

There exists a number of research studies regarding the mechanical behavior of clean sands. These studies confirm that sand behavior is complex, and its mechanical behavior depends on the size and shape of particles, mineralogy, and packing of the particles, stress and density states of the sand. Depending on these factors, the response of sand can be significantly different. Compared with the other engineering materials, geotechnical engineering material properties cannot be specified and produced, but instead, they should be measured and identified (Wroth and Houlsby, 1985).

Sand behavior under high stress levels is also a concern with advances in the construction of high-rise buildings, high earth-fill dams, and deep tunnels, etc. Stress levels on foundation soils can reach to MPa levels. At these high stress levels, sand may be subjected to grain crushing. After crushing, both the physical and engineering properties of sand may significantly differ from their initial configuration. Therefore, it is essential to identify the crushing stress levels and understand the behavior of sand after crushing.

Researchers from different regions have studied their local sands and calibrated their responses (Toyoura sand-Japan, Ottawa sand-Canada, Sacramento sand-US, Sydney sand-Australia, etc.). However, there are not many studies that focus on regional sands from Turkey.

This research study aims to investigate the shear and volumetric straining response of a local sand, Kızılırmak sand, and introduce this sand to the literature as a "standard sand" from Turkey. Kızılırmak sand is obtained from a local sand quarry

in Kırıkkale. It is not a widely studied sand in the literature, only a few studies available about Kızılırmak sand (e.g. Tatar (2018) and Bilge (2005)). For this purpose, a laboratory testing program was designed. As a part of the testing program, 20 monotonic strain-controlled consolidated undrained triaxial tests, 7 one-dimensional compression tests and soil index tests (minimum and maximum void ratio determination, grain size distribution and specific gravity determination) were performed. The results were compared with the available literature.

1.2   Research Objectives

The research objectives of this study are described as follow;

1. To investigate the effects of stress states on the two-dimensional (triaxial) stress-strain behavior and strength of relatively loose and dense Kızılırmak sand specimens.

2. To investigate the effects of density states on the two-dimensional (triaxial) stress-strain behavior and strength of Kızılırmak sand specimens consolidated to different confining pressures.

3. To investigate the effects of density states on one-dimensional compression behavior of Kızılırmak sand.

4. To define stiffness (E_{TRX}) correlations for Kızılırmak sand on the basis of elasto-plastic constitutive models.

5. To define shear strength and state parameters specific for Kızılırmak sand.

1.3   Scope of the Thesis

Following this introduction, a brief summary of the available literature focusing on the sand behavior in terms of shearing and volumetric responses, and aspects that affect these behaviors is presented in Chapter 2.

In Chapter 3, detailed testing program, descriptions of test equipment, sample preparation techniques, and testing procedures are discussed.

Test results and their interpretation are presented in Chapter 4. They are discussed in both conventional Mohr-Coulomb failure, stress-strain, and critical state domains. Also, test results are compared with the available literature.

In Chapter 5, the conceptualized constitutive modeling of Kızılırmak sand is presented. Linear elastic and nonlinear elastic-perfectly plastic constitutive modeling parameters are developed on the basis of triaxial test results, and elastic moduli are suggested for Kızılırmak sand.

Finally, a summary of this research is presented, and major conclusions and recommendations are listed in Chapter 6.

CHAPTER 2

LITERATURE REVIEW

2.1 Introduction

Soil behavior has been studied over many decades, which resulted in a valuable and an extensive literature on this topic. A humble, yet comprehensive summary of available literature will be presented in this chapter. Firstly, shear straining response of sands will be explained. Related to that response, critical state concepts will be explained. Secondly, one-dimensional straining response of sands will be briefly introduced. Finally, stiffness of sandy soils will be discussed.

2.2 Shear Straining Response of Sandy Soils

Sandy soils behave differently under different density and stress states. These parameters together control whether the soil has dilative or contractive behavior. Loading conditions are also important when sandy soil behavior is taken into consideration. During loading, excess pore water pressure is accumulated followed by a relatively fast dissipation due to porous structure of sandy soils, immediate upon the completion of loading. Therefore, a significant portion of stresses is carried by soil grains. This loading type is simulated by drained experiments in laboratory testing. On the other hand, if the loading rate is faster than the excess pore water dissipation rate, excess pore water pressure continues to accumulate. Therefore, negative or positive excess pore water pressures, depending on the density and stress states of soils, will be built up. This loading type is simulated by undrained tests in the laboratory environment. The loose and dense soil responses change depending on the state parameters along with the type of loading: i.e.: drained or undrained (Figure 2.1).
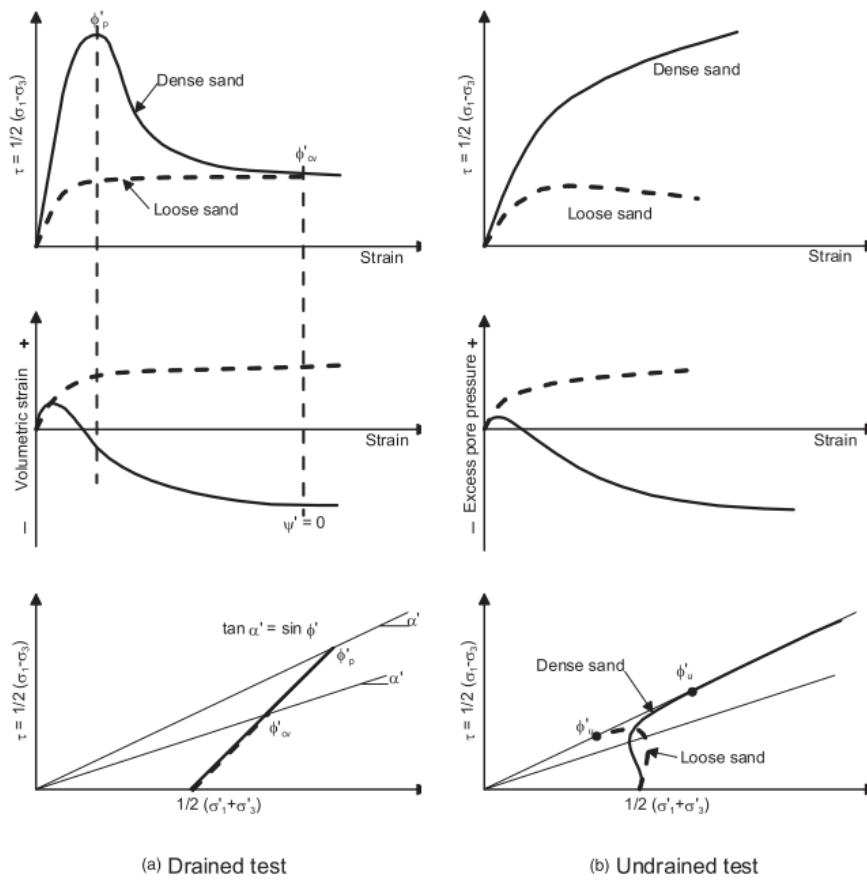
Figure 2.1. Loose and dense sand behavior under drained and undrained loading (Andersen and Schjetne, 2013)

Loose sands show contractive behavior; water dissipates with increasing strain under drained loading, which leads to a decrease in specimen's volume. No definite peak strength is observed; a hardening response up to a critical/steady state under drained loading is common. On the other hand, under undrained loading, volume cannot change, but positive excess pore water pressure builds up. Excess pore water build-up controls the stress state, or vice versa. The strength and straining responses are then governed by effective stresses. Loose sand reaches a peak strength, and then its strength decreases to critical (steady) state strength under undrained loading conditions.

Dense sand exhibits contractive behavior at small strain levels, and then it starts to dilate as strain increases. Therefore, at first, its volume decreases a little at low

strains, and during dilation, specimen's volume increases, and it absorbs water under drained loading. A peak strength is observed, and then its strength decreases to critical state strength. Under undrained loading conditions, volume will be constant. However, negative excess pore water pressure builds up during dilation, and this controls the effective stresses, which in turn controls the behavior of the sand and its strength. Dense sand does not show a definite peak strength; it hardens with increasing strain under undrained loading, i.e.: its strength will increase progressively.

As can be understood by the above discussions, the states of sandy soils relative to critical state, dilation and contraction responses control the behavior of sandy soils. The relationship between these features and sand behavior will be examined in detail in the following sections.

2.2.1   Critical State Concept

As soil is sheared up to high strain levels under constant loading, it reaches to a state at which no further volume change is observed. In this state, soil behaves as a frictional fluid, and it is called as critical state. Void ratio and the mean effective stress are the two important parameters used in critical state soil mechanics. The void ratio at the critical state is called critical void ratio, and it decreases with increasing effective stress. The relation between the critical void ratio and effective stress is called the critical state locus (CSL) (Jefferies and Been, 2006). Dense sand reaches critical state by dilation, and loose sand reaches by contraction.

Simple shear tests result, performed by Roscoe, Schofield and Wroth (1958), given in Figure 2.2, shows that all the specimens converge to a unique void ratio.
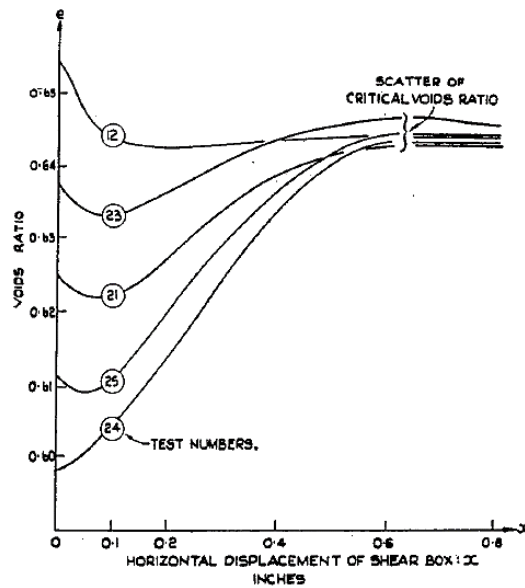
Figure 2.2. Change in void ratio with shear displacement (Roscoe *et al.*, 1958)

Schofield and Wroth (1968) classified soils as "wet soil" if their state is looser than the critical state. During deformation under drained conditions, wet soil dissipates water to reach critical state, and its volume decreases (contraction). If it is sheared under undrained condition, its effective stress decreases, by an increase in pore water pressure, to be able to reach to the critical state. The soil, which is denser than critical state, is classified as "dry soil". During deformation under drained conditions, water is absorbed ("dry soil") to reach to critical state, and its volume increases (dilation). If it is sheared under undrained conditions, negative pore pressure needs to be generated to be able to increase effective stresses, which is necessary to reach to critical state (Figure 2.3).
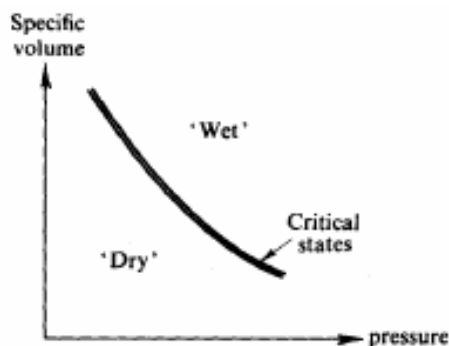
Figure 2.3. Critical states in the specific volume vs. pressure space along with the position of the wet and dry state (Schofield and Wroth, 1968)

8

In a drained test, critical void ratio is defined as the void ratio at which the soil under shearing is not subjected to any volume change. In an undrained test, critical void ratio is defined as the void ratio, at which the effective stress remains constant during shearing. If one unique line is obtained under different loading paths of both drained and undrained tests, that line is defined as the critical void ratio line Roscoe *et al*. (1958). The critical void ratio line is a projection of a curve in an e-p'-q space. This curve is presented in Figure 2.4.
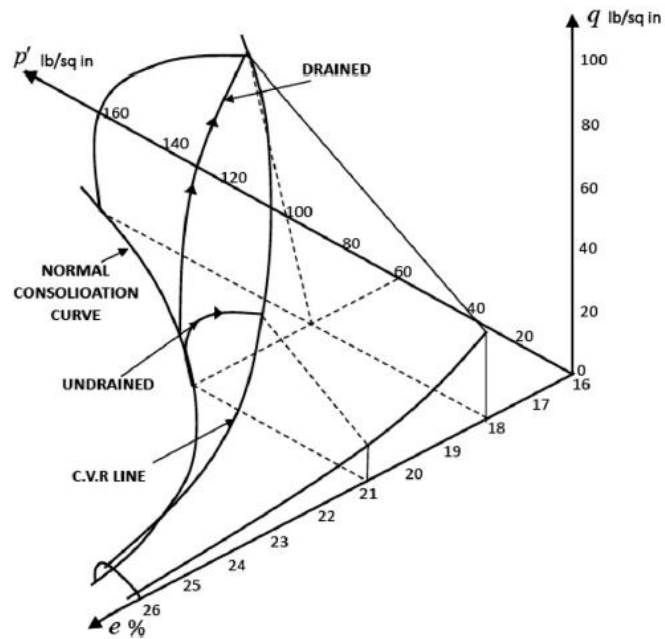
Figure 2.4. Critical state line, drained and undrained loading paths in e-p'-q space (Roscoe *et al.*, 1958)

At this point, the definition of the steady state and the critical states should be explained in order to prevent confusion. At critical state, the specimen behaves like a frictional fluid and keeps its volume constant. The plastic yielding occurs continuously without any q or v change. On the other hand, steady state is defined as "a soil can flow at a constant void ratio, constant effective minor principal stress, and constant shear stress" by Castro and Poulos (1977). Poulos (1981) pointed out that the main differences between critical state and the steady state are as; (i) "an oriented flow structure" where the soil grains flow in the direction of the shearing and, (ii) "constant velocity" at which the strain rate is also constant. In critical state,

these two conditions remain undefined. Therefore, steady state is widely accepted by the researchers as a specific version of critical state.

The historical development of critical state and steady state concepts is presented in Figure 2.5.
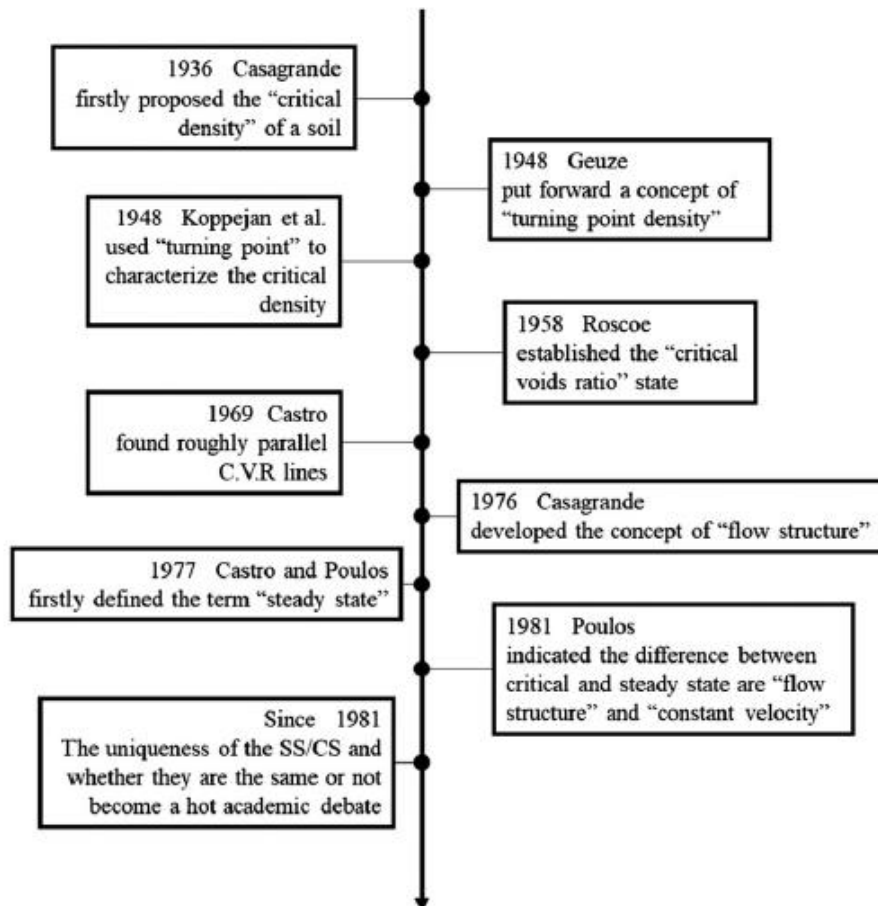
Figure 2.5. A brief summary of the development of the critical state and steady state concepts (Kang *et al.*, 2019)

The factors that influence the critical/steady states are briefly given in Figure 2.6. Since the researchers have a different perspective on the subject, there is not a consensus about the governing factors that influence the critical/steady state (Kang *et al.*, 2019).
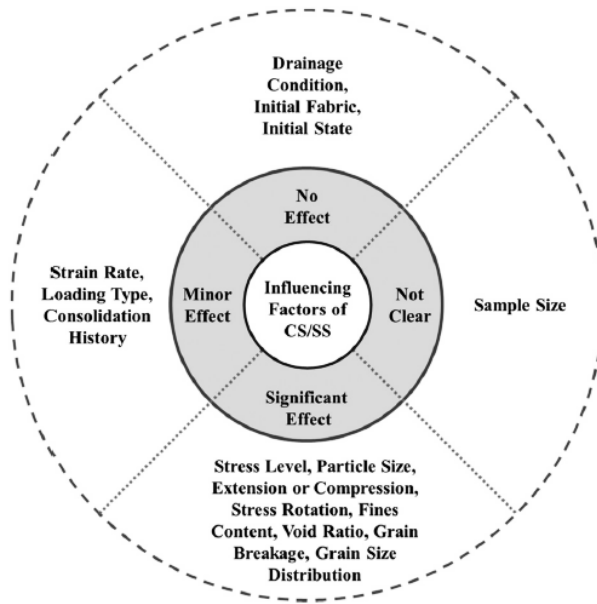
Figure 2.6. Factors effecting the critical/steady state (Kang *et al.*, 2019)

Experimental evidence of the critical state line is presented in Figure 2.7. Simple shear tests performed by Stroud (1971) on sand specimens over a range of stresses lie on a line in the specific volume at critical state vs. logarithm of the stress plot.
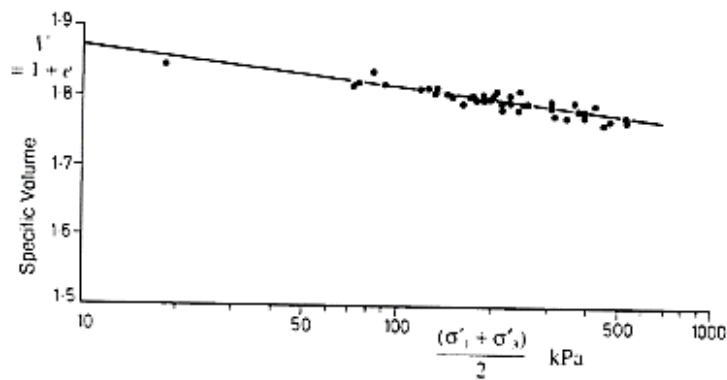
Figure 2.7. Critical state line as defined by a simple shear test data (Stroud, 1971)

The critical state line is defined by Eqn. 2-1 and Eqn. 2-2, as given by Schofield and Wroth (1968):

$$q = Mp'$$ Eqn. 2-1

$$\Gamma = v + \lambda lnp'$$ Eqn. 2-2

11

where q is the deviator stress, M is the frictional constant, p' is the mean effective stress, v is the specific volume, Γ is the specific volume at a reference stress (generally 1 atm. pressure), and λ is the slope of the critical state line.

2.2.2   Dilation

Sand tends to expand or contract its volume to be able to reach to critical state while undergoing shear deformation. This behavior is called dilatancy. Volume expansion is accepted as positive dilatancy, and the volume contraction is accepted as negative dilatancy in soil mechanics. Within the confines of this thesis, positive dilatancy will be referred to as "dilative behavior". Similarly, negative dilatancy will be referred to as "contractive behavior". There are two different approaches followed to define dilatancy; (i) absolute definition and, (ii) rate definition. Absolute definition considers the change in the volume relative to its initial condition, and rate definition considers the rate of volume change (Jefferies and Been, 2006). The differences are illustrated in Figure 2.8.
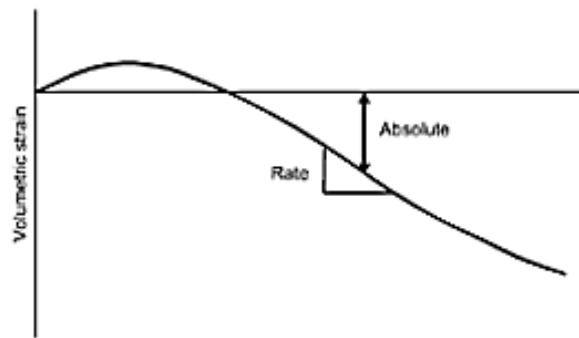
Figure 2.8. Absolute and rate definitions of dilatancy (Jefferies and Been, 2006)

Initial relative density and confining stress are the two major factors that affect dilatancy. Dense soils tend to dilate (expand in volume), and loose soils tend to contract (decrease in volume) to reach to critical state. Soils sheared under high confining stresses exhibit contractive, and soils sheared under low confining stresses exhibit dilative responses. These two mechanisms control overall dilatancy response.

Barden, Ismail and Tong (1969) tested River Welland sand in a plane strain compression test and concluded that dense soil under high confining stresses mimicked loose soil response. At high stress levels, particle crushing occurs, and dilation is overcome by those high stresses. Figure 2.9 shows the River Welland sand test results. It is seen in the figure that the specimen, which is consolidated to a lower confining pressure, shows dilative response when compared to the specimen prepared at the same initial porosity but consolidated under higher confining pressure. Furthermore, the specimen, which is prepared at lower initial porosity, but consolidated to the same confining pressure, shows more dilative behavior compared to the one that was prepared at higher initial porosity.
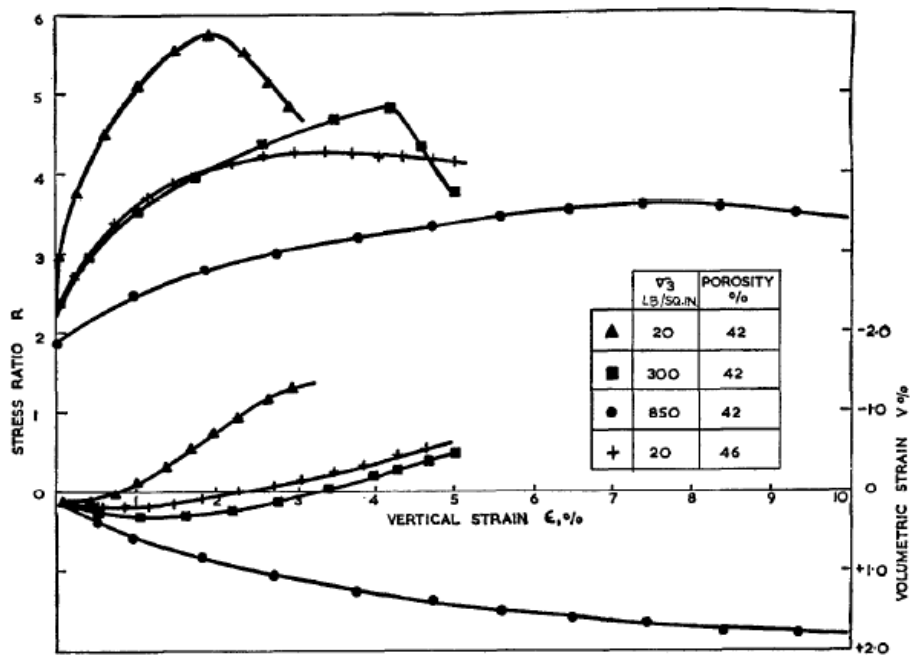
Figure 2.9. Test results of the River Welland sand (Barden *et al.,* 1969)

Bishop's (1966) study on Ham River sand shows the influence of initial relative density on dilation. Based on test results of Ham River sand, it is seen that volume change responses differ between initially loose and dense specimens under low confining stress (Figure 2.10). Denser specimen dilates more when compared to looser specimen. However, at high confining stress levels, dilation tendency decreases and even disappears.

13
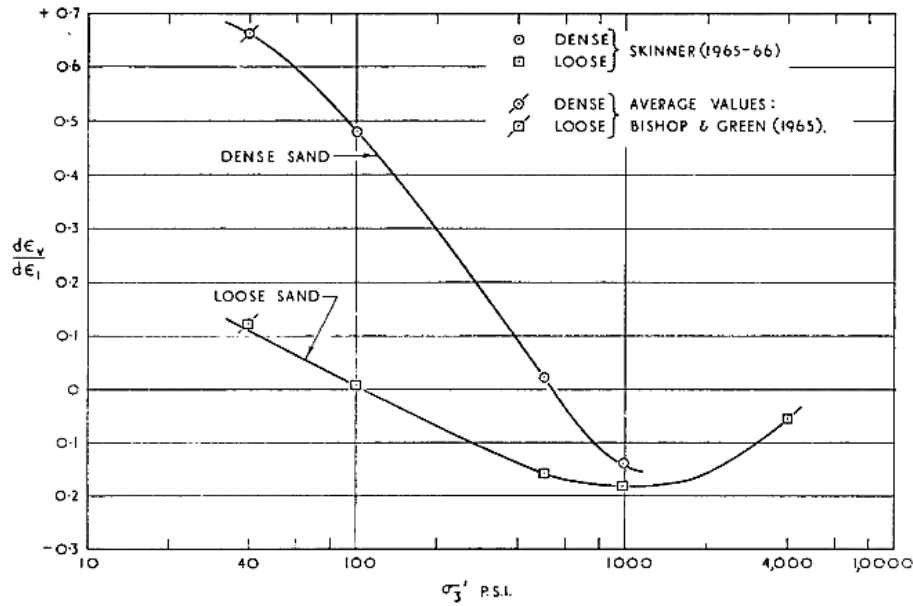
Figure 2.10. Test results of the Ham River sand (Bishop, 1966)

The effect of particle crushing on dilatancy is explained by Bishop (1966) as "at initial stages, local crushing occurs with increasing stresses", that is, intrusions and the protrusions on the sand or gravel particles are crushed. Therefore, volume increase (dilation) due to particles climbing over each other is lost. At higher stresses, sand and gravel grains themselves start to fracture. After these crushing mechanisms, dilation considerably decreases. In the light of these explanations, it is understood that particle shape is another critical factor that affects dilatancy. Angular particles tend to dilate more when compared to rounded ones.

2.3   Shear Strength of Sandy Soils

After discussing the shear straining response, shear strength concepts and the factors affecting it will be discussed next. The shear strength of sandy soils depends on many factors such as initial relative density, confining stress, particle morphology, mineralogy, fabric, gradation, boundary conditions, and loading path (Alshibli and Cil, 2018).

14

Shear strength estimation by following two different approaches i) classical soil mechanics and, ii) critical state soil mechanics approaches will be examined in the following sections.

2.3.1   Classical Soil Mechanics Concepts for Strength Assessments

In classical soil mechanics, the Mohr-Coulomb failure criterion is widely used as a failure criterion. Shear strength is defined as given in Eqn. 2-3;

$$\tau = c' + \sigma' * tan\phi' \qquad \text{Eqn. 2-3}$$

where c' is cohesion, σ' is the effective confining stress, and ϕ' is the angle of shearing resistance.

In this study, clean sand is used so that its cohesion value is known to be zero. Therefore, consistent with this, cohesion term will not be assessed. Confining stress and angle of shearing resistance terms will be the main focus in the following discussions.

2.3.1.1   Effective confining stress

Soil strength increases with increasing confining stress. In Figure 2.11, Mohr circles of drained and undrained tests are presented, and it can be seen that the shear strength increases with increasing confining stress.
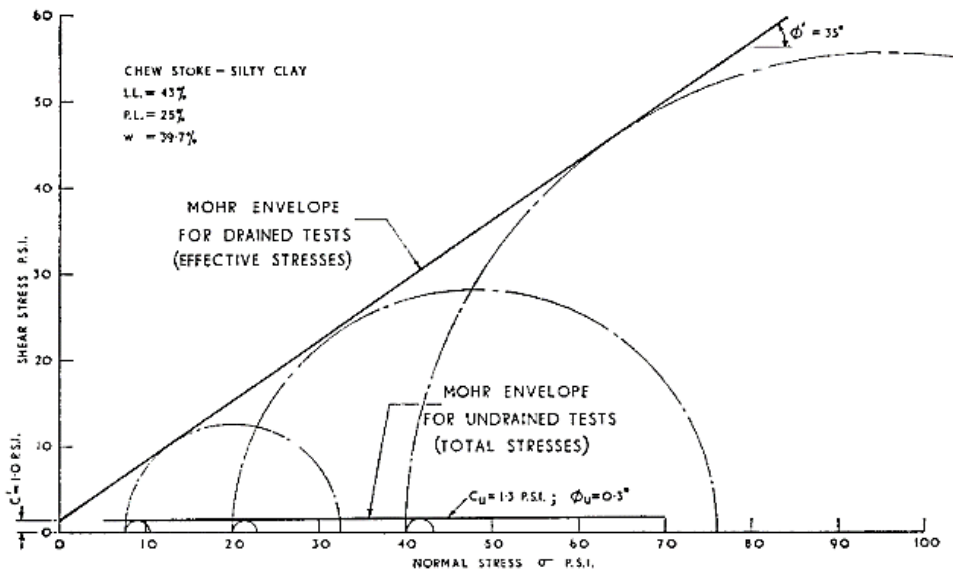
Figure 2.11. Mohr circles and failure envelopes for drained and undrained tests (Bishop, 1966)

Figure 2.12 presents the Ham River sand drained test results taken from Bishop (1966). From these results, the effect of confining pressures on the shear strength is clearly understood. In both dense and loose specimens, shear strength increases with increasing confining stress levels.

16
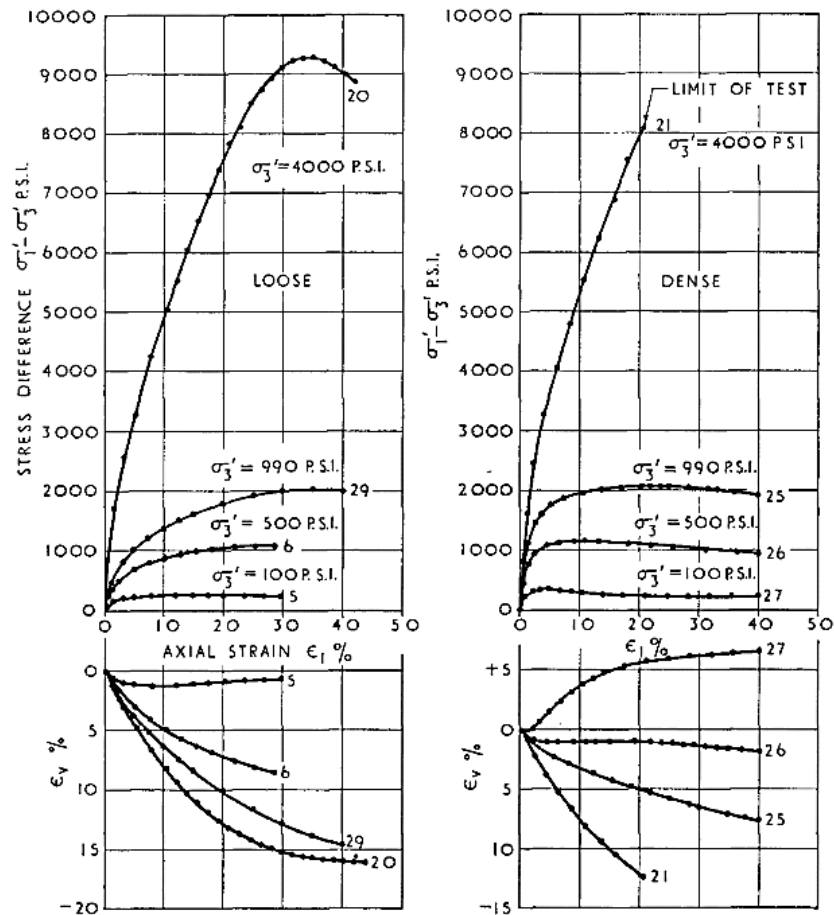
Figure 2.12. Stress-strain and volumetric strain vs. axial strain plots of Ham River sand (Bishop, 1966)

2.3.1.2   Angle of shearing resistance

The angle of shearing resistance is the other strength parameter of Mohr-Coulomb failure criterion. It is a function of critical state friction angle and dilatancy. Recall from section 2.2.2; dilatancy is governed by initial relative density, confining stress, and particle shape and size effects, etc.

Friction and dilation angles can be estimated from the Mohr circle and the Mohr-Coulomb failure envelope (Figure 2.13).
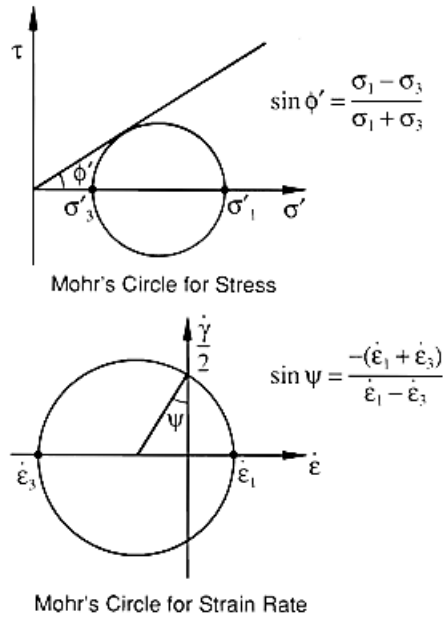
Figure 2.13. Friction angle and dilation angle definitions (Houlsby, 1991)

Bolton (1986) stated that the critical state/constant volume friction angle (ϕ_{cv}) is a function of particle mineralogy. It also depends on particle shape. A typical value is roughly suggested by Bolton (1986) as 33° for quartz and 40° for feldspar. By itself, the critical state friction angle is not sufficient to determine the friction angle of a specimen. Because of dilation, specimen gains an extra shearing resistance; therefore, it has a higher friction angle (ϕ_{max}) than its critical state friction angle. Higher rate of dilation ($d\varepsilon_v / d\varepsilon_a$) results in higher ϕ_{max}. The difference between ϕ_{max} and ϕ_{cv} is defined as dilation angle (ψ). Maximum friction angle (ϕ_{max}) and dilation angle (ψ) are defined by Bolton (1986) as given in Eqn. 2-4 and Eqn. 2-5;

$$\sin \phi'_{max} = \left[\frac{\tau_{13}}{(\sigma_1' + \sigma_3')/2} \right]_p \qquad \text{Eqn. 2-4}$$

$$\sin \psi_{max} = \left(-\frac{d\varepsilon_v}{(d\gamma_{13})} \right)_p \qquad \text{Eqn. 2-5}$$

where τ_{13}: shear stress at the peak, σ_1': major principal stress at the peak, σ_3': minor principal stress at the peak, $d\varepsilon_v$: change in the volumetric strain at the peak, $d\gamma_{13}$: change in the shear strain at the peak.

Here ϕ' represents secant friction angle, determined by the line which passes through the origin and drawn tangent to Mohr circles. Elementary relation between friction and dilation, as suggested by Bolton (1986), is given in Eqn. 2-6;

$$\phi' = \phi'_{crit} + \psi \qquad \text{Eqn. 2-6}$$

where ϕ'_{crit} is critical state friction angle and ψ dilation angle.

Sliding of granular particles along each other can be explained with an analogy with a sawtooth, as given in Figure 2.14. If one flat block slides on another flat block, the friction between surfaces is defined as the ratio of the normal stress to the shear stress given in Eqn. 2-7;

$$\frac{\tau}{\sigma_n'} = \tan \phi'_{cv} \qquad \text{Eqn. 2-7}$$

where τ: shear stress, σ_n': normal effective stress, ϕ'_{cv}: constant volume friction angle.

If the surface between blocks is a rough surface (like soil grains), then this rough surface can be represented by a sawtooth shape. The angle of the sawtooth teeth by the horizontal is ψ, and from simple statics, the friction between surfaces now equals to;

$$\frac{\tau}{\sigma_n'} = \tan \phi' = \tan(\phi'_{cv} + \psi) \qquad \text{Eqn. 2-8}$$

Summation of the friction angle at the constant volume and the dilation angle gives the resulting friction angle. This type of definition of the relation between friction angle and the dilation angle is called flow rule.
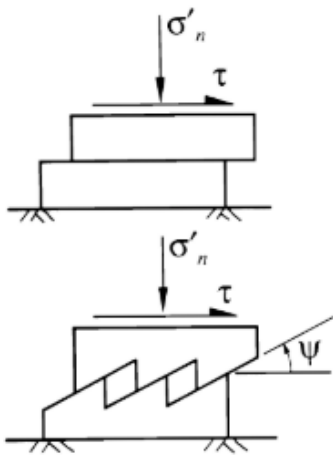
Figure 2.14. The sawtooth analogy for
dilatancy (Houlsby, 1991)
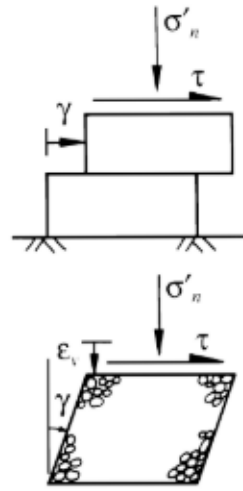
Figure 2.15. Taylor's energy correction analogy
(Houlsby, 1991)

Taylor's energy correction approach is another alternative to relate friction and the dilation angles. Taylor (1948) equates the work done by the external forces to the dissipation of the energy during sliding. Taylor's energy correction analogy is presented in Figure 2.15.

Energy correction approach can be implemented to soil response in simple shear with the addition of the normal stress term in the work-done as follows;

$$\dot{W} = \sigma'_n\dot{\varepsilon}_v + \tau\dot{\gamma} = \left(\tan\phi'_{cv}\right)\sigma'_n\dot{\gamma} \qquad \text{Eqn. 2-9}$$

where σ'_n: effective normal stress, $\dot{\varepsilon}_v$: volumetric strain rate, τ: shear stress, $\dot{\gamma}$: shear strain rate, ϕ'_{cv}: constant volume friction angle

From the $tan\phi' = \tau/\sigma'_n$ and $tan\psi = -\varepsilon_v/\gamma$ definitions, the relation between friction angle and the dilation becomes as in Eqn. 2-10;

$$\tan\phi' = \tan\phi'_{cv} + \tan\psi \qquad \text{Eqn. 2-10}$$

Rowe (1962) puts an effort to define the relation between friction and dilation angles on the basis of tests performed using steel balls. First, stress ratio σ'_1/σ'_3 and the strain ratio $\varepsilon_3/\varepsilon_1$ are defined for the regular structure of spheres. Then an analogy

between soil particles and irregularly structured spheres is introduced. Sliding is assumed to take place on the sawtooth plane, as shown in Figure 2.16.
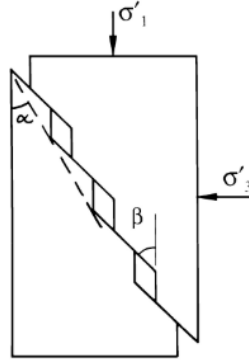
Figure 2.16. Rowe's stress-dilatancy mechanism (Houlsby, 1991)

The stress ratio is expressed as in Eqn. 2-11;

$$\frac{\sigma'_1}{\sigma'_3} = \frac{\tan(\phi_\mu + \beta)}{\tan \beta} \frac{\dot{\varepsilon}_3}{\dot{\varepsilon}_1}$$

Eqn. 2-11

where ϕ_μ is the fundamental angle of friction for grain-to-grain contact. Rowe (1962) considers the minimum energy ratio to derive $\beta = \pi/4 - \phi_\mu/2$. The final expression is;

$$\frac{\sigma'_1}{\sigma'_3} = \tan^2\left(\frac{\pi}{4} + \frac{\phi_u}{2}\right)\left(\frac{-\dot{\varepsilon}_3}{\dot{\varepsilon}_1}\right)$$

Eqn. 2-12

As an alternative to these theoretical relations, an empirical relation can also be used. Bolton (1986) suggests an empirical fit by using an extensive database on friction and dilation angles. The empirical equation is given as follows;

$$\phi' = \phi'_{crit} + 0.8\psi$$

Eqn. 2-13

The approaches discussed above were compared by Houlsby (1991) in Figure 2.17. Bolton's empirical fit and Rowe's approach give very close predictions, and they fall in the middle of the lines recommended by alternative approaches. The problem with these relations is that each failure mode needs different constants, e.g., constant fiction angle is different in simple shear and triaxial compression tests.
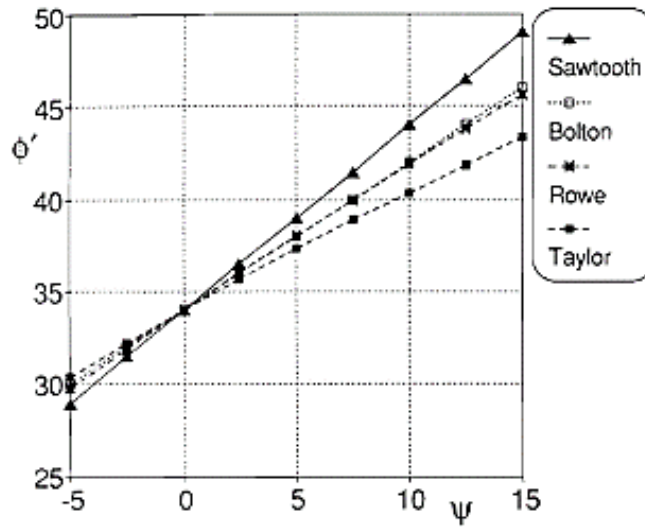
Figure 2.17. Comparison of friction and dilatancy angles estimations (Houlsby, 1991)

To examine the behavior of sand, Bishop (1966, 1972) performed experiments on the deformable but unbreakable steel shot and confirmed that the maximum friction angle reduces with an increase in confining pressure. In granular soils, particle breakage under high stress levels also affects the dilation as well as maximum friction angles (Vesic and Clough, 1968; Bishop, 1972).

In Figure 2.18, Bolton (1986) presents the Mohr circles for dense specimens under low and high confining pressures. As the figure reveals, under high pressures, dilation angle and maximum friction angle (i.e., shear strength) of dense sands are estimated to be lower than those values obtained under low pressures. Based on these, it can be said that higher pressures reduce the maximum friction angle (ϕ_{max}).

22
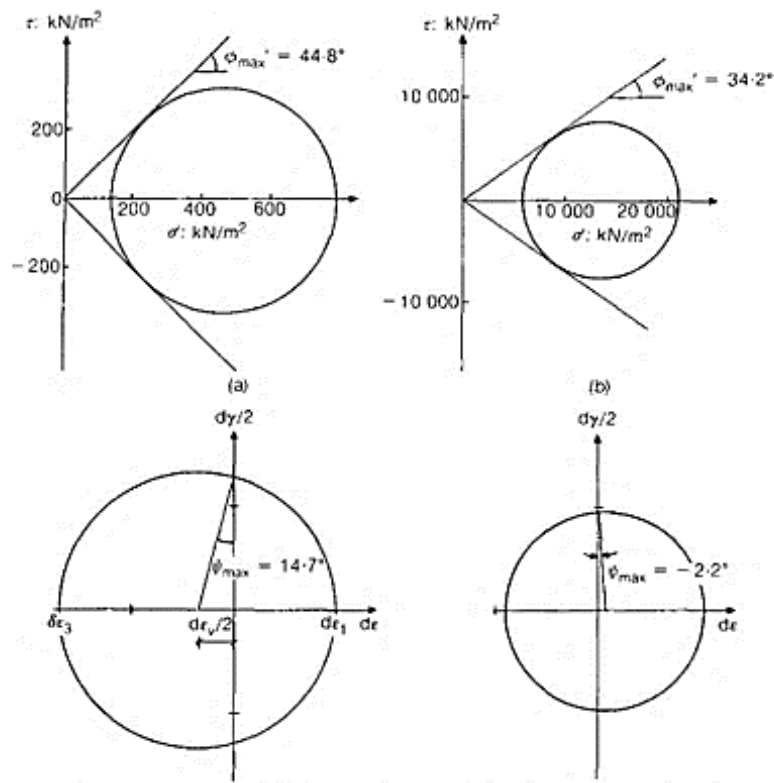
Figure 2.18. Mohr circles for the specimens under low pressure and high pressure (Bolton, 1986)

Bishop (1966) compiled a database of friction angle vs. effective stress data from different soil specimens, as presented in Figure 2.19.
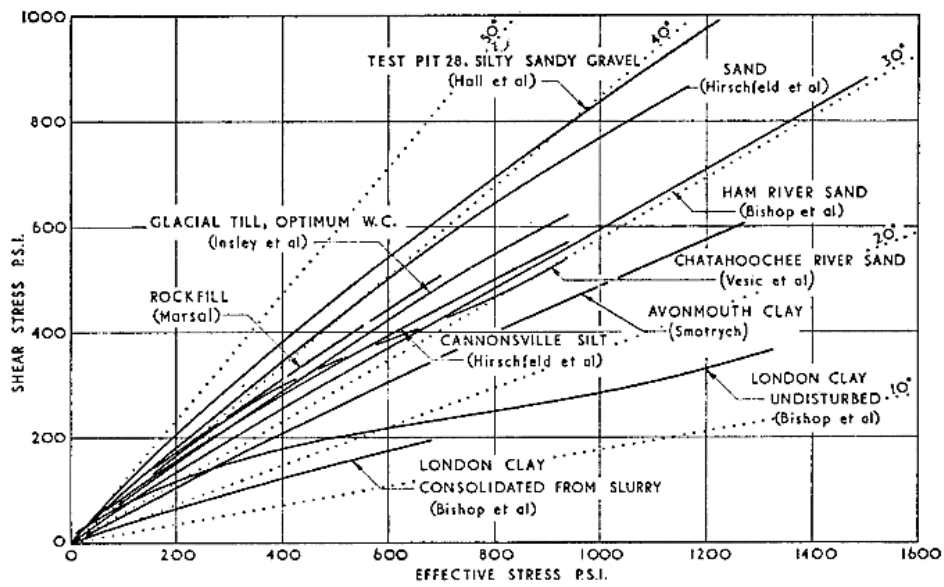
Figure 2.19. Failure envelopes for different types of sandy soils (Bishop, 1966)

From this figure, it can be seen that Mohr-Coulomb failure envelopes have curved-shapes with a decreasing slope by increasing effective stress. This means that friction angle decreases with increasing effective stress. Curved-shape Mohr-Coulomb envelopes are observed more clearly on granular soil tests. This can be attributed to particle crushing as suggested by Bishop (1966). In Figure 2.20, at low confining pressures, friction angle difference between a loose and a dense soil sample is approximately 6°, and this difference is closing gradually with the increasing effective stress. After 1000 psi, friction angles became the same for the initially dense and loose specimens (Bishop, 1966).
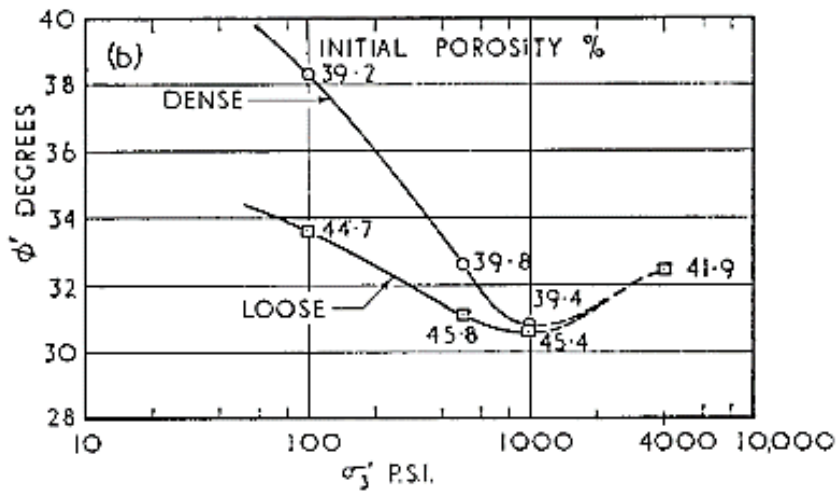
Figure 2.20. Friction angle vs. effective stress relation (Bishop, 1966)

Cornforth (1973) defines a density factor to find a relation between relative density and friction angle. He normalized the maximum strength by dividing it by its ultimate strength, and defines this ratio as a density factor. He observed that the density factor increases with increasing relative dry density. The relation between normalized maximum strength and relative dry density gives the strength that comes from the density component. The difference between drained strength parameter (ϕ_d) obtained from plain strain and triaxial compression tests increases with increasing relative density, and the plain strain tests always produce higher values. The ultimate friction angle of the sand is almost constant without being affected by relative density.

24

The relation between dry density factor and density component (ϕ_{dc}) is given in Figure 2.21. Since these curves are dimensionless, friction angle can be calculated for a given density and ϕ_{cv}. Calculated friction angle values for a given ultimate strength friction angle are summarized in a graph given in Figure 2.22.
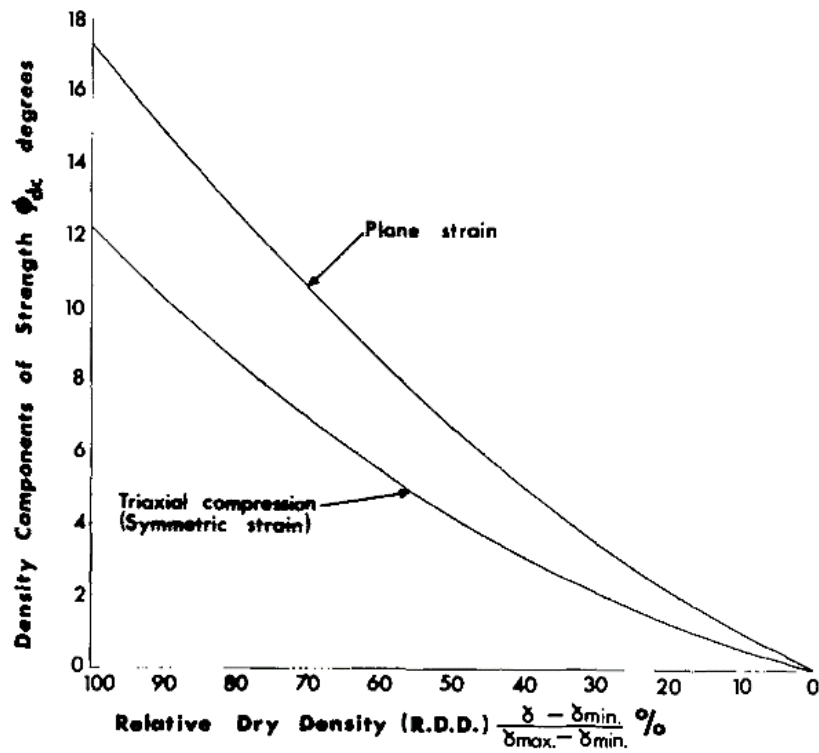
Figure 2.21. The relation between density component of strength and relative dry density for plane strain and triaxial compression tests (Cornforth, 1973)
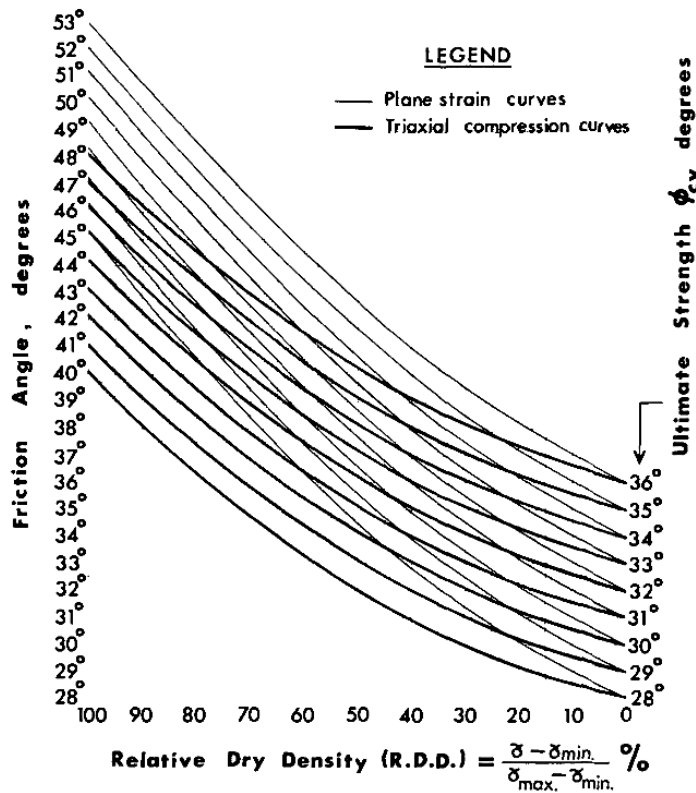
Figure 2.22. The relation between friction angle and relative dry density for plane strain and triaxial compression tests (Cornforth, 1973)

Bolton (1986) correlates the maximum friction angle with both relative density and confining stress by defining a relative dilatancy index term, as defined in Eqn. 2-14 through Eqn. 2-16.

$$I_R = I_D(10 - lnp') - 1 \qquad \text{Eqn. 2-14}$$

$$lnp'_{crit} = Q - \frac{R}{I_D} \qquad \text{Eqn. 2-15}$$

$$I_D = \frac{e_{max} - e}{e_{max} - e_{min}} \qquad \text{Eqn. 2-16}$$

where I_R is relative dilatancy index, I_D is relative density, e_{max} is the maximum void ratio, e_{min} is the minimum void ratio, e is specimen's void ratio, p'_{crit} is mean effective stress at failure, and Q is a material constant.

For plain strain test;

26

$$\phi'_{max} - \phi'_{crit} = 0.8\psi = 5I_R°$$ Eqn. 2-17

For triaxial strain test;

$$\phi'_{max} - \phi'_{crit} = 0.8\psi = 3I_R°$$ Eqn. 2-18

For both tests;

$$\left(-\frac{d\varepsilon_v}{d\varepsilon_1}\right)_{max} = 0.3I_R°$$ Eqn. 2-19

I_R in between 0 and 4.

where ϕ'_{max} is the peak angle of shearing resistance, ϕ'_{crit} is the critical state angle of shearing resistance, ψ is the dilation angle, I_R is the relative dilatancy index, ε_v volumetric strain, and ε_1 is the major principal strain

Experiment results by Andersen and Schjetne (2013) indicate that maximum friction angle increases with increasing relative density, and decreases with increasing confining stress. Stress levels higher than 5 MPa results in crushing and suppresses the dilation. Therefore, maximum friction angle decreases. Test results also showed that at these high stress levels, initial relative density contribution on the friction angle disappears. In their study, it is stated that the angular particles have higher maximum friction angles when compared to rounded ones. A small relation between mean particle size (D_{50}) and maximum friction angle is discovered: maximum friction angle has higher values when the specimens have higher D_{50}. A relation between the coefficient of uniformity (C_u) and the friction angle cannot be verified.

Andersen and Schjetne (2013) also compiled undrained effective stress friction angle data, as shown in Figure 2.23. The data support that increasing relative density increases friction angle. However, no apparent effect of confining stress, when it is higher than 100 kPa, on the friction angle is observed.
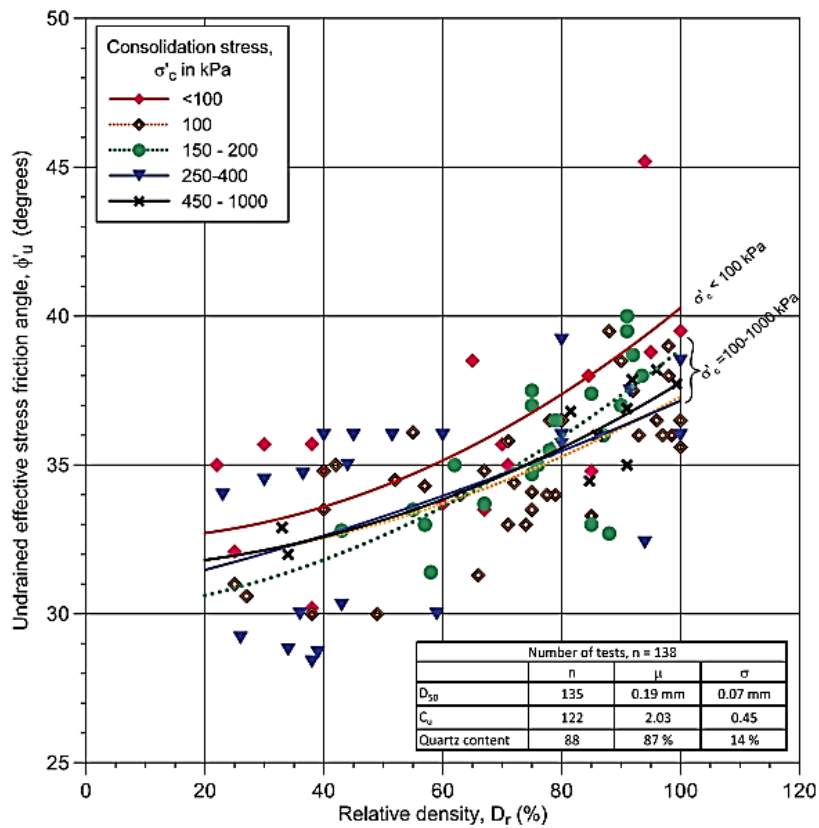
Figure 2.23. Undrained effective stress friction angle (ϕ'_u) vs relative density (Andersen and Schjetne, 2013)

The relation between relative density and undrained effective stress friction angle (ϕ'_u), drained peak friction angle (ϕ'_p), and drained constant volume friction angle (ϕ'_{cv}) is shown in Figure 2.24. The difference between constant volume friction angle and drained peak friction angle increases with increasing relative density. Similar trend is observed on the relation in constant volume friction angle and undrained effective stress friction angle.
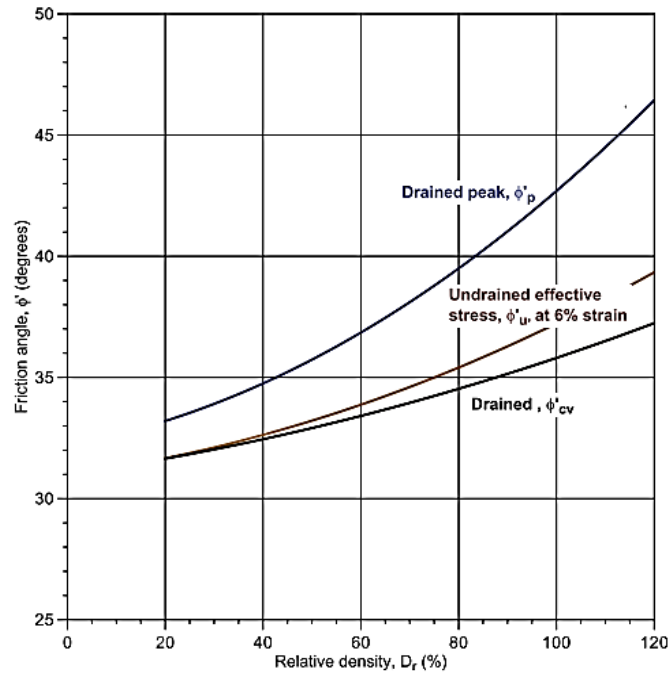
Figure 2.24. Change in the difference of ϕ'_p-ϕ'_u-ϕ'_{cv} with relative density (Andersen and Schjetne, 2013)

Koener (1968) states that internal friction angle of granular materials is affected by angularity and gradation, as well as other factors. Angular particles show higher friction than rounded ones. In their experimental study, Alshibli and Alsaleh (2004) observed that the friction angle increases by angularity and particle roughness. Shape and angularity were studied in 2D images by Alshibli and Alsaleh (2004). Alshibli and Cil (2018) investigated the particle characterization and its effect on the friction angles and dilatancy of uniform silica sand from 3D images. In this recent study, they examined the particle characterization in terms of sphericity (I_{sph}), roundness (I_R), elongation (F), and surface texture (R_q). After the experiments, they concluded that particle fracture did not depend on specimen density, but on type of sand. As presented in Figure 2.25, dilatancy angle increased with I_R, R_q and D_r, whereas it decreased with p'_0/p_{atm}. There was no clear trend between dilatancy and F. This might be because of the combined effect of F, R_q and I_R. Alshibli and Cil (2018) proposed equations (Eqn. 2-20 - Eqn. 2-22) for ϕ_{cs}, ϕ_p and ψ which were functions of F, I_R, R_q, D_r and p'_0/p_{atm}.
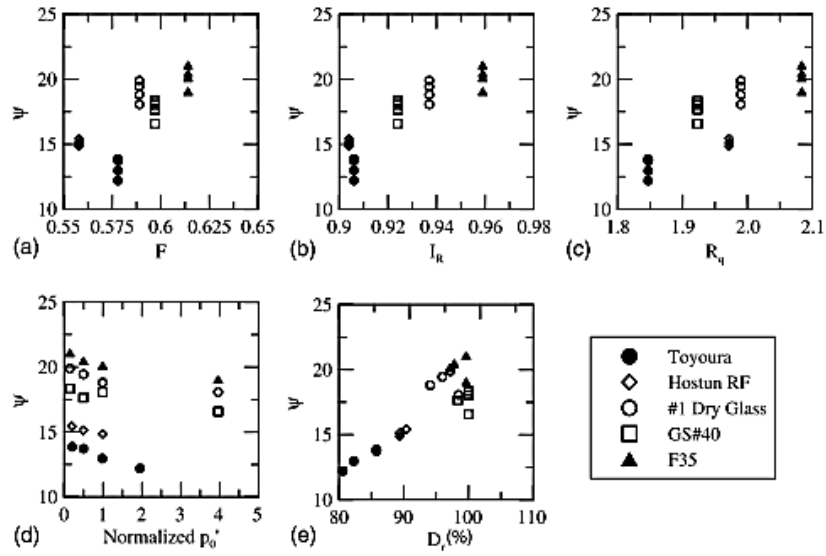
Figure 2.25. Relation between dilatancy angle and (a) form, (b) roundness, (c) surface texture, (d) normalized mean effective stress, (e) relative density (Alshibli and Cil, 2018)

$$\phi_{cs} = 23 - 134.06F + 142.04I_R - 21.02R_q - 0.861\left(\frac{p'_0}{p_{atm}}\right) + 0.043D_r \quad \text{Eqn. 2-20}$$

$$\phi_p = 23 + -62.90F + 67.00I_R - 9.02R_q - 0.932\left(\frac{p'_0}{p_{atm}}\right) + 0.160D_r \quad \text{Eqn. 2-21}$$

$$\psi = 77.720F - 76.35I_R + 12.77R_q - 0.486\left(\frac{p'_0}{p_{atm}}\right) + 0.196D_r \quad \text{Eqn. 2-22}$$

2.3.2   Basic Concepts of Critical State Soil Mechanics

As previously discussed in chapter 2.2.1, critical state is a state at which soil is subjected to unlimited shear deformation without any volume and stress change. In this chapter, shear strength and soil behavior assessments by using critical state soil mechanics concepts will be discussed.

Been and Jefferies (1985) suggested a state parameter to express behavior of sands. State parameter represents both density and stress state effects on response of sands. They define the state parameter as the distance between current state and steady state of the sand's void ratio at the same stress state (Figure 2.26).
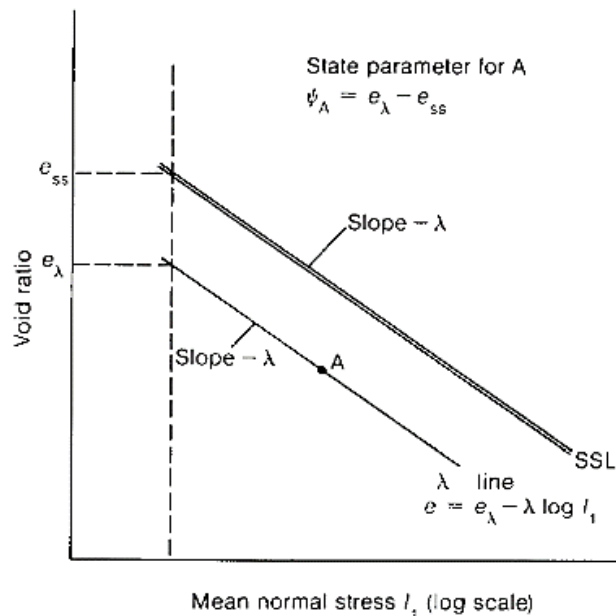
Figure 2.26. State parameter as defined by Been and Jefferies (Been and Jefferies, 1985)

They stated that similar state parameters lead to similar behavior independent of initial void ratio and effective stress combinations. In Figure 2.27, the behavior of specimens with test ID of 103 and 108, and 112 and 45 are similar, although they have different initial void ratios. This similarity is because of the similar state parameter values. Despite the fact that specimens 37 and 103, and 112 and 113 have the same initial void ratios, but they behave differently. This figure tells us, relative density by itself is not a good parameter to represent the overall behavior. The state parameter is a simple, single parameter that combines both stress and density state effects. However, attention should be paid that the state parameter concept does not consider the fabric, which also affects the behavior of sand.

Test	e	I_{1c} kPa	D_r %	ψ
37	0·71	350	33	+ 0·03
103	0·71	50	33	− 0·03
108	0·65	300	50	− 0·033

Test	e	I_{1c} kPa	D_r %	ψ
45	0·67	350	56	0·11
112	0·58	1100	75	0·11
113	0·59	152	72	− 0·04
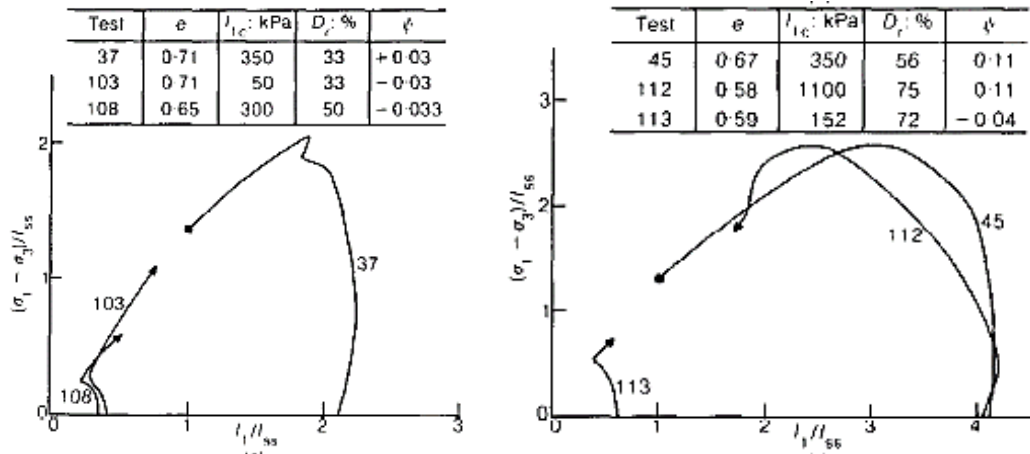
Figure 2.27. Stress paths of Kogyuk sand for samples at the same relative density and state parameter (Been and Jefferies, 1985)

Been and Jefferies (1985) observe a good correlation between normalized strength and normalized pore pressure and state parameter (Figure 2.28). They also present friction angle and state parameter relation (Figure 2.29) for different sands compiled from the literature. They explain the scatter in this figure with the lack of fabric effects in definition of the state parameter.
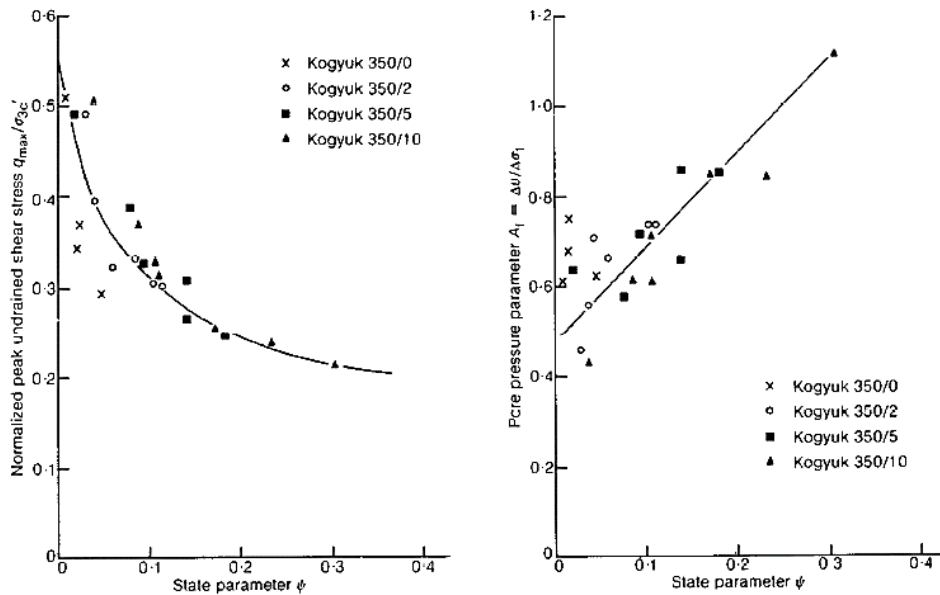
Figure 2.28. The relation between normalized undrained shear stress and pore pressure parameter and state parameter (Been and Jefferies, 1985)

32
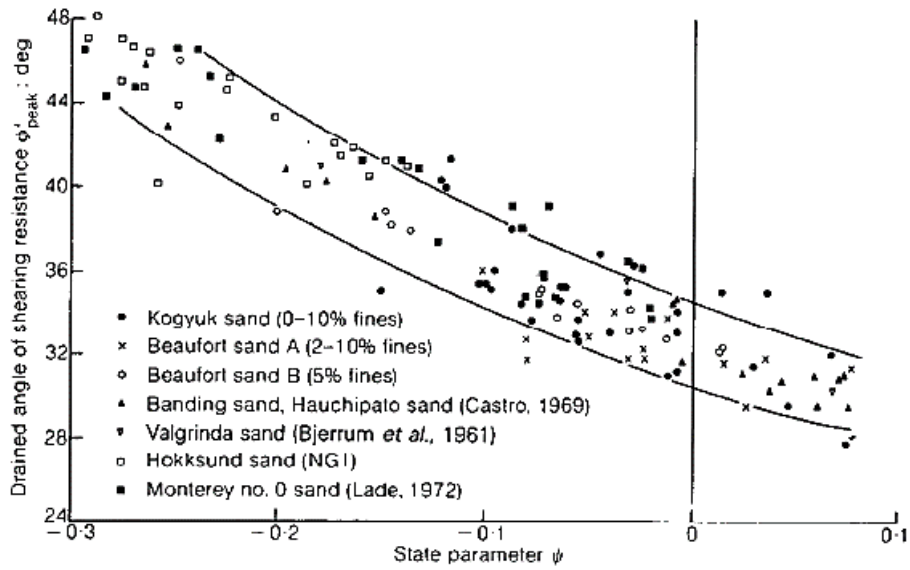
Figure 2.29. The relation between friction angle and state parameter for different sands (Been and Jefferies, 1985)

Ishihara (1993) argues to the statement that sand specimens behave similarly if their state parameter values are similar. He stated that this argument holds for the medium and dense sands under relatively high confining stress. However, when the void ratio is high, the behavior of the sand is more sensitive to the small variations in the void ratio. Moreover, in the case of medium and dense sand under relatively small confining stress, again, the use of a state parameter concept is judged not to be reliable. In order to cover these drawbacks of the state parameter, he suggests a state index (I_s) as given in Eqn. 2-23 and presented in Figure 2.30.

$$I_s = \frac{e_0 - e}{e_0 - e_s}$$

Eqn. 2-23

where e_0 is the threshold void ratio which divides the zero and non-zero residual strength responses. Specimens prepared looser than e_0 have zero steady state strength. e_s is the void ratio on quasi-steady state curve, and e is the void ratio of the specimen. p'_{cr} is the intersection of the $e = e_0$ line and the isotropic compression line of the sample prepared at the loosest possible state.

33
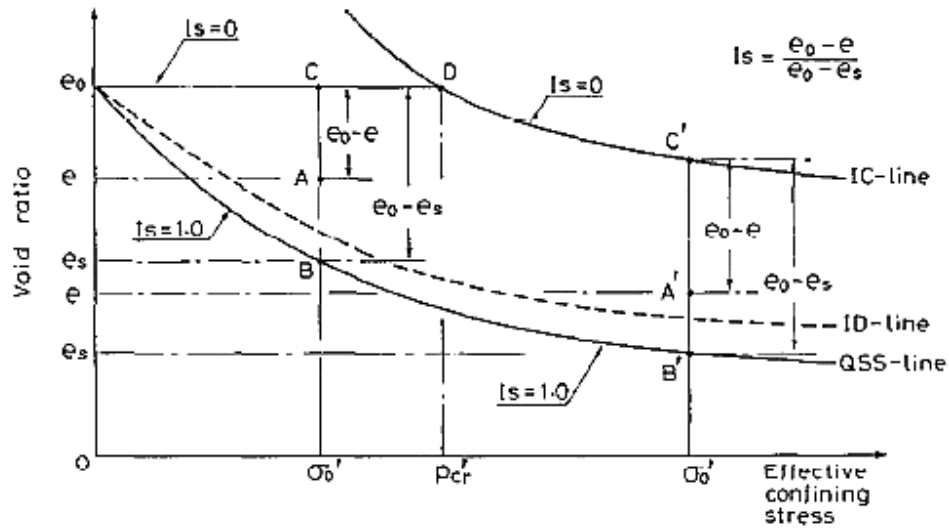
Figure 2.30. Definition of state index, I_s (Ishihara, 1993)

Sand specimens that have similar state index show similar behavior (Figure 2.31); however, the quantitative values of shear strength or mean effective stress values depend on the initial confining stress. In addition, it is important to state that I_s is specific to the specimen preparation technique or mode of sand deposition. The fabric significantly affects the void ratio at zero strength and the quasi-steady state line (Ishihara, 1993).

34

(a) I$_s$=1.93-1.98   (b) I$_s$=0.6-0.7
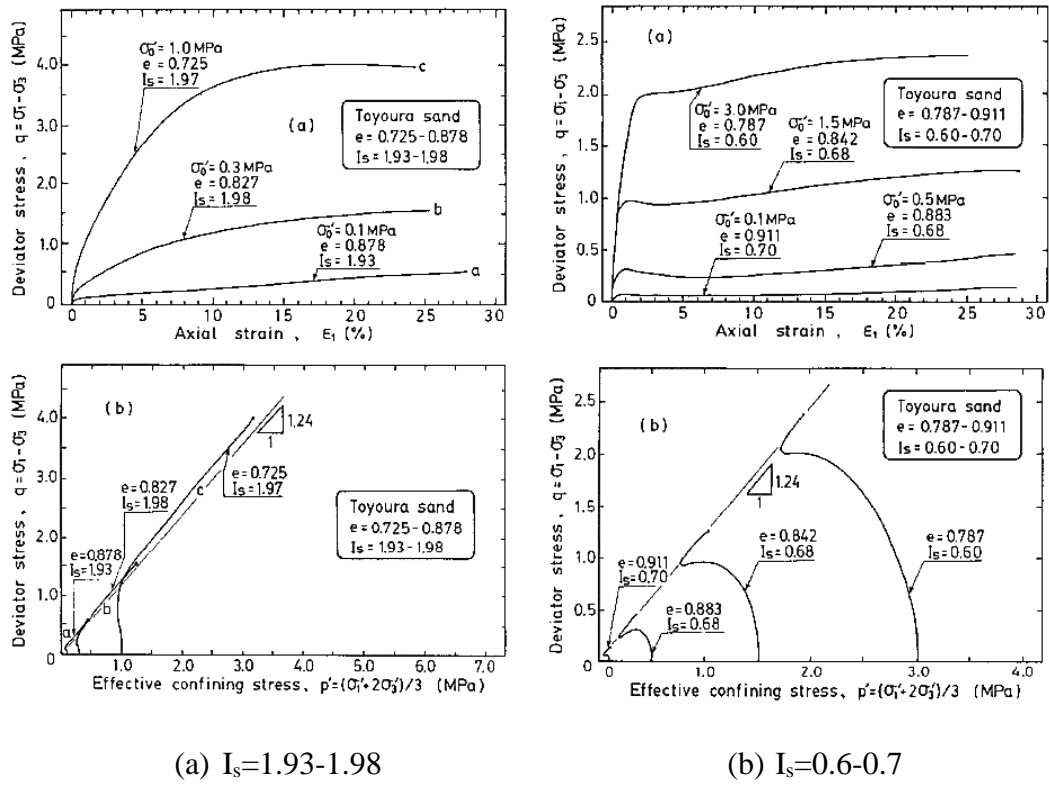
Figure 2.31. Comparison of stress-strain and stress path plots of Toyoura sand at the state index 1.93-1.98 and 0.6-0.7 (Ishihara, 1993)

Figure 2.32 reveals that normalized peak strength has a linear relationship with the state index.
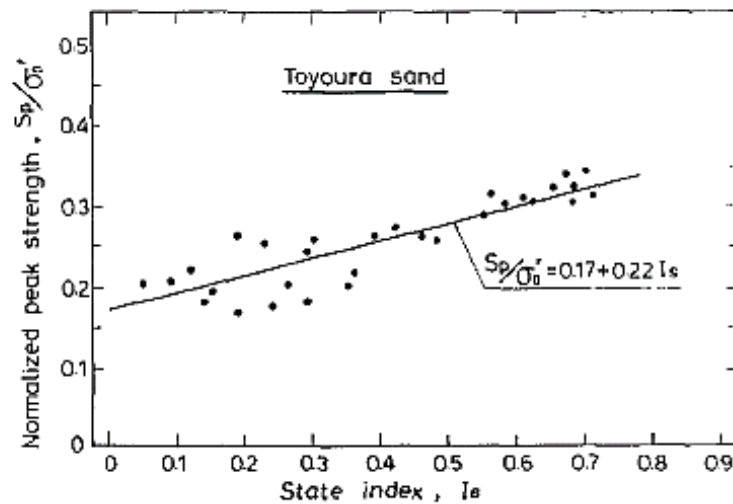
Figure 2.32. The relation between normalized peak strength and state index (Ishihara, 1993)

2.4   Volumetric Straining Response of Sandy Soils

Volumetric straining behavior controls the volumetric settlements of soils. Sand subjected to vertical stress is re-packed due to the inter-particle slip and rotation of the grains. It is compressed, and its volume decreases due to loading. Its stiffness may decrease or increase according to the mechanism behind the volumetric behavior.

Two particle response mechanisms are observed when soils are loaded vertically; locking and unlocking mechanism. Engaging of the particles to each other and compression (i.e., re-packing of the grains) are the components of locking mechanisms. Interparticle friction should be overcome for rearrangement of the grains. Interparticle slip and particle damage are the unlocking mechanisms. Again, when the interparticle friction is overcome, interparticle slip occurs. When particle strength is exceeded, particle damage occurs. Particle damage is classified into three levels; level I, level II, and level III. Level I damage is the erosion of the particle surface roughness. Level II damage is the crushing of the angular particle's corners and/or crushing of the particle's protrusions. Level III damage is the crushing, fracturing of the particle itself (Roberts and de Souza, 1958; Marsal, 1967; Hardin, 1985; Coop, 1990; Pestana and Whittle, 1995; Nakata, Kato, *et al.*, 2001; Chuhan *et al.*, 2002, 2003).

Volumetric behavior is controlled by the net effect of the locking and unlocking mechanisms. When locking mechanism overcomes the unlocking, constrained modulus (M) increases. When unlocking dominates the response, constrained modulus decreases. If they are in balance, no change in the constrained modulus is observed (Chuhan *et al.*, 2002, 2003; Mesri and Vardhanabhuti, 2009).

Volumetric straining response of granular materials can be examined in terms of primary compression and secondary compression behavior. Primary compression occurs under increasing stress, and secondary compression response occurs under constant stress. End of primary compression void ratio (EOP void ratio) vs. logarithm

of the effective vertical stress ($log\sigma'_v$) plot represents the primary compression behavior. Primary compression behavior of the granular materials is divided into three; Type A, Type B, and Type C responses (Mesri and Vardhanabhuti, 2009).

In Type A compression behavior, there are three stages of the compression behavior. In the first stage, locking mechanism overcomes the unlocking, and constrained modulus increases with effective vertical stress. At this stage, level I and level II particle damages are observed (e.g., Vaid, Chern and Tumi, 1985; Yudhbir and Rahim, 1987; Rahim, 1989). In the second stage, unlocking overcomes the locking, and decrease in constrained modulus is observed with increasing effective stress. At this stage, level III particle damage is reported (Cundall and Strack, 1979; McDowell and Harireche, 2002). In the final stage, increase in constrained modulus is observed (locking dominates the unlocking). Level I, II, and III particle damages occur. Beginning of the second stage is defined as the effective stress corresponding to maximum constrained modulus ($\sigma'_v(M_{Max})$). Similarly, the end of the second stage is defined as the effective stress corresponding to minimum constrained modulus ($\sigma'_v(M_{Min})$). These points are interpreted from the EOP void ratio vs. effective vertical stress plot as the first and second inflection points (Mesri and Vardhanabhuti, 2009).

Type B compression behavior is a transition between Type A and C. It is similar to Type A, since it displays three stages. It is similar to Type C, since constrained modulus does not decrease with increasing effective stress. In the first stage, locking dominates the unlocking, and M increases with increasing effective stress. In the second stage, locking and unlocking effects are in balance, and M does not change with vertical effective stress. In the final stage, M increases with effective vertical stress (Nakata, Hyodo, *et al.*, 2001; Nakata, Kato, *et al.*, 2001; Chuhan *et al.*, 2003). Mesri and Vardhanabhuti (2009) defines $\sigma'_v(M_{Max})$ and $\sigma'_v(M_{Min})$ as the same in Type A, start, and the end of the second stage.

In Type C behavior, decrease in M is not observed. Locking mechanism overcomes the unlocking mechanisms during vertical loading (e.g. Pestana and Whittle, 1995).

Level I and II particle damages are observed effectively at low stress stage, and particle damage continues with level III at high stress levels (Coop, 1990, 1993; Chuhan *et al.*, 2003).

Type A compression behavior generally observed in clean, well-rounded, and strong coarse particles such as mono-quartz sand (Nakata, Kato, *et al.*, 2001; Chuhan *et al.*, 2002), whereas Type C behavior generally observed in angular and weak particles such as carbonate sands (Hardin, 1985; Chuhan *et al.*, 2002, 2003). Type B is less common compression behavior when compared to Type A and C behavior.

Examples of EOP void ratio vs. effective vertical stress plots of Type A, B, and C compression behavior are taken from Mesri and Vardhanabhuti (2009) study and presented in Figure 2.33 through Figure 2.35.
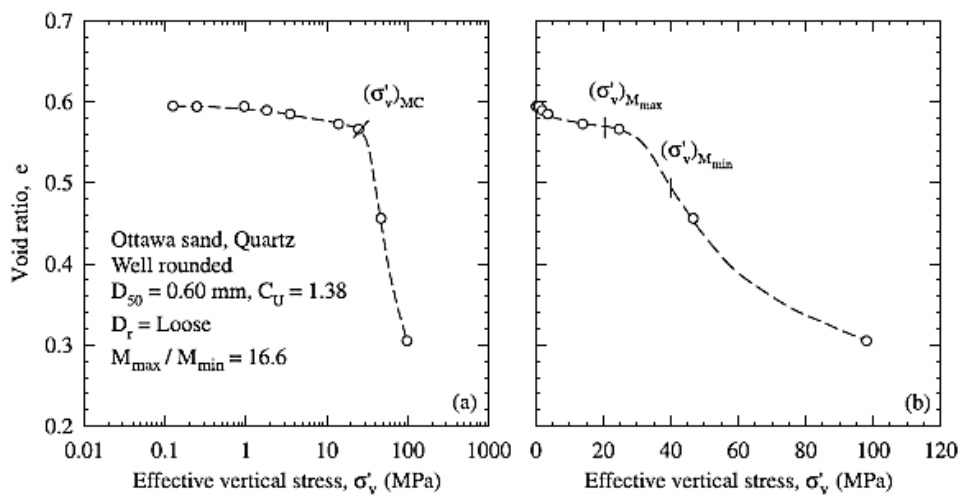
Figure 2.33. An example of Type A compression behavior (Mesri and Vardhanabhuti, 2009)
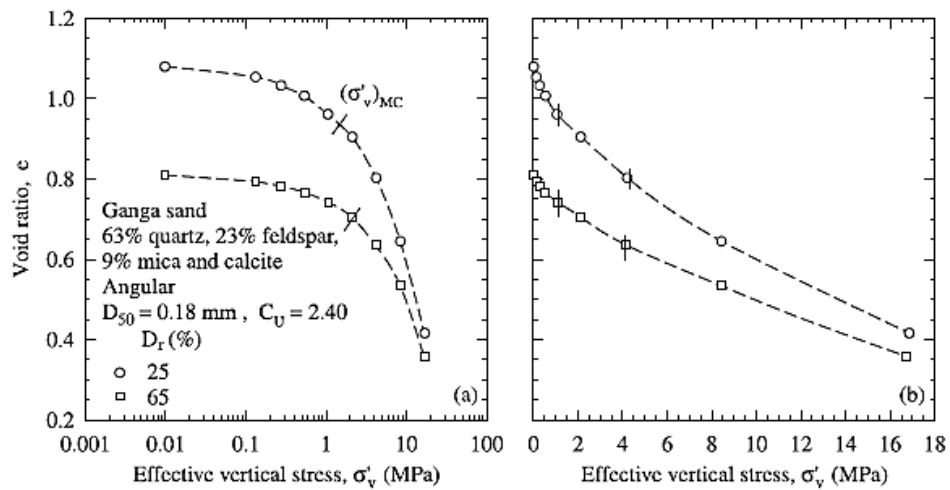
Figure 2.34. An example of Type B compression behavior (Mesri and Vardhanabhuti, 2009)
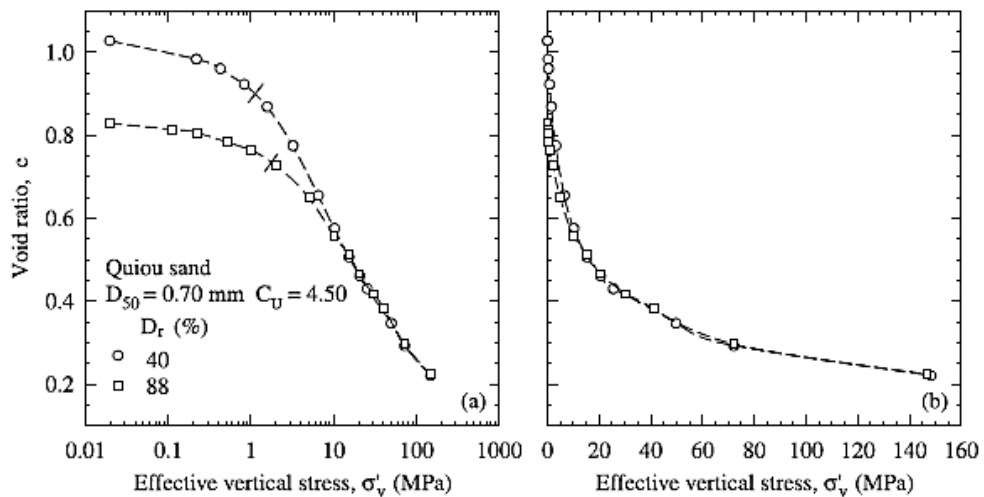
Figure 2.35. An example of Type C compression behavior (Mesri and Vardhanabhuti, 2009)

When granular particles are crushed, they go under irrecoverable deformation. Particle crushing causes change in the mechanical behavior of sandy soils, such as an increase in compression behavior. Therefore, a sudden change in the void ratio vs. logarithm of stress plot is observed. This point of abrupt change, corresponding to the maximum curvature of the void ratio vs. logarithm of the stress plot, is defined as "yield point" by Roberts and de Souza (1958) and "break point" by Roberts (1965). Chuhan *et al.* (2003) and Nakata, Kato, *et al.* (2001) state that this yield point is a sign of particle crushing. Hagerty *et al.*, (1993); McDowell, Bolton and Robertson (1996); Nakata, Hyodo, *et al.* (2001); Nakata, Kato, *et al.* (2001); McDowell and

39

Harireche (2002); Chuhan *et al.* (2003) are the other researchers that define yield stress as the maximum curvature of the $e - log\sigma'_v$ plot. Different then these definitions, Mesri and Vardhanabhuti (2009) defines yield stress as the stress where M_{max} is observed.

Hagerty *et al.* (1993) present the compression test results as a graph of $D_{50}/D_{50uncrushed}$ vs. maximum stress of the corresponding test (Figure 2.36). He defines the breakage stress as the stress corresponding to $D_{50}/D_{50uncrushed}$ ratio to be 1.
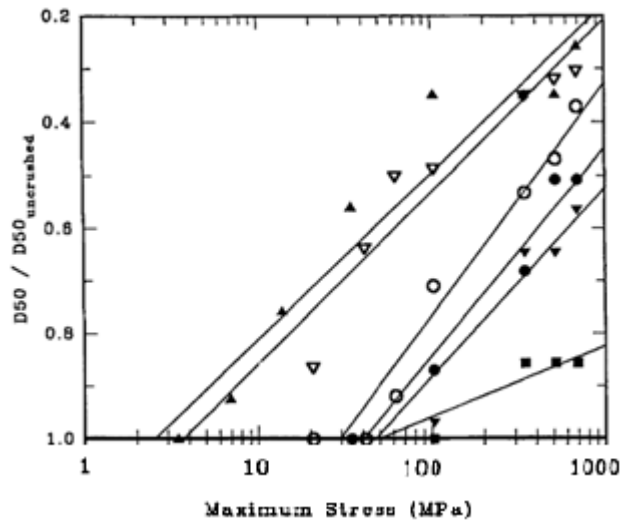
Figure 2.36. $D_{50}/D_{50uncrushed}$ vs. stress plots (Hagerty *et al.*, 1993)

The ratio of M_{max}/M_{min} is used to see the degree of a sudden change in the particle damage. High M_{max}/M_{min} values are reported for the well-rounded, coarse, uniform, and strong particles. There is an abrupt change from stage one to two in these types of particles. However, there is a smoother transition in the well-graded sands (McDowell and Bolton, 1998; Nakata, Hyodo, *et al.*, 2001).

Increase in stiffness during loading because of densification of granular material was observed in a study by Wu, Yamamoto and Izumi (2016). This increase can be understood from the shape of stress-strain plots in Figure 2.37. Hagerty *et al.* (1993) explains the increase in stiffness mechanism as "At stresses above the crushing stress, the additional stress increments cause additional fracturing and extensive rearrangement of particles. Therefore, the slope of the stress-strain plot decreases

40

with increasing stress. As the mean particle size reduced and particle rearrangement causes a significant reduction in voids, the number of particle contact per volume increases. Gradually, this particle fragmentation and rearrangement leads to a reduction in average stress. The stress reduction leads to less additional crushing and increase in stiffness." He stated that although the initial properties (e.g., initial relative density, particle shape, particle mineralogy) were different, after the extensive particle crushing, specimens showed little differences in final constrained modulus.

(a) Toyoura sand
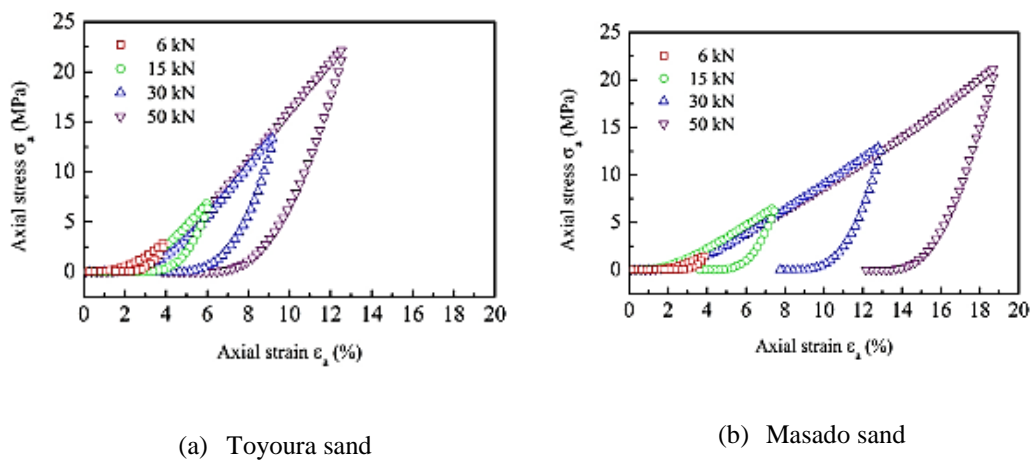
(b) Masado sand

Figure 2.37. Axial stress vs. axial strain plots of Toyoura and Masado sand (Wu *et al.*, 2016)

Studies show that all compression mechanisms (particle slipping, rotation, and crushing) continue with time. This compression behavior is called as secondary compression. Secondary compression should be differentiated from creep. Creep is defined as the time-dependent behavior under drained or undrained loading when soil is subjected to external shear stresses (e.g. Mesri *et al.*, 1981; Murayama, 1983; Murayama, Michihiro and Sakagami, 1984). However, secondary compression is used for the drained, laterally constrained, one-dimensionally loaded specimens; or drained, equal all-round loaded specimens. The major difference of these terms is explained by the statement that "the global failure may occur due to creep but cannot be observed due to secondary compression" as stated in Mesri and Vardhanabhuti (2009).

Studies on the compression behavior of granular materials show that the compression index (C_c) changes with effective vertical stress. Particle mineralogy and initial relative density affect the compression index. Particle shape is also a factor at low stresses. Chuhan *et al.* (2003) explain the angularity effects on compression behavior by stating that angular particles undergo local grain crushing at contact points. This breakage leads to an increase in contact area and a decrease in contact stresses. Therefore, the specimen becomes less compressible at higher stresses. In fact, at high stresses, major effects of grain size, grain shape, grain mineralogy on compression behavior are observed to disappear. In Figure 2.38, C_c data compiled from literature by Mesri and Vardhanabhuti (2009) is presented.
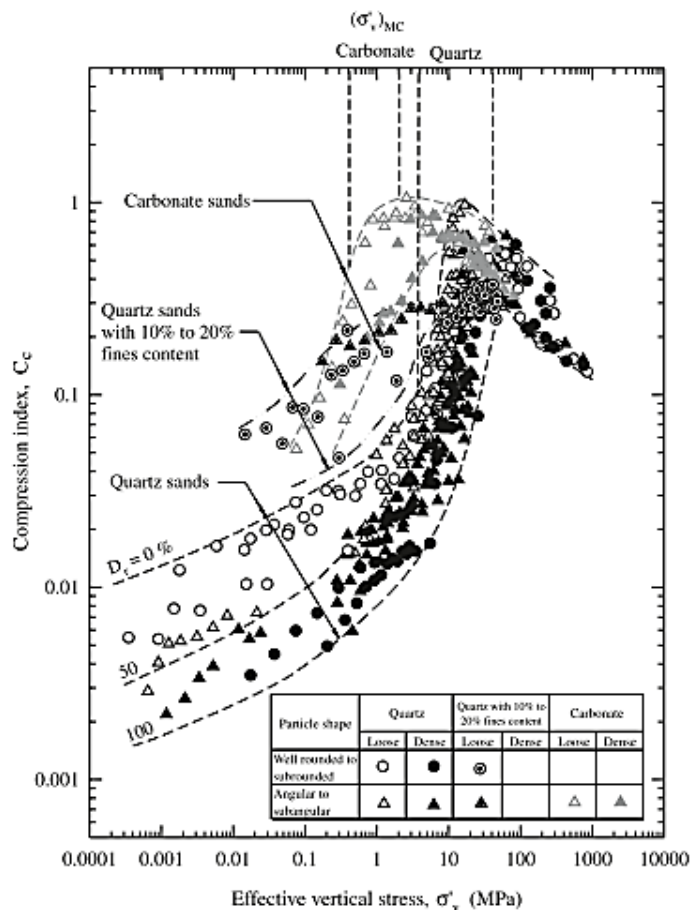
Figure 2.38. C_c vs. effective stress plot for different type of sands (Mesri and Vardhanabhuti, 2009)

In addition to the changes in the slope of $e - log\sigma'_v$ plot, the slope of $e - logt$ plot also changes under loading after crushing. The secondary compression index

42

increases with increasing effective stress and becomes significant after the yield point is passed, and particle crushing (level III) was started (Lade and Liu, 1998). The mechanism of time-dependent behavior is explained with the particle crushing in Takei, Kusakabe and Hayashi (2001). Particles are crushed into fragments, and these fragments are rearranged into a new packing. With this new packing, particle stresses are re-distributed and reach to a new equilibrium. Then, again particles are crushed under new re-arranged stress distribution. New fragments are re-arranged into a new packing, and again, stresses are re-distributed. The crushing process goes on in this pattern. For angular materials (more specifically, quartz particles in their study), time-dependent behavior is related to the breakage of angular edges and the local crushing at contact areas.

2.4.1 Factors Effecting the Particle Breakage

Particle crushing is affected by the initial relative density, gradation, median grain size, particle mineralogy, particle shape, stress path, and loading type (Roberts and de Souza, 1958; Hardin, 1985; Hagerty *et al.*, 1993; Nakata, Hyodo, *et al.*, 2001; Nakata, Kato, *et al.*, 2001).

Initial relative density - Yield stress increases with the increase in initial relative density, and level III damage is observed at higher $\sigma'_v(M_{Max})$. This response is explained as the particle crushing starting at higher stress levels on the specimens with higher initial relative density. This behavior is observed due to the lower particle stress distribution in higher relative density specimens (Roberts and de Souza, 1958; De Beer, 1963; Coop, 1993; Hagerty *et al.*, 1993; Lade, Yamamuro and Bopp, 1996; Nakata, Kato, *et al.*, 2001; Chuhan *et al.*, 2003). Therefore, particle breakage potential decreases with increasing relative density (Hardin, 1985). However, Chuhan *et al.* (2003) observed in their study that the loose and dense specimen's porosity-stress plots are joined and continue together after the yield stress of the dense specimen has been passed.

Gradation - Similar to high relative density specimens, well-graded sands have higher grain contact; therefore, lower contact stress distribution. Then, they show higher $\sigma'_v(M_{Max})$ than uniformly graded sands (Lade *et al.*, 1996; Nakata, Hyodo, *et al.*, 2001).

Particle mineralogy – Chuhan *et al.* (2003) studied the particle mineralogy effect on compression behavior by using mono-quartz sand, lithic sand, and carbonate sand. Very coarse-grained chert-rich sand and fine-grained mica-rich sand are also tested. They stated in their study that chert-rich sands have higher yield stress than other sands. Carbonate and mica-rich sand have highest porosity loss values at low stresses (0-5 MPa). Lithic sand, mono-quartz sand, and chert-rich sand follow, respectively, the carbonate and mica-rich sands in the means of porosity loss. Porosity vs. stress curves of different sands follow a general trend that the difference between the curves becomes smaller with increasing grain size, i.e., increasing grain size reduces the mineralogical effects on compression behavior. After some point, these effects disappear.

Particle shape - Significant level I and level II particle damage are observed in angular sands because of the higher tension and shear stresses at interparticle contact points. This results in lower $\sigma'_v(M_{Max})$ values. Hagerty *et al.* (1993) explain the behavior with the following hypothesis: There occurs eccentric loading on angular particles compared to spherical particles. This eccentricity is the reason of the higher shear and tensile stresses (Hagerty *et al.*, 1993; Lade *et al.*, 1996; McDowell and Bolton, 1998).

Particle size – The particle breakage potential is proportional to the particle size. It increases with increasing particle size. This is explained with the same mechanisms, valid for high relative density and well-graded sands: particle contact forces increase with particle size. Therefore, breakage increases with size (Hardin, 1985). Chuhan *et al.* (2003) studied the grain size effect on compression behavior by using mono-quartz, lithic, and carbonate sands. At low stresses (0-5 MPa), they observe a small increase in porosity loss with the increase in grain size. At intermediate stresses (5-

25 MPa), they observe a strong proportional relation between particle size and porosity loss. At high stresses (25-50 MPa), similar porosity loss values are observed for all types of sands. In addition, they stated that yield stress increases with a decrease in grain size.

Stress path - Effective stress and effective stress paths also play an important role in particle breakage. Hardin (1985) reported that breakage potential increases with increasing effective stress and increasing σ'_1/σ'_3 ratio.

Loading type - Loading mode also affects particle crushing (Altuhafi and Coop, 2011; Miao and Airey, 2013). In isotropic compression tests, level III particle damage starts at higher stresses when compared to one-dimensional tests (Kwag, Ochiai and Yasufuku, 1999; Nakata, Kato, *et al.*, 2001). The reason behind this is explained with the contribution of the shear stresses in one-dimensional compression (De Beer, 1963; Bishop, 1966; Lee and Farhoomand, 1967; Coop, 1993; Pestana and Whittle, 1995). Also, triaxial compression tests result in higher percent of particle crushing. An example of the GSD curves for different loading modes are presented in Figure 2.39.

(a) Toyoura sand
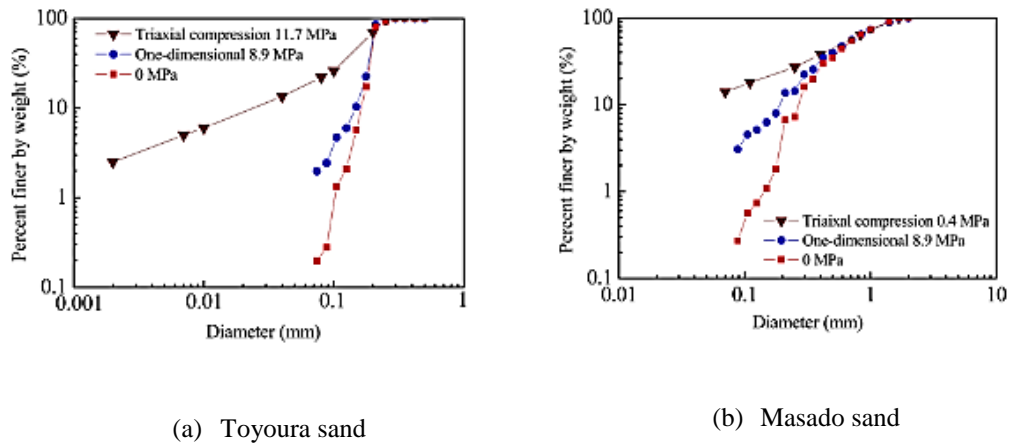
(b) Masado sand

Figure 2.39. Grain size distribution curves of Toyoura and Masado sand under triaxial compression and one-dimensional loading (Wu *et al.*, 2016)

2.4.2 Particle Breakage Measurements

The amount of particle breakage can be identified from sieve analysis which are performed on the specimens before and after the compression tests. There are some measures in the literature to express the amount of breakage quantitatively. Some of them can be listed as follows;

- Leslie (1963) used the increase in percent passing on sieve size as compared to the sieve size where original material was 100 % retained

- Later Leslie (1975) again defined a breakage measure as the increase in percent passing on the sieve size, at which the original material was 90% retained.

- Marsal (1965) defines a breakage measure as the increase in percent passing on the sieve size, at which the highest increase was observed. However, if increase in percent passing occurs at more than one diameter, breakage measure is then used as the sum of these percent passing.

- Lee and Farhoomand (1967) used the D_{15i}/D_{15a} ratio as a breakage measure. D_{15i} is the diameter of the 15% of the original sample to be finer, and D_{15a} is the diameter of the 15% of the loaded sample to be finer.

In Figure 2.40, these breakage measurement methods are presented on a GSD graph's sketch.
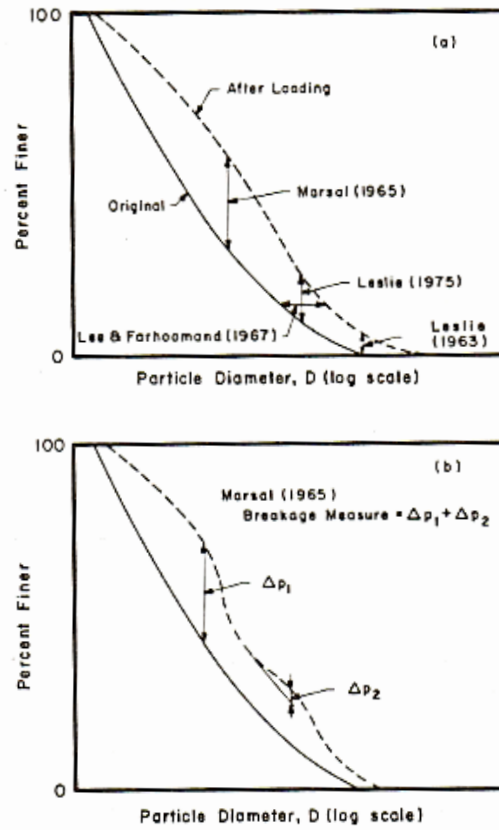
Figure 2.40. Particle breakage measurements (Hardin, 1985)

Hardin (1985) uses the relative breakage definition as a breakage measure. Relative breakage (B_r) is defined as the ratio of the total breakage to the breakage potential. All relevant parameters are defined in Eqn. 2-24a through Eqn. 2-27 and Figure 2.41.

$$b_p = \log_{10}\left[\frac{D\ (mm)}{0.074}\right]\ for\ D \geq 0.074\ mm \qquad \text{Eqn. 2-24a}$$

$$b_p = 0\ for\ D < 0.074\ mm \qquad \text{Eqn 2.24b}$$

$$B_p = \int_0^1 b_p df \qquad \text{Eqn. 2-25}$$

$$B_t = \int_0^1 (b_{p0} - b_{pl})df \qquad \text{Eqn. 2-26}$$

$$B_r = B_t/B_p \qquad \text{Eqn. 2-27}$$
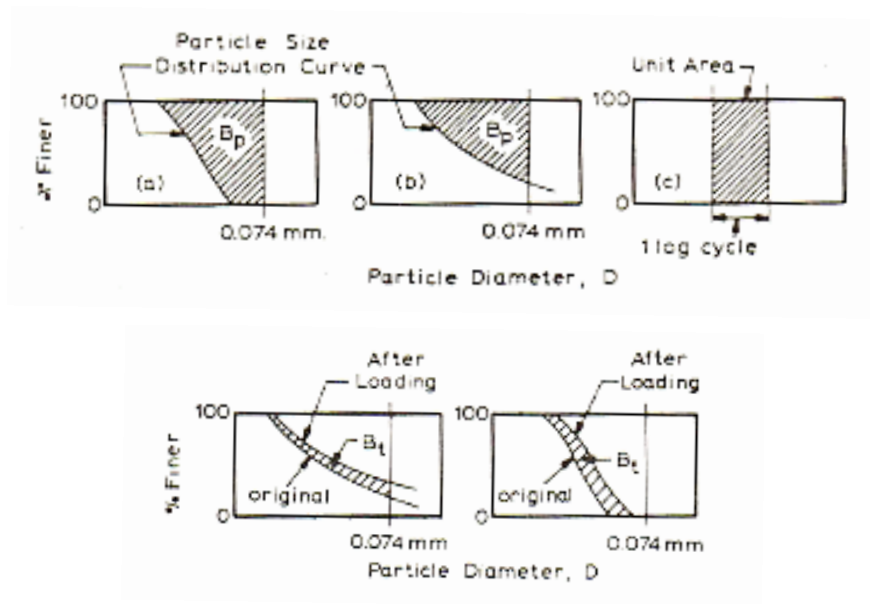
Figure 2.41. Definition of particle breakage measurement suggested by (Hardin, 1985)

2.5   Stiffness of Sandy Soils

Stiffness estimations are listed as one of the important problems in soil mechanics. The stiffness that was measured in the laboratory, and the one which was back-calculated from the observations on ground movements in the field, showed significant differences. Lately, researchers understand these differences in the light of properties of soil stiffness, especially non-linearity in the behavior (Atkinson, 2000).

Figure 2.42 presents the general stress-strain curves for undrained shearing and isotropic compression tests.

(a) Shearing   (b) Compression
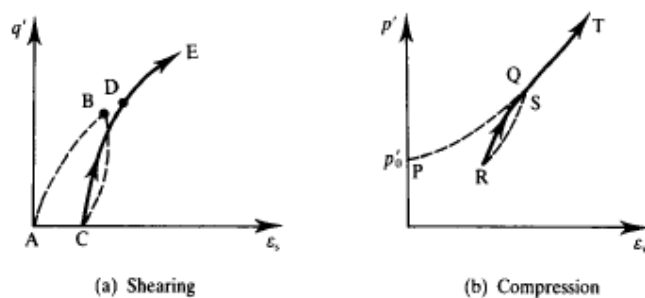
Figure 2.42. General stress-strain curves for (a) shearing and (b) compression (Atkinson, 2007)

Different modulus definitions for different tests are given in Figure 2.43. From uniaxial loading test Young's modulus, from simple shear test shear modulus, from isotropic compression test bulk modulus, and from confined compression test constrained modulus can be estimated.
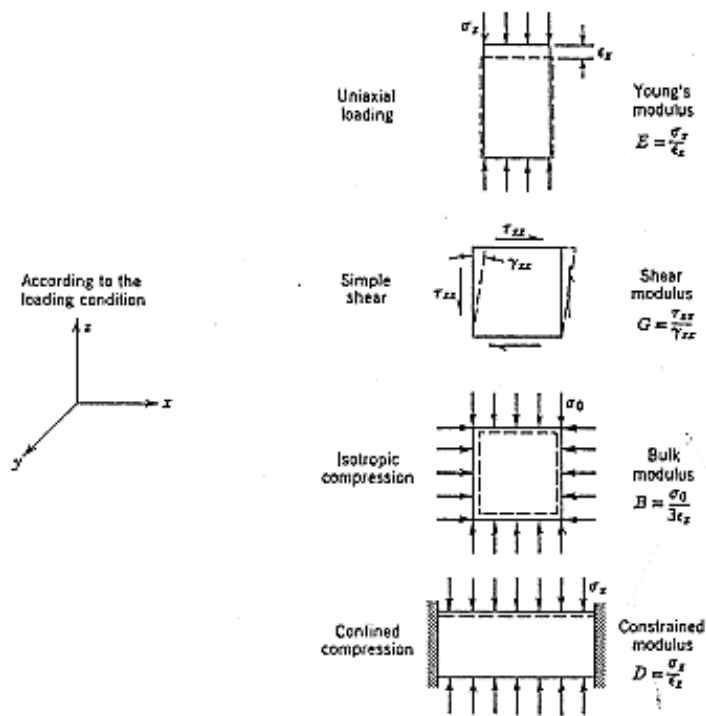
Figure 2.43. Different modulus types (Lambe and Whitman, 1969)

Basic stiffness parameters from a triaxial test are presented in Figure 2.44. When the specimen is loaded, a non-linear stress-strain curve is observed, and two different Young's moduli are defined as the tangent modulus and the secant modulus. Very small strain, small strain, and large strain levels are defined by Atkinson and Sallfors (1991). At very small strain level, stiffness reaches to its maximum constant value. At small strain levels, modulus decreases non-linearly with strain. At larger strain level, stiffness decreases significantly to a relatively very small value (Atkinson, 2000).
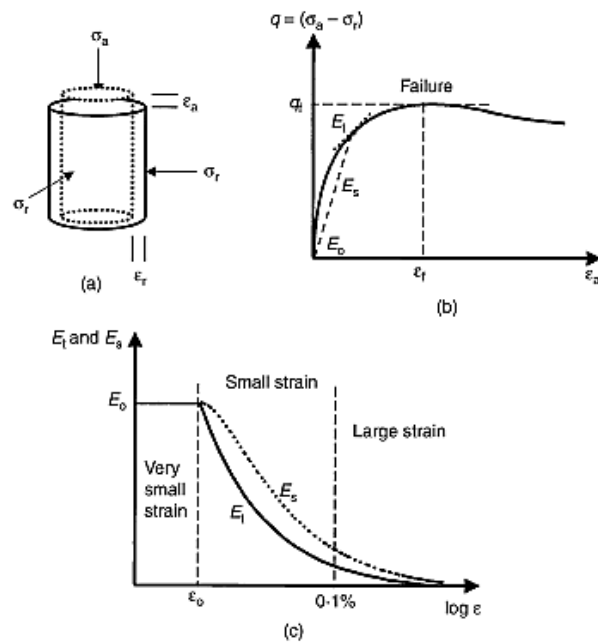
Figure 2.44. Basic stiffness parameters (Atkinson, 2000)

The typical stiffness strain curve is an S-shaped curve in the semi-log space and presented in Figure 2.45. Atkinson (2007) refers the behavior in the very small strain levels (up to ~0.001%) as linear; hence, stiffness is constant. At small strain level (in between ~0.001% to ~1%), stress-strain relation is non-linear; therefore, stiffness decreases with increasing strain increments. At large strains, soil state is on the yield surface, and elastoplastic behavior is observed. Benz (2007) defines these strain level boundaries as ~0.0001% and ~0.1% for very small strain and large strain levels, respectively.
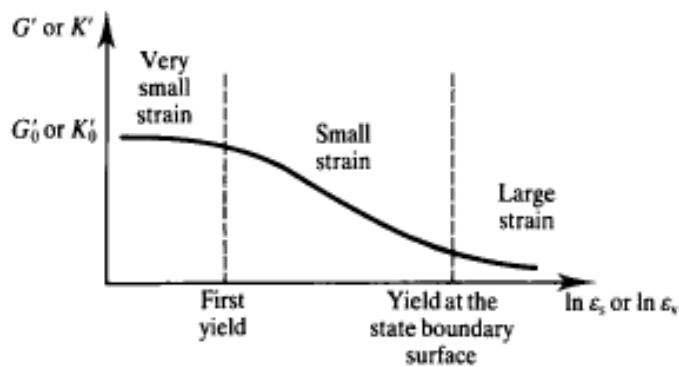
Figure 2.45. Stiffness strain relation (Atkinson, 2007)

50

Typical strain ranges are recommended by Mair (1993) for the structures constructed in or on London Clay, along with the proper testing technique for different ranges of strain, as shown in Figure 2.46. Traditional soil tests can be used to observe the behavior at large strains. Dynamic measurements are needed to measure stiffness at small strains. The basic method is based on shear wave velocity measurement as given in Eqn. 2-28. To estimate stiffness at small strain levels, there is a need for the internal local gauges on the sample to capture very small strain responses, which is not possible at conventional triaxial tests.

$$G'_0 = \frac{\gamma V_s^2}{g}$$

Eqn. 2-28
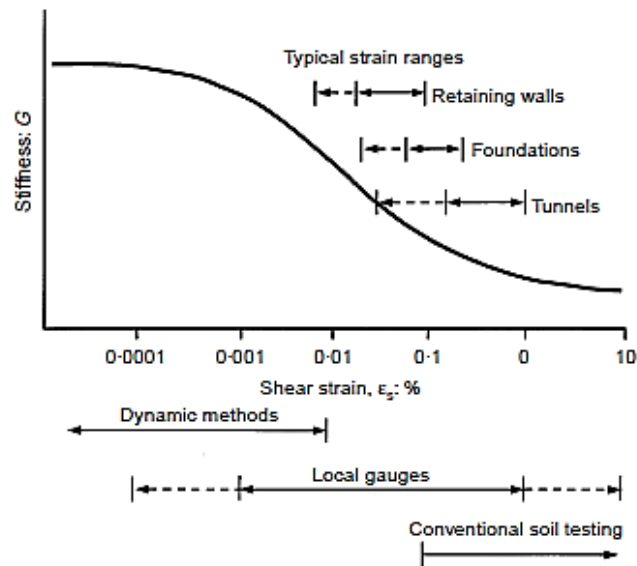
Figure 2.46. Typical strain ranges for laboratory tests and typical structures (Atkinson, 2000)

Although the soil is a highly non-linear material, generally, simple analyses are performed assuming that soil behavior is linear and elastic. A comprehensive analysis of a geotechnical structure requires special laboratory tests and complex calculations (Atkinson, 2000).

In Figure 2.47, strength and stiffness relationship of the soil is presented. ε_r, the reference strain, is defined as the ratio of the peak stress and initial tangent modulus (Eqn. 2-29). In this figure, solid line presents the non-linear behavior, and the dashed

line presents the idealized behavior. Remember that the q'_p equals to the area under the stiffness-strain curve from the origin to the peak state. Therefore, the area under the solid line and the dashed line should be equal as shown in Figure 2.47.

$$\varepsilon_r = \frac{q'_p}{E'_0}$$
Eqn. 2-29
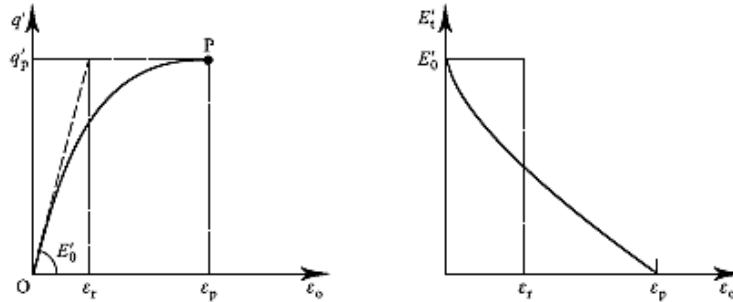
Figure 2.47. Typical strength-strain and stiffness-strain relation and their idealizations (Atkinson, 2007)

Atkinson (2007) suggests that elastoplastic models, like Cam clay model, can be used to model soil behavior for large strain levels. He suggests that the Eqn. 2-30 can be used to model the almost linear stress-strain behavior for very small strain levels. He also suggests that Eqn. 2-31 is suitable to model highly non-linear response.

$$\frac{G'_0}{p'_r} = A \left(\frac{p'}{p'_r} \right)^n Y_p^m$$
Eqn. 2-30

$$\frac{G'_0}{p_r} = A Y_p^m$$
Eqn. 2-31

Lade and Nelson (1987) pointed out that the granular material's response to loading includes both elastic and plastic straining components. Elastic strains are relatively small when compared to plastic strains; however, at the initial portion of the stress-strain relation, an elastic region is observed. Constitutive models need elastic parameters to cover this elastic response range. Occasionally, elastic models are used to understand general soil response even at larger strain levels. Thus, although the

elastic straining range is small, it cannot be ignored, it should be well-understood and defined (Lade and Nelson, 1987).

The elastic behavior of granular material is assumed to be isotropic and depends on the density and stress states of the material. According to Hooke's law, two independent variables are needed to model the elastic behavior of an isotropic material from among the following; Poisson's ratio, v, Young's modulus, E, bulk modulus, B, and shear modulus, G. The elastic-theory based relations between these parameters are given in Eqn. 2-32 and Eqn. 2-33.

$$B = \frac{E}{3(1 - 2v)}$$
Eqn. 2-32

$$G = \frac{E}{2(1 + v)}$$
Eqn. 2-33

Experimental studies show that the E, B and G values depend on the stress state and Poisson's ratio mostly assumed as constant (Lade and Nelson, 1987).

The initial slope of the stress-strain plot from triaxial compression test or the initial tangent modulus is the most basic and widely used modulus due to its ease of estimation from conventional triaxial tests. The modulus relation was originally proposed by Janbu (1963), which is widely accepted and used. This typical power function is given as follows:

$$E = Kp_a \left(\frac{\sigma_3'}{p_a}\right)^n$$
Eqn. 2-34

where K is modulus constant, p_a is atmospheric pressure, σ_3' is confining stress, and n is modulus exponent.

Biarez and Hicher (1994) proposed a relation for Young's modulus as a function of void ratio, as given in Eqn. 2-35.

$$E_0 = \frac{140}{e} \sqrt{\frac{p'}{p_{ref}}} \qquad \text{Eqn. 2-35}$$

where e is void ratio, p' is mean effective stress, p_{ref} is reference stress.

Maximum shear modulus is expressed as functions of confining stress and void ratio as given in Eqn. 2-36.

$$G_{max} = AF(e)\sigma_0'^n \qquad \text{Eqn. 2-36}$$

where A is modulus constant, $F(e)$ is void ratio function, σ_0' is initial effective stress, and n is modulus exponent.

Hardin and Black (1969) proposed an empirical relation for maximum shear modulus as given in Eqn. 2-37.

$$G_0 = 33 \frac{(2.97 - e)^2}{1 + e} \sqrt{\frac{p'}{p_{ref}}} \qquad \text{Eqn. 2-37}$$

where e is void ratio, p' is mean effective stress, p_{ref} is reference stress.

There are different modulus relationships and void ratio functions used in the literature, only a couple of them were presented in this thesis.

CHAPTER 3

LABORATORY TESTING PROGRAM AND PROCEDURES

3.1 Introduction

In this chapter, the laboratory testing program and testing procedures are described. The experimental study was carried out on Kızılırmak sand. The laboratory testing program consists of four soil index tests, 20 monotonic strain-controlled consolidated undrained triaxial tests, and 7 one-dimensional compression tests. Triaxial tests and one-dimensional compression tests were performed on relatively loose and dense, reconstituted sand samples. Kızılırmak sand is a preprocessed in sand quarry. It is further sieved through No. 4 sieve and coarser fraction is excluded. Then, it is sieved through No. 200 sieve and the finer fraction is washed out. While preparing soil samples, the under-compaction method was used for triaxial tests, and the air pluviation (dry) method was used for one-dimensional compression tests.

3.2 Soil Index Testing and Mineralogy

For Kızılırmak sand, index properties including specific gravity (G_s), minimum void ratio (e_{min}), maximum void ratio (e_{max}), and gradation were determined. To find specific gravity (G_s), four specimens were prepared, and tests were performed according to ASTM D854-14. The average G_s of the Kızılırmak sand was determined as 2.65. Individual results of all tests are presented in Appendix A.

Maximum void ratio (e_{max}) was determined by following the ASTM D4254-16. Minimum void ratio (e_{min}) was determined by vibrating and compressing the soil into a container in three layers. Experiments were repeated three times for e_{max} and two times for e_{min} determinations. The volume of the container was measured, and the volume of solids and voids were calculated. e_{max} was determined as 0.799 and

e_{min} was determined as 0.453 by taking the average of the calculated values. The detailed calculation steps are presented in Appendix B.

Gradation of the Kızılırmak sand was determined by sieve analysis in accordance with ASTM D6913/6913M-17. Grain size distribution is presented in Figure 3.1. In this figure, red line represents the average of three experiments. The uniformity coefficient was determined as 6.07, and the coefficient of curvature was determined as 0.94. Therefore, according to USCS (Unified Soil Classification System), Kızılırmak Sand is classified as poorly graded sand. Table 3.1 presents the grain size characteristics of Kızılırmak Sand.
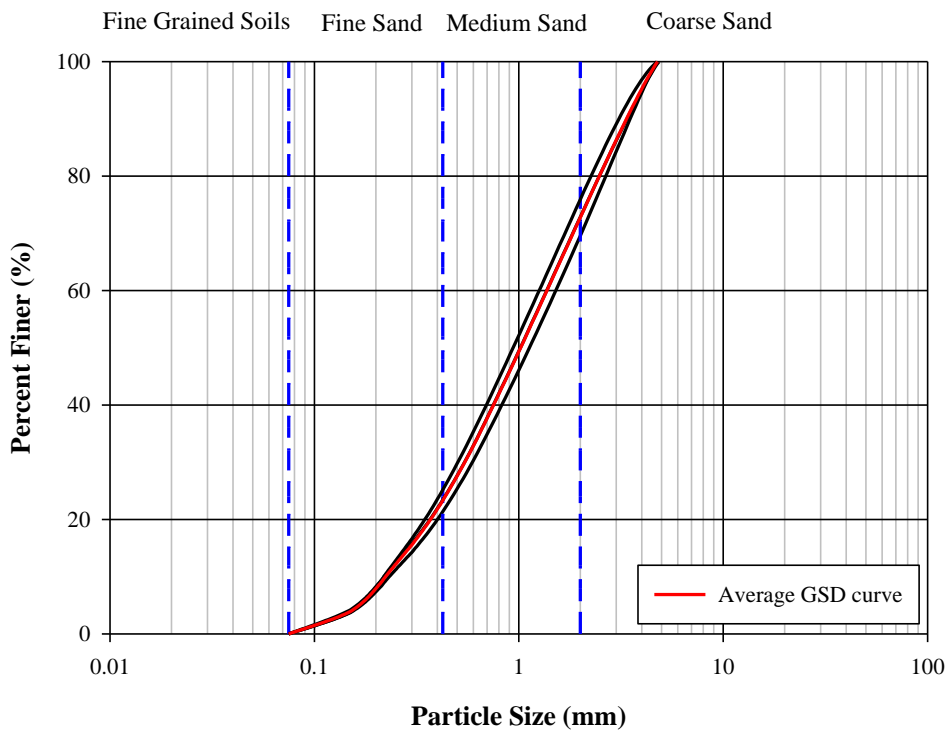
Figure 3.1. Grain size distribution curves of Kızılırmak sand

Table 3.1 Grain size distribution characteristics of Kızılırmak sand

USCS:	SP
D_{10}**:**	0.22
D_{30}**:**	0.54
D_{50}**:**	1.01
D_{60}**:**	1.36
C_u**:**	6.07
C_c**:**	0.94

Particle mineralogy was also studied for Kızılırmak sand. It was examined using optical magnification. As a result of this examination, it was observed that Kızılırmak sand mostly consists of quartz grains, while relatively coarse grains also include agglomerate and andesite rock fragments (Figure 3.2). Kızılırmak sand showed a very weak reaction with dilute (10 %) hydrochloric acid. This weak reaction suggests a minor amount of carbonate minerals in Kızılırmak sand.

Figure 3.2. Agglomerate and andesite rock fragments (2 – 3 mm diameter) observed in Kızılırmak sand

In addition to visual examinations, X-Ray powder diffraction analysis was performed on Kızılırmak sand which was sieved through no. 40 sieve. X-Ray powder

diffraction analysis was performed by METU Civil Engineering Department Construction Materials Laboratory. XRD pattern of the Kızılırmak sand sample is given in Figure 3.3. Qualx2 (Altomare *et al.*, 2015) software was utilized to analyse the XRD pattern and identify main mineral constituents. XRD pattern shows distinct quartz mineral peaks. Secondary mineral is albite which is a plagioclase feldspar (mainly Na plagioclase). A minor peak at 29.4o 2-theta indicates a small amount of calcite mineral.
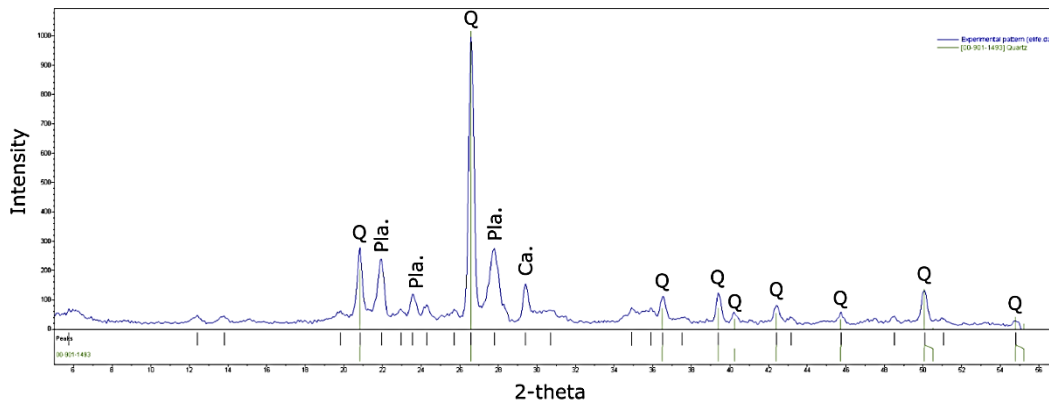
Figure 3.3. X-Ray powder diffraction pattern and identified minerals of Kızılırmak sand

3.3 Triaxial Testing

The aim of this experimental study is to investigate the volumetric and shear straining response of Kızılırmak sand. To examine the shear straining response, a laboratory testing program consisting of 20 monotonic strain-controlled consolidated undrained triaxial tests with pore water pressure measurement was designed. ASTM D4767-11 procedure was adopted, although the standard is usually used for cohesive soils. Due to ease of pore pressure transducer calibration as oppose to volume transducers, CU tests were preferred as compared to CD tests. Sand specimens were prepared at various relative densities and consolidated to different cell pressures. The triaxial testing program is presented in Table 3.2.

Table 3.2 Triaxial testing program

Relative Density / Consolidation Pressure				
	σ'_c=50 kPa	σ'_c=100 kPa	σ'_c=200 kPa	σ'_c=400 kPa
D_R = 35 %	35% / 50kPa	35% / 100kPa	35% / 200kPa	35% / 400kPa
D_R = 45 %	45% / 50kPa	45% / 100kPa	45% / 200kPa	45% / 400kPa
D_R = 60 %	60% / 50kPa	60% / 100kPa	60% / 200kPa	60% / 400kPa
D_R = 75 %	75% / 50kPa	75% / 100kPa	75% / 200kPa	75% / 400kPa
D_R = 80 %	80% / 50kPa	80% / 100kPa	80% / 200kPa	80% / 400kPa

3.3.1   Sample Preparation

To be able to have homogeneous specimens, reconstituted sand specimen preparation techniques are generally used in laboratory testing. Ishihara (1996) suggests three reconstituted sample preparation methods: dry deposition, water sedimentation, and moist placement.

In the dry deposition method, an oven-dried sand specimen is put into a funnel. Then, it is poured into the mold through this funnel with zero height and constant velocity. Target density can be obtained by applying tapping energy by hitting the side of the mold. By adjusting tapping energy, specimens can be prepared at any density.

In the water sedimentation method, sand is mixed with de-aired water and poured into the mold with zero height at a constant velocity. In an alternative method, de-aired water is put into the mold, and dry sand is poured into the mold just above the water surface. In both water sedimentation methods, it is essential that the sand deposited under water without considerable sedimentation. If the denser specimen is aimed, then tapping can be applied by hitting the side of the mold.

In moist placement method, specimen is mixed with de-aired water (about 5%) and is divided into 5 or 6 equal-weight layers. Each layer of the specimen is poured into the mold and tamped by a rod. Tamping energy should be arranged considering the

target initial density. If a loose specimen is to be prepared, low amount of energy is needed. If a dense specimen is to be prepared, high amount of energy is needed. This method allows to prepare a specimen within a wide range of void ratios.

In the moist placement method, it may be hard to apply the same energy to each layer all the time. Additionally, even though the same energy is applied, due to the compaction energy transferred from upper layers to lower ones, bottom layers of the specimen may be over-compacted. To eliminate these problems under-compaction method is proposed by Ladd (1978). In this method, each layer is compacted to a lower density than the desired density. This predetermined amount of low compaction called as percent under-compaction (U_n). Percent under-compaction value increases linearly from the bottom to the top, and it becomes zero at the top layer. In brief, the bottom layer has the maximum U_n value and the top layer has U_n=0. Figure 3.4 illustrates the method by using a graph. Percent under-compaction in a layer is calculated by the following formula;

$$U_n = U_{ni} - \left[\frac{(U_{ni} - U_{nt})}{n_t - 1} * (n - 1) \right] \qquad \text{Eqn. 3-1}$$

where,

U_{ni}: pecent undercompaction selected for first layer

U_{nt}: pecent undercompaction selected for final layer,usually zero

n: number of layer being considered

n_i: first (initial) layer

n_t: total numner of layers (final layer)
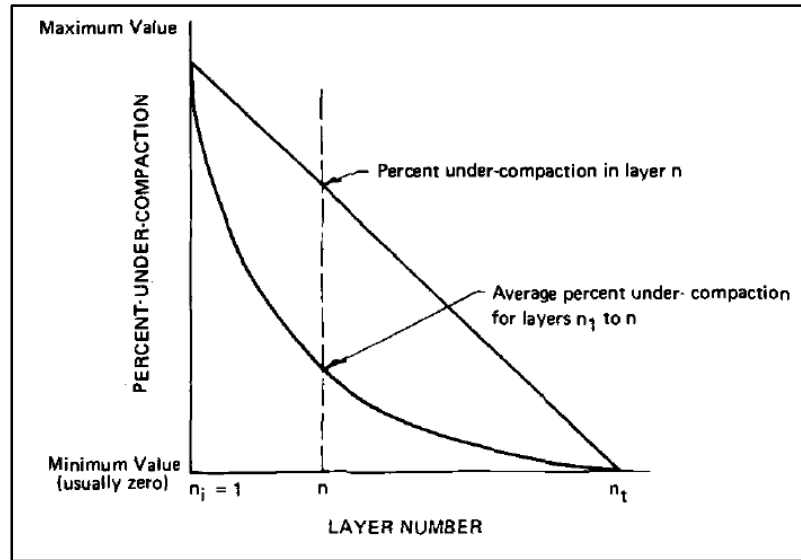
Figure 3.4. Under-compaction method (Ladd, 1978)

The under-compaction method was used as a specimen preparation technique in this study. Layer number and U_n values were selected as 10 and 4%, respectively. All specimens were prepared with a water content of 5%. Required height of each layer is calculated by;

$$h_n = \frac{h_t}{n_t}\left[(n-1) + \left(1 + \frac{U_n}{100}\right)\right]$$

Eqn. 3-2

where,

h_t: final (total)height of the specimen

n_t: total number of layers

n: number of the layer being considered

U_n: percent undercompaction for layer being considered

Required weight of the specimen is calculated by;

$$W_{specimen} = W_{solids} + 0.05 * W_{solids}$$

Eqn. 3-3

61

$$W_{solids} = G_s * \frac{V}{1 + e} * \gamma_w \qquad\qquad \text{Eqn. 3-4}$$

where,

V: volume of specimen (volume of the mold)

G_s: specific gravity of the soil,2.65

e: void ratio of the specimen

γ_w: unit weight of the water

The void ratio at the desired relative density is calculated as:

$$e = e_{max} - D_R * (e_{max} - e_{min}) \qquad\qquad \text{Eqn. 3-5}$$

where,

e_{max}: maximum void ratio,0.799

e_{min}: minimum void ratio,0.453

D_R: aimed relative density

3.3.2 Monotonic Triaxial Testing

3.3.2.1 Apparatus

Triaxial tests were performed by using the VJ TECH triaxial testing system shown in Figure 3.5. The system includes:

- A triaxial cell,
- A loading-frame,
- An automated pressure controller with a pressure transducer to apply and measure the cell pressure throughout the test,

- An automated pressure controller with a pressure transducer to apply and measure the back pressure. In addition, it also measures the volume change of the specimen throughout the test,

- A load cell to measure the deviatoric load acting on the specimen,

- A linear variable displacement transducer (LVDT) to measure the axial deformation of the specimen,

- A data logger (MPX3000 with $\mp$5V range and 16 bits resolution) to monitor the deviatoric load and axial deformation,

- A computer to use Clips software, which controls the automated pressure control units and allows monitoring the deviatoric load and axial deformation.

Figure 3.5. VJ TECH triaxial testing system

3.3.2.2   Setup of the specimen

At the beginning of the all experiments, cleaning of the apparatus (soil grains from the previous experiment were removed from the pedestal with the help of a brush, back pressure, cell pressure, pore-water pressure, and top cap lines were cleaned by flushing de-aired water) has been performed. Porous disks were boiled to prevent

any blockage in the pores and to eliminate remains from the previous experiment. Then, a latex membrane was fitted inside the mold, and a filter paper was placed between the latex membrane and the mold to evenly distribute the suction around the membrane and protect it from the suction of the vacuum pump. After this, the mold was connected to the vacuum pump to stretch membrane to mold's wall. In this step, a vacuum regulator was also connected to the system to control the amount of vacuum applied to the specimen during specimen preparation. Vacuum regulator is important to prevent the application of vacuum pressures higher than the predetermined consolidation pressure. Higher vacuum pressure than the predetermined consolidation pressure results in an over-consolidated reconstituted specimen that is not intended for this study. 20 kPa vacuum pressure was used for the specimens being consolidated to 50 kPa consolidation pressures, and 50 kPa vacuum pressure is used for the specimens being consolidated to 100 kPa or higher consolidation pressures. The prepared mold was placed on the pedestal, where bottom porous disk had already been placed. Prepared mold and vacuuming line is shown in Figure 3.6.
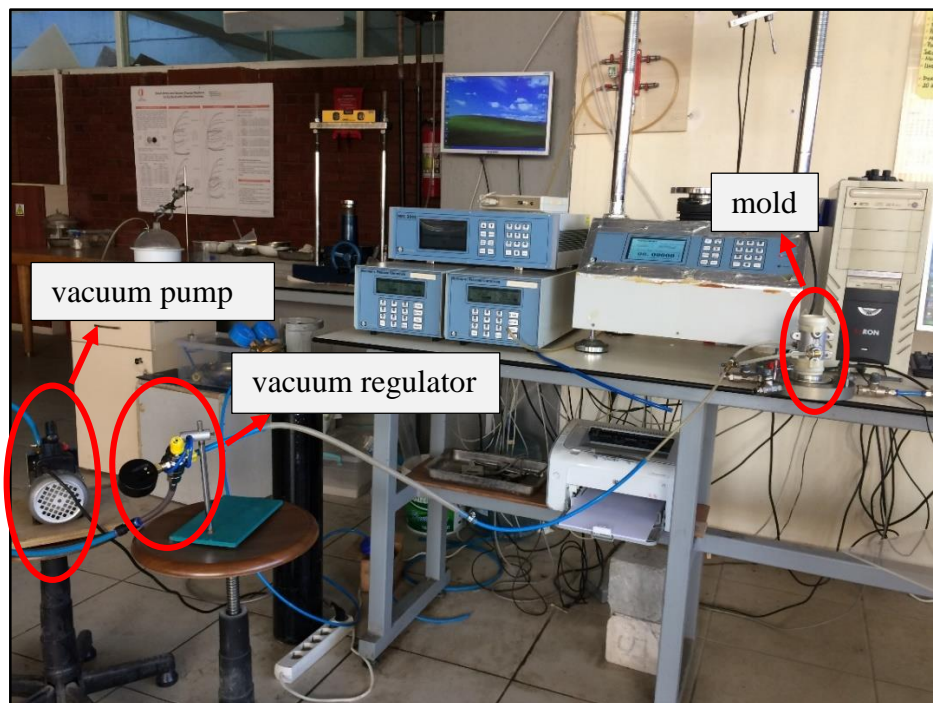
Figure 3.6. Prepared mold for the experiment

The calculated amount of specimen was weighed and mixed with de-aired water to get ready for the under-compaction process. The specimen amount was decided to reach to the target relative density. Corresponding equations are provided in Chapter 3.3.1. After adding de-aired water, the specimen was covered with a wet towel to prevent the loss of water by evaporation. In Figure 3.7, the wetted specimen is presented.

Figure 3.7. Wetted specimen

As a next step, the specimen was prepared by using the under-compaction method proposed by Ladd (1978). While applying the method, 10 layers were chosen to get a more uniform specimen. In this method, soil mass in the layers stays constant, and layers' heights are changed to achieve predetermined density for that layer. An adjustable tamping rod, presented in Figure 3.8, was used for this process.

Figure 3.8. Tamping rod and caliper

The calculated amount of mass for one layer was taken from the wetted specimen, and poured into the mold by using a funnel. After that, the soil specimen was compacted with the tamping rod previously adjusted to the desired height. Then, the layer's surface was scratched to increase the bond between soil layers. All these processes are illustrated in Figure 3.9 through Figure 3.14, and are repeated until a complete sample is prepared. During specimen preparation, it is essential to keep vacuum pressure constant by using the vacuum regulator.

Figure 3.9. Height adjustment of the tamping rod

Figure 3.10. Mass measurement for a layer

Figure 3.11. Measured mass and funnel

Figure 3.12. Tamping process

Figure 3.13. End of the compaction process
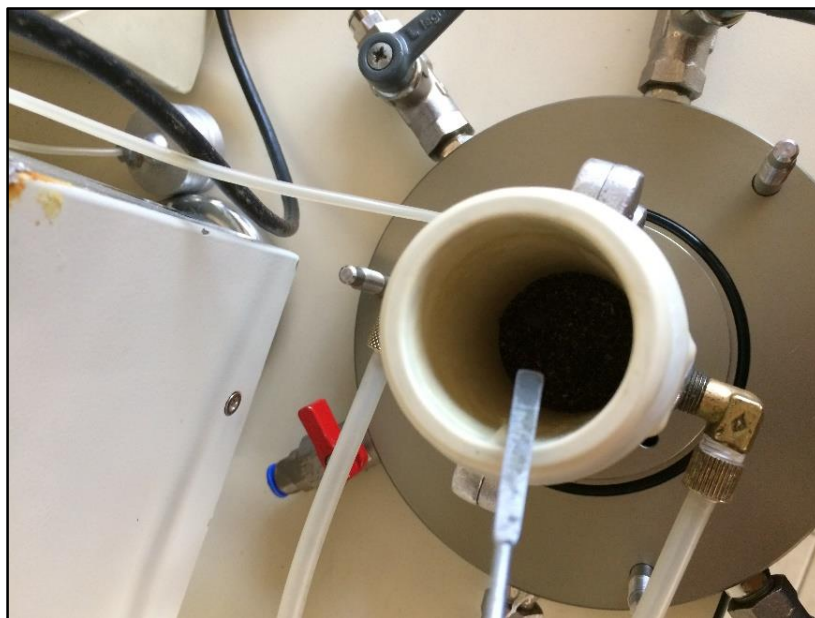
Figure 3.14. Scratching the compacted surface

After 10 layers were compacted, top porous stone and top cap were placed on the specimen. The top cap level was checked by using water gauge in all experiments to see whether the specimen's surface was flat or not. The flat surface is important to prevent the loading applied eccentrically. Then, the membrane was fitted to the top cap, and one of the O-rings from both bottom and top were placed, and then vacuum pressure was applied to the specimen through the back pressure line. Then, the second O-rings were placed, and the mold was taken out. The final specimen looks like the one given in Figure 3.15. Diameter measurements were taken from three different places of the specimen in different directions. The average of these measurements was used as a specimen diameter when the volume of the specimen was calculated.

Figure 3.15. Prepared specimen

After this step, the pedestal was placed on the triaxial setup. The triaxial cell was placed, and water was filled in it. 20 or 50 kPa cell pressure, according to the predetermined consolidation pressure, was applied. 20 kPa was used for the specimens consolidated to 50 kPa consolidation pressure, and 50 kPa was used for the specimens consolidated to 100 kPa or higher consolidation pressure. During this process, vacuum pressure was gradually decreased to reach the target effective

stresses. After reaching the target cell pressure and decreasing vacuum to zero, the vacuum pump was disconnected from the setup, and the specimen was ready to saturation, which will be discussed in the next section.

3.3.2.3   Saturation and Consolidation

Saturation is an essential process for an undrained test to avoid measurement errors in pore-water pressure. Flushing of de-aired water along with back pressuring were used in this study to saturate the specimen. To increase the effect of flushing, the specimen was first flushed with CO_2, a gas more soluble than air, before the de-aired water. Flushing with both CO_2 and de-aired water were performed from bottom to top. The pace of the flushing gas and fluid is important to avoid any undesired reorientation of the sand grains in the specimen or piping problem. CO_2 was applied for approximately 40 minutes, with the rate of 2-3 bubbles in a minute. The CO_2 flushing process can be seen in Figure 3.16 and Figure 3.17.
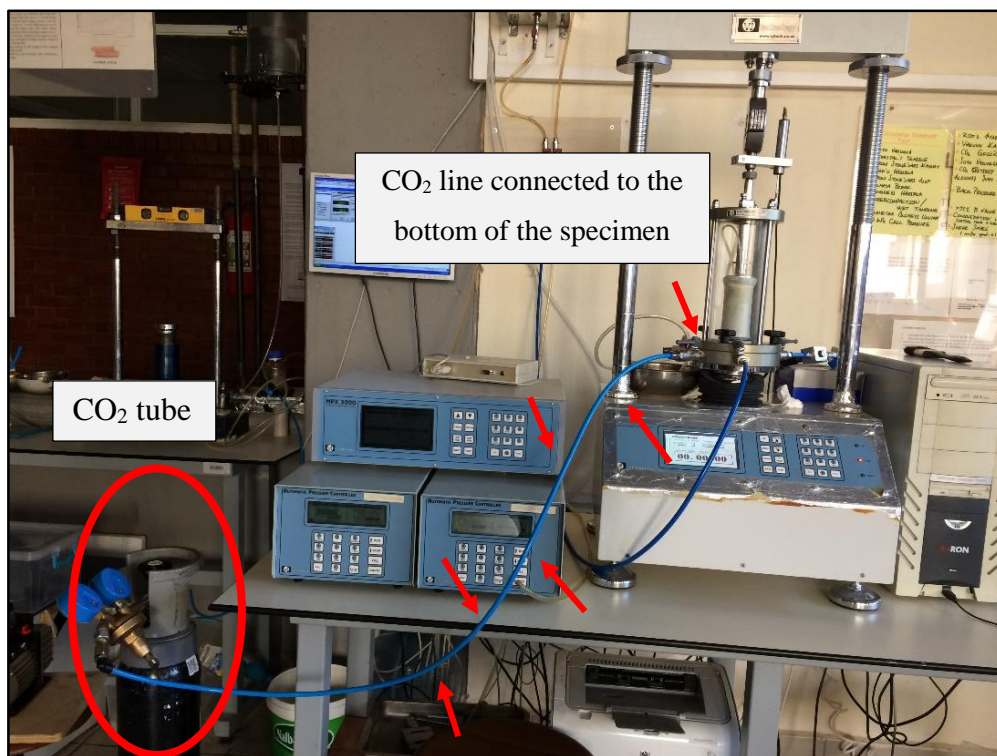
Figure 3.16. A general view of the CO_2 tube and CO_2 line
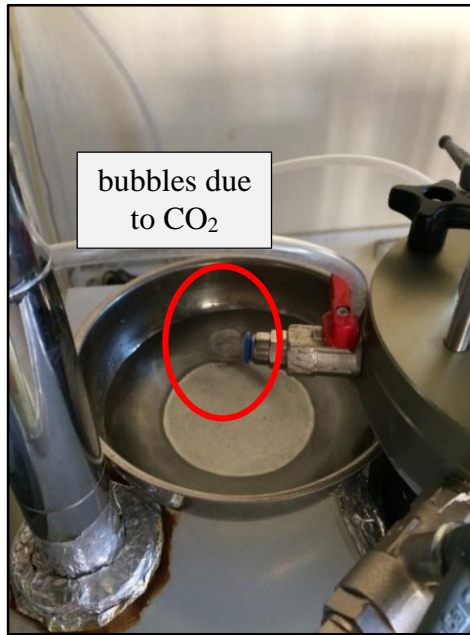
Figure 3.17. CO_2 outlet valve

After CO_2, 250-300 ml de-aired water was flushed through the specimen (bottom to top) to fill voids, as shown in Figure 3.18. In Figure 3.19, bleeding of water from the specimen top cap can be seen.
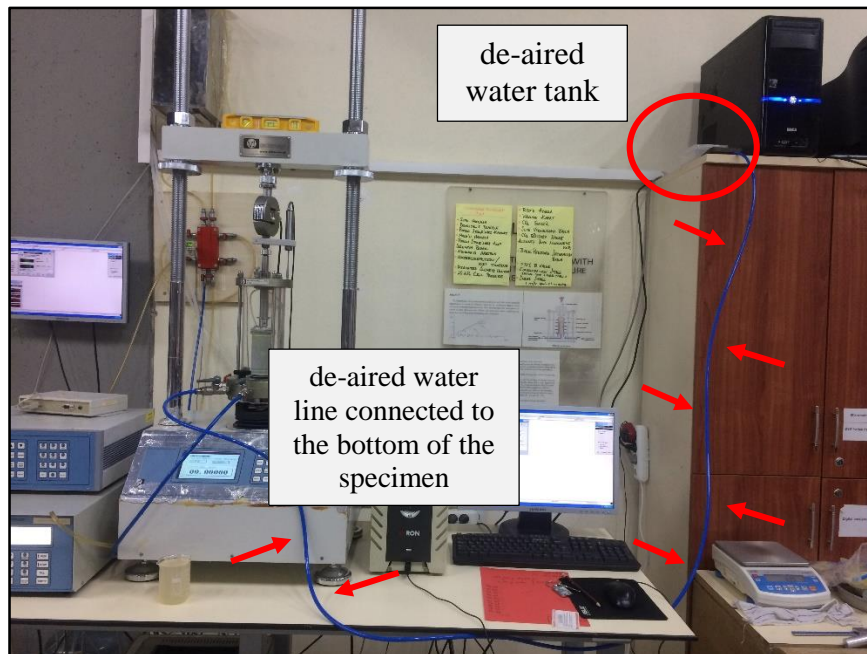
Figure 3.18. De-aired water flushing
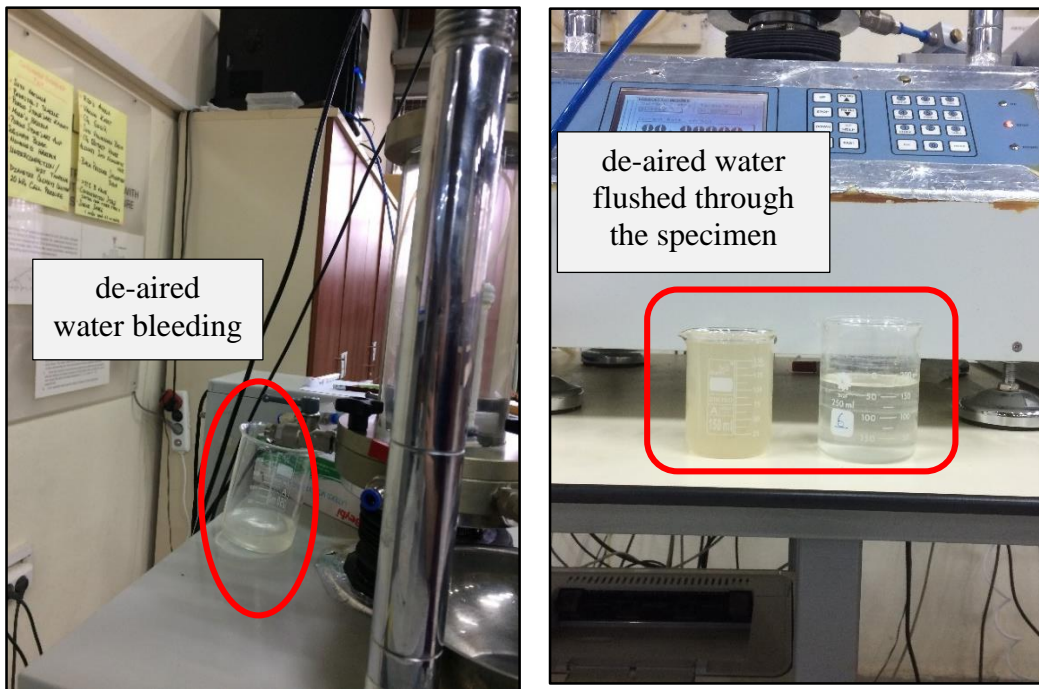
Figure 3.19. Bleeding water from the specimen

During this process, water in the back-pressure water tank was replaced with de-aired water. After de-aired water flushing was completed, the back pressure saturation process has begun.

This method takes advantage of the compressibility and solubility of air (CO_2 in our case) in water. Both compressibility and solubility increase with increasing pressure (Boyle's and Henry's law, respectively). This process has two basic application methods. In the first one, cell pressure is increased while the drainage line (goes to specimen) is closed. In the second one, cell pressure and the back pressure in the specimen are increased simultaneously to keep effective pressure constant. The second method was preferred and used in this study. Cell and back pressure increments were adjusted to not over-consolidate the specimen. Therefore, 20 kPa or 50 kPa increments were applied according to predetermined consolidation pressures. These increments were continued until full saturation was obtained. Saturation was checked by Skempton's B-value, which is calculated as follows;

$$B = \frac{\Delta u}{\Delta \sigma_3} \qquad\qquad \text{Eqn. 3-6}$$

where,

Δu: change in pore water pressure

$\Delta \sigma_3$: change in cell pressure

A B-value of 1 is considered as full saturation. However, one should not forget that B-value depends on the compressibility of the pore fluid and soil grains. The same B-value may mean 99% saturation for a stiff soil but only 95% saturation for a soft soil. Therefore, B-value higher than 95% does not have the same meaning in all cases. Rather than checking B-value itself, checking its change with pressure may be more meaningful. When full saturation is achieved, no more change in B-value will occur. Both B-value itself and its change were monitored in this study.

After each pressure increment, approximately 20-25 minutes was allowed for the dissolution of the gas in the specimen. Then, the back pressure (drainage) line was closed, and cell pressure was increased by 20 kPa. The B-value check was done by dividing the change in pore water pressure by 20 kPa (increase in cell pressure). If desired B-value and/or change in B-value was not reached, back pressure and cell pressure was continued to be increased to get the desired B-value. B $\geq$ 0.93 was considered to be full saturation for Kızılırmak sand and generally achieved at 500-600 kPa back pressures.

For the consolidation phase, the back pressure valve was closed, and predetermined consolidation pressure was applied to the specimen isotropically by increasing the cell pressure. A few minutes were waited for pore-water pressure stabilization. After pore-water was stabilized, the consolidation phase was started by opening the drainage valve. During the consolidation, time vs. volume change data were recorded. When volume change with time became constant, the consolidation stage was stopped. For Kızılırmak sand specimens, this took approximately 10 seconds. The height and the area after consolidation were re-calculated, and in the shearing

stage, these updated (corrected) values were used. Axial strain, volumetric strain, corrected height, and corrected area are calculated by using the Eqn. 3-7 - Eqn. 3-10.

$$\varepsilon_a = \frac{\varepsilon_v}{3}$$ Eqn. 3-7

$$H_c = H_0 * (1 - \varepsilon_a)$$ Eqn. 3-8

$$\varepsilon_v = \frac{\Delta V}{V_0}$$ Eqn. 3-9

$$A_c = A_0 * \frac{1 - \varepsilon_v}{1 - \varepsilon_a} = \frac{V_0 - \Delta V}{H_c}$$ Eqn. 3-10

where,

H_c: height of the specimen after consolidation

H_0: initial height of the specimen

ε_a: axial strain

ε_v: volumetric strain

V_0: initial volume of the specimen

ΔV: change in volume of the specimen during consolidation stage

A_c: area of the specimen after consolidation

A_0: initial area of the specimen

3.3.2.4   Monotonic Loading

After the completion of the consolidation stage, the back pressure valve was closed again to perform the undrained test. The machine shearing rate was set to 1mm/min, and the last stage of the experiment was started. Applied deviatoric load, deformation, and pore-water pressure measurements were recorded at every 0.1 mm

deformation, and each test was continued to reach to a maximum 15-20% axial strain.

Before each experiment, the loading rod was lubricated to eliminate the piston friction. Therefore, piston friction correction was not applied, assuming frictionless response. To confirm this, at the beginning of shearing, zero force reading was taken while the axial motor moves at the designated shearing rate without the piston touching the top cap so that any piston friction and uplift force could be eliminated during calculations.

Axial strain, deviatoric and mean effective stress, and excess pore-water pressure were calculated, and four-way plots were prepared for each experiment. The effects of parabolic and cylindrical area corrections were comparatively tested. It was concluded that both of the correction schemes produce almost identical failure shear stresses. However, at larger strains getting close to steady state parabolic area correction scheme produce approximately 5% smaller shear stresses. Due to their relative insignificance it was decided to continue with cylindrical area correction procedure. Therefore, at any stage of shearing, the height and the area of the specimen were recalculated as given in Eqn. 3-11 through Eqn. 3-13, by assuming the cylindrical shape of the specimen was not disturbed during the shearing stage.

$$H_c^* = H_c - \Delta H \qquad\qquad \text{Eqn. 3-11}$$

$$A_c^* = \frac{A_c}{1 - \varepsilon_a} \qquad\qquad \text{Eqn. 3-12}$$

$$\varepsilon_a = \frac{\Delta H}{H_c} \qquad\qquad \text{Eqn. 3-13}$$

where,

H_c^*: height of the specimen after each shearing stage

H_c: height of the specimen after consolidation

ΔH: axial deformation of the specimen in each shearing stage

A_c^*: area of the specimen after each shearing stage

A_c: area of the specimen after consolidation

ε_a: axial strain in each shearing stage

Deviatoric stress, principal effective stresses and half of the deviatoric stress (shear stress, q) and mean effective stress (p') were calculated by using the following formulae;

$$\sigma_d = F/A_c^* \qquad\qquad \text{Eqn. 3-14}$$

$$\sigma'_1 = \sigma_{cell} + \sigma_d - u \qquad\qquad \text{Eqn. 3-15}$$

$$\sigma'_3 = \sigma_{cell} - u \qquad\qquad \text{Eqn. 3-16}$$

$$p' = (\sigma'_1 + \sigma'_3)/2 \qquad\qquad \text{Eqn. 3-17}$$

$$q = (\sigma'_1 - \sigma'_3)/2 \qquad\qquad \text{Eqn. 3-18}$$

where,

σ_d: deviatoric stress

F: force on the specimen

σ'_1: major effective stress

σ'_3: minor effective stress

σ_{cell}: cell pressure

u: pore water pressure

p': mean effective stress

q: half of deviatoric stress (shear stress)

A sample four way plot is given in Figure 3.20.
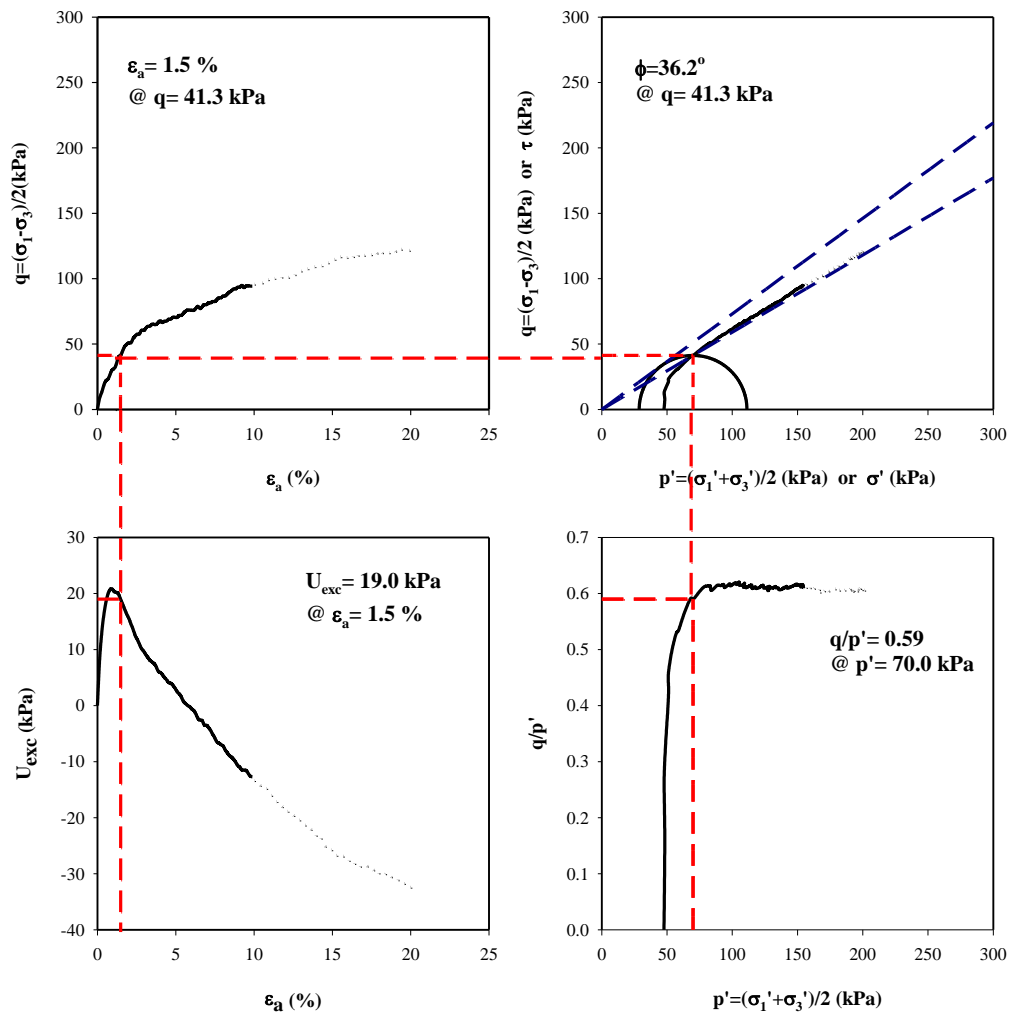
Figure 3.20. An example of four-way plot (TRX_45-50)

3.4   One-Dimensional Compression Test

To examine the volumetric straining response, a laboratory testing program, consisting of 7 oedometer tests was designed. Sand specimens were prepared at 25-35-45-60-75-80-85 % relative densities, and loaded up to an axial stress of ~33.5 MPa. ASTM D2435/D2435M-11 procedure was adopted, although the standard is widely used for cohesive soils.

3.4.1   Sample Preparation

To be able to get homogeneous specimens, reconstituted sand specimen preparation techniques were used as part of the laboratory testing program. The dry deposition method was preferred for one-dimensional testing. In this method, an oven-dried specimen was placed into a funnel. Then, the soil was poured into the mold through this funnel at zero dropping height and constant velocity. Target density is obtained by applying tapping energy, hitting the side of the mold. By adjusting tapping energy, specimens can be prepared at target densities (Ishihara, 1996).

Required weight of the specimen was calculated as:

$$W_{soil} = G_s * \frac{V}{1 + e} \qquad \text{Eqn. 3-19}$$

where,

V: volume of specimen (volume of the mold)

G_s: specific gravity of the soil,2.65

e: void ratio of the specimen

The void ratio at the desired relative density was calculated as:

$$e = e_{max} - D_R * (e_{max} - e_{min}) \qquad \text{Eqn. 3-20}$$

where,

e_{max}: maximum void ratio,0.799

e_{min}: minimum void ratio,0.453

D_R: target relative density

3.4.2 One-Dimensional Compression Testing Procedure

3.4.2.1 Apparatus

One-dimensional compression tests were performed by using the SOILTEST oedometer apparatus and a data acquisition system, shown in Figure 3.21. The system includes:

- An oedometer apparatus with loading frame and two levels of the lever arm to apply the load on the specimen,
- An oedometer mold with a diameter of 50 mm to prepare the specimen,
- 21 metal weights, ranging from ~250 gr. up to ~16 kg., to load the specimen,
- A linear variable displacement transducer (LVDT) to measure the axial deformation of the specimen,
- A data acquisition system (TestBOX1001 with $\mp 10V$ range and 16 bit resolution) to monitor axial deformations,
- A computer where Test Lab software and the axial deformation data were installed and saved, respectively.
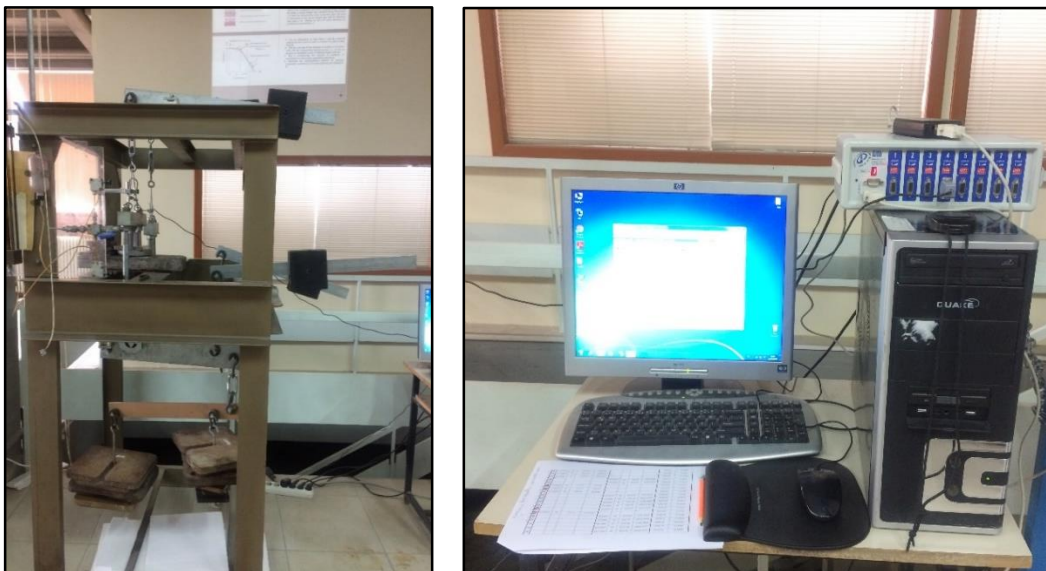
Figure 3.21. SOILTEST oedometer apparatus and data acquisition system

The oedometer apparatus used for the experiments has two loading posts. One has an overall load magnification of 1:10 lever ratio, and the other 1:40, as shown in Figure 3.22.
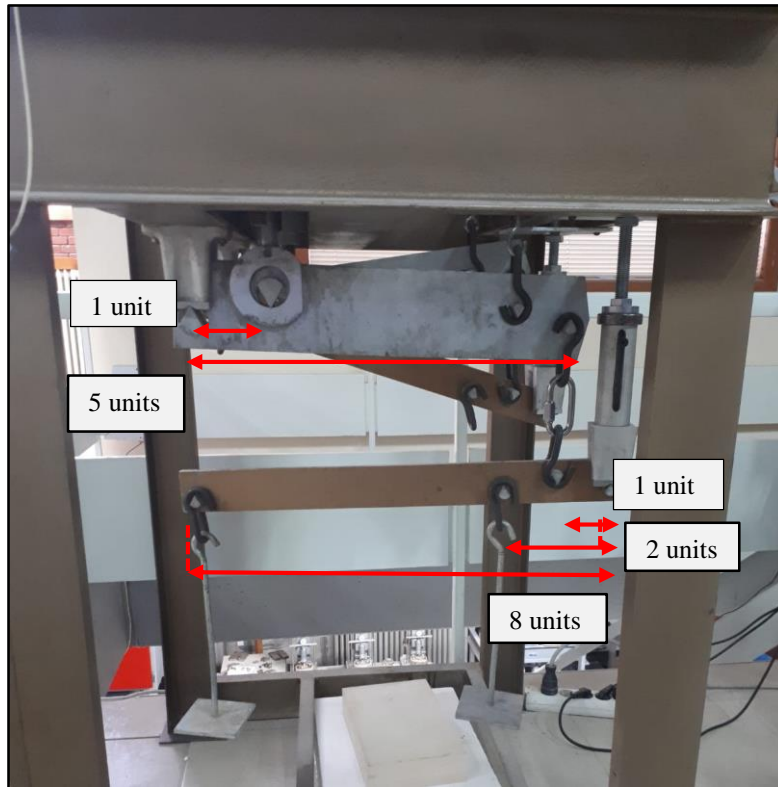
Figure 3.22. SOILTEST oedometer apparatus' lever ratios

3.4.2.2 Loading

Both of the two hangers discussed previously were used during the experiments. First, the 1:10 lever ratio part of the apparatus was used to apply relatively small pressures on the specimen. Then, the 1:40 lever ratio part was used for higher stresses. During loading, at selected point, reloading was performed, and then the test was continued with loading again. Five loading and unloading cycles were performed on each test. A total of 41 loadings were applied as part of these 5 cycles. The predetermined loading pattern is presented in Table 3.3. In this table, the black

font represents loading, whereas the red and italic font unloading. Applied loads on specimens were calculated by using the 1:10 and 1:40 lever ratios.

Table 3.3 One-dimensional test loading increments

Step	Load (kg)	Lever Ratio	Load on Specimen (kg)	Pressure (kPa)	Load (kg)	Lever Ratio	Load on Specimen (kg)	Pressure (kPa)	Total Load on Specimen (kg)	Total Pressure (MPa)
1	0.255	10	3.13	15.49					3.13	0.0155
2	0.510	10	5.68	28.12					5.68	0.0281
3	0.967	10	10.25	50.77					10.25	0.0508
4	1.970	10	20.28	100.47					20.28	0.1005
5	*0.510*	*10*	*5.68*	*28.12*					*5.68*	*0.0281*
6	*0.255*	*10*	*3.13*	*15.49*					*3.13*	*0.0155*
7	0.510	10	5.68	28.12					5.68	0.0281
8	1.970	10	20.28	100.47					20.28	0.1005
9	3.967	10	40.25	199.39					40.25	0.1994
10	7.956	10	80.14	397.00					80.14	0.3970
11	15.953	10	160.11	793.15					160.11	0.7931
12	*3.967*	*10*	*40.25*	*199.39*					*40.25*	*0.1994*
13	*0.510*	*10*	*5.68*	*28.12*					*5.68*	*0.0281*
14	3.967	10	40.25	199.39					40.25	0.1994
15	15.953	10	160.11	793.15					160.11	0.7931
16	31.958	10	320.16	1586.00					320.16	1.5860
17	51.956	10	520.14	2576.68					520.14	2.5767
18					10.004	40	400.72	1985.1229	920.86	4.5618
19					25.976	40	1039.60	5150.0253	1559.74	7.7267

Table 3.3 One-dimensional test loading increments (cont'd)

20	51.956	10	520.14	2576.68					2576.68	2.5767
21	15.953	10	160.11	793.15					793.15	0.7931
22	51.956	10	520.14	2576.68					2576.68	2.5767
23					25.976	40	1039.60	5150.0253	1559.74	7.7267
24					42.509	40	1700.94	8426.1708	2221.08	11.0029
25					58.485	40	2339.96	11591.7469	2860.10	14.1684
26					73.297	40	2932.45	14526.8510	3452.59	17.1035
27					25.976	40	1039.60	5150.0253	1559.74	7.7267
28	51.956	10	520.14	2576.68	25.976	40	1039.60	5150.0253	2576.68	2.5767
29					25.976	40	1039.60	5150.0253	1559.74	7.7267
30					73.297	40	2932.45	14526.8510	3452.59	17.1035
31					89.297	40	3572.44	17697.2422	4092.58	20.2739
32					105.306	40	4212.80	20869.5158	4732.94	23.4462
33					121.311	40	4853.00	24040.9374	5373.14	26.6176
34					137.316	40	5493.22	27212.4977	6013.36	29.7892
35					153.320	40	6133.39	30383.7608	6653.53	32.9604
36					89.297	40	3572.44	17697.2422	4092.58	20.2739
37					25.976	40	1039.60	5150.0253	1559.74	7.7267
38	51.956	10	520.14	2576.68					2576.68	2.5767
39	15.953	10	160.11	793.15					793.15	0.7931
40	3.967	10	40.25	199.39					199.39	0.1994
41	0.255	10	3.13	15.49					15.49	0.0155

3.4.2.3 Loading weights and oedometer lever ratio calibration

In order to check the ratio of the lever arm and to confirm that the loads were applied accurately and precisely, a calibration scheme was followed by using a calibrated load cell. For this process, a load cell was placed into the cell, in the place of the specimen.

A load cell, which has a 10 ton capacity was used for the calibration process. It was loaded in the pattern given in Table 3.3 without any inter-reloading pattern. Three loading and unloading cycles were performed. The calibration line for the 1:40 lever ratio is presented in Figure 3.23. In order to avoid the non-linearity in the smaller loads, another load cell with a smaller capacity was used. Loads up to 520 kg were calibrated by this 1-ton capacity load cell. It was loaded in the load pattern of the load number 1-4, 9-11, 16-17 (i.e., up to ~500 kg on the specimen but without any inter-reloading) given in Table 3.3. Loading and unloading cycles were performed 3 times. The calibration line is presented in Figure 3.24. Figure 3.23 and Figure 3.24 confirm the 1:40 and 1:10 lever ratios of the apparatus.
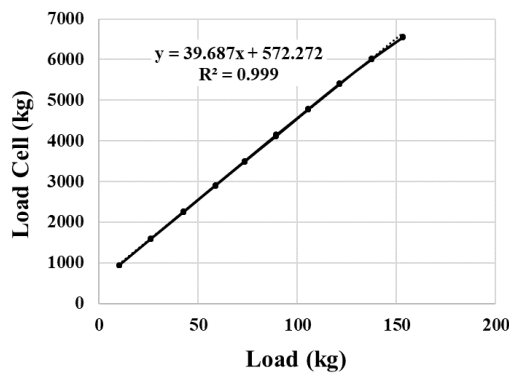
Figure 3.23. Calibration line for the load higher than ~500 kg
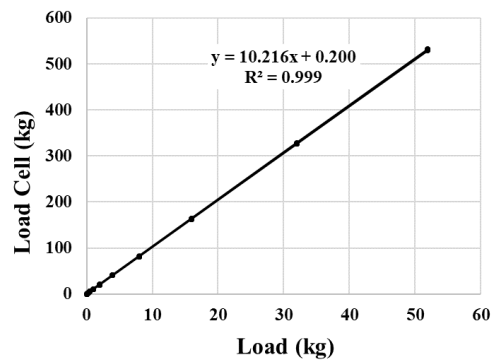
Figure 3.24. Calibration line for the load smaller than ~500 kg

In conclusion, true loads were estimated as given in Table 3.4.

Table 3.4 Comparison of calculated and calibrated loads

Load on ×10 (kg)	Load on ×40 (kg)	Calculated Load on Specimen (kg)	Calculated Pressure (MPa)	True Load on Specimen (kg)	True Pressure (MPa)
0.255		2.55	0.0126	3.38	0.0170
0.510		5.10	0.0253	5.99	0.0301
0.967		9.67	0.0479	10.66	0.0536
1.970		19.70	0.0976	20.91	0.1052
3.967		39.67	0.1965	41.31	0.2078
7.956		79.56	0.3941	82.07	0.4129
15.953		159.53	0.7903	163.77	0.8239
31.958		319.58	1.5831	327.29	1.6466
51.956		519.56	2.5738	531.61	2.6746
	10.004	919.71	4.5561	969.87	4.8794
	25.976	1558.59	7.7210	1603.76	8.0685
	42.509	2219.93	10.9971	2259.93	11.3697
	58.485	2858.94	14.1627	2893.95	14.5595
	73.297	3451.43	17.0978	3481.82	17.5171
	89.297	4091.42	20.2682	4116.81	20.7117
	105.306	4731.79	23.4405	4752.17	23.9082
	121.3106	5371.99	26.6119	5387.36	27.1039
	137.3162	6012.21	29.7835	6022.59	30.2997
	153.3203	6652.37	32.9547	6657.75	33.4952

3.4.2.4   Machine deflection calculations

To eliminate the displacements due to machine deflection/seating during testing, four tests were performed, without sand samples inplace. The oedometer apparatus was loaded following the same loading pattern; however, a sand specimen was not placed into the mold. Therefore, measured deformations were uniquely due to machine deflection/seating.
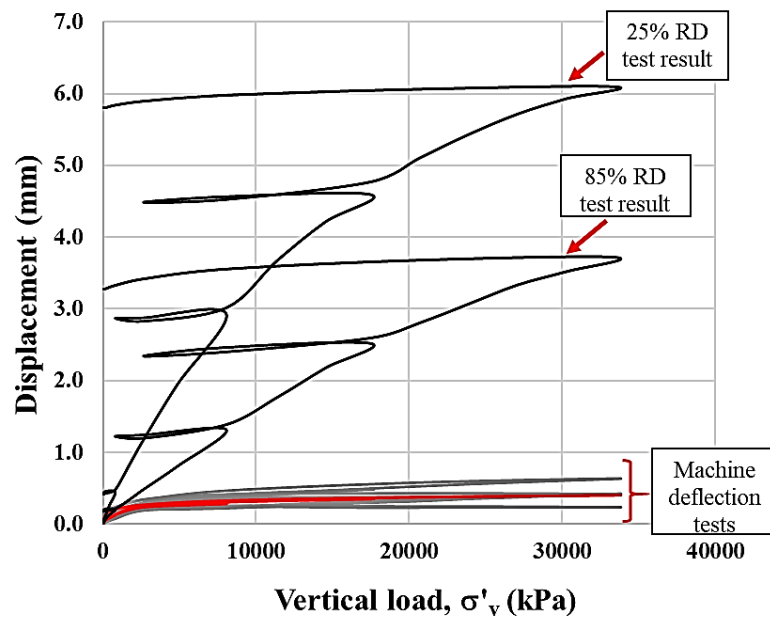
Figure 3.25. Machine deflections as compared with some oedometer tests performed on Kızılırmak sand

A comparison of the machine deflection/seating deformation and oedometer test data with Kızılırmak sand is presented in Figure 3.25. As can be seen from Figure 3.25, machine deflection/seating deformation values are very small compared to sand deformations, and all four tests gave slightly different deflection results. Therefore, it was concluded that there exists some randomness in machine deflections and their measurements. This could be due to their relatively low magnitude and intrinsic variabilities in machine preparations. The average of these results was used as machine deflection/seating deformation data, and subtracted from oedometer test

data with Kızılırmak sand samples inplace. This average is presented in Figure 3.25 by a red line.

3.4.2.5 Setup of the specimen

At the beginning of all experiments, cleaning of the mold, especially top cap, from the crushed material which could be stuck in the metal joints, has been performed. Then, the required mass of sand specimen was calculated and put into the mold with the help of a spoon and funnel. After pouring sand into the mold, vibration was applied by using a metal rod to reach to the target relative density. After tapping, the top cap was placed, and the flatness of the specimen's surface was checked by a water level. These procedures are shown in Figure 3.26 through Figure 3.28.

Figure 3.26. Pieces of equipment used for specimen preparation; a bowl, balance, spoon, funnel, oedometer mold and top cap

Figure 3.27. Dry pluviation process and the sample after the completion of pluviation

Figure 3.28. Tapping and checking the flatness of the specimen's surface

After the specimen is prepared, the mold was placed on the oedometer apparatus, and the load frame's height was adjusted to touch the top cap with applying zero load on the specimen, as shown in Figure 3.29. Then, LVDT was placed on the load frame to measure the axial deformations. After the completion of these procedures, the specimen was ready for loading. At the end of each experiment, the specimen was saved in a bag to perform sieve analysis. In Figure 3.29 through Figure 3.33, LVDT placement, apparatus under maximum load, and removal process of the specimen can be seen.

Figure 3.29. Placement of the prepared specimen under the loading frame

Figure 3.30. Placement of the LVDT on the loading frame

Figure 3.31. Apparatus under maximum load

Figure 3.32. A view of the specimen after the test

Figure 3.33. Removing specimen from the mold

3.4.2.6   One dimensional loading

After the preparation stage, the specimen was loaded, starting from ~14 kPa to ~33.5 MPa by following the load pattern given in Table 3.3. After the application of each load, approximately 30 minutes were waited. Generally, at the 20th loading cycle, specimen had to stay under the same load, during the entire night due to work hour limitations. Axial deformation readings were recorded at every second of the loading. Strain and void ratio calculations were performed by using the following formulae:

$$V_s = \frac{M}{G_s \rho_w}$$ Eqn. 3-21

$$H_s = \frac{V_s}{A}$$ Eqn. 3-22

$$e_0 = \frac{H_0 - H_s}{H_s}$$ Eqn. 3-23

$$\Delta H = d_{eop} - d_0 - d_a$$ Eqn. 3-24

$$H = H_0 - \Delta H$$ Eqn. 3-25

$$e = \frac{H - H_s}{H_s}$$ Eqn. 3-26

where,

V_s: volume of solids

M: mass of the specimen

G_s: specific gravity of Kızılırmak sand

ρ_w: density of water

H_s: equivalent height of the solids

A: area of the specimen

e_0: initial void ratio of the specimen

H_0: initial height of the specimen

ΔH: change in specimen height at the end of primary consolidation

d_{eop}: deformation reading in each loading stage at the end of primary compression

d_0: initial deformation reading in each loading stage

d_a: apparatus deformation in each stage

H: height of the specimen at the end of primary consolidation

e: void ratio of the specimen at the end of primary consolidation

$$\varepsilon = \frac{\Delta H}{H_0} * 100 \qquad\qquad \text{Eqn. 3-27}$$

where,

ε: axial strain at the end of primary consolidation

$$\sigma_a = \left(\frac{P + M_a * g}{A}\right) \qquad\qquad \text{Eqn. 3-28}$$

where,

σ_a: axial stress

P: load acting on the specimen

M_a: mass of the top cap

g: acceleration due to gravity, 9.81 m/s^2

A: area of the specimen

The end of primary compression displacement (d_{eop}) was calculated by drawing axial deformation vs. logarithm of the time plot as suggested by Casagrande (1963). However, the procedure was adopted to sand's behavior by taking the interception of

two linear parts of deformation vs. log-time graph as the end of the primary compression value. At high pressures, after crushing was occurred, this method could not be applied due to the highly creeping response of the crushed sand. For these pressures, displacement vs. square root of time graph was plotted as recommended by Taylor (1948). The end of primary consolidation value (d_{100}) defined in Taylor's method was taken as the end of primary compression (d_{eop}). Primary compression ended in 2 to 10 seconds after loading. This is illustrated in in Figure 3.34.
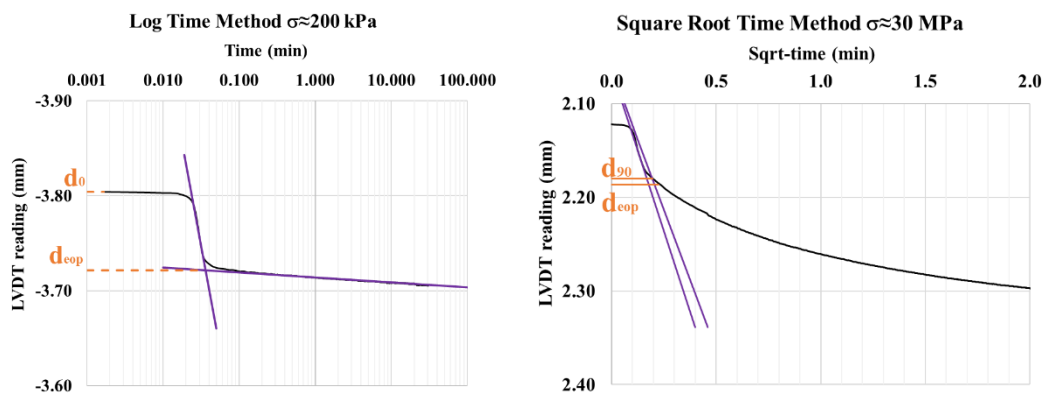
Figure 3.34. Example plots for determination of end of primary compression

Tangent compression and recompression indices and constrained moduli were calculated by using the following formulae:

$$C_c \text{ or } C_r = \frac{\Delta e}{\Delta log \sigma'_v}$$ Eqn. 3-29

$$M = \frac{\Delta \sigma'_v}{\Delta \varepsilon_a}$$ Eqn. 3-30

where,

C_c: tangent compression index

C_r: tangent recompression index

M: tangent constrained modulus

Δe: change in void ratio

92

$\Delta\sigma'_v$: change in axial stress

$\Delta\varepsilon_a$: change in axial strain

Secondary compression index was calculated by Eqn. 3-31.

$$C_\alpha = \frac{\Delta e}{\Delta log t}$$ Eqn. 3-31

where,

C_α: secondary compression index

CHAPTER 4

TEST RESULTS AND THEIR INTERPRETATIONS

4.1   Introduction

In this chapter, results of CU-triaxial and oedometer tests are presented and compared with the available literature. For this purpose, four-way plots were prepared to illustrate the response of Kızılırmak sand under shear straining. Also, to examine the relative density and confining stress effects on the shearing response and strength, comparative graphs were prepared. For the oedometer tests, e vs. $\log\sigma'_v$ graphs were prepared. Constrained modulus, compression index, secondary compression index, and yield stress were calculated corresponding to different stress levels and relative densities.

4.2   CU Monotonic Triaxial Test Results

In Table 4.1, initial relative density (D_R), initial void ratio (e_0), consolidation pressure (σ'_c), void ratio after consolidation (e_c), axial strain value at failure ($\varepsilon_{a,failure}$) and effective stress angle of shearing resistance (ϕ') are summarized.

Table 4.1 Summary of the triaxial test results

Test Name	D_R(%)	e_0	σ'_c (kPa)	e_c	$\varepsilon_{a,failure}$ (%)	ϕ'(°)
TRX_35-50	34	0.681	53.5	0.672	1.3	36.4
TRX_35-100	35	0.678	97.6	0.657	2.0	36.3
TRX_35-200	36	0.674	97.6	0.640	2.0	35.4
TRX_35-400	34	0.682	398.9	0.612	4.1	38.7
TRX_45-50	46	0.641	47.7	0.634	1.5	36.2
TRX_45-100	45	0.643	88.8	0.624	2.0	36.4
TRX_45-200	47	0.636	203.1	0.607	2.0	37.8
TRX_45-400	47	0.636	397.7	0.590	2.6	40.2
TRX_60-50	59	0.595	50.7	0.589	0.8	40.5
TRX_60-100	60	0.591	99.3	0.577	1.1	40.4
TRX_60-200	60	0.592	191.8	0.567	1.5	39.2
TRX_60-400	59	0.594	399.9	0.558	2.1	39.8
TRX_75-50	74	0.544	52.6	0.538	0.9	42.3
TRX_75-100	72	0.550	96.9	0.539	1.0	41.6
TRX_75-200	73	0.545	184.5	0.524	1.3	41.0
TRX_75-400	73	0.547	402.7	0.519	1.8	40.6
TRX_80-50	81	0.519	53.8	0.514	1.2	43.7
TRX_80-100	83	0.512	94.0	0.499	0.9	43.5
TRX_80-200	83	0.511	199.8	0.486	1.5	42.8
TRX_80-400	82	0.516	400.7	0.486	1.5	41.9

Half of the deviatoric stress (shear stress) vs. axial strain (q vs. ε_a), half of the deviatoric stress (shear stress) vs. mean effective stress (q vs. p'), shear stress vs. effective stress (τ vs. σ'), excess pore water pressure vs. axial strain (U_{exc} vs. ε_a), effective stress ratio (stress obliquity) vs. mean effective stress (q/p' vs. p') graphs are presented in the form of four-way plots. Failure point was estimated benefitting from maximum obliquity criterion, and these points are shown in the graphs mentioned above. Four-way plots of each CU triaxial test are presented in Figure 4.1 through Figure 4.20.
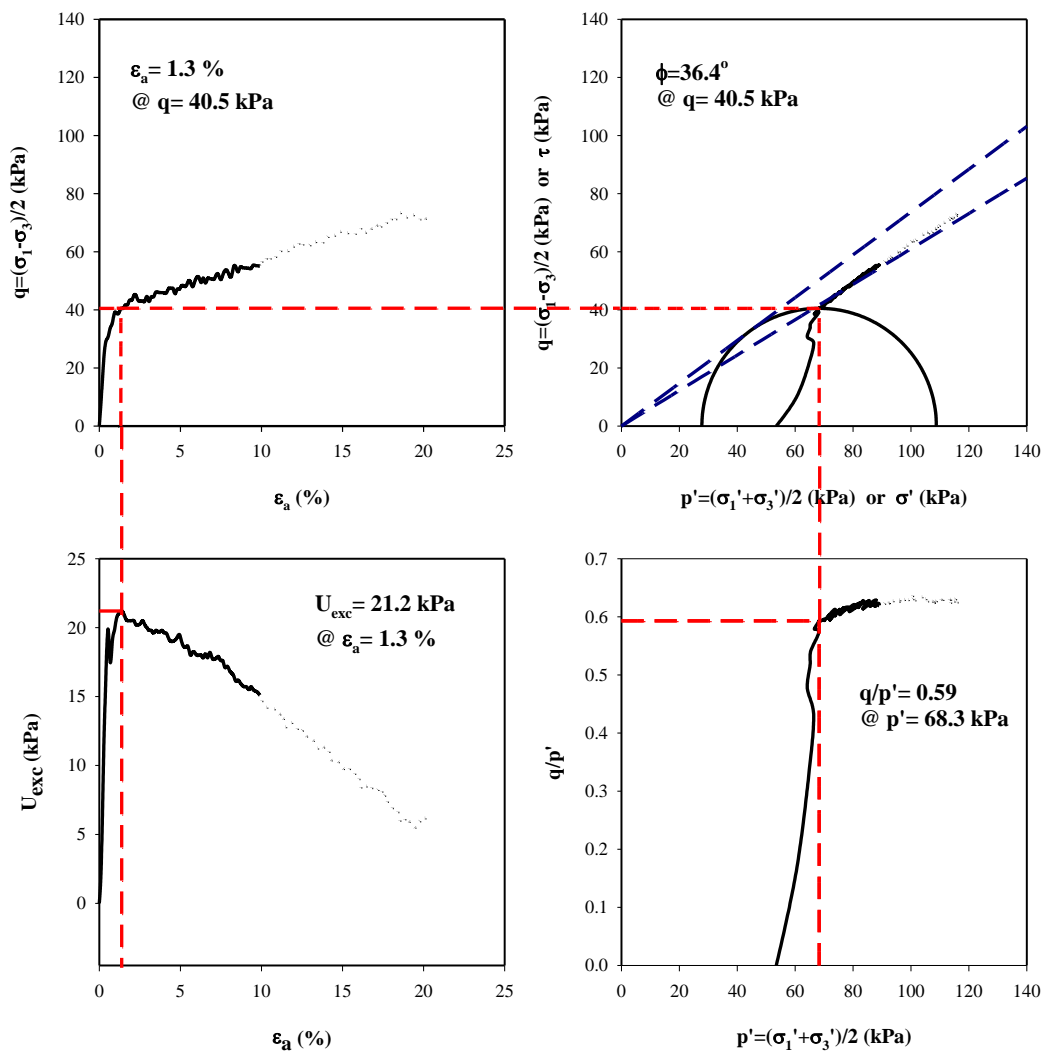
Figure 4.1. Four-way plots of TRX_35-50
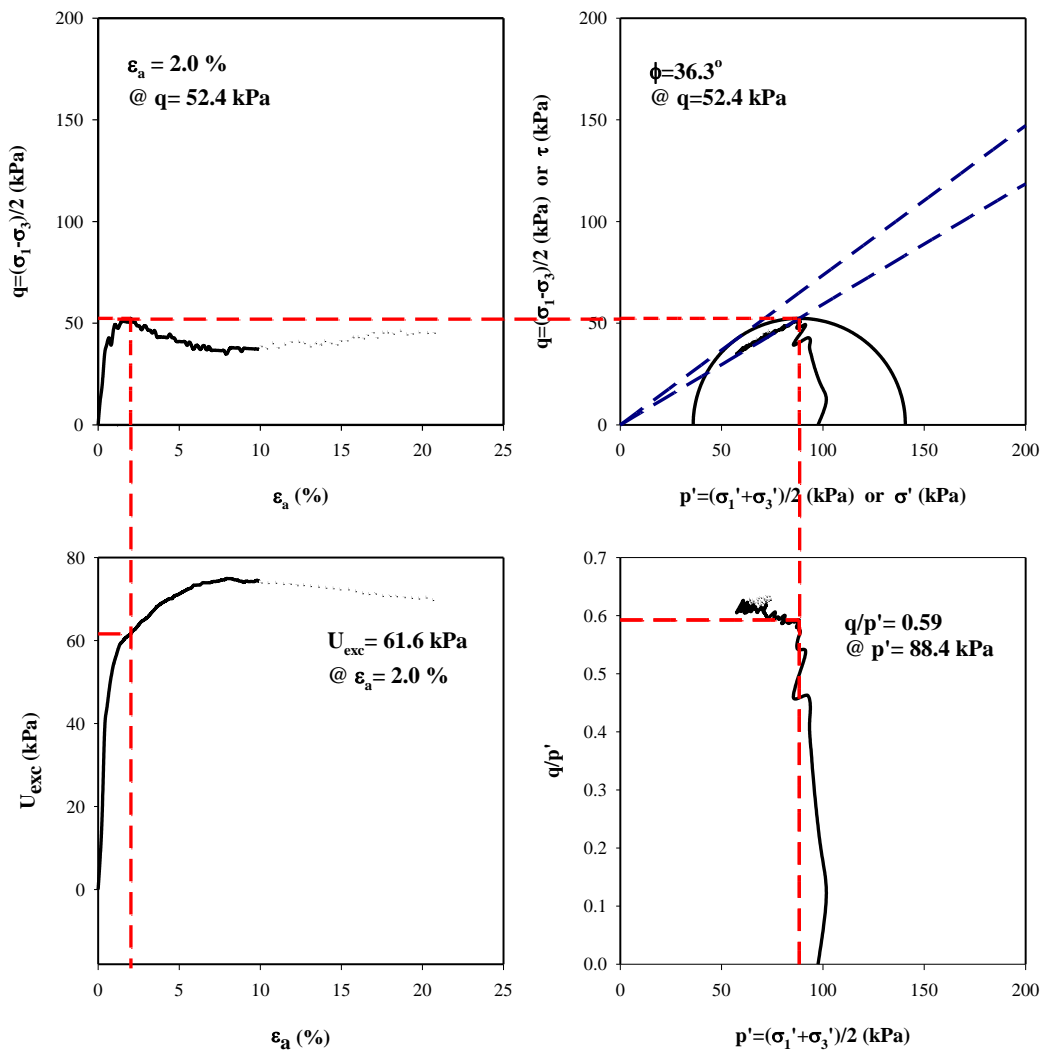
Figure 4.2. Four-way plots of TRX_35-100
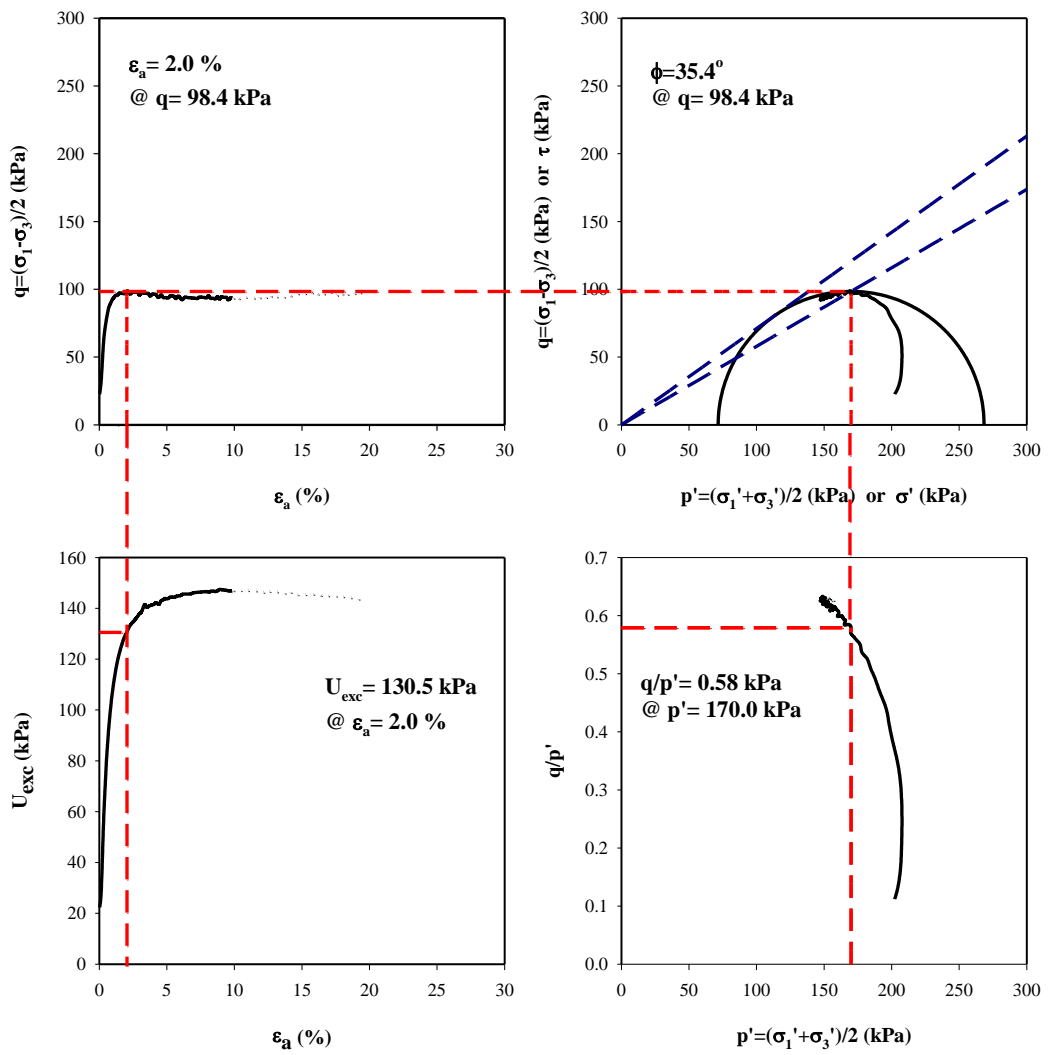
Figure 4.3. Four-way plots of TRX_35-200
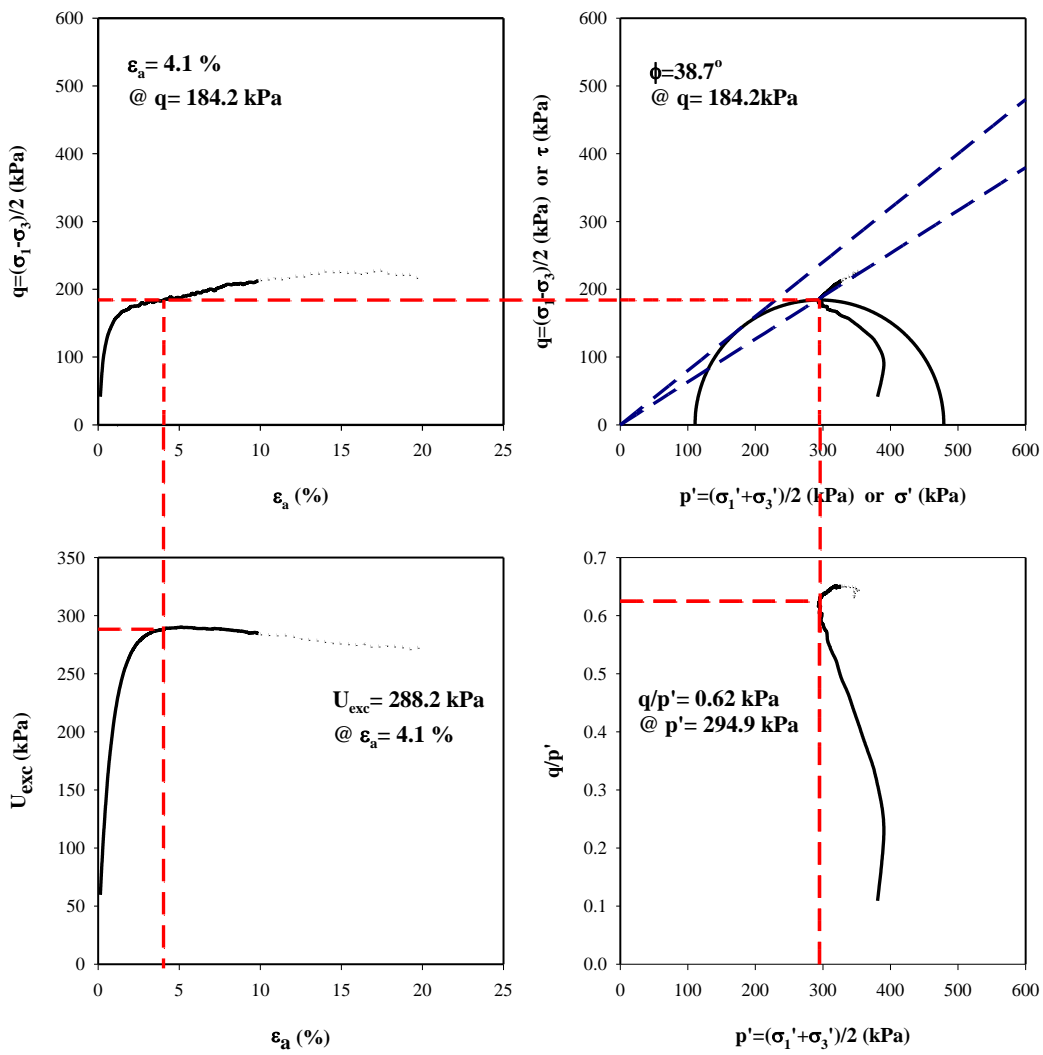
Figure 4.4. Four-way plots of TRX_35-400
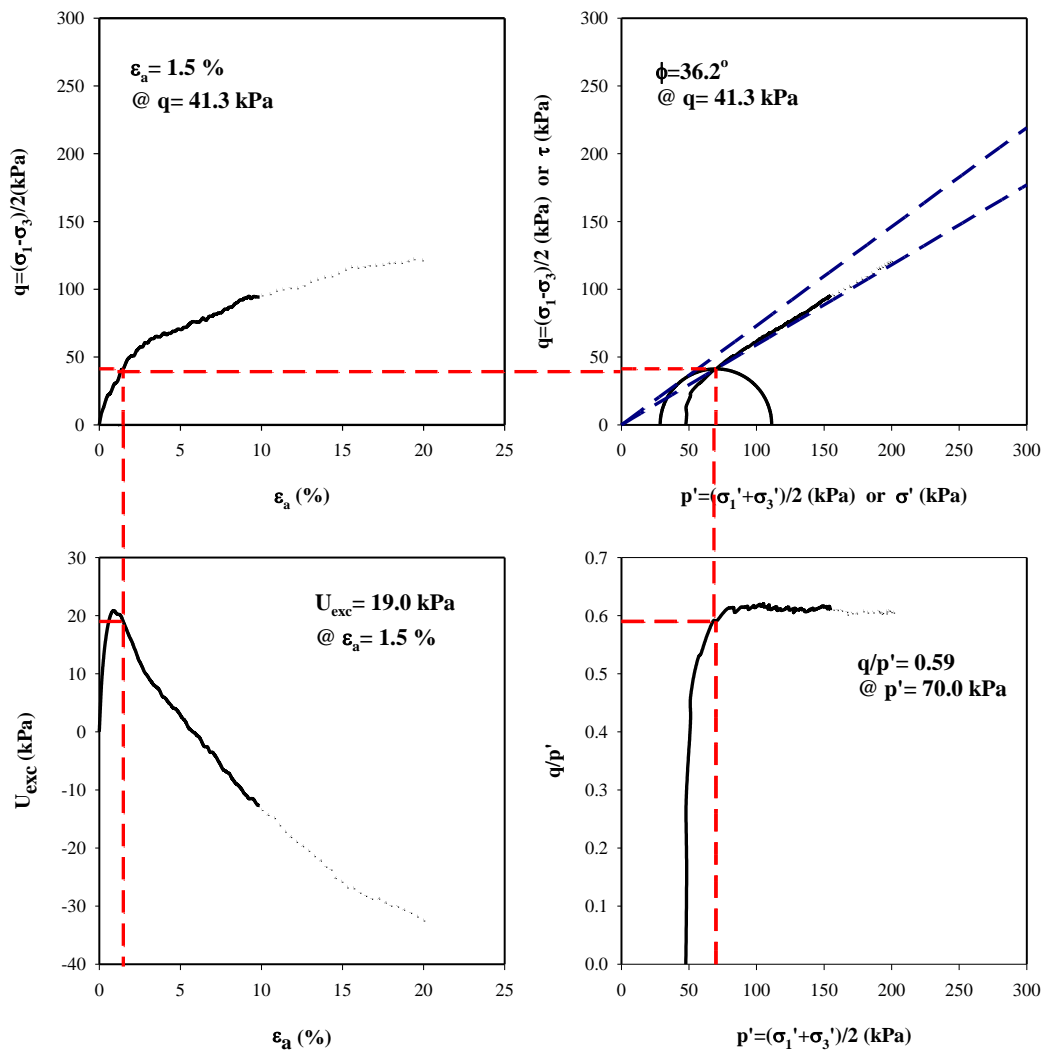
Figure 4.5. Four-way plots of TRX_45-50
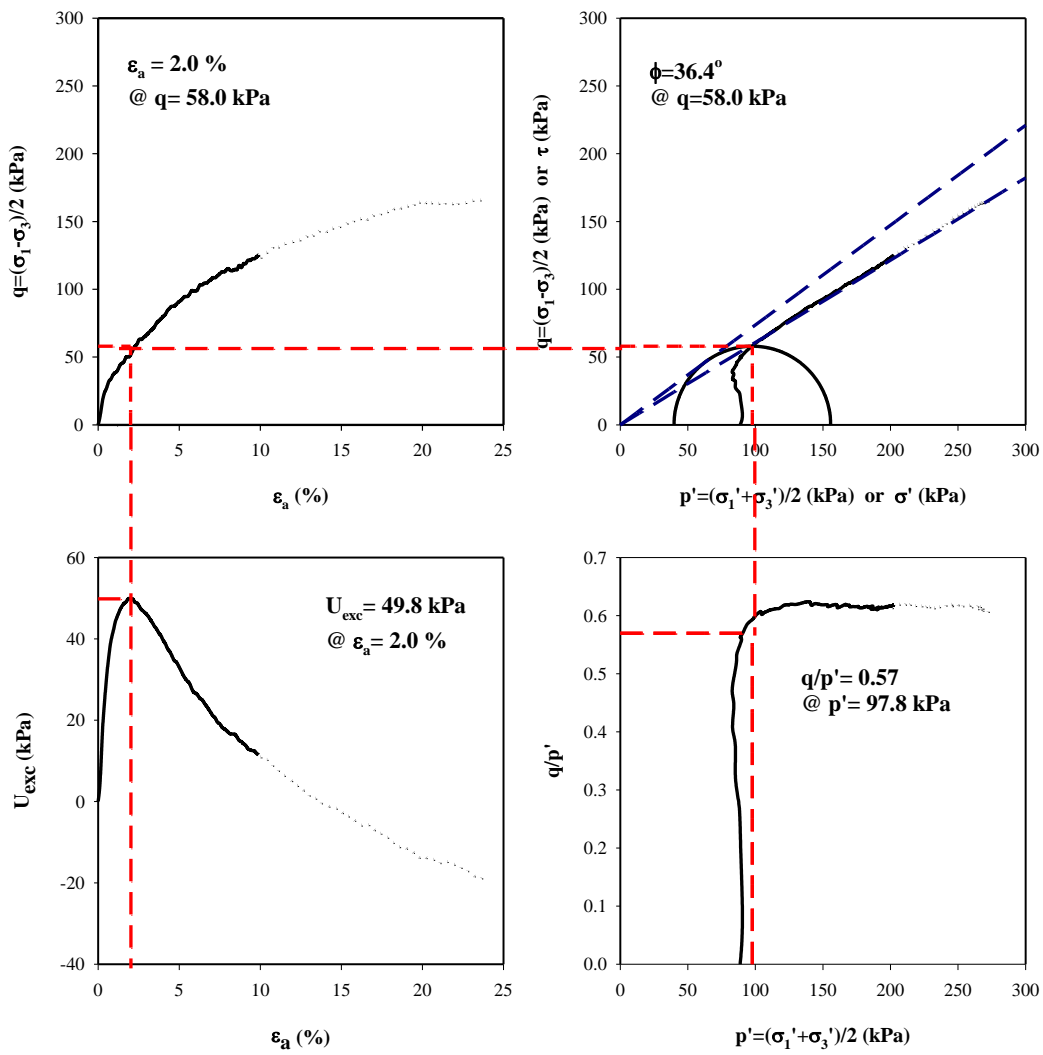
Figure 4.6. Four-way plots of TRX_45-100
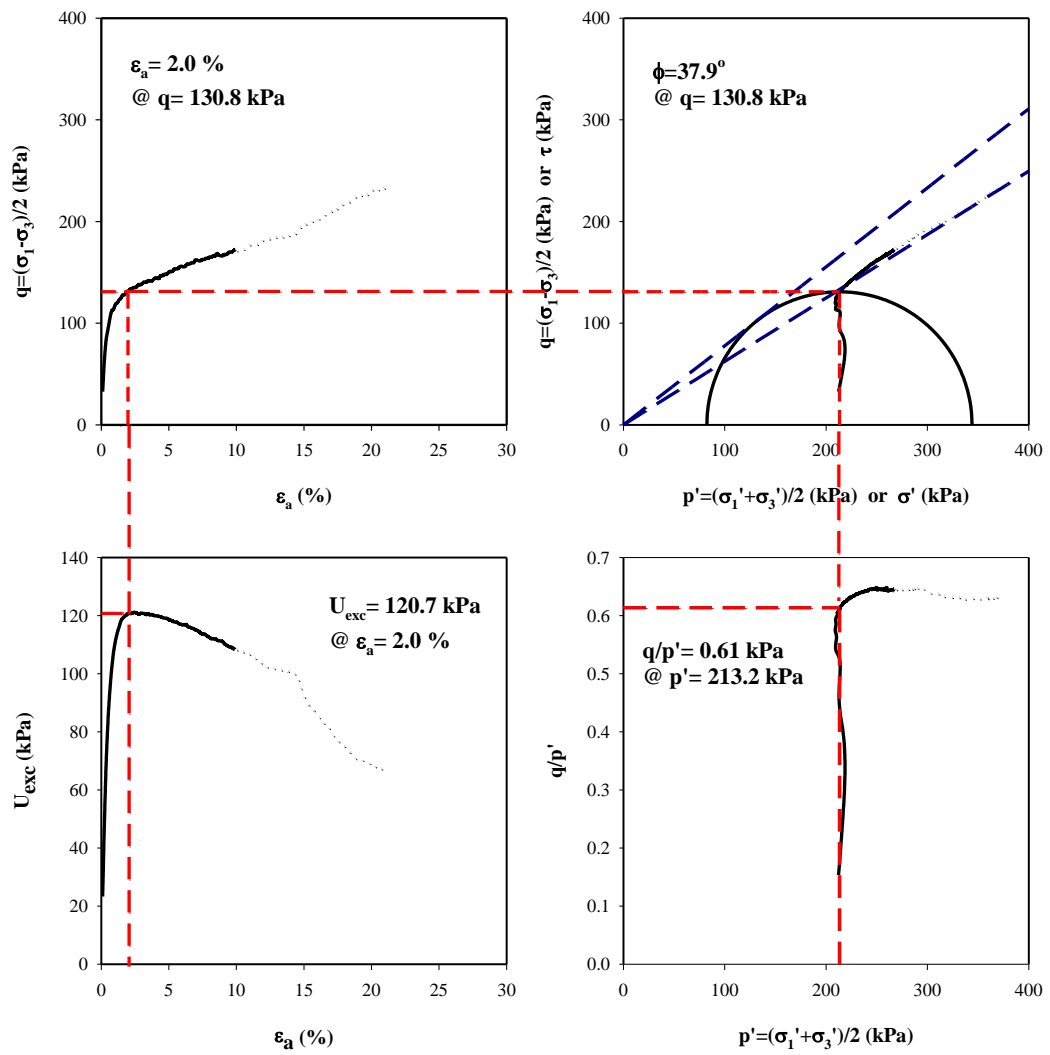
Figure 4.7. Four-way plots of TRX_45-200

103
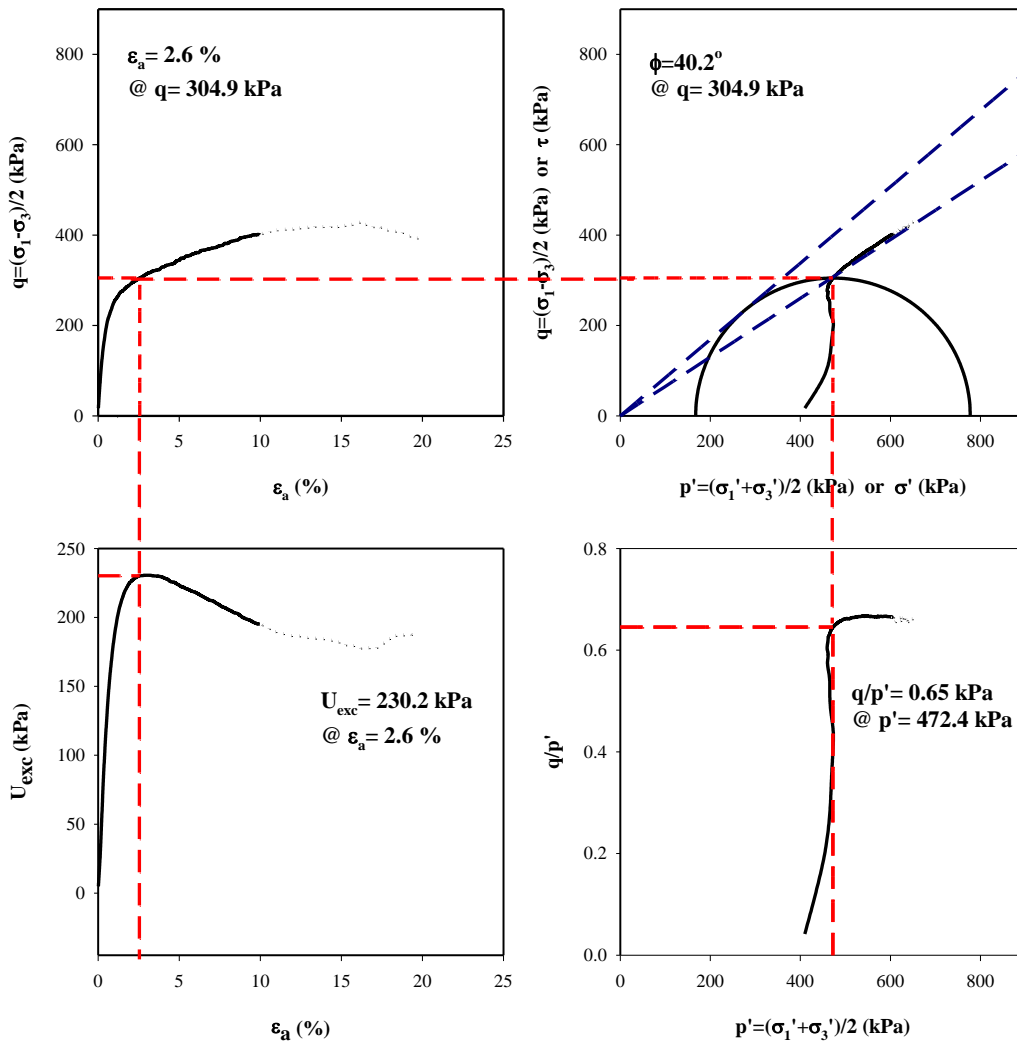
Figure 4.8. Four-way plots of TRX_45-400
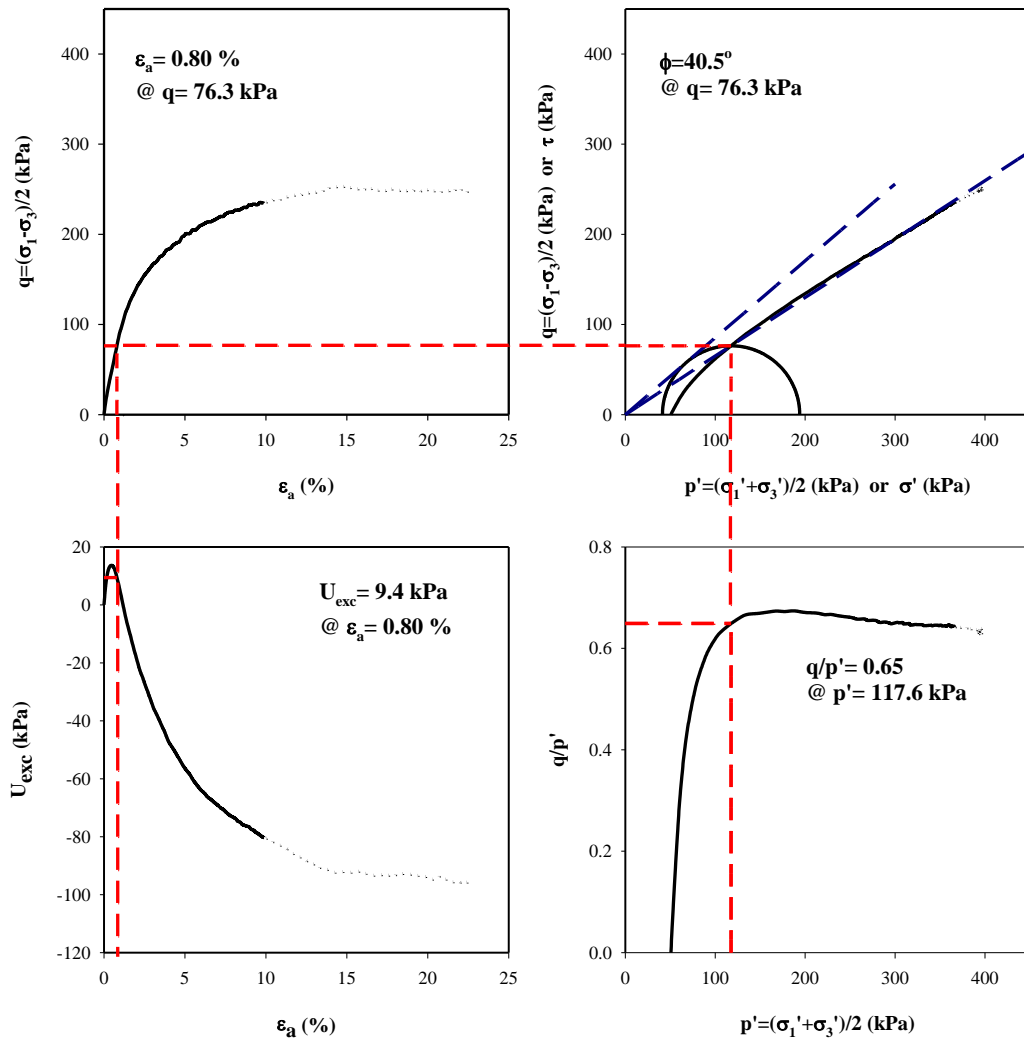
Figure 4.9. Four-way plots of TRX_60-50
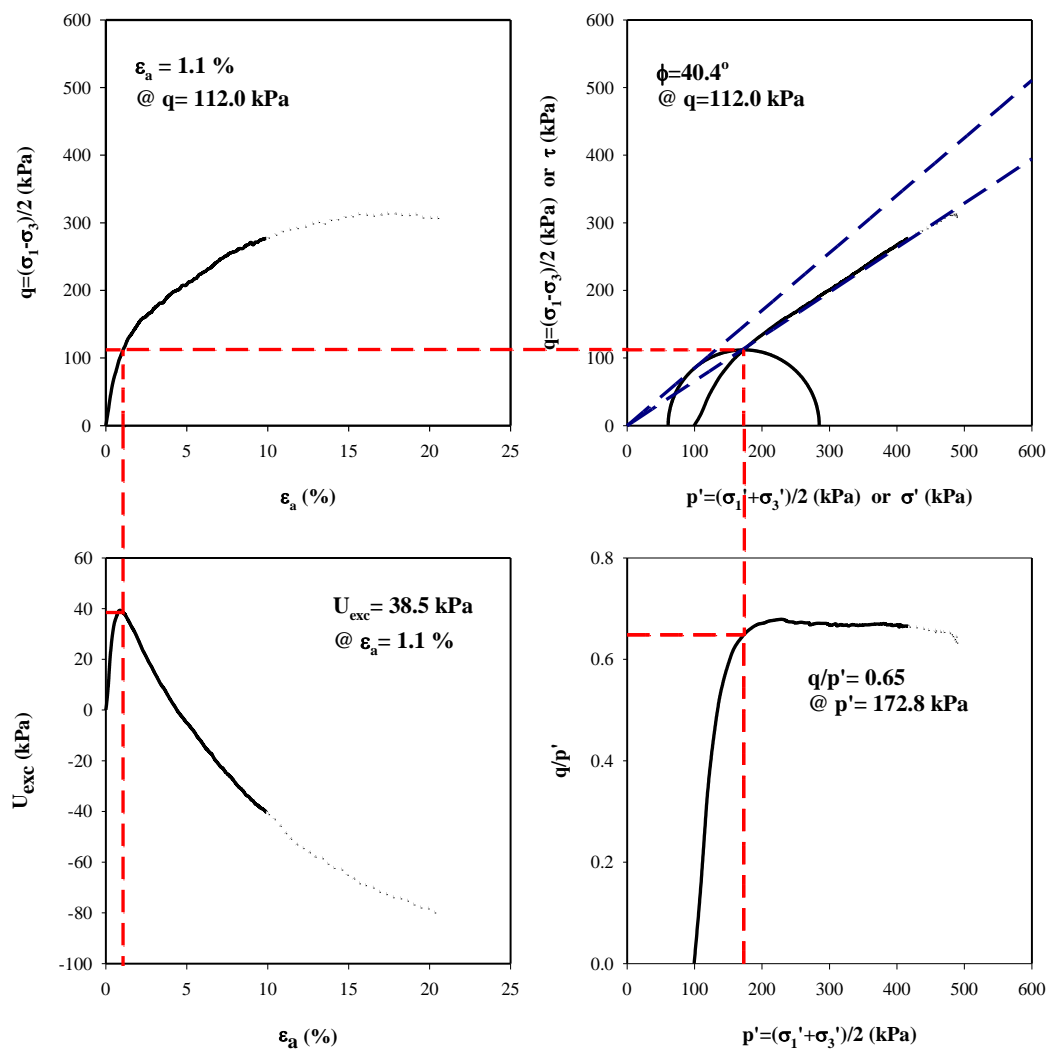
Figure 4.10. Four-way plots of TRX_60-100
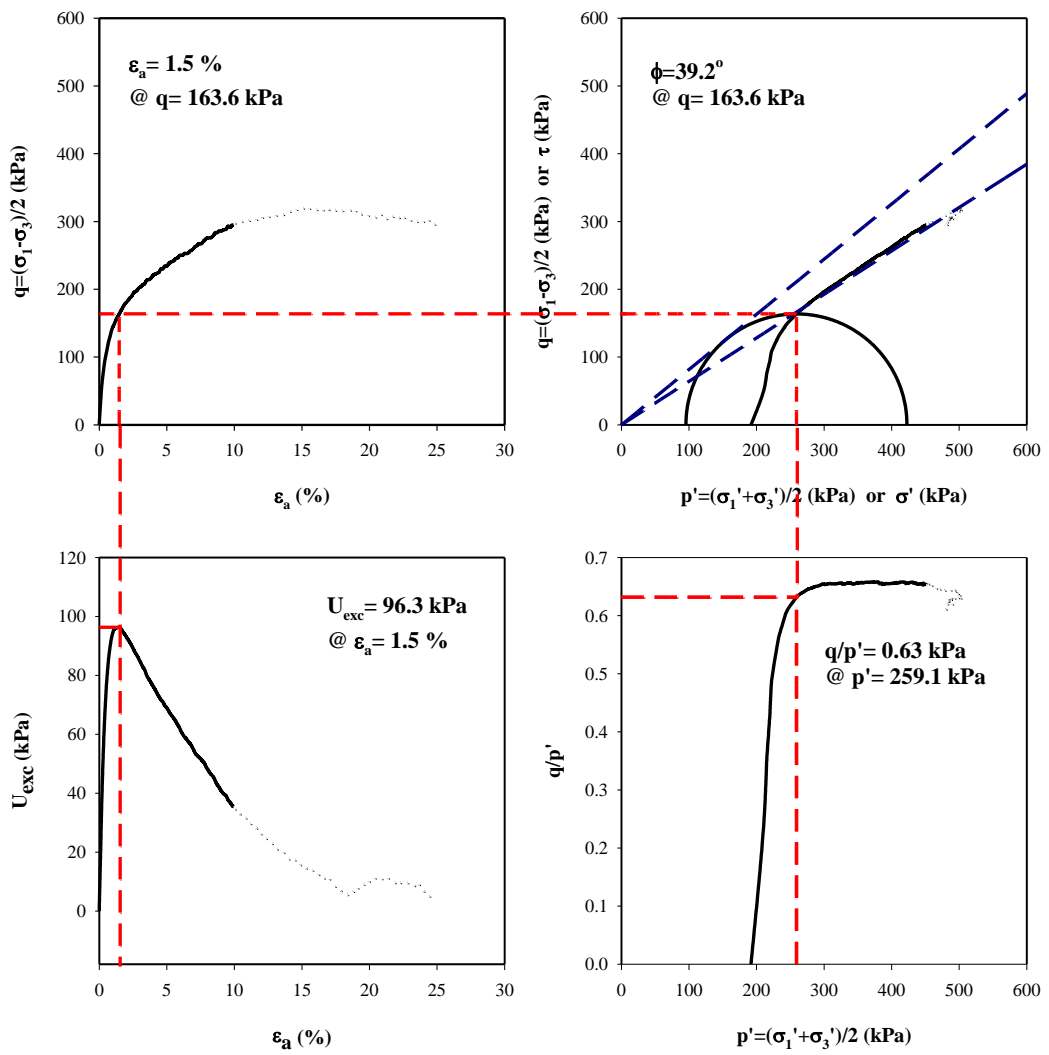
Figure 4.11. Four-way plots of TRX_60-200
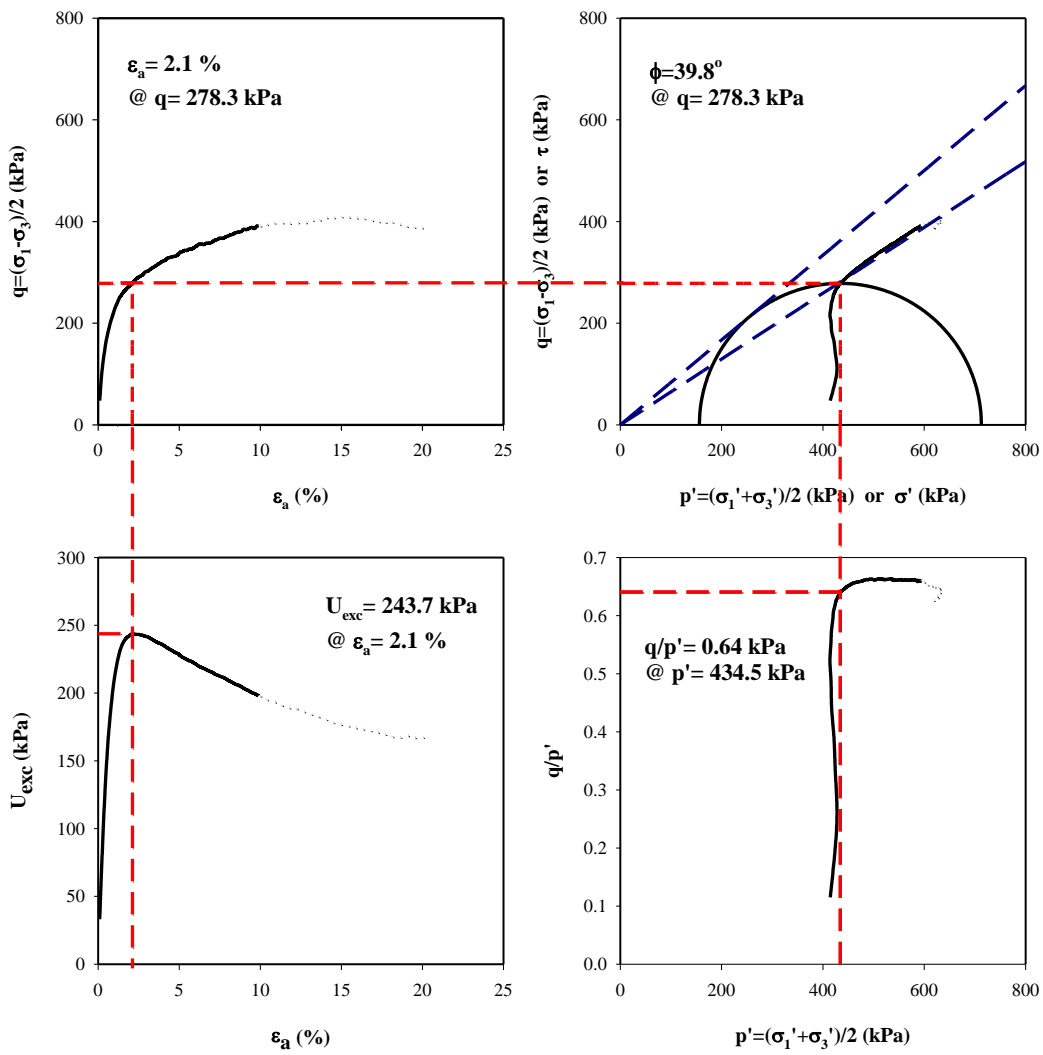
Figure 4.12. Four-way plots of TRX_60-400
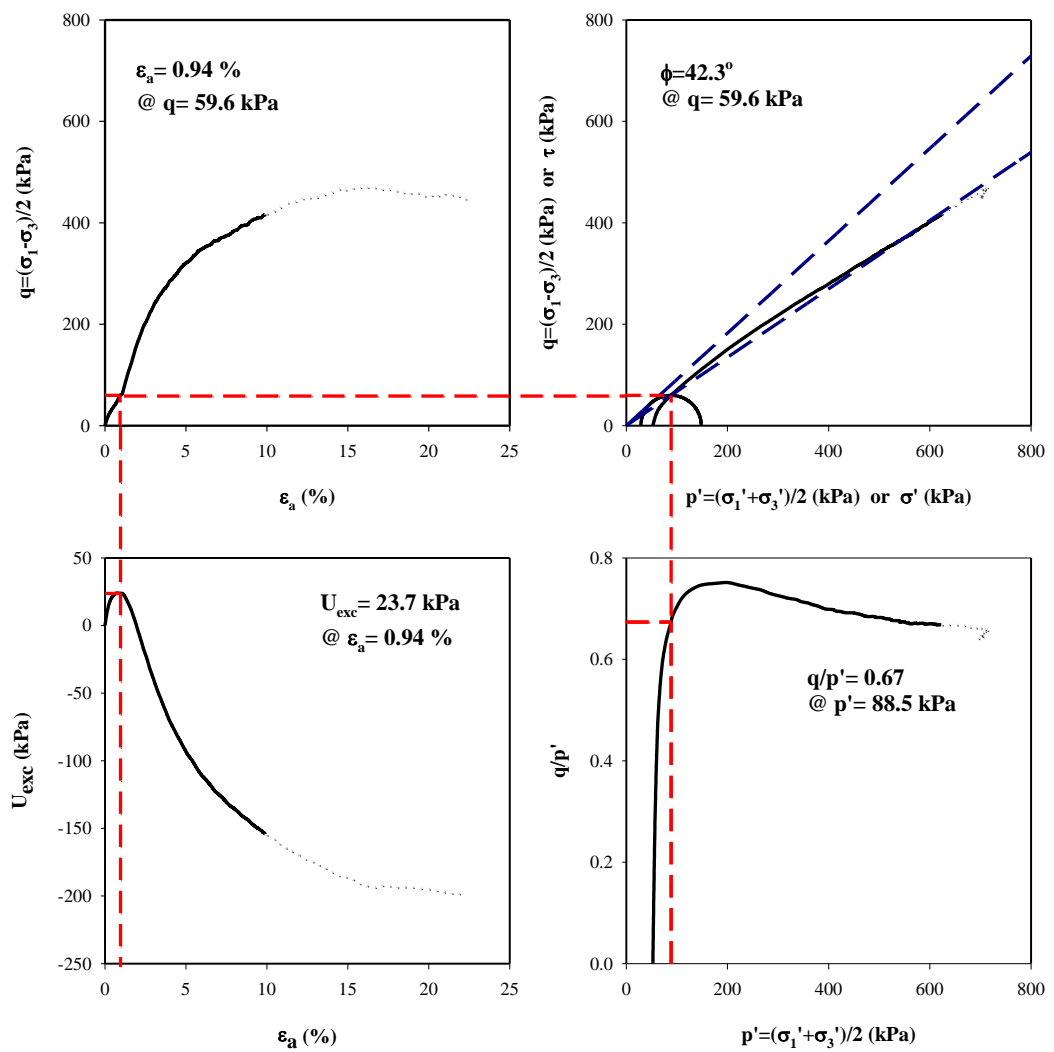
Figure 4.13. Four-way plots of TRX_75-50
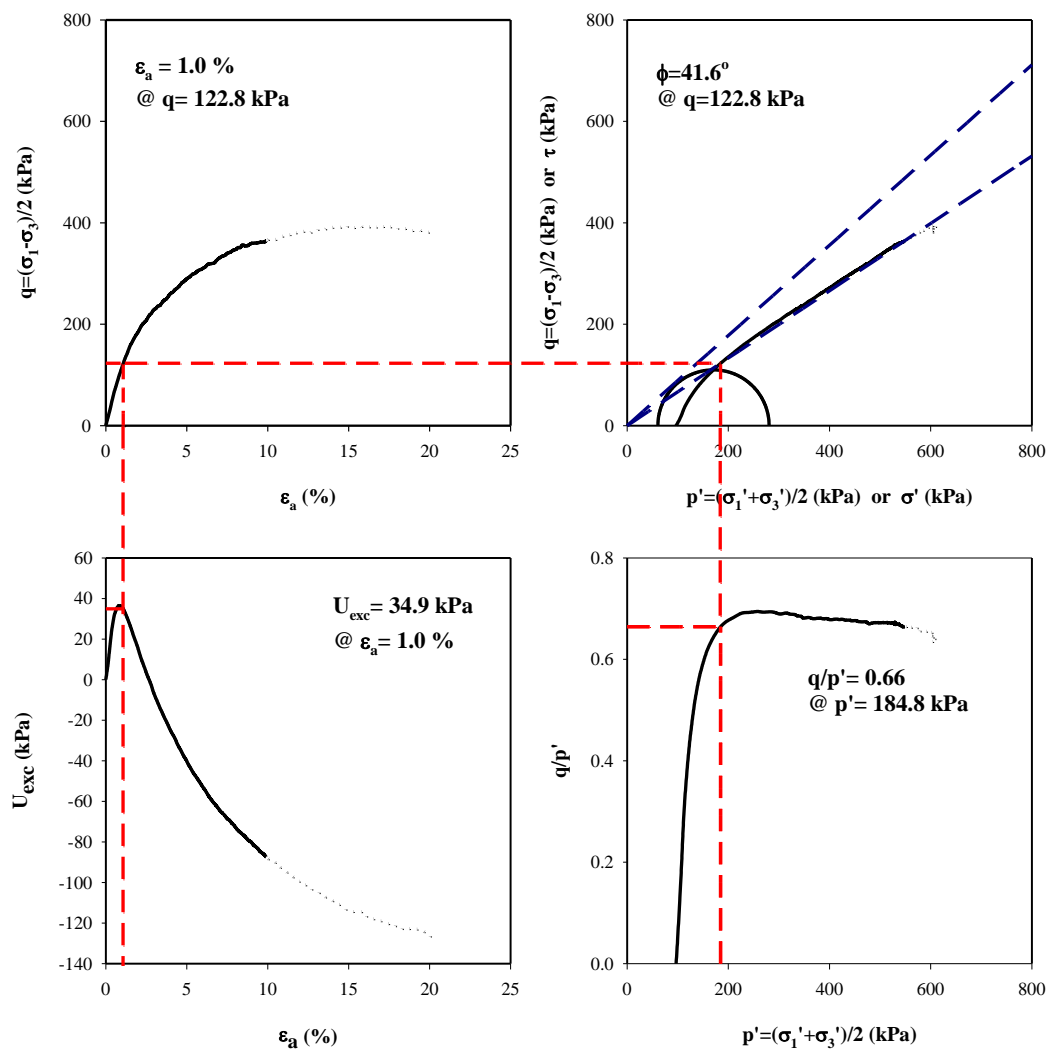
Figure 4.14. Four-way plots of TRX_75-100
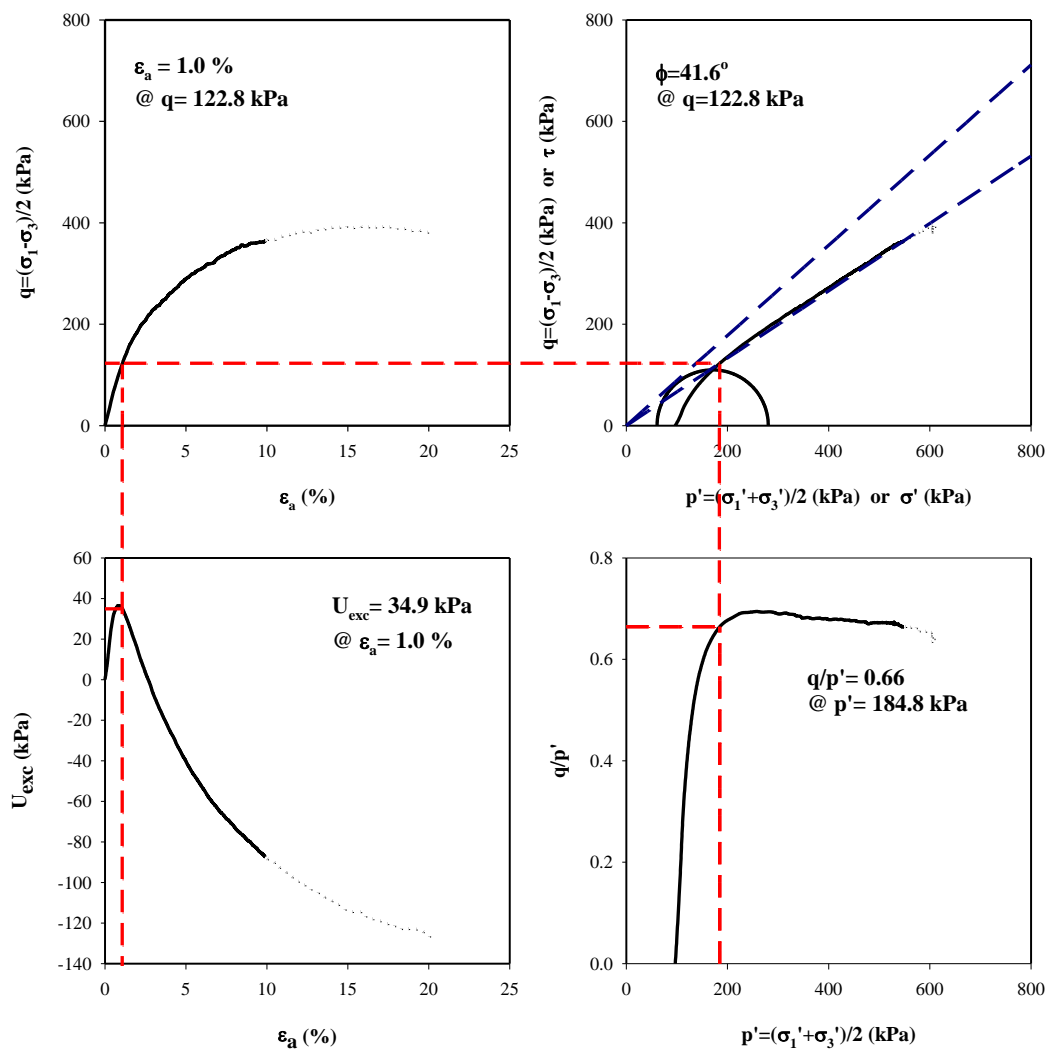
Figure 4.15. Four-way plots of TRX_75-200
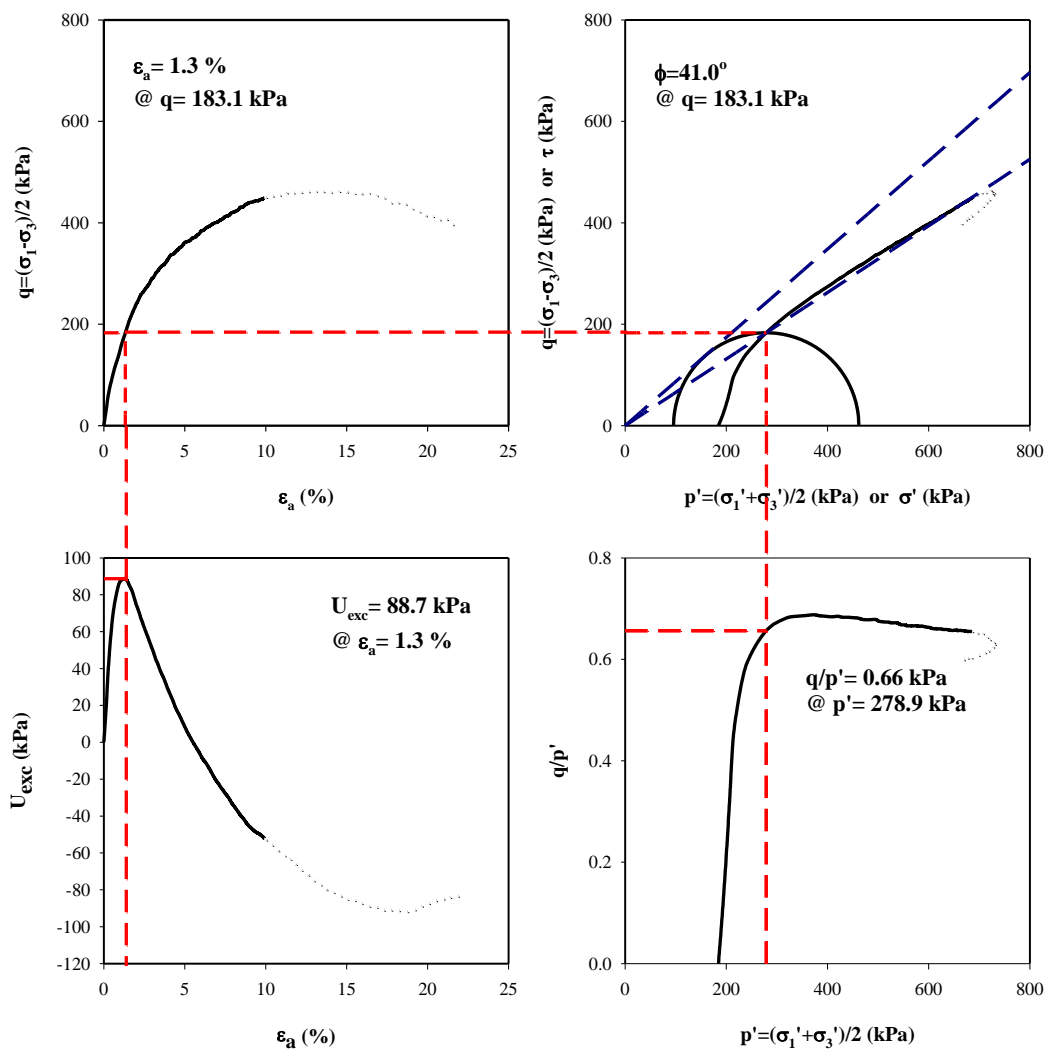
Figure 4.16. Four-way plots of TRX_75-400
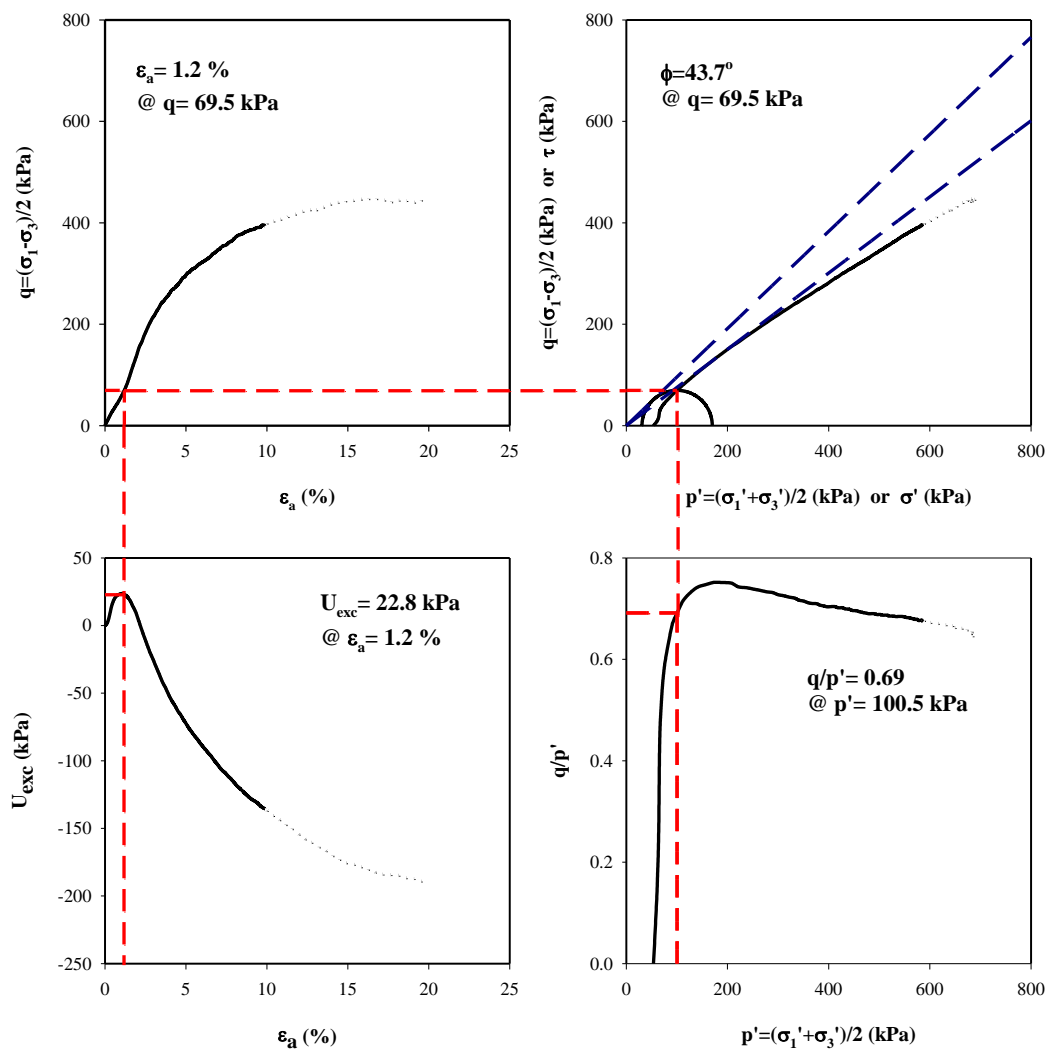
Figure 4.17. Four-way plots of TRX_80-50
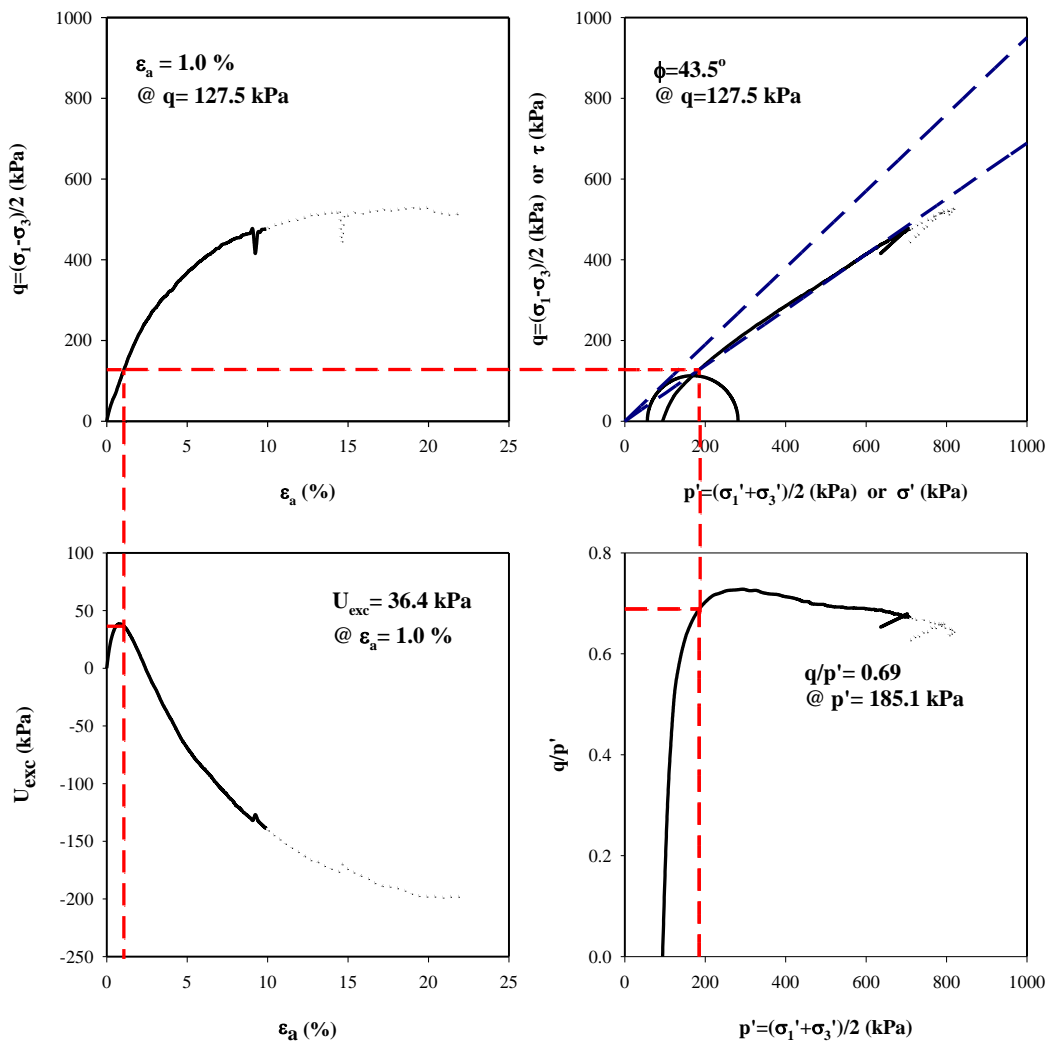
Figure 4.18. Four-way plots of TRX_80-100

114
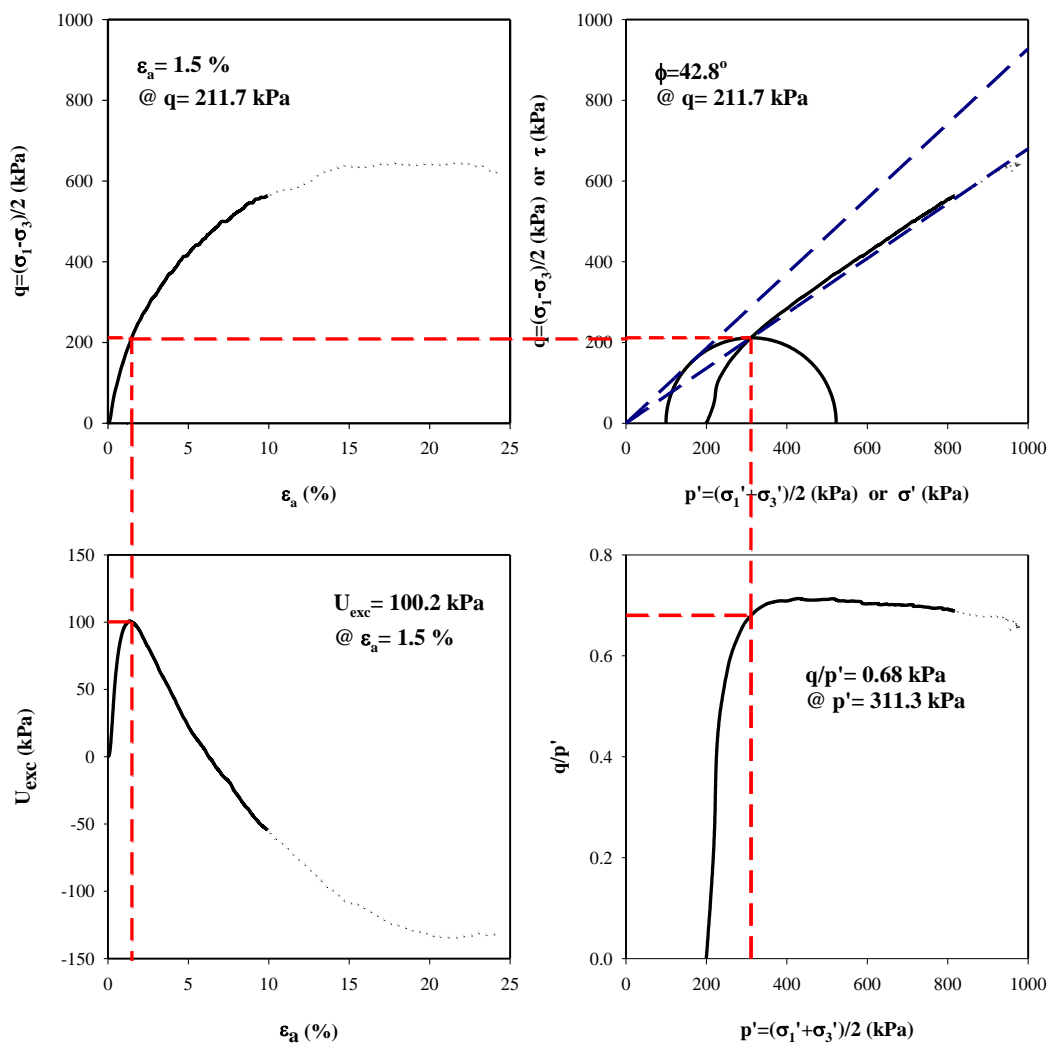
Figure 4.19. Four-way plots of TRX_80-200
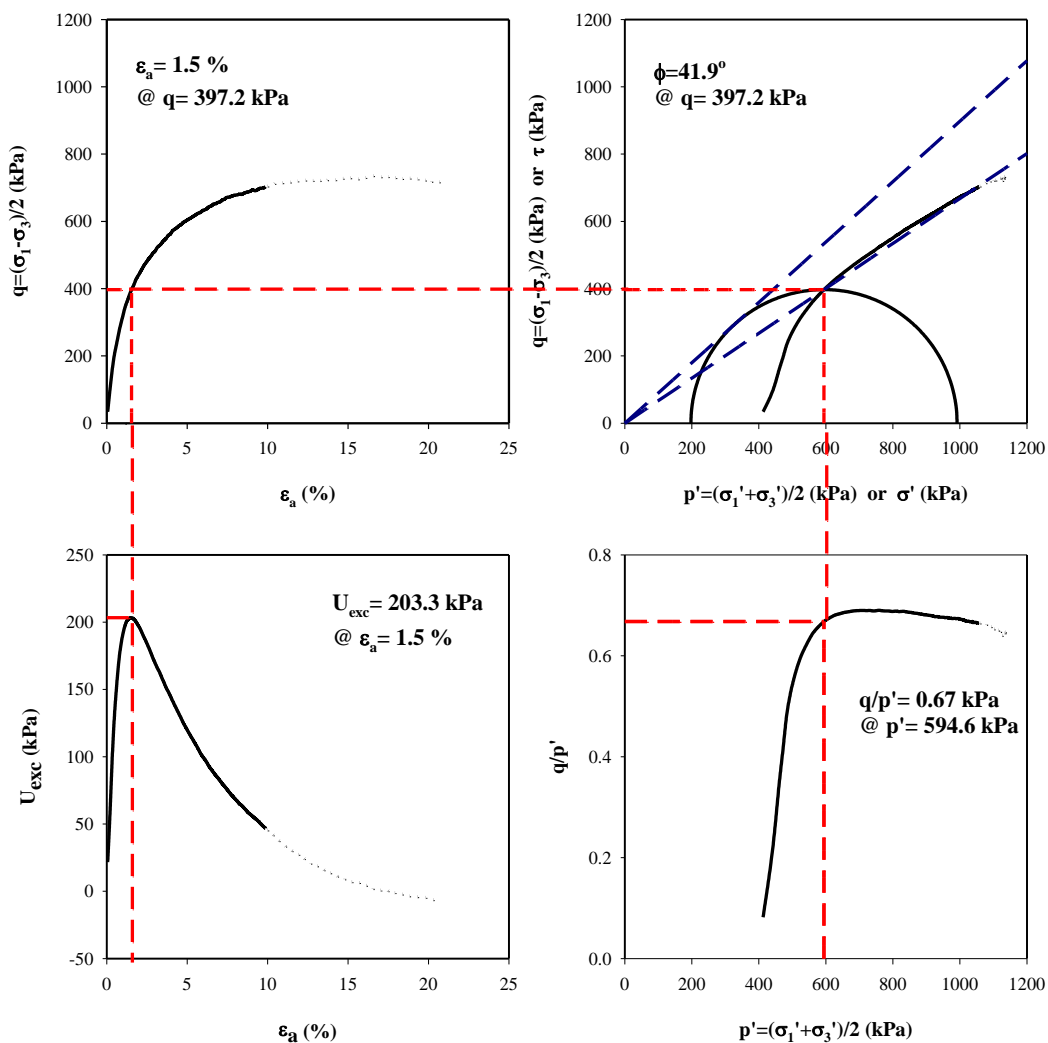
Figure 4.20. Four-way plots of TRX_80-400

4.3 Interpretation of CU Monotonic Triaxial Test Results

Comparative plots were prepared to examine the relative density and confining effective stress effects on the shearing response and strength. The specimens prepared at the same relative densities but consolidated to different confining stresses were grouped together and compared to understand the confining stress effects on the shearing response. For this purpose, q vs ε_a and U_{exc} vs. ε_a graphs were prepared, as shown in Figure 4.21 - Figure 4.25.
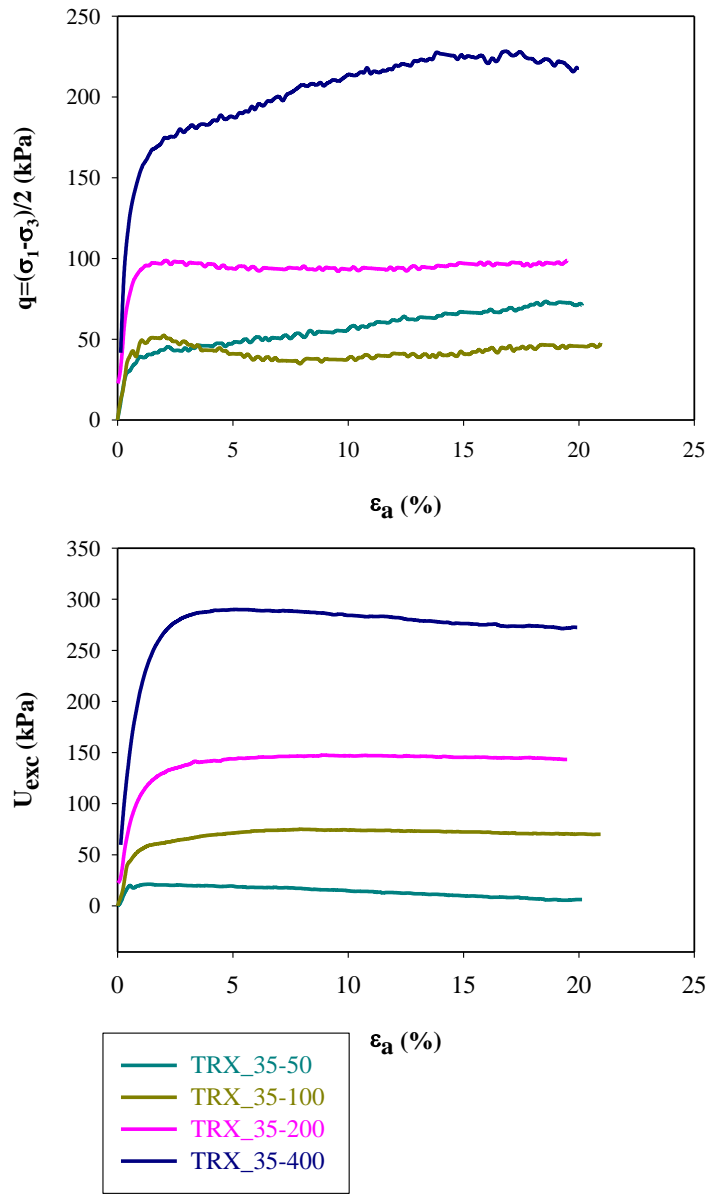
116

Figure 4.21. q vs. ε_a and U_{exc} vs. ε_a graphs for the specimens prepared at ≈35% relative density and consolidated to 50 kPa, 100 kPa, 200 kPa, and 400 kPa stresses
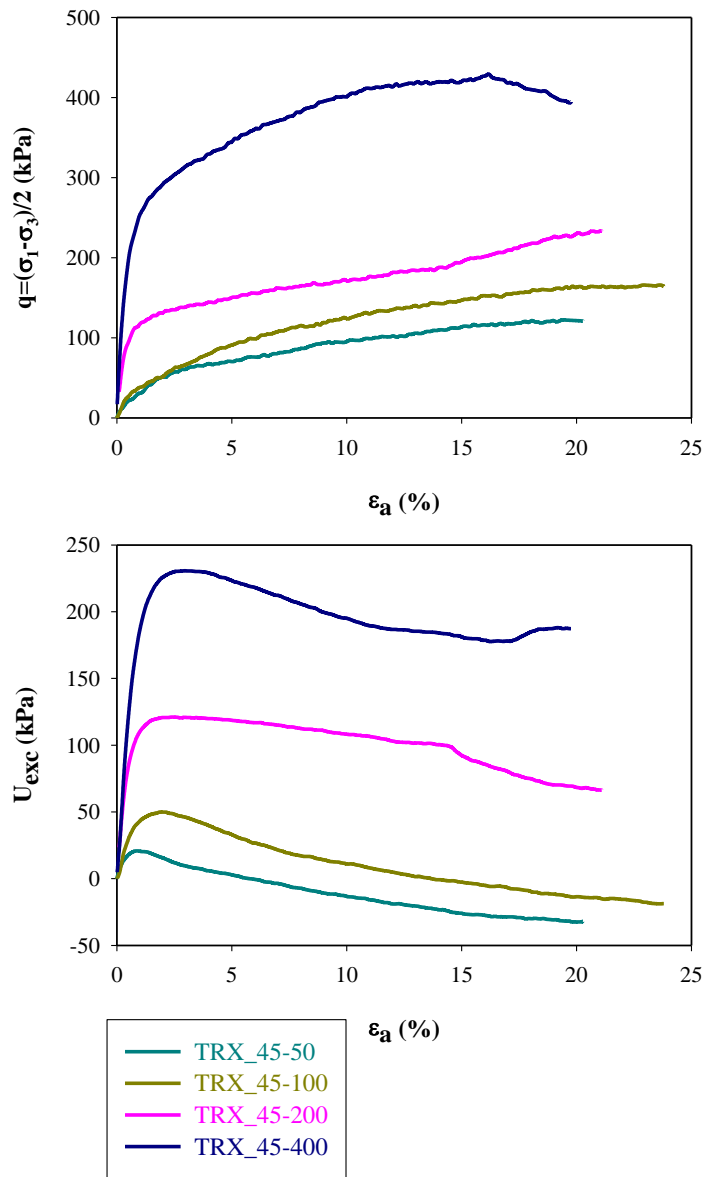
Figure 4.22. q vs. ε_a and U_{exc} vs. ε_a graphs for the specimens prepared at ≈45% relative density and consolidated to 50 kPa, 100 kPa, 200 kPa, and 400 kPa stresses
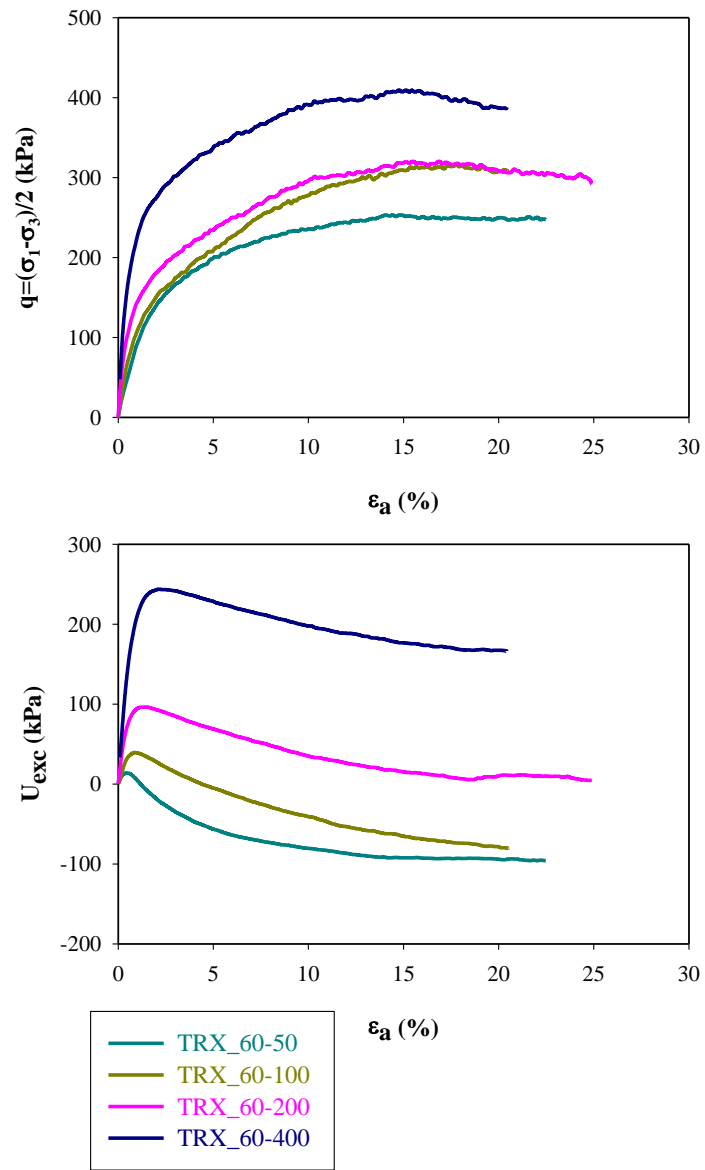
Figure 4.23. q vs. ε_a and U_{exc} vs. ε_a graphs for the specimens prepared at ≈60% relative density and consolidated to 50 kPa, 100 kPa, 200 kPa, and 400 kPa stresses
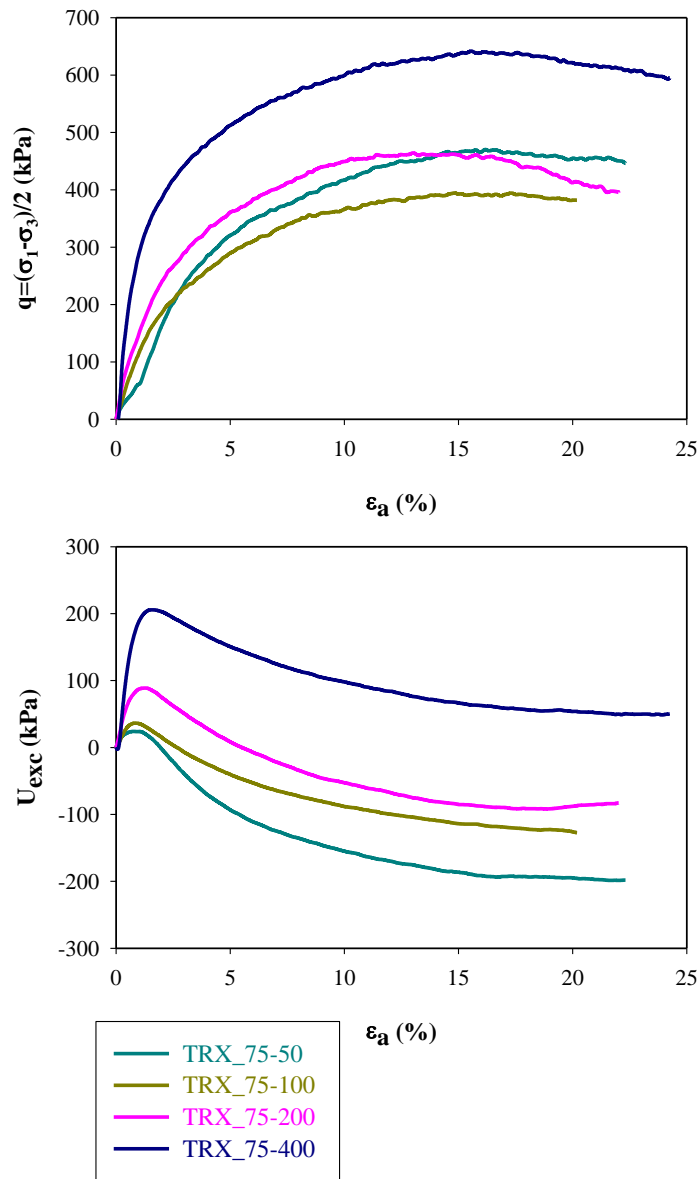
Figure 4.24. q vs. ε_a and U_{exc} vs. ε_a graphs for the specimens prepared at 75% relative density and consolidated to 50 kPa, 100 kPa, 200 kPa, and 400 kPa stresses
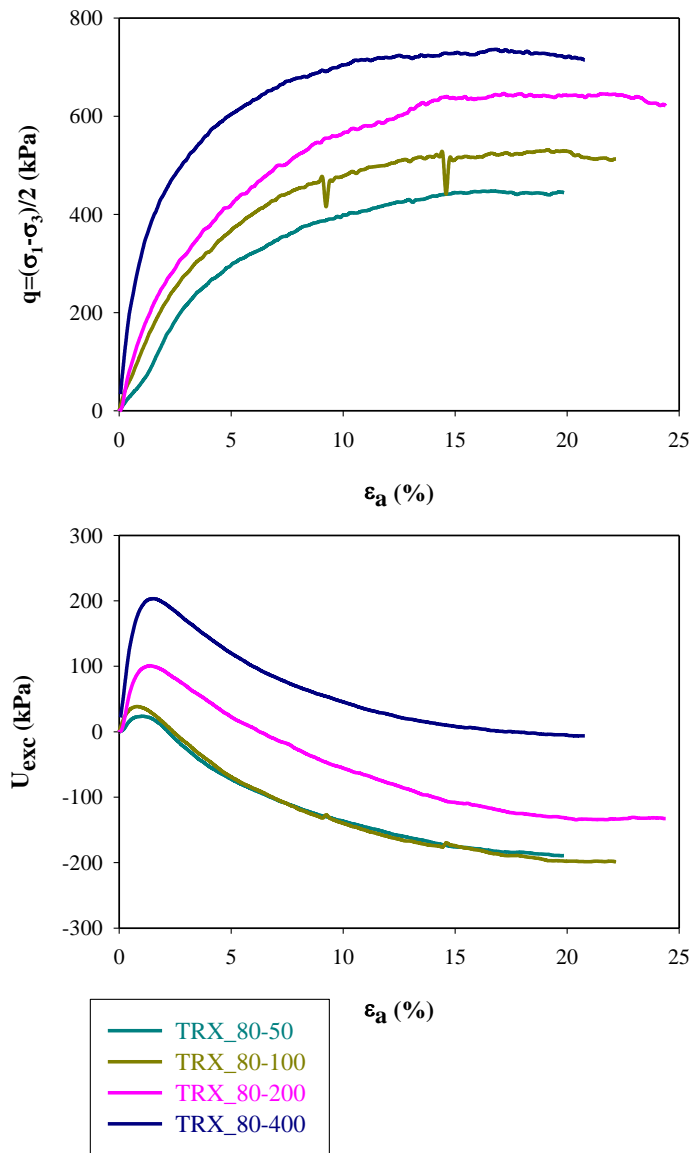
Figure 4.25. q vs. ε_a and U_{exc} vs. ε_a graphs for the specimens prepared at ≈80% relative density and consolidated to 50 kPa, 100 kPa, 200 kPa, and 400 kPa stresses

q vs. ε_a plots reveal that increasing confining stress increases the shear strength of the specimen, conformably with the literature (e.g. Bishop, 1966; Bolton, 1986; Andersen and Schjetne, 2013). In excess pore water vs. strain graphs, it can be seen that the dilation rate (speculated from the rate of negative excess pore water pressure generation in undrained test) is in a decreasing trend with increasing effective stress.

To understand the confining stress effects on the strength, Mohr circles, and failure envelopes for the specimens which were prepared at the same relative density but consolidated to different confining stresses, were drawn. Figure 4.26 through Figure 4.30 present these comparative Mohr circles.
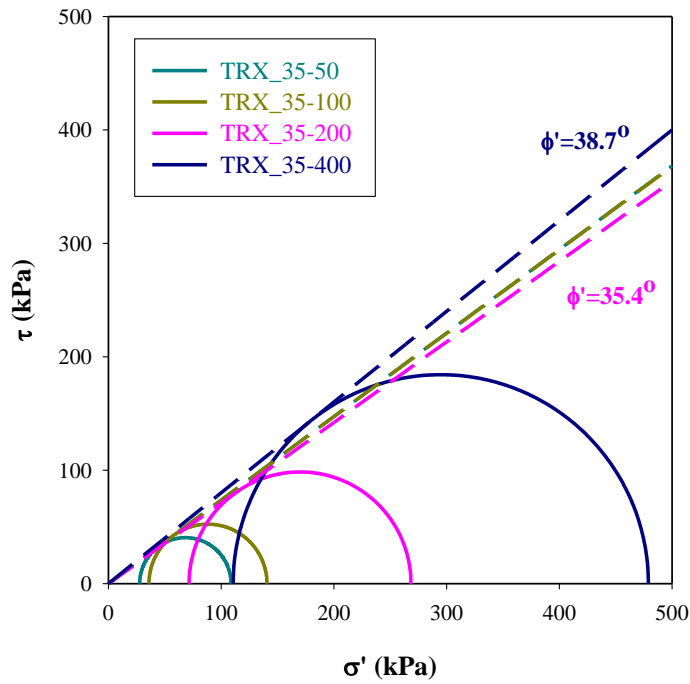
Figure 4.26. Mohr circles and corresponding failure envelopes of the specimens prepared at 35% relative density and consolidated to 50 kPa, 100 kPa, 200 kPa, and 400 kPa stresses
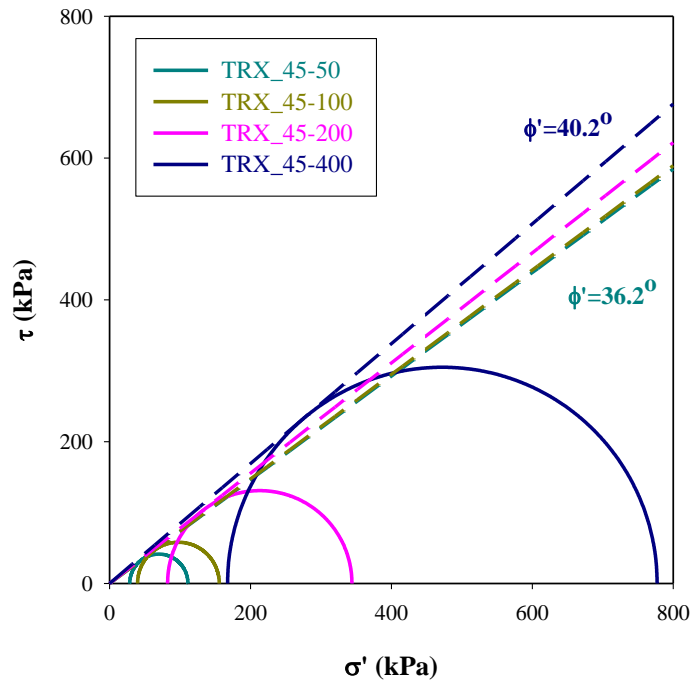
Figure 4.27. Mohr circles and corresponding failure envelopes of the specimens prepared at 45% relative density and consolidated to 50 kPa, 100 kPa, 200 kPa, and 400 kPa stresses
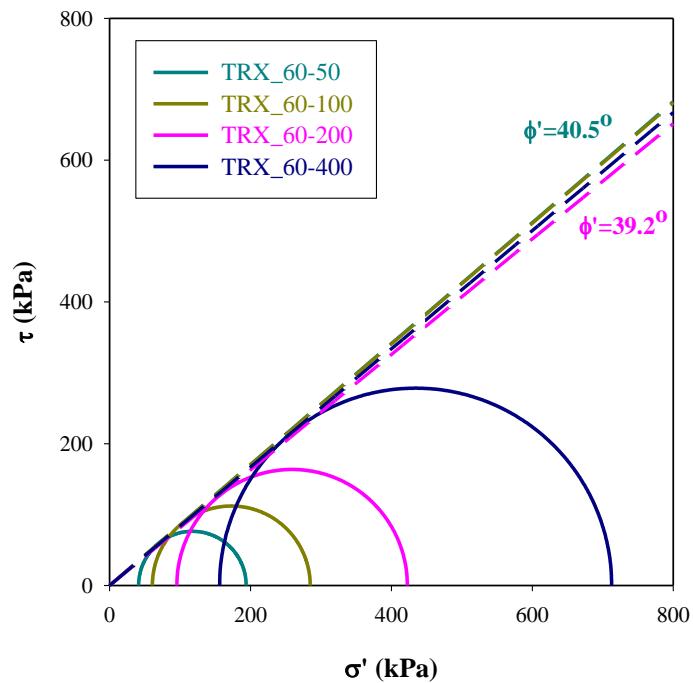
Figure 4.28. Mohr circles and corresponding failure envelopes of the specimens prepared at 60% relative density and consolidated to 50 kPa, 100 kPa, 200 kPa, and 400 kPa stresses

123
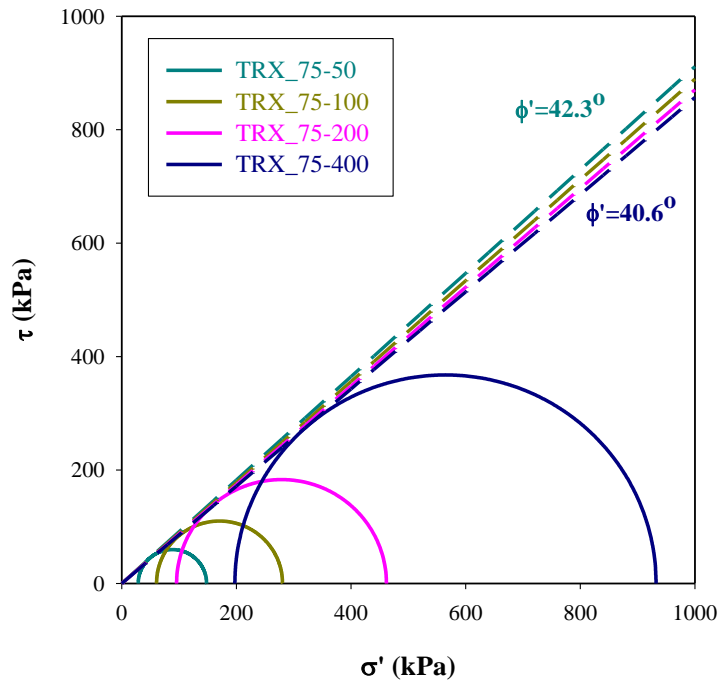
Figure 4.29. Mohr circles and corresponding failure envelopes of the specimens prepared at 75% relative density and consolidated to 50 kPa, 100 kPa, 200 kPa, and 400 kPa stresses
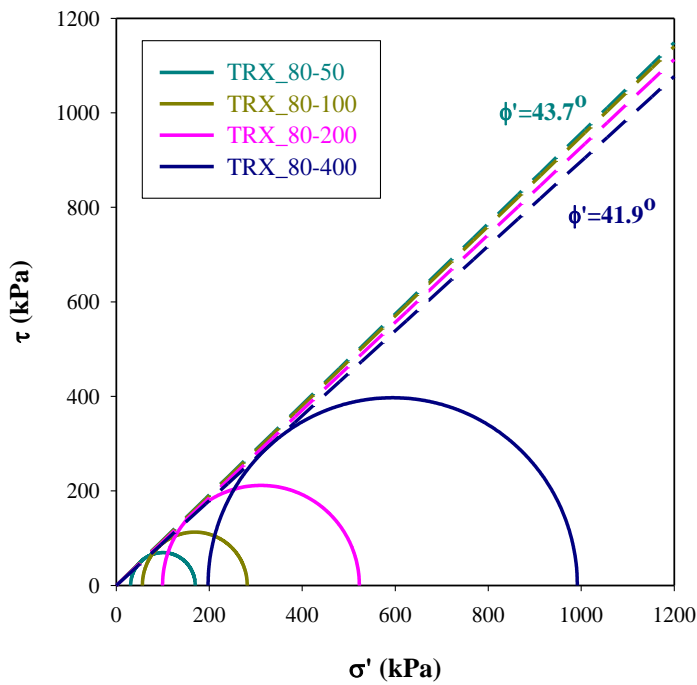
Figure 4.30. Mohr circles and corresponding failure envelopes of the specimens prepared at 80% relative density and consolidated to 50 kPa, 100 kPa, 200 kPa, and 400 kPa stresses

124

In the literature (e.g. Bishop, 1966; Bolton, 1986; Andersen and Schjetne, 2013) friction angle decreases with increasing effective stress due to crushing of angular edges, and suppression of dilation at higher confining stresses. Confirmably, test results mostly show the same response.

The specimens, which were consolidated to the same effective stress but prepared at different relative densities, were compared to understand the relative density effects on the shearing response. For this purpose, q vs. ε_a and U_{exc} vs. ε_a graphs were plotted. Figure 4.31 to Figure 4.34 presented these comparative graphs.
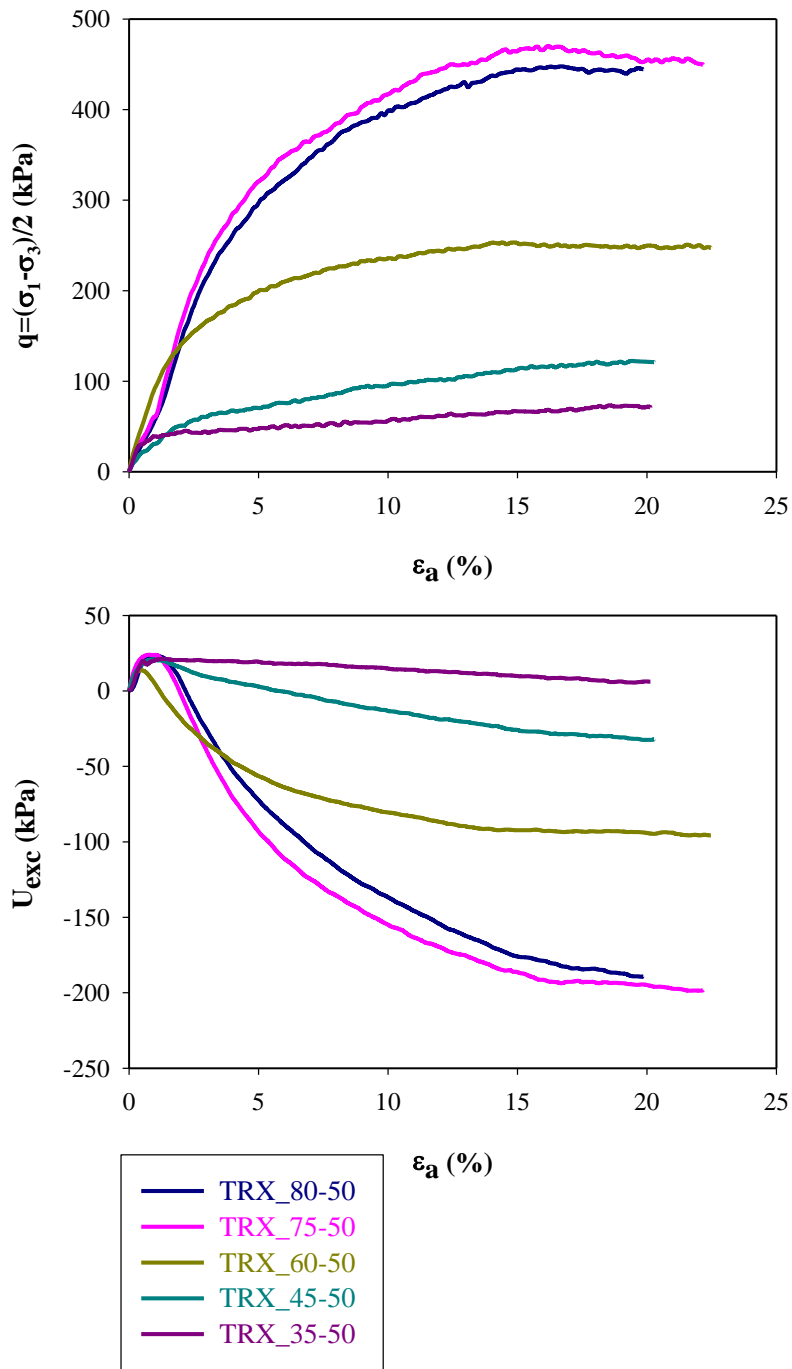
Figure 4.31. q vs. ε_a and U_{exc} vs. ε_a graphs for different relative density specimens consolidated to 50 kPa
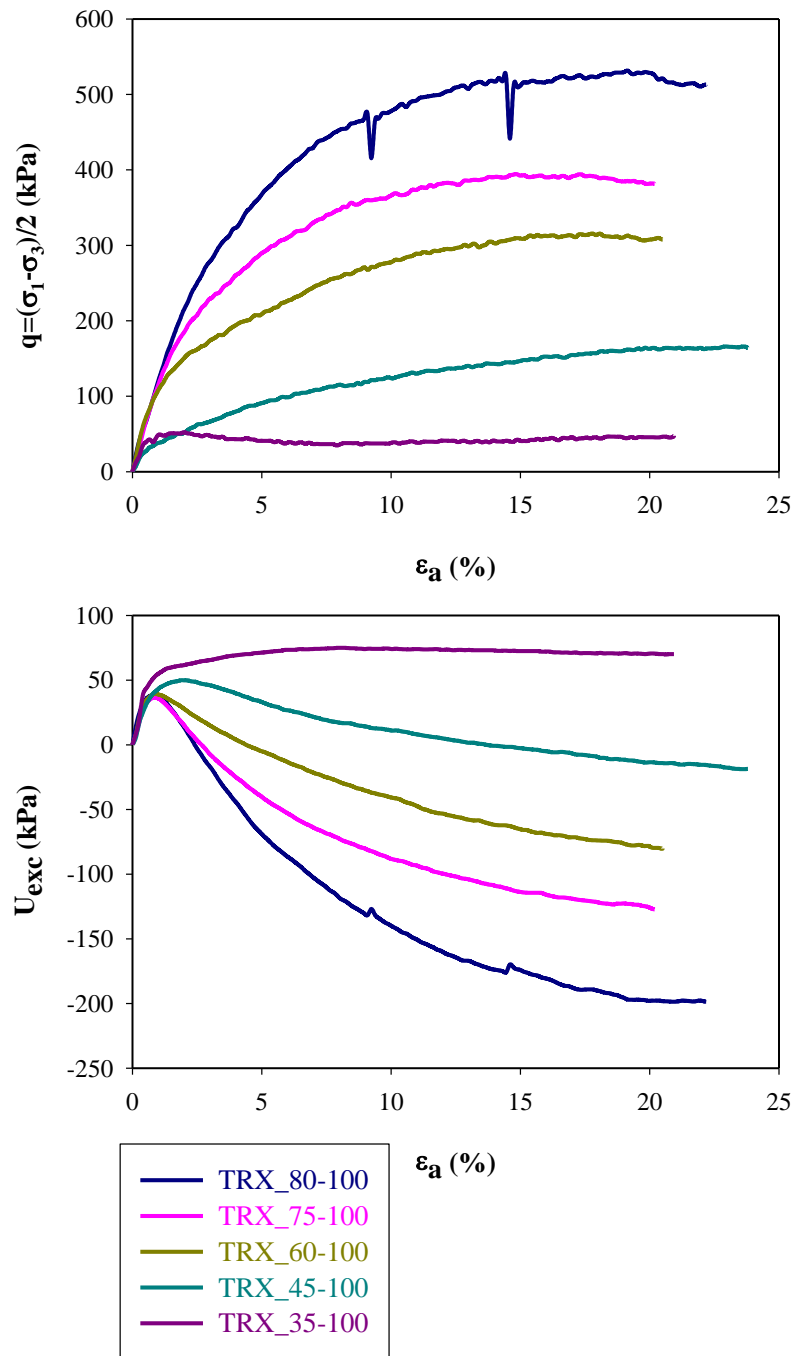
Figure 4.32. q vs. ε_a and U_{exc} vs. ε_a graphs for different relative density specimens consolidated to 100 kPa
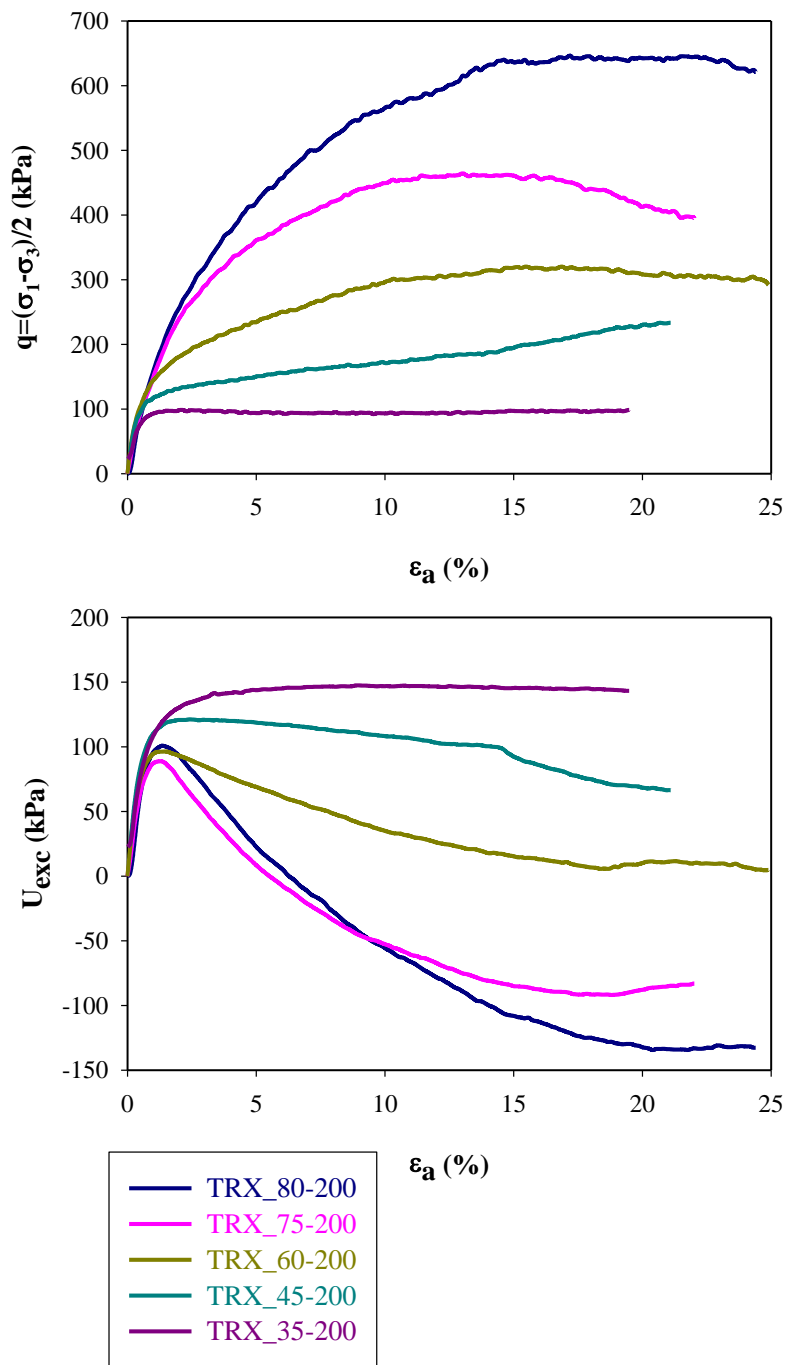
Figure 4.33. q vs. ε_a and U_{exc} vs. ε_a graphs for different relative density specimens consolidated to 200 kPa
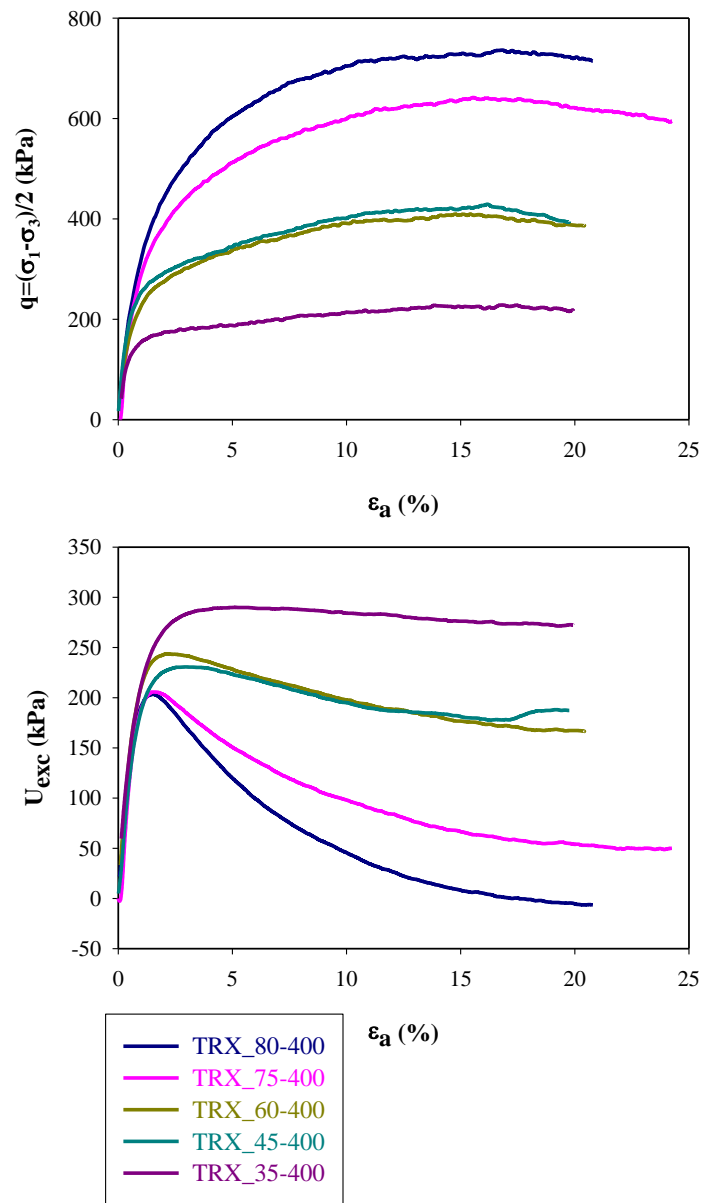
Figure 4.34. q vs. ε_a and U_{exc} vs. ε_a graphs for different relative density specimens consolidated to 400 kPa

As plots reveal, increasing the rate of dilation results in an increase in the shear strength. The rate of dilation is proportional to the relative density at constant consolidation pressure. When relative density increases, the rate of dilation increases. Hence, strength also increases.

To understand the relative density effects on the strength, Mohr circles, and failure envelopes for the specimens, which were consolidated to the same effective stress but prepared at different relative densities, were drawn. Figure 4.35 through Figure 4.38 present these comparative Mohr circles.
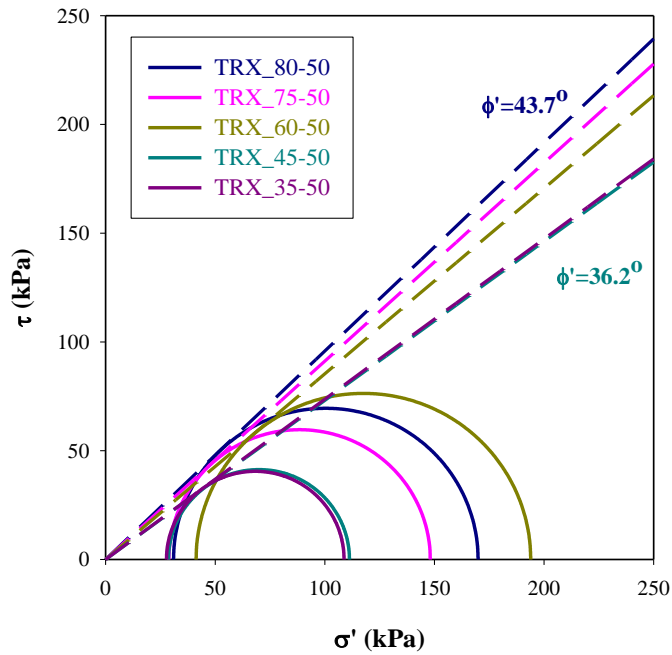
Figure 4.35. Mohr circles and corresponding failure envelopes of the specimens consolidated to 50 kPa and prepared at different relative densities
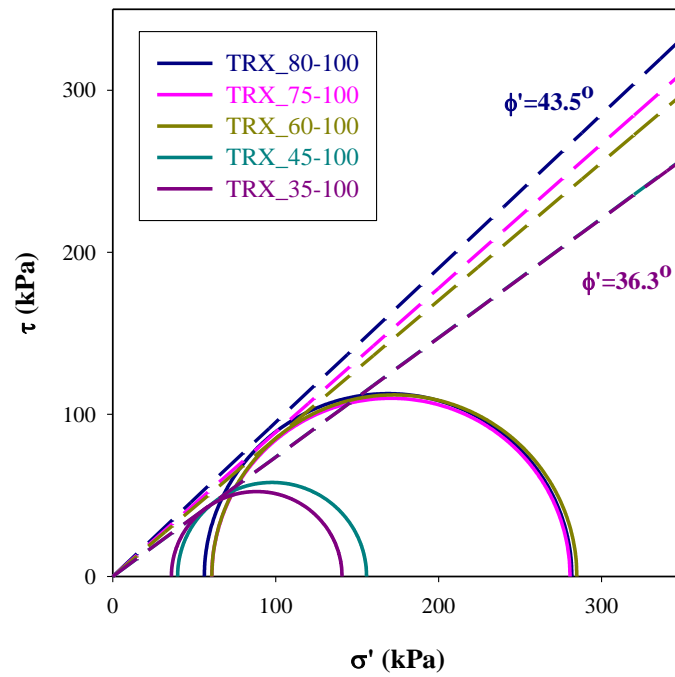
Figure 4.36. Mohr circles and corresponding failure envelopes of the specimens consolidated to 100 kPa and prepared at different relative densities
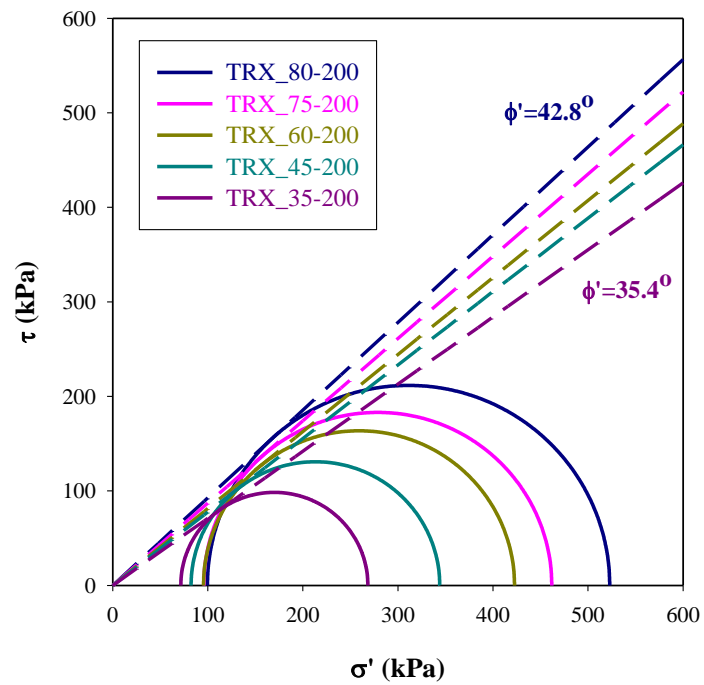
Figure 4.37. Mohr circles and corresponding failure envelopes of the specimens consolidated to 200 kPa and prepared at different relative densities
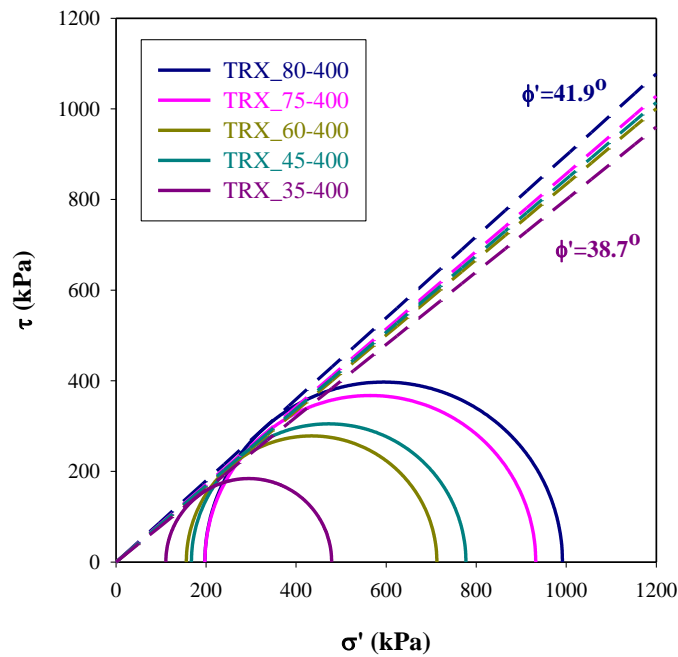
Figure 4.38. Mohr circles and corresponding failure envelopes of the specimens consolidated to 400 kPa and prepared at different relative densities

The effective stress friction angles of the specimens are in an increasing trend with the increase in relative density, as suggested in the literature (e.g. Bishop, 1966; Cornforth, 1973; Bolton, 1986; Andersen and Schjetne, 2013). Effective friction angle values are in the range of 35.5°-38.5° for loose specimens and 42°-44° for dense specimens.

Effective stress friction angle vs. relative density values were compared with the test data presented by Andersen and Schjetne (2013), as shown in Figure 4.39. Triangles represent Kızılırmak sand, whereas circles are the data from Andersen and Schjetne (2013).
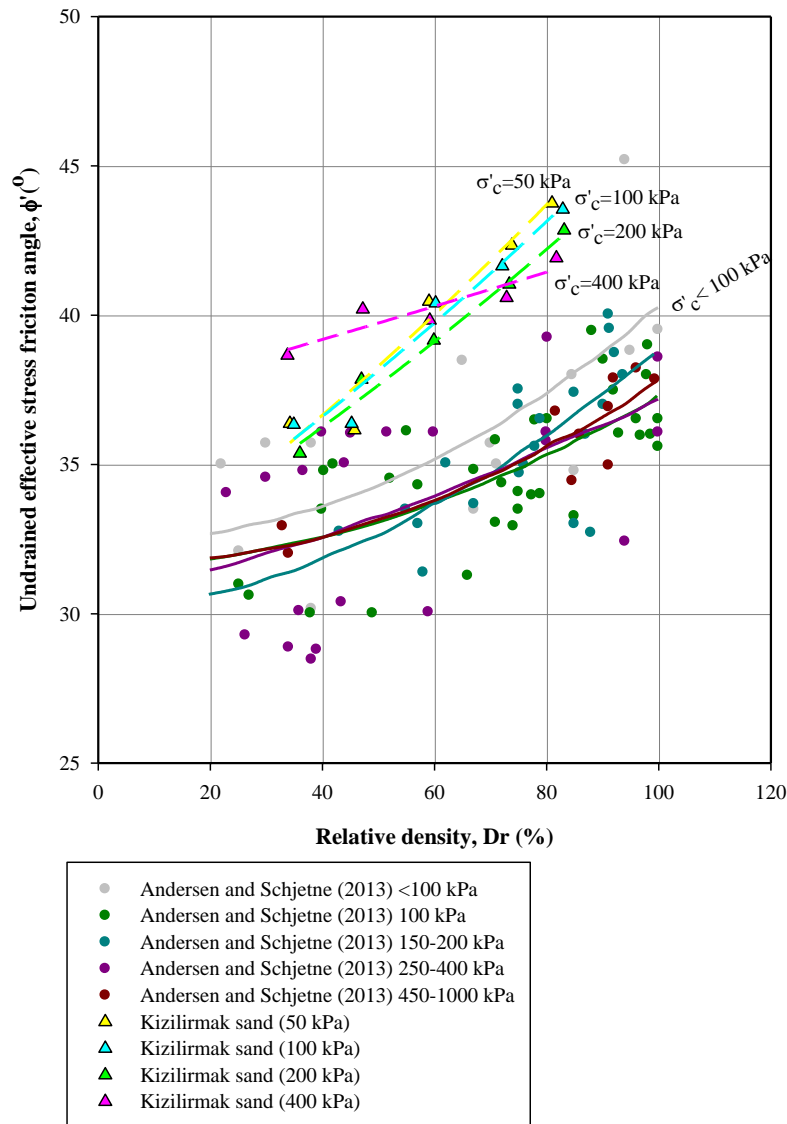
Figure 4.39. Relative density vs. effective stress friction angles adapted from Andersen and Schjetne (2013) as compared with the findings of this study for Kızılırmak sand

As shown in Figure 4.39, friction angle increases with increasing relative density. However, this trend is affected by the confining stress. Increase in confining stress suppress the relative density effects. This trend is compatible with the literature. However, the estimated friction angles for Kızılırmak sand are higher than the values reported by Andersen and Schjetne (2013). These high friction angle values are judged to be due to the angularity of the Kızılırmak sand. To examine the shape of

the Kızılırmak sand more deeply, SEM (Scanning Electron Microscope) images were taken at the METU Central Laboratory. Some of the SEM images are presented in Figure 4.40.
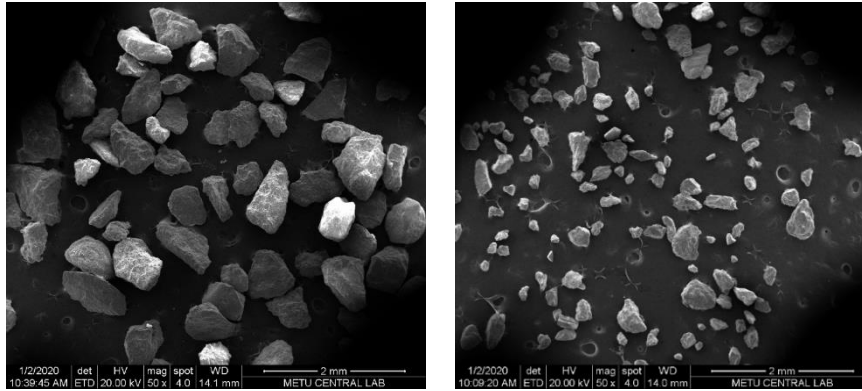
Figure 4.40. SEM images are taken from the Kızılırmak sand

Sphericity and angularity measures were made by using the method proposed in Cho, Dodds and Santamarina (2006) with the help of SEM images. This method is a modification of the Krumbein and Sloss (1963) method. In this method, sphericity is defined as the ratio of the r_{max-in} (maximum circle radius which fits inside the grain) and $r_{min-cir}$ (minimum circle radius which encircled the grain); roundness is defined as the ratio of the $\Sigma r_i/N$ (average radius of the circles which fit the grain's protrusion) and r_{max-in}. In Figure 4.41, these parameters are clearly illustrated by a sketch, and particle shape determination chart for the visual examination (proposed by Krumbein and Sloss (1963)) is presented.
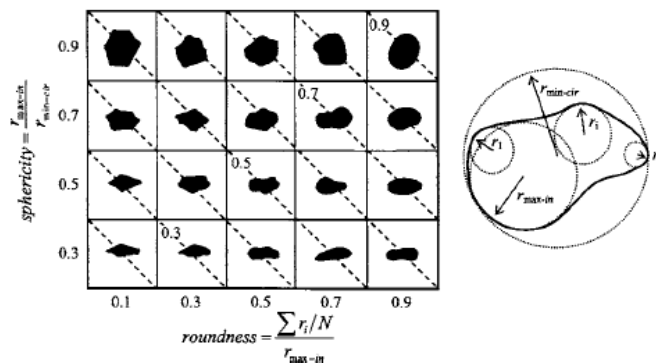
Figure 4.41. A sketch for sphericity and roundness calculation parameters and particle shape determination chart (Cho *et al.* 2006)

134

By following the steps defined in Cho *et al.* (2006), the sphericity (S) and roundness (R) values of Kızılırmak sand were calculated as 0.60 and 0.26, respectively. An example of the calculation process, and S and R values for the whole inspected grains, are given in Figure 4.42 and Figure 4.43.
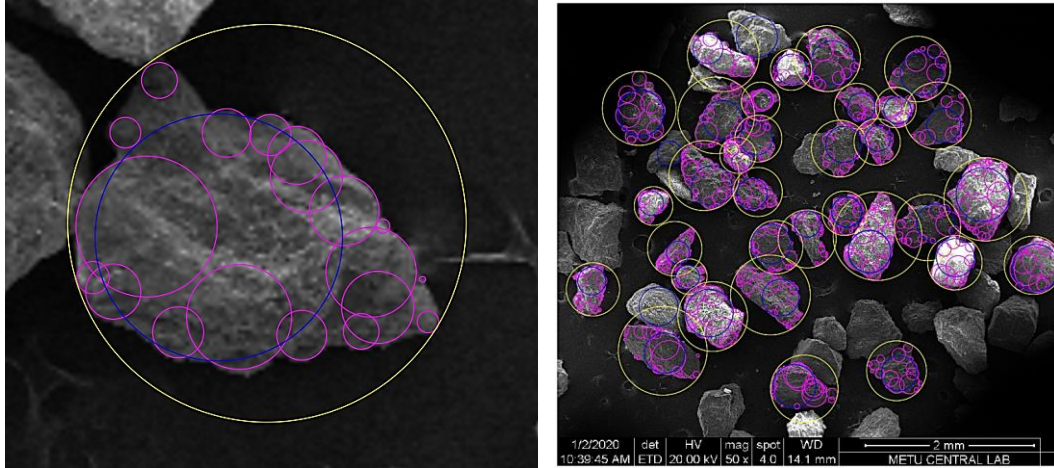
Figure 4.42. Example views from sphericity and roundness calculation process of Kızılırmak sand
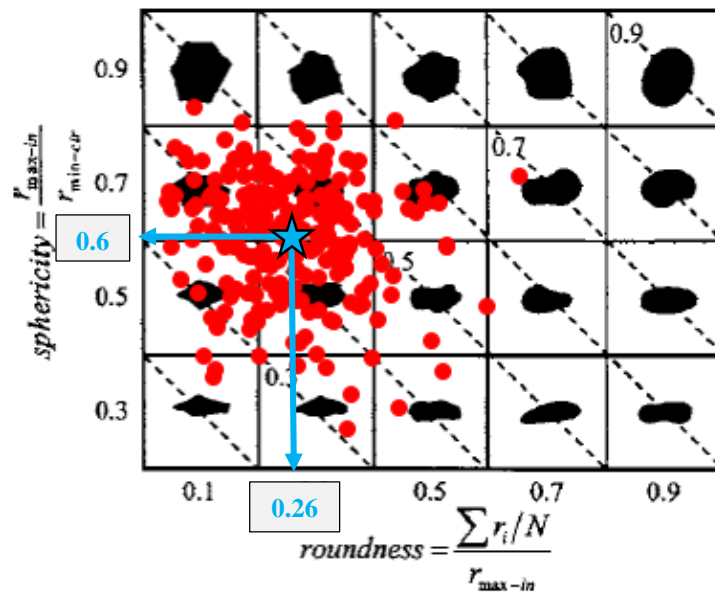
Figure 4.43. Sphericity and roundness of the inspected Kızılırmak sand grains (after Cho *et al.*, 2006)

Figure 4.44 shows the critical state friction angle value and angularity relation for the data in Cho *et al.* (2006). The critical state friction angle and angularity are

135

claimed to be proportional to each other. When angularity increases (decreasing roundness), critical state friction angle increases. For a roundness value equal to 0.26 and sphericity equal to 0.6, Cho *et al.* (2006) predict critical state friction angle value to be in between 37° and 39.5°. Therefore, it is not surprising that the effective stress friction angle of the Kızılırmak sand is relatively high, when relatively higher critical state friction angle and dilation components are considered.
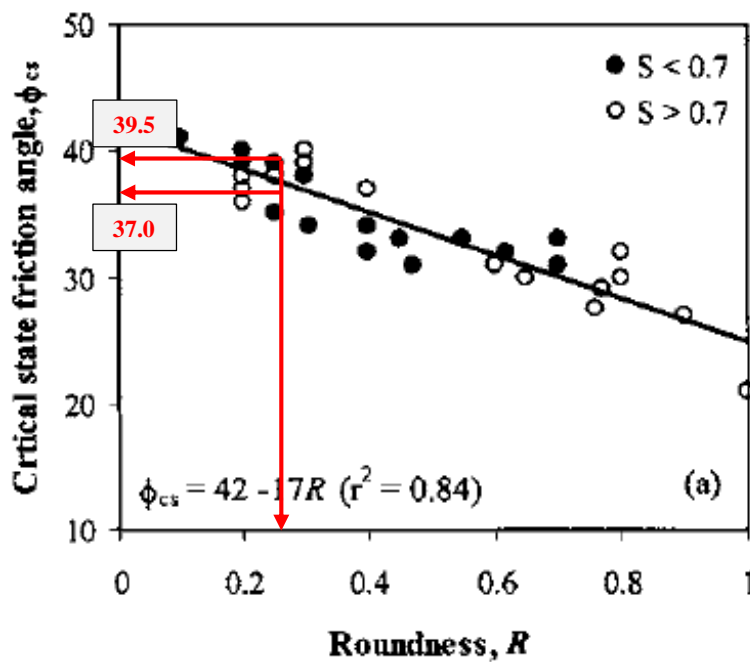
Figure 4.44. Critical state friction angle vs. roundness (Cho *et al.*, 2006)

4.4 Oedometer Test Results

In Table 4.2, relative density (D_R), initial void ratio (e_0), yield stress (σ'_{yield}), effective axial stress corresponding to maximum and minimum constrained modulus (σ'_v (M_{max}) and σ'_v (M_{min})), and effective axial stress corresponding to maximum compression index (σ'_v ($C_{c_{max}}$)) values, are summarized.

Table 4.2 Summary of the oedometer test results

Test Name	D_R (%)	e_0 (−)	σ'_{yield} (MPa)	$\sigma'_v (M_{max})$ (MPa)	$\sigma'_v (M_{min})$ (MPa)	$\sigma'_v (C_{c_{max}})$ (MPa)
OED_25	25	0.712	2.1	~0.8	~6.5	~6.5
OED_35	35	0.678	2.2	Not Applicable	Not Applicable	~6.5
OED_45	45	0.643	2.7	~0.3	~3.8	~13.0
OED_60	60	0.591	3.4	~1.2	~8.1	~13.0
OED_75	75	0.538	3.8	~1.2	~8.1	~13.0
OED_80	80	0.522	4.0	~0.8	~8.1	~13.0
OED_85	85	0.505	3.9	~1.2	~6.5	~13.0

Void ratio vs. logarithm of the effective vertical stress (e vs. $log\sigma_v'$), void ratio vs. effective vertical stress (e vs. σ'), and effective vertical stress vs. axial strain (σ' vs. ε_a) plots are presented in Figure 4.45 to Figure 4.51, along with the yield stress and stress at which M_{max} and M_{min} are observed. These stresses were determined by visual interpretation from void ratio vs. effective vertical stress plots.
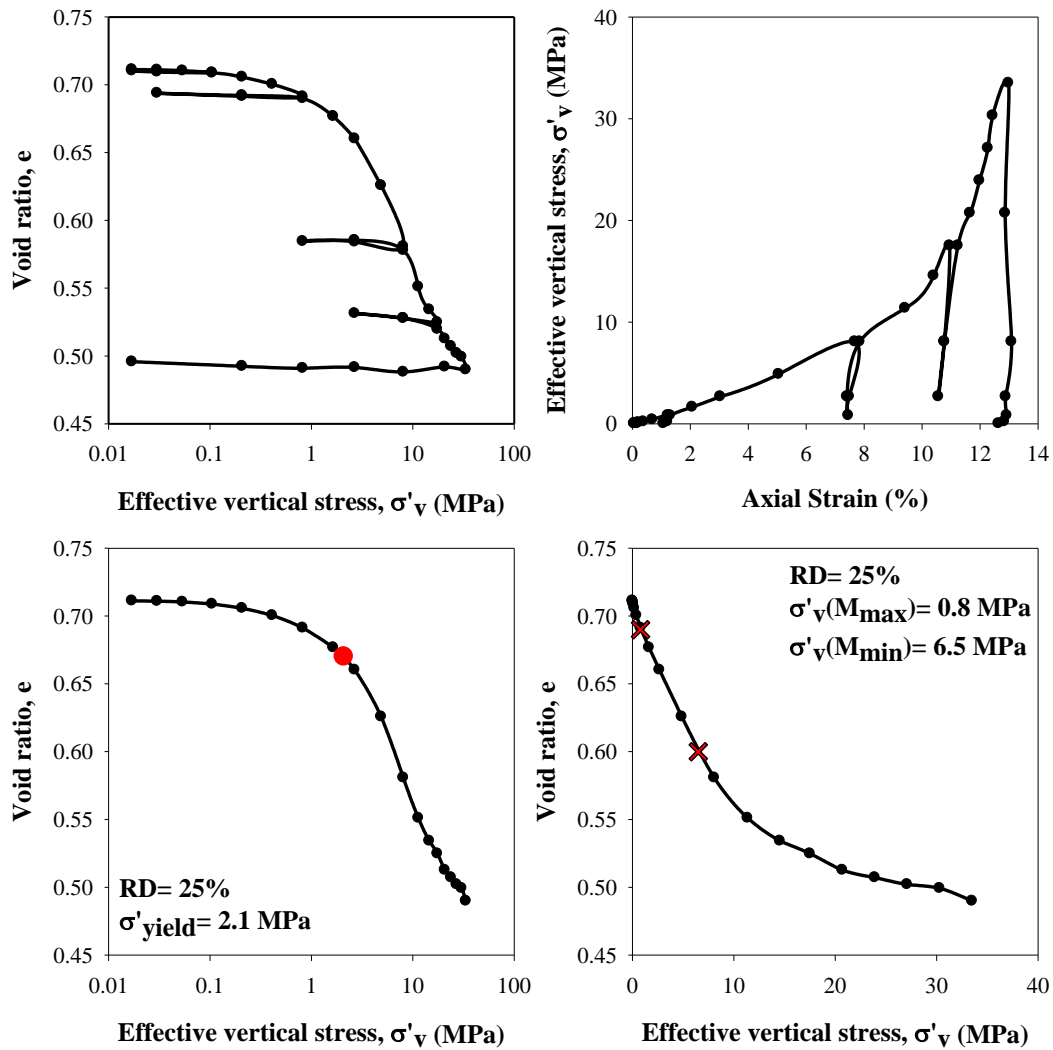
Figure 4.45. Void ratio vs. vertical stress and vertical stress vs. axial strain plots for the specimen at 25% relative density
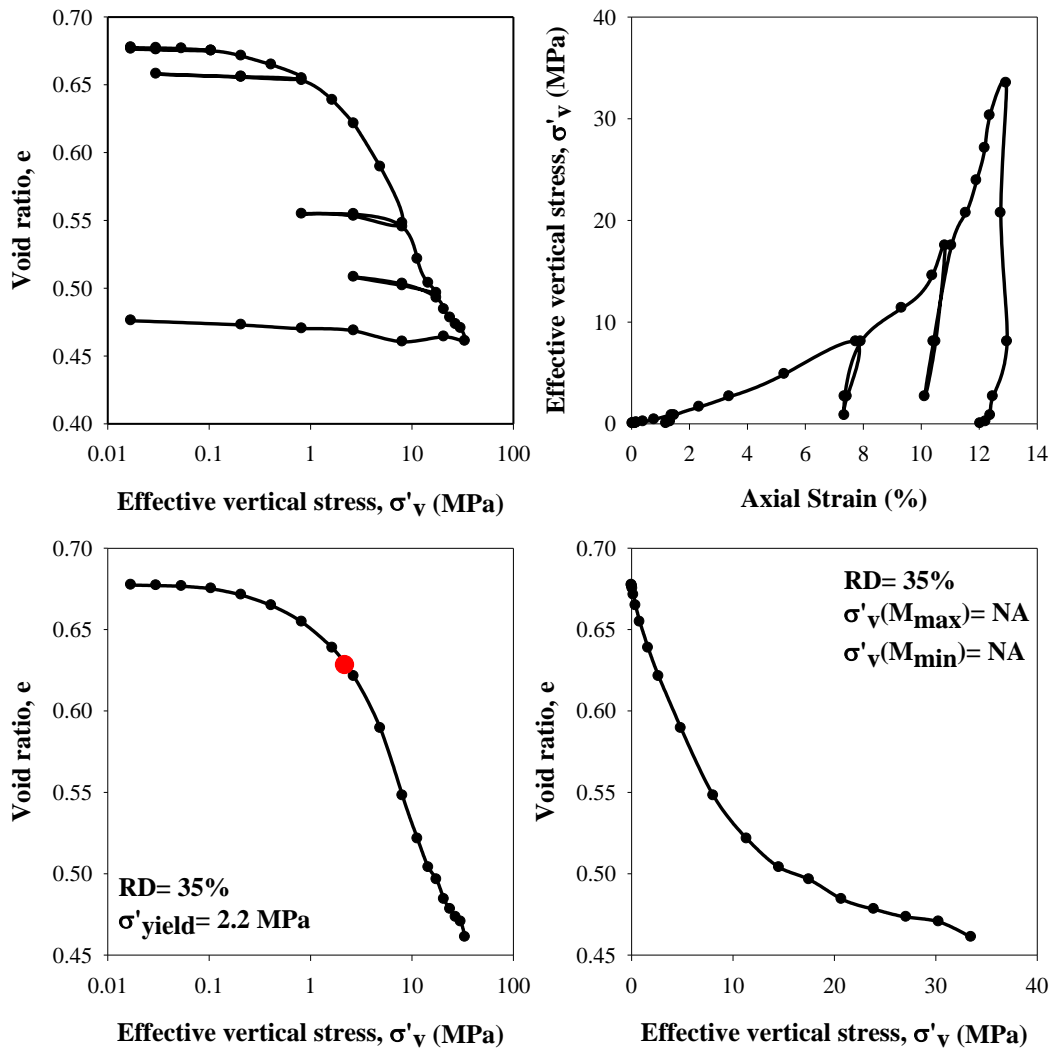
Figure 4.46. Void ratio vs. vertical stress and vertical stress vs. axial strain plots for the specimen at 35% relative density
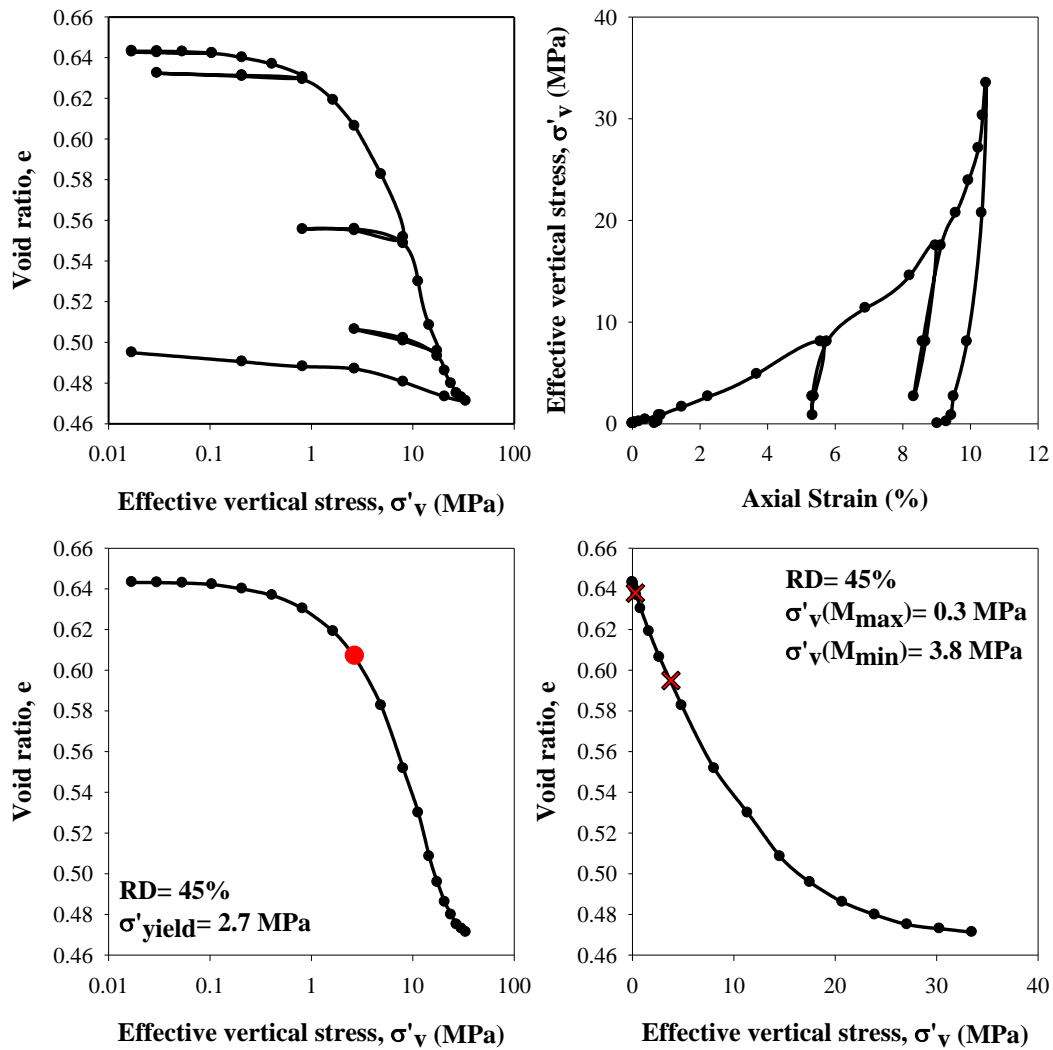
Figure 4.47. Void ratio vs. vertical stress and vertical stress vs. axial strain plots for the specimen at 45% relative density
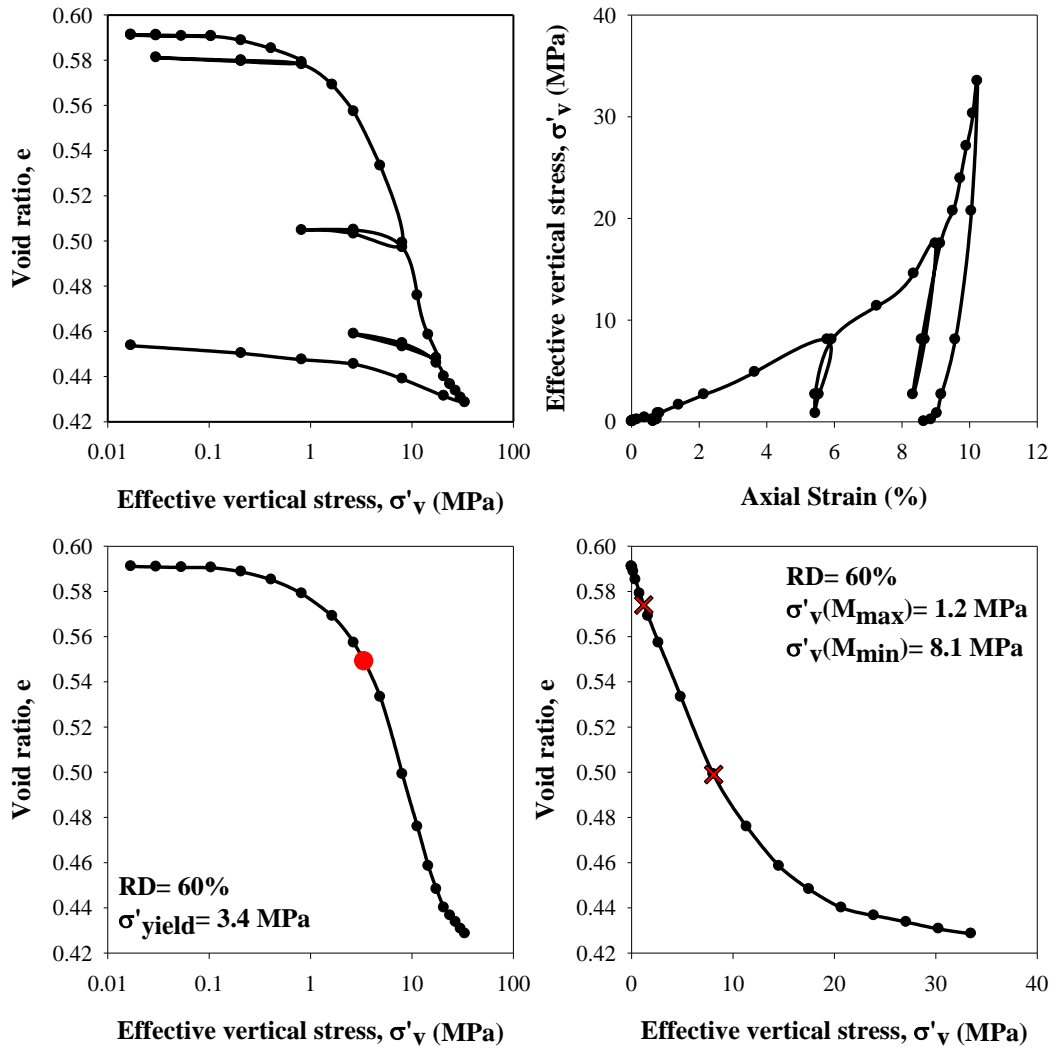
Figure 4.48. Void ratio vs. vertical stress and vertical stress vs. axial strain plots for the specimen at 60% relative density
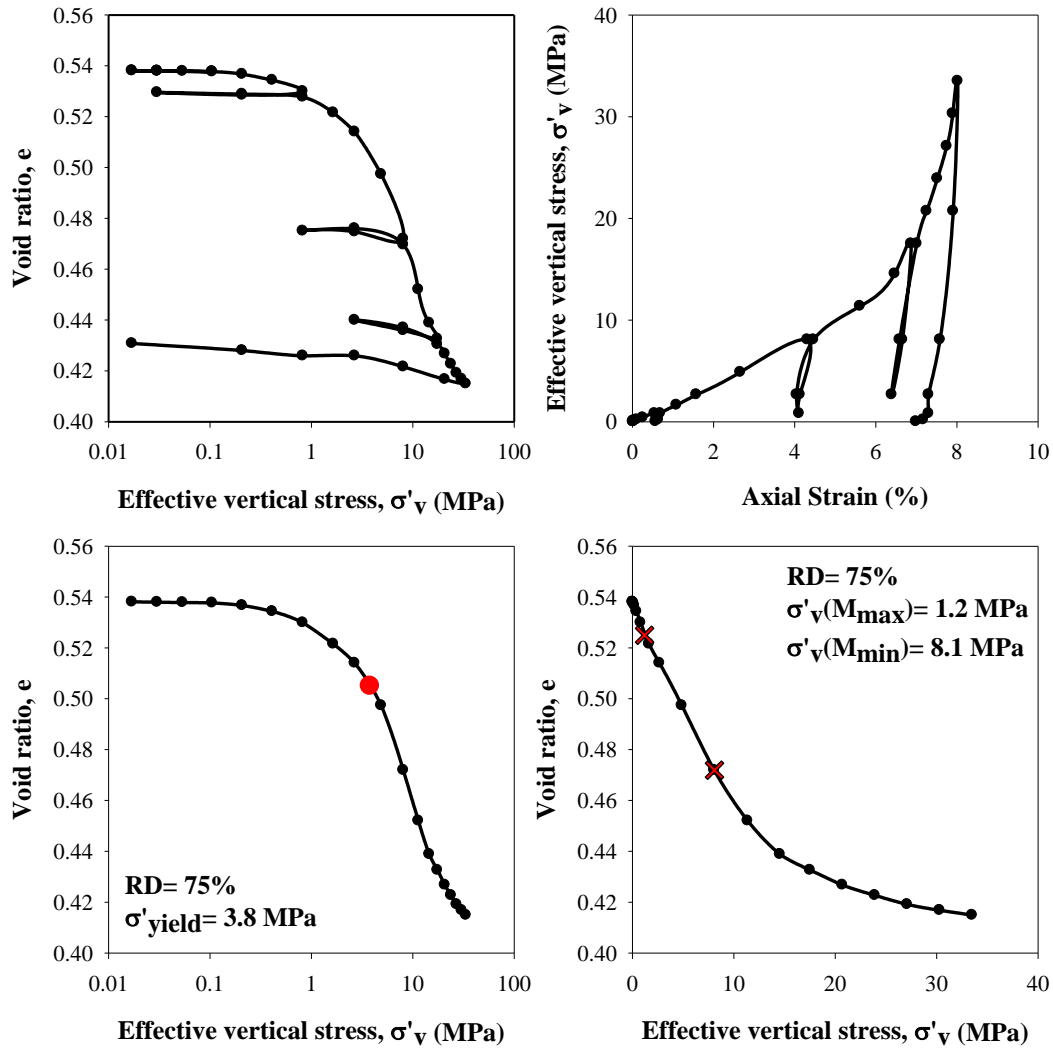
Figure 4.49. Void ratio vs. vertical stress and vertical stress vs. axial strain plots for the specimen at 75% relative density

142
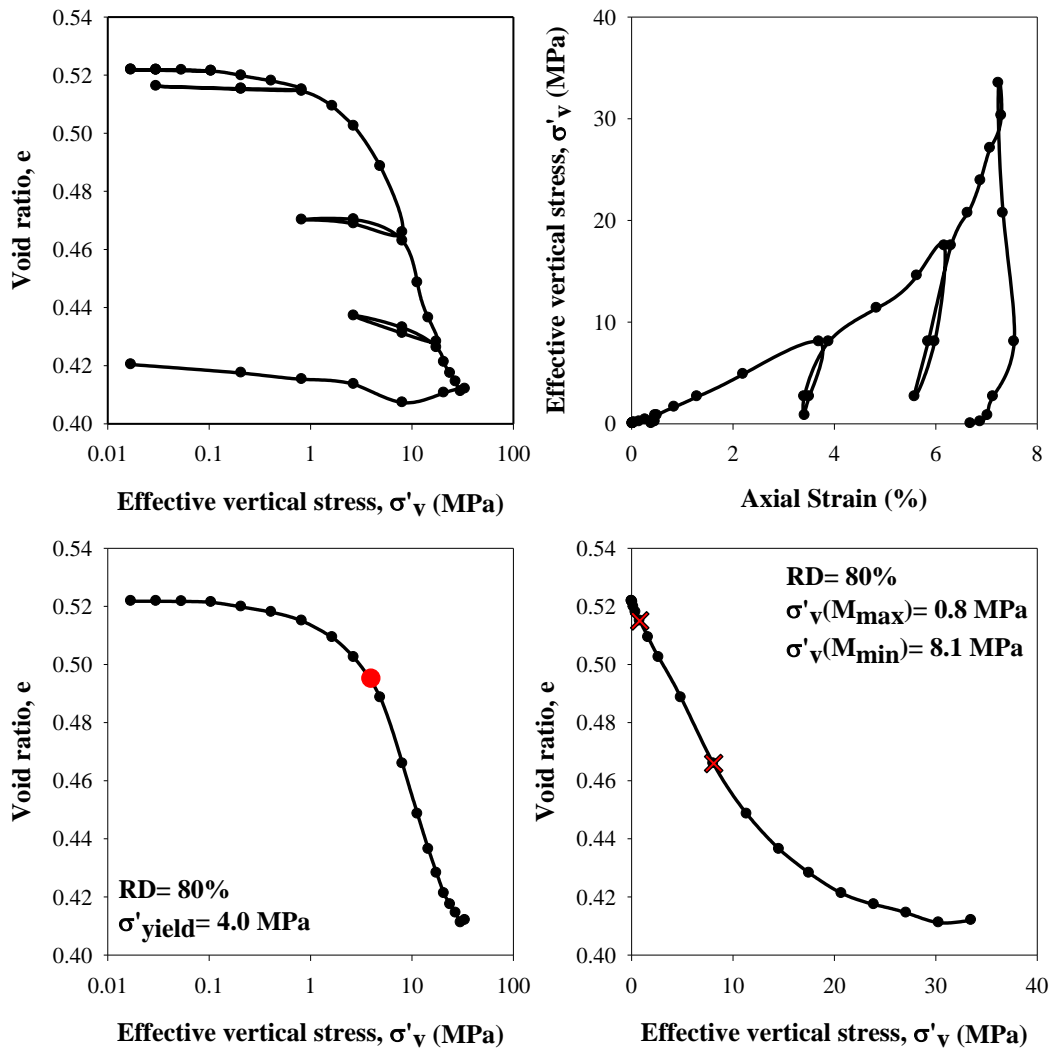
Figure 4.50. Void ratio vs. vertical stress and vertical stress vs. axial strain plots for the specimen at 80% relative density
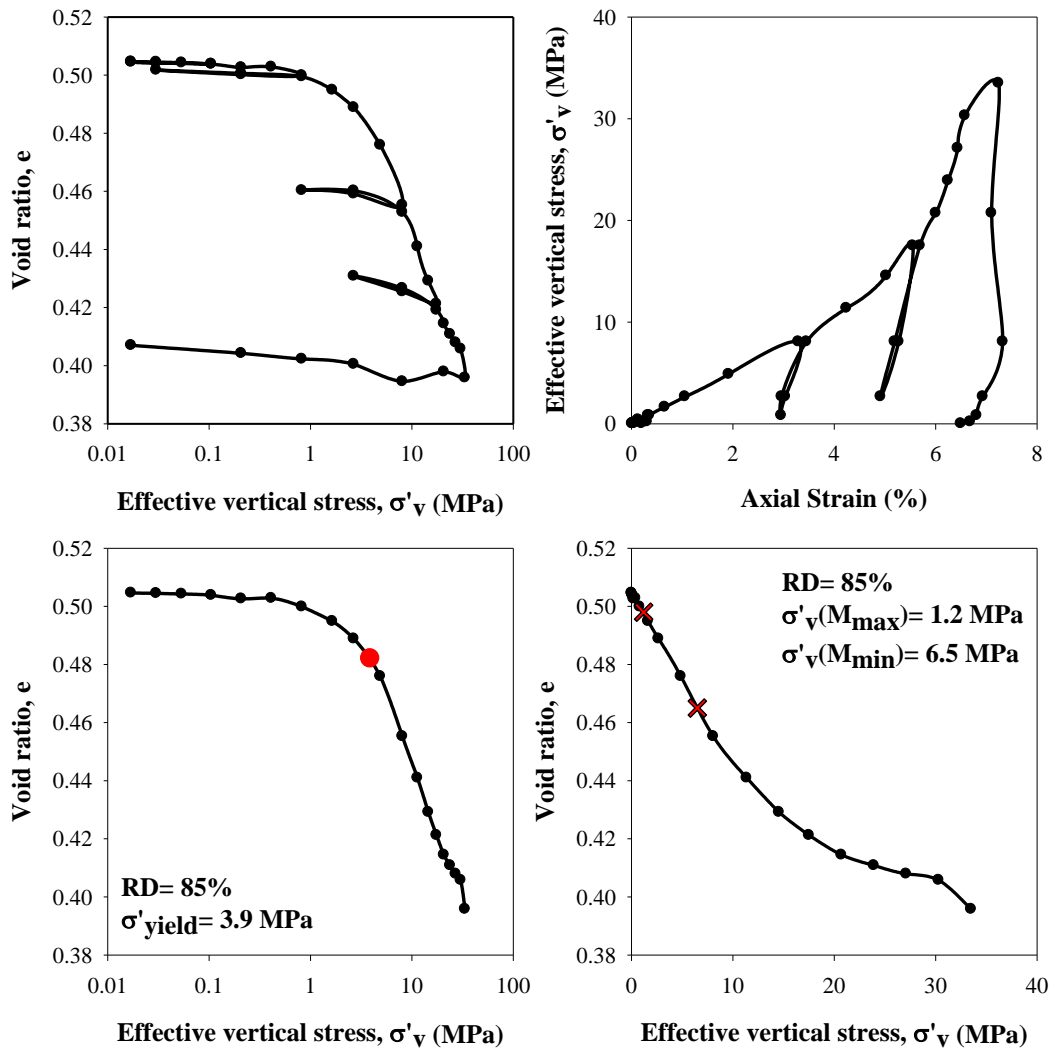
Figure 4.51. Void ratio vs. vertical stress and vertical stress vs. axial strain plots for the specimen at 85% relative density

4.5 Interpretation of Oedometer Test Results

In order to observe the initial relative density effects on yield (crushing) stress, void ratio vs. logarithm of the effective vertical stress plots were drawn for all relative densities. They are presented in Figure 4.52. This figure reveals that yield stress slightly increases with increasing initial relative density.
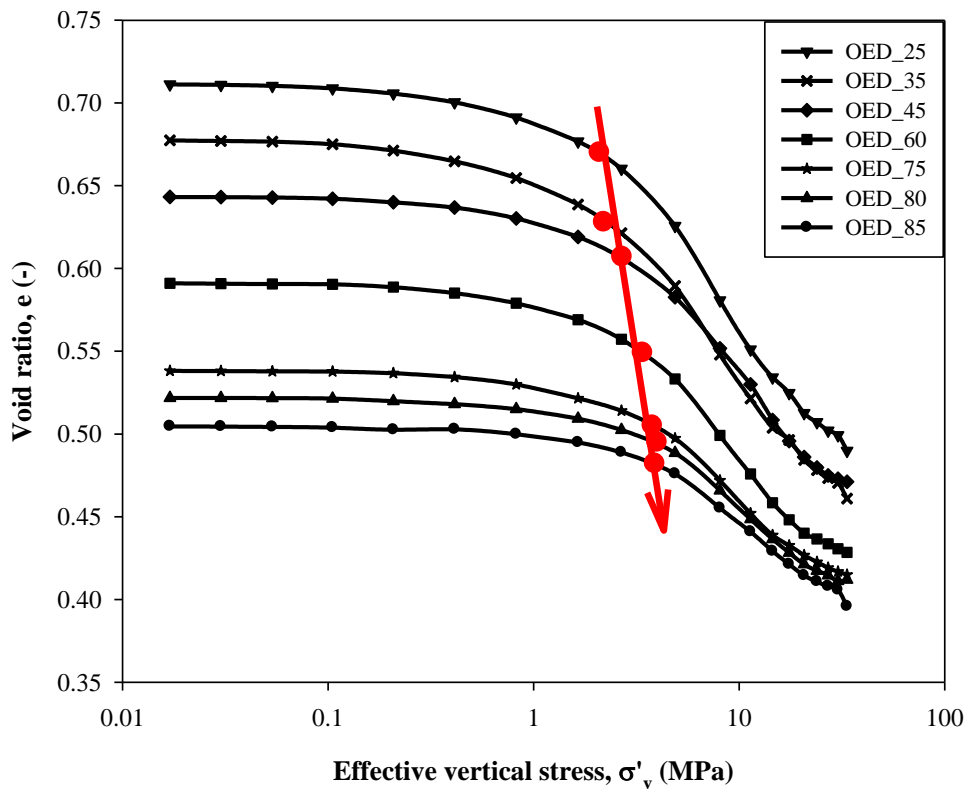
Figure 4.52. Void ratio vs. vertical stress plots for the specimen at different relative densities

One-dimensional constrained moduli, compression, recompression, and secondary compression indices were calculated to assess Kızılırmak sand's volumetric straining response. To assess the change in constrained moduli and compression indices with effective vertical stresses, and the relation between secondary compression index and compression index, and the relation between compression index & recompression index were assessed as given in Figure 4.53 through Figure 4.59. Note that all the

compression, recompression and secondary compression indices are tangential indices.
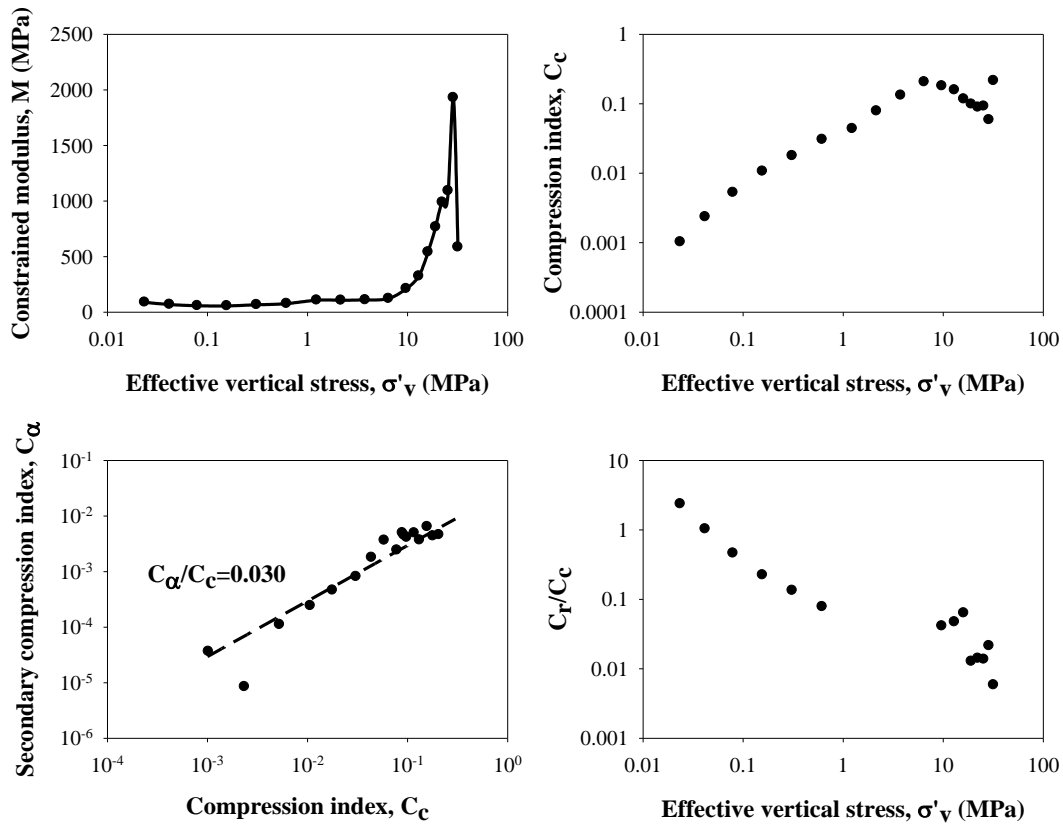
Figure 4.53. Change in constrained modulus and compression index with effective vertical stress, the relation between secondary compression index & compression index, and the relation between compression index & recompression index for the specimen at 25% relative density
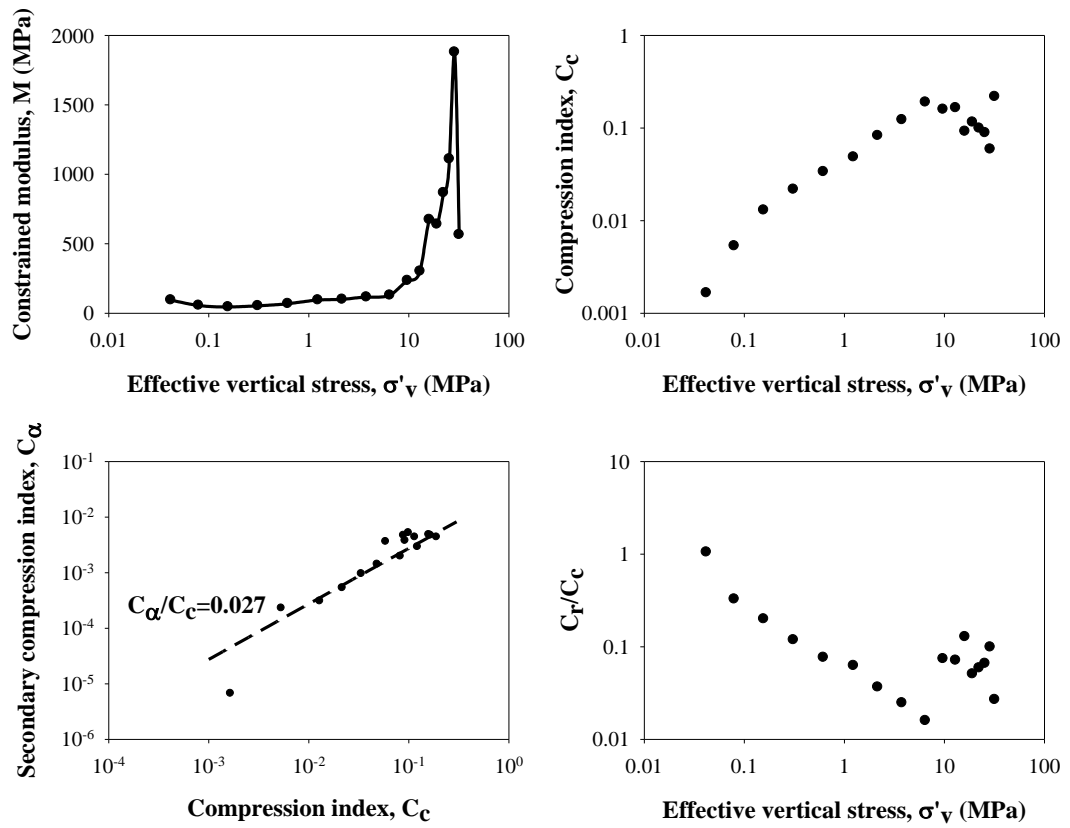
Figure 4.54. Change in constrained modulus and compression index with effective vertical stress, the relation between secondary compression index & compression index, and the relation between compression index & recompression index for the specimen at 35% relative density
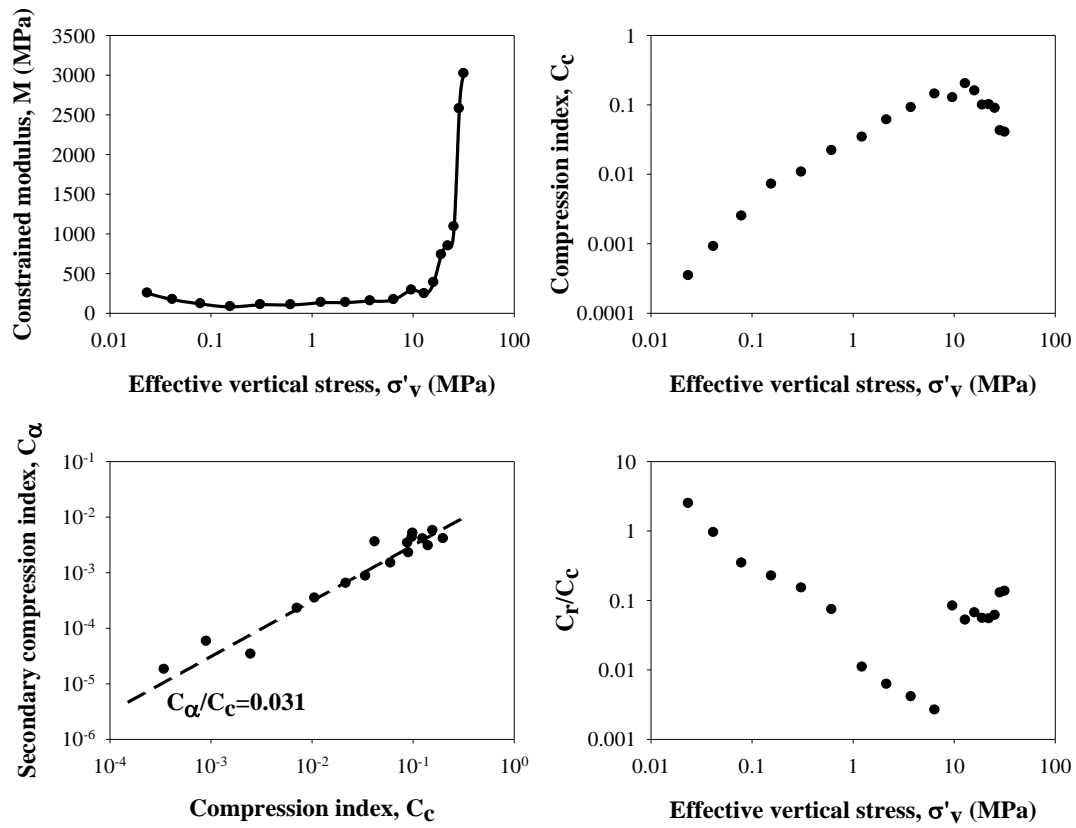
Figure 4.55. Change in constrained modulus and compression index with effective vertical stress, the relation between secondary compression index & compression index, and the relation between compression index & recompression index for the specimen at 45% relative density

148
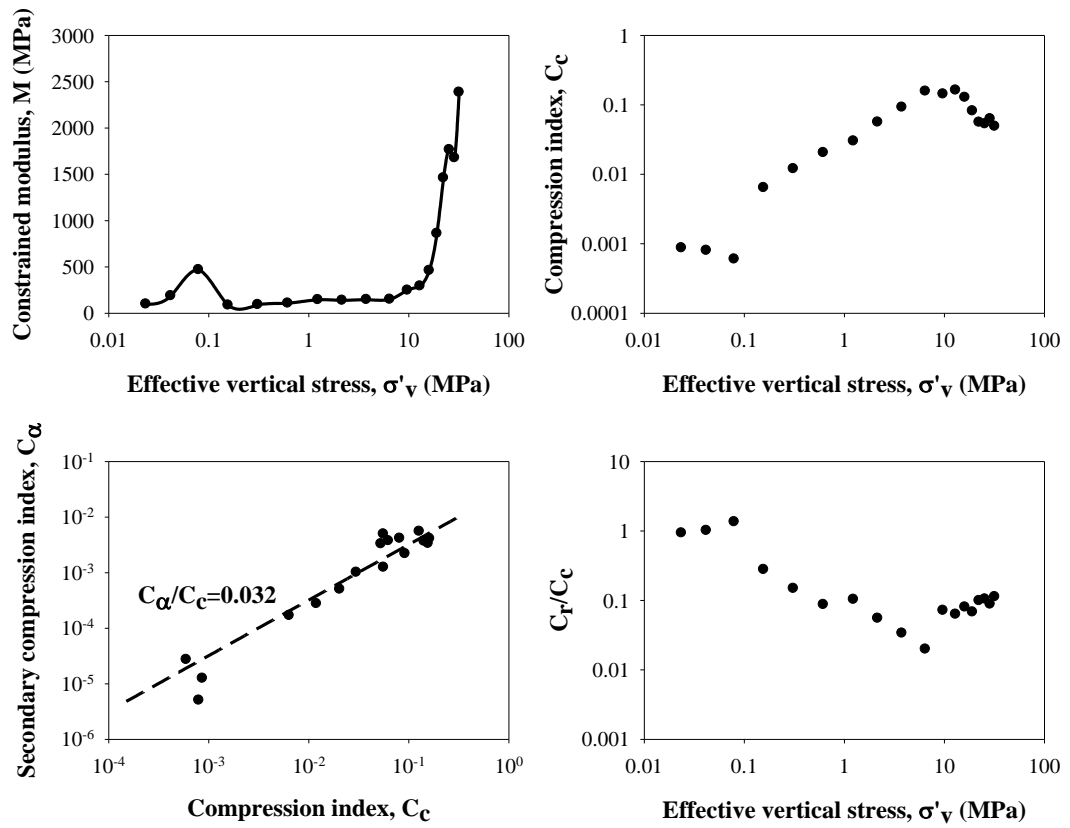
Figure 4.56. Change in constrained modulus and compression index with effective vertical stress, the relation between secondary compression index & compression index, and the relation between compression index & recompression index plots the specimen at 60% relative density
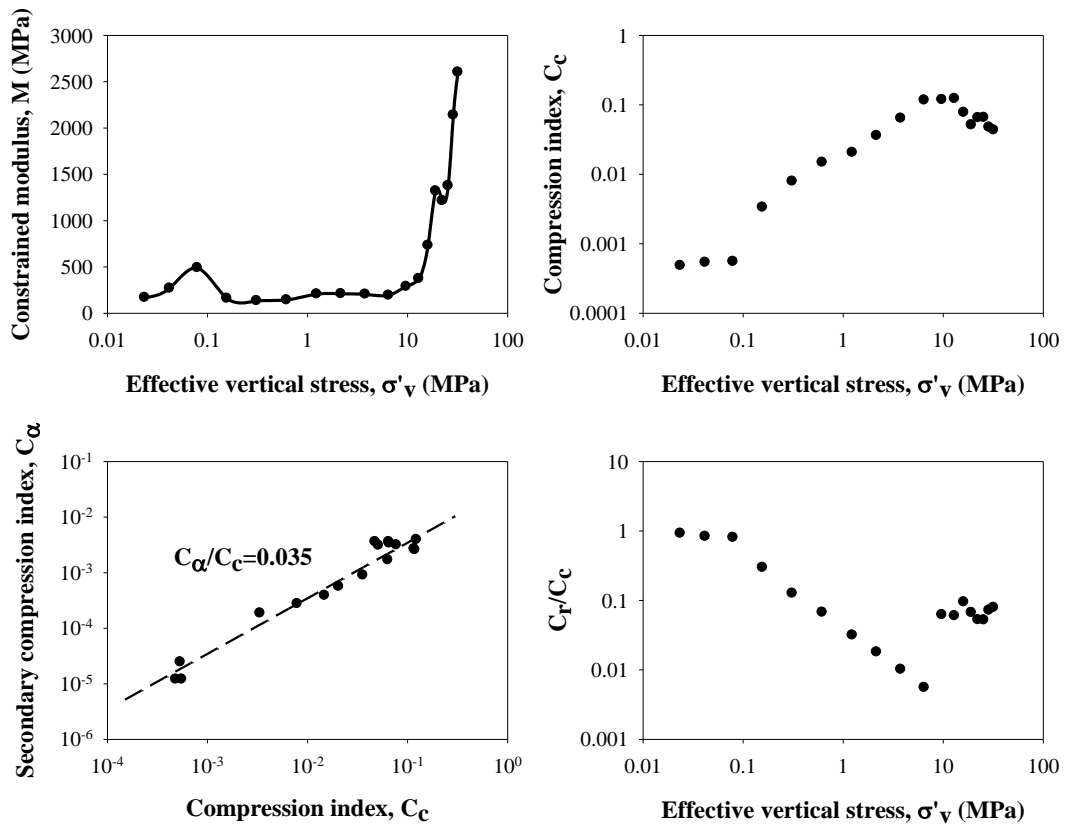
Figure 4.57. Change in constrained modulus and compression index with effective vertical stress, the relation between secondary compression index & compression index, and the relation between compression index & recompression index plots the specimen at 75% relative density
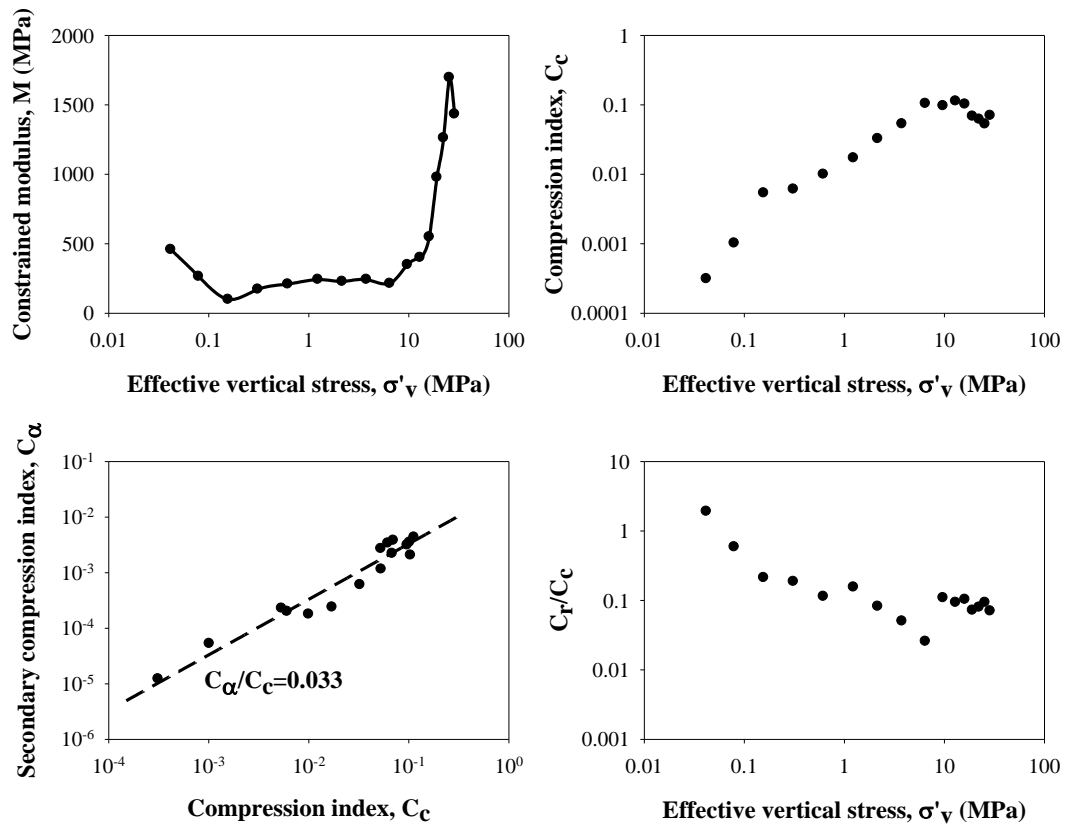
Figure 4.58. Change in constrained modulus and compression index with effective vertical stress, the relation between secondary compression index & compression index, and the relation between compression index & recompression index plots the specimen at 80% relative density
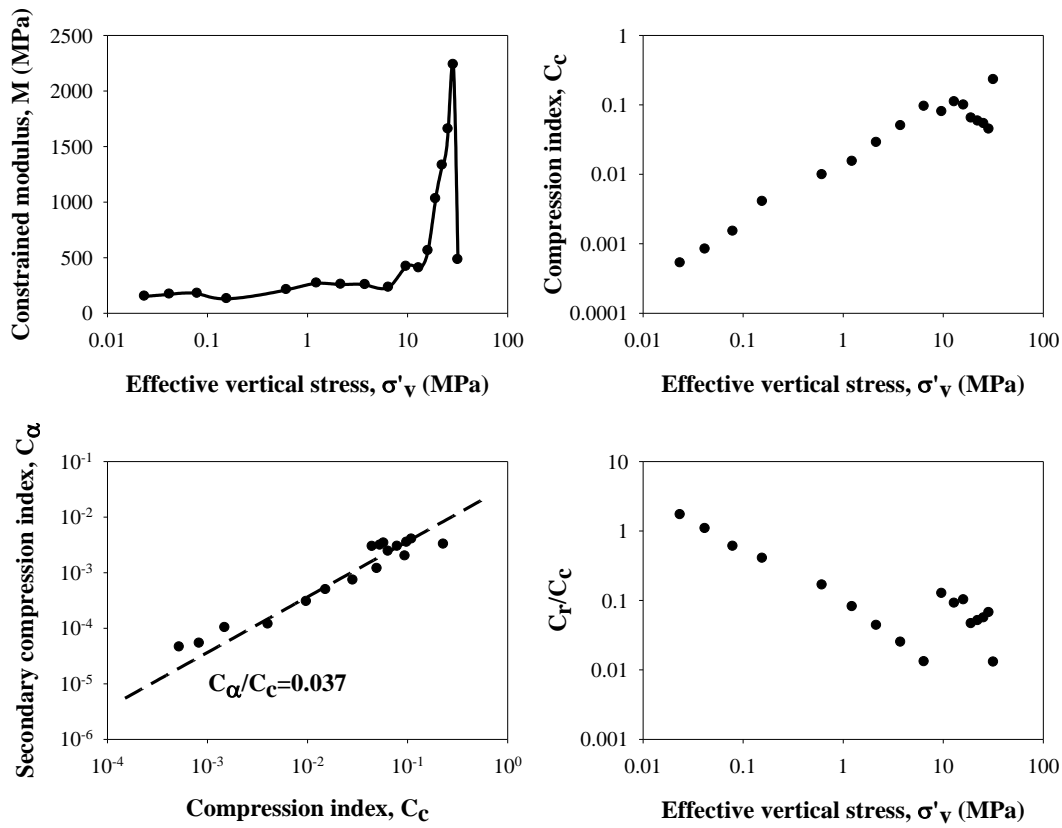
Figure 4.59. Change in constrained modulus and compression index with effective vertical stress, the relation between secondary compression index & compression index, and the relation between compression index & recompression index plots the specimen at 85% relative density

Mesri and Vardhanabhuti (2009) classify the volumetric compression response into three types: Type A, Type B, and Type C. In Type A response, at the low stress levels, stiffness increases with increasing stress. As the effective vertical stress keeps increasing, stiffness starts to decrease with an increase in stress. Finally, at high effective vertical stress levels, stiffness starts to increase with increasing stress. Hence, there are three stages in Type A response. In Type B response, there are three compression stages similar to Type A. However, instead of decreasing stiffness in the second stage, constant stiffness response is observed. Type C response exhibits only one stage; stiffness increases with increasing effective vertical stress. More detailed discussions of these compression responses are made in chapter 2.4.

152

Based on the above-discussed definitions of Type A, B, and, C volumetric straining responses and constrained modulus vs. effective stress plots given in Figure 4.53 to Figure 4.59, it is concluded that Kızılırmak sand exhibit a Type B volumetric straining response. As suggested in Mesri and Vardhanabhuti (2009), effective vertical stresses at the initial and the endpoints of the constant stiffness range were taken as σ'_v (M_{max}) and σ'_v (M_{min}), respectively.

Based on the compression index (C_c) vs. effective vertical stress plots given in Figure 4.53 to Figure 4.59, it is observed that C_c, i.e., the compressibility of the specimen, increases with increasing effective stress up to threshold stress. Then, it starts to decrease. This decrease means that the specimen's compressibility starts to decrease, and a stiffer material is obtained. Also, note that the threshold vertical stress is corresponding to the maximum C_c value after yielding fall in the range of 6-10 MPa.
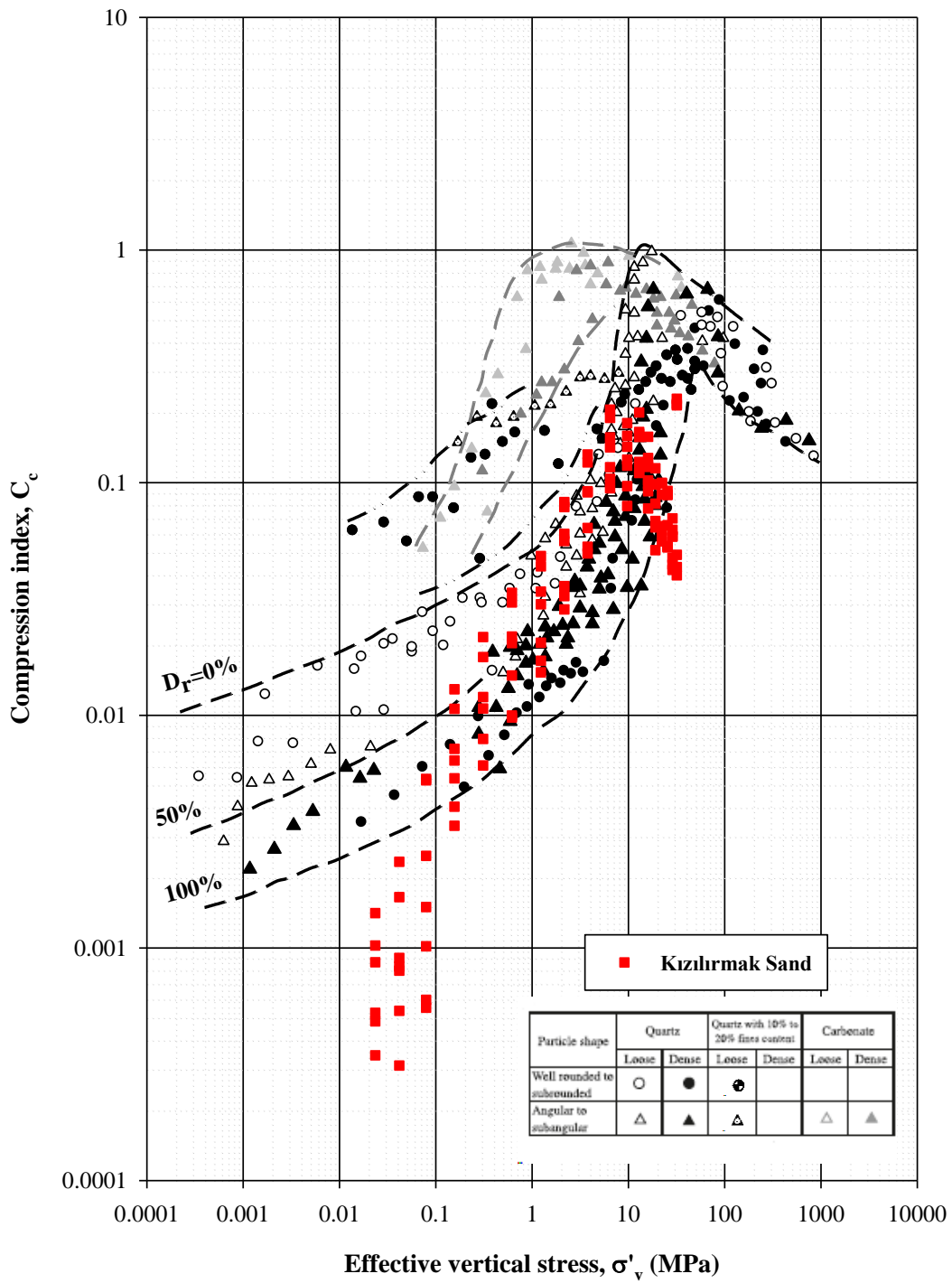
Figure 4.60. Comparison of the compression index of Kızılırmak sand with Mesri and Vardhanabhuti (2009) database

154

C_c values were compared with the Mesri and Vardhanabhuti (2009) database, as given in Figure 4.60. At low stresses, Kızılırmak sand's compressibility is observed to be lower than the granular material responses given in Mesri and Vardhanabhuti (2009) study.

A linear trend is observed in primary compression vs. secondary compression index plots, as shown in Figure 4.53 to Figure 4.59. C_α/C_c ratios for Kızılırmak sand changes from 0.027 to 0.037 with decreasing relative density. When all experimental results are considered as presented in Figure 4.61, C_α/C_c ratio is calculated as 0.03. Mesri and Vardhanabhuti (2009) reported a C_α/C_c ratio in the range of 0.015 to 0.03 for different granular materials (Figure 4.62). Therefore, it can be said that Kızılırmak sand's C_α/C_c ratio falls in the upper range given in Mesri and Vardhanabhuti (2009) study.
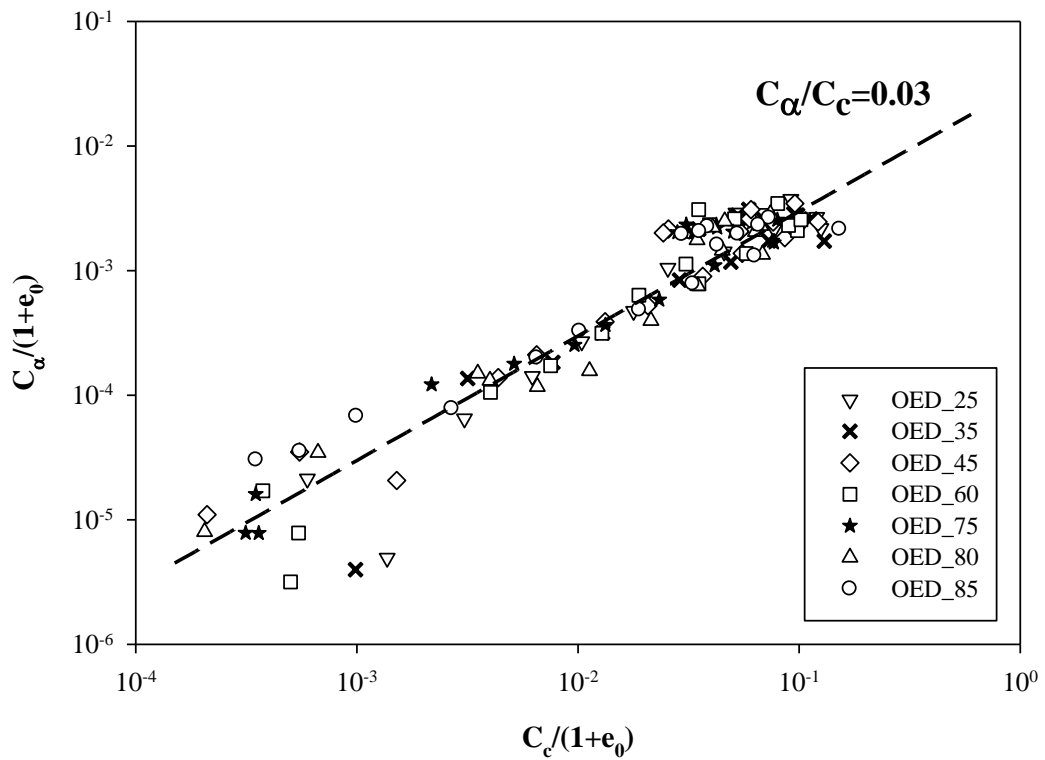
Figure 4.61. Relation in between compression and secondary compression indices of Kızılırmak sand
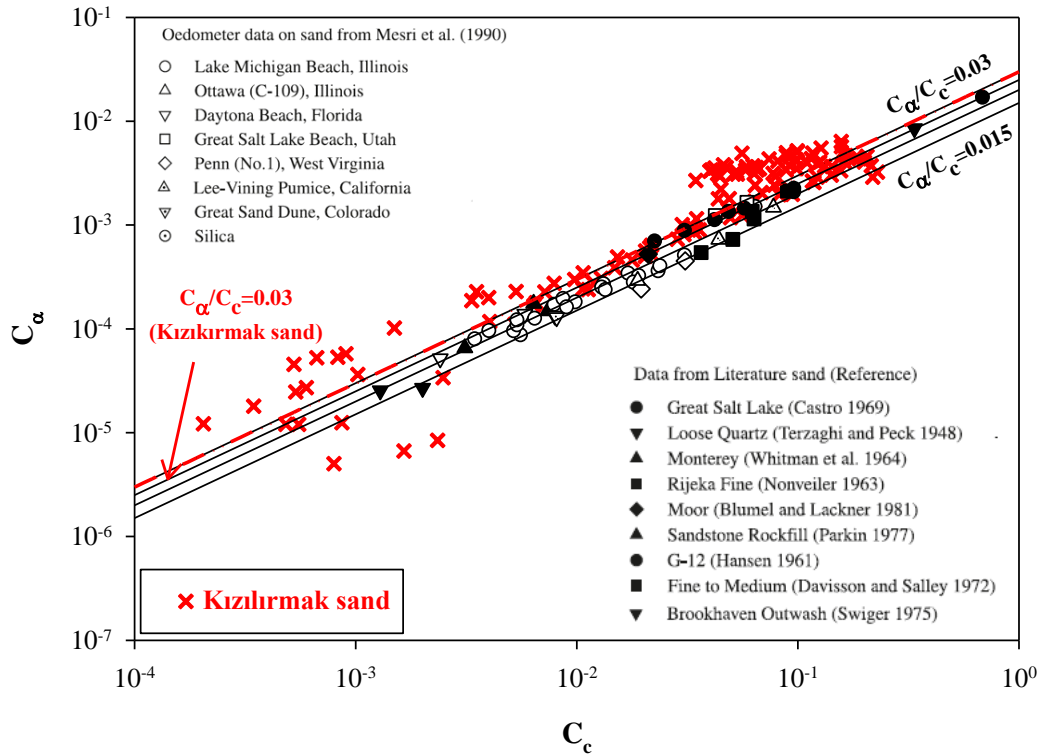
Figure 4.62. Comparison of the compression index of Kızılırmak sand as compared with data adapted from Mesri and Vardhanabhuti (2009)

Sieve analyses were performed on the specimens after the oedometer tests. Grain size distribution curves of the loaded specimens are presented in Figure 4.63, along with the original grain size distribution curve. GSD curves are shifted towards the upper side of the original sample's GSD. This shift is interpreted as particle diameters to be finer due to particle breakage during one-dimensional loading. Besides, the figure shows the increase in fines content (<0.074 mm diameter). The original sample was a clean sand sample whose fines content was zero.
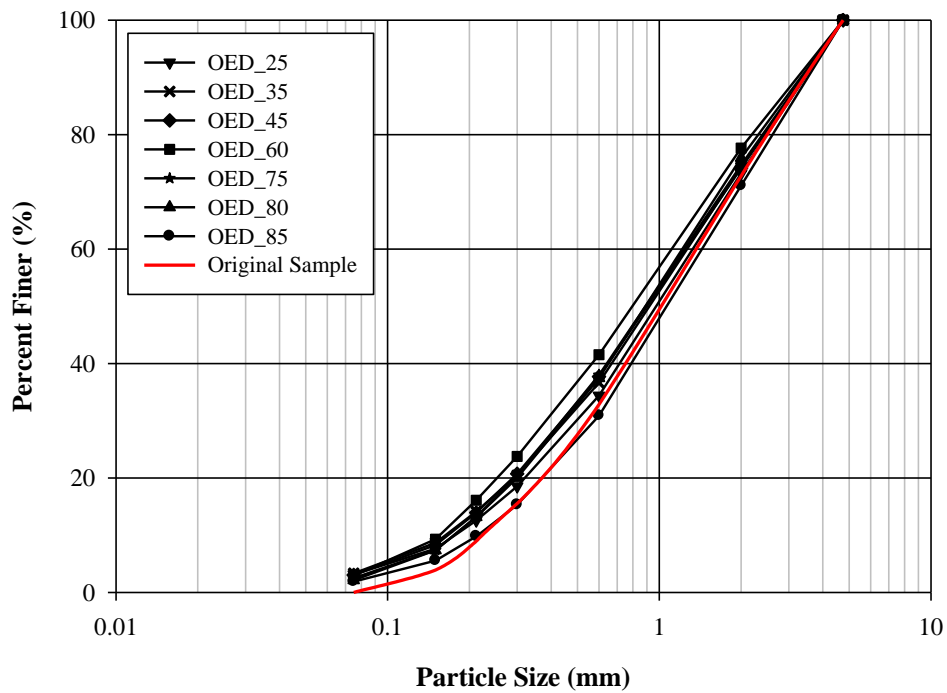
Figure 4.63. Sieve analysis results after one-dimensional loading

There are various breakage measures presented in chapter 2.4.2 to assess breakage quantitatively. If a reminder should be made, Leslie (1963) breakage measure compares the increase in the passing percent of a sieve size where 100% of the original material was retained. Later, Leslie (1975) changed the reference sieve size to those where 90% of the original material was retained. Marsal (1965) defines the maximum increase in percent passing as a breakage measure. Lee & Farhoomand (1967) use D_{15i}/D_{15a} ratio as a breakage measure. D_{15i} is the diameter of the 15% of the original sample to be finer, and D_{15a} is the diameter of the 15% of the loaded sample to be finer. These particle breakage measures were estimated for Kızılırmak sand and listed in Table 4.3.

157

Table 4.3 Estimated particle breakage measures of the Kızılırmak sand

	OED_25	OED_35	OED_45	OED_60	OED_75	OED_80	OED_85	average
Leslie 1963 (%)	3.1	3.3	3.1	2.9	2.5	2.1	1.9	2.7
Leslie 1975 (%)	3.5	5.1	5.0	7.3	4.3	4.2	0.7	4.3
Marsal 1965 (%)	3.7	5.2	5.2	8.7	5.1	4.6	1.9	4.9
Lee and Farhoomand 1967 (-)	1.193	1.311	1.303	1.455	1.261	1.253	0.990	1.252

Wu *et al.* (2016) reported that B_{15} values (breakage measurement suggested by Lee and Farhoomand (1967)) for Toyoura sand, Masado sand, and Glass beads ballotini are 1.089, 1.175, 1.022, respectively. In their study, the maximum vertical stress which was reported to be 22.5 MPa. Kızılırmak sand was loaded up to 33.5 MPa; thus stress levels are close enough for particle breakage measurement comparison. Kızılırmak sand's average B_{15} value equals to 1.252. Therefore, it is concluded that Kızılırmak sand has a higher breakage potential than the reported ones due to its angular nature.

Additionally, the specimens prepared at 35% relative density were loaded up to different stresses to observe the particle breakage amount. Their GSD curves and breakage measures are presented in Figure 4.64 and Table 4.4.
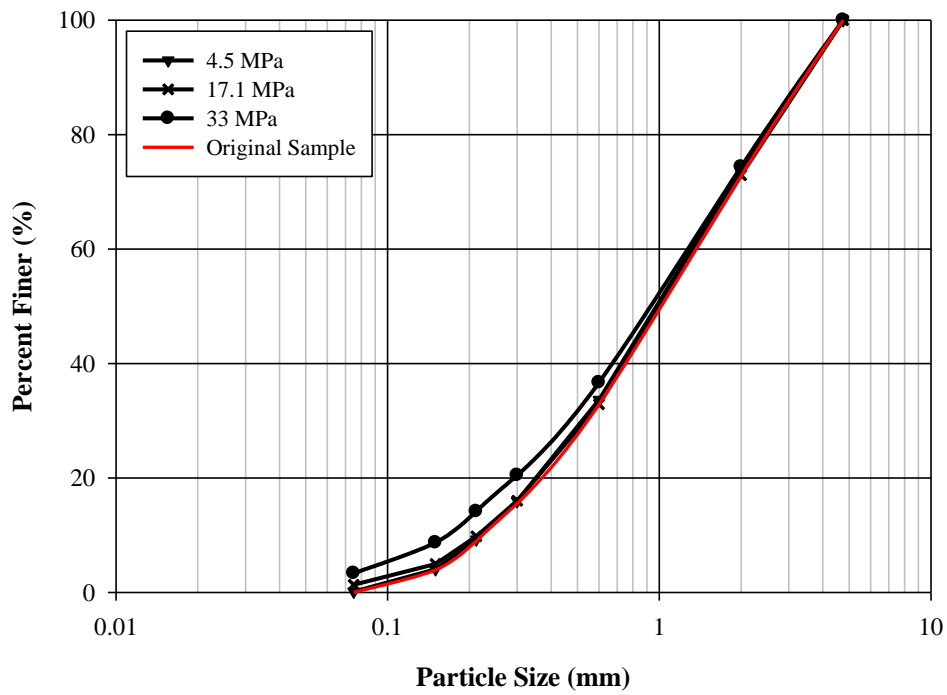
Figure 4.64. Sieve analysis results of the 35% relative density specimens loaded to a maximum load of 4.5, 17.1 and 33.5 MPa

Table 4.4 Comparison of the particle breakage measures for the specimen prepared at 35% relative density and loaded to 4.5, 17.1 and 33.5 MPa

	4.5 MPa	17.1 MPa	33.5 MPa
Leslie 1963 (%)	0.1	1.3	3.3
Leslie 1975 (%)	0.3	0.8	5.1
Marsal 1965 (%)	1.3	1.3	5.2
Lee and Farhoomand 1967 (-)	1.021	1.028	1.311

4.6 Interpretation of Results in Terms of Critical State Soil Mechanics Approach

In some experiments, it was observed that triaxial test specimens reached or were close to reach its quasi-steady state and steady state. Based on these observations steady state line, steady state friction angle, initial dividing line were estimated for Kızılırmak sand as defined by Ishihara (1996). Moreover, state parameters of the experiments were calculated, and the relation between state parameter vs. stress ratio at failure $((q/p')_f)$ and state parameter vs. peak friction angle are presented. Before the presentation of calculation and analysis results, a brief summary is given to remind the terms such as steady state, quasi-steady state, and initial dividing line.

The steady state of sand is defined as "The state of the sand deforming continually, keeping the volume constant, under constant shear stress and confining stress." by Castro (1975) and Castro and Poulos (1977). The quasi-steady state of sand is defined as "A temporary drop in shear stress takes place over a limited range of shear strains. Such a case was termed as quasi-steady state." by Alarcon-Guzman, Leonards and Chameau (1988), Been, Hachey and Jefferies (1991), and Vaid, Chung and Kuerbis (1990), as opposed to conventional steady state definitions, which is reached at larger shear strains. An example of a steady state and quasi-steady state of Toyoura sand is presented in Figure 4.65. In this figure, Q and P points show quasi-steady state, and R shows steady state.
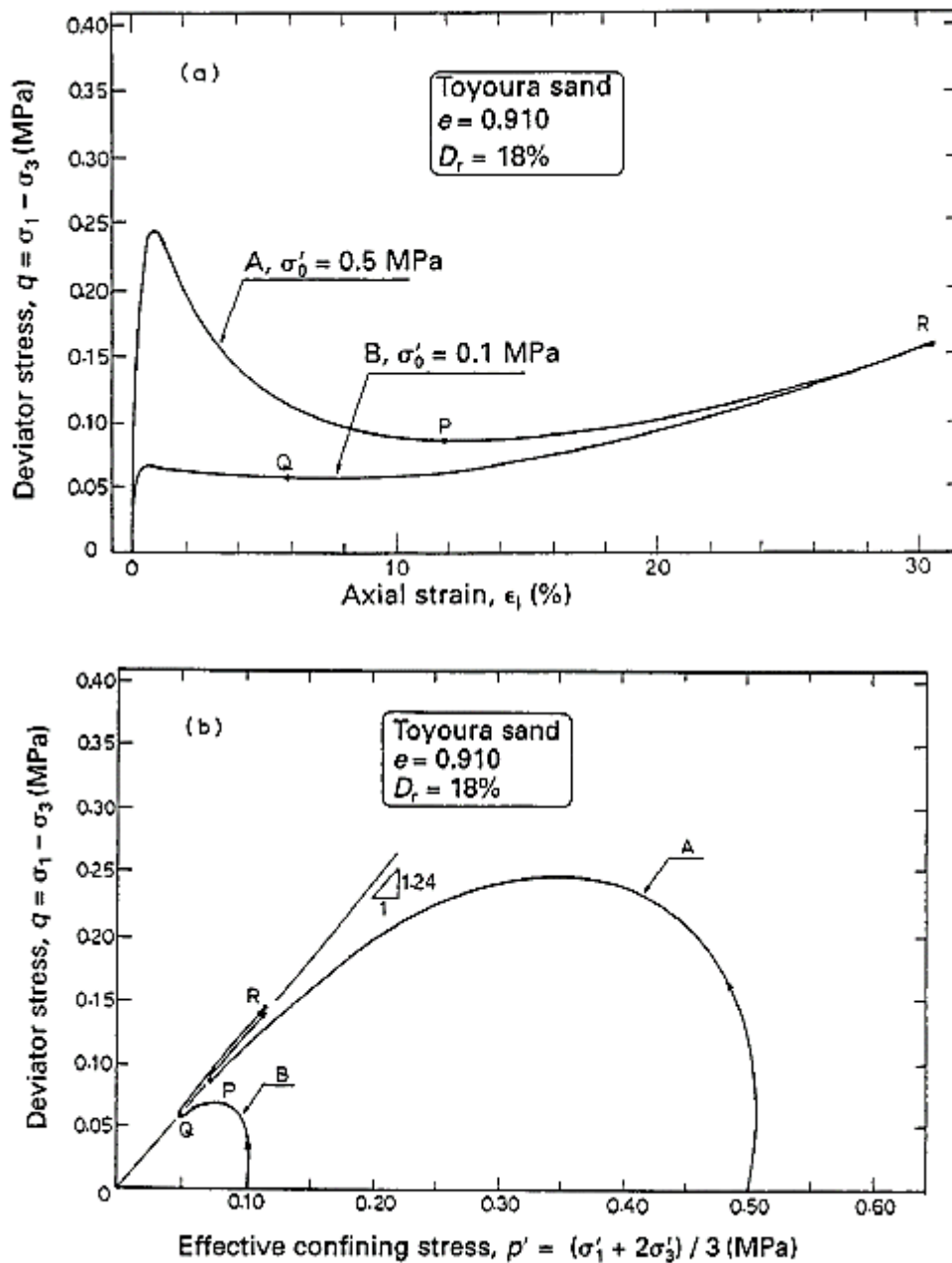
Fig. 11.10 (a), (b)

Figure 4.65. Example points corresponding steady state and quasi-steady state on a stress-strain plot and stress path of Toyoura sand (Ishihara, 1996)

The development of this temporary shear strength drop depends on the void ratio and stress state of the specimen. When a set of experiment results, at which the quasi-steady state is observed and is not observed, are plotted, a boundary between those

two-different responses is formed. This boundary is introduced as initial dividing line by Ishihara (1993) to identify whether a specimen exhibits quasi-steady state or not. An example of initial dividing line defined for Toyoura sand is given in Figure 4.66. Specimens above the initial diving line first go through a quasi-steady state at which shear strength is smaller than the shear strength at steady state. After quasi-steady state, they reach steady state. Specimens below the initial dividing line directly reach their steady states. An important note at this point: initial dividing line is not a projection on the e-p' plane. It lies directly on the e-p' plane, just as isotropic compression lines.
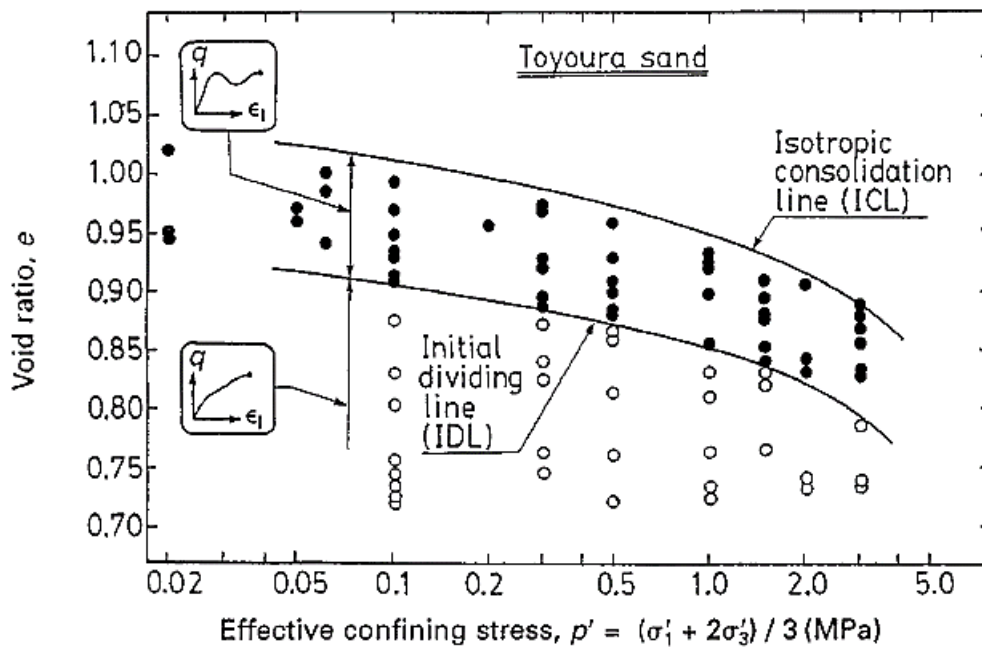
Figure 4.66. Initial dividing line of Toyoura sand (Ishihara, 1996)

An additional reminder should be made regarding effect of specimen fabric on quasi-steady state. Specimen fabric (e.g., sample preparation technique) plays an important role when drawing quasi-steady state line and initial dividing line. In contrast, steady state does not depend on specimen fabric (Ishihara, 1996). In Figure 4.67, different quasi-steady state lines result from different specimen preparation techniques that can be seen for Tia Juana silty sand. In this figure, isotropic compression lines belong to these different preparation techniques and steady state line are also presented.

162
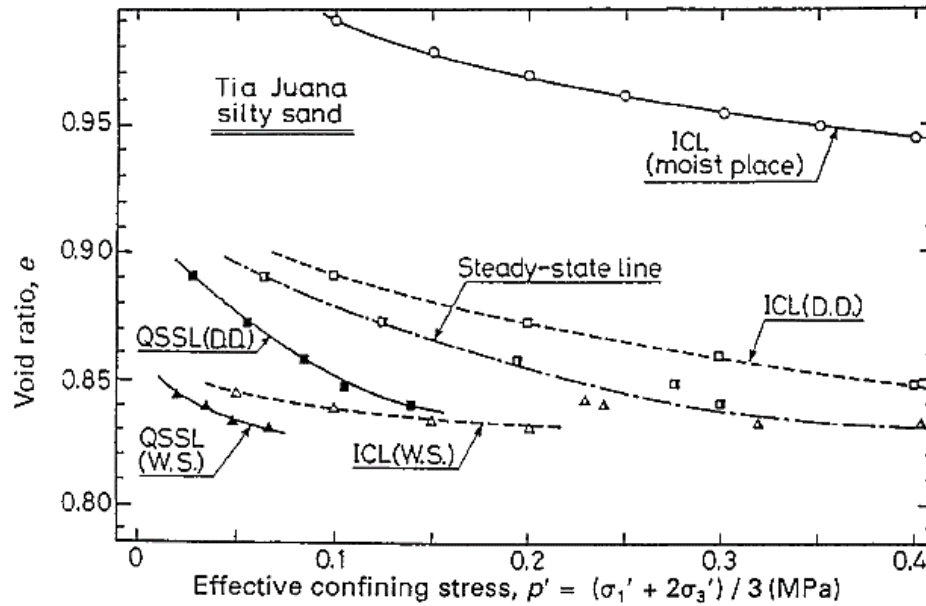
Figure 4.67. Effect of specimen fabric on the ICL, SSL, and QSSL of Tia Juana silty sand specimens sand (Ishihara, 1996)

Isotropic compression lines of Kızılırmak sand were manipulated from one-dimensional compression tests. Mean effective stresses were calculated by assuming a K_0 with the help of friction angles estimated from triaxial tests. Isotropic compression lines for e_{min} and e_{max} were plotted by using compression index values estimated from tests OED_25 and OED_85, respectively. Isotropic compression lines of the Kızılırmak sand and the comparison with Toyoura sand whose data were taken from Ishihara (1996), are presented in Figure 4.68 and Figure 4.69.
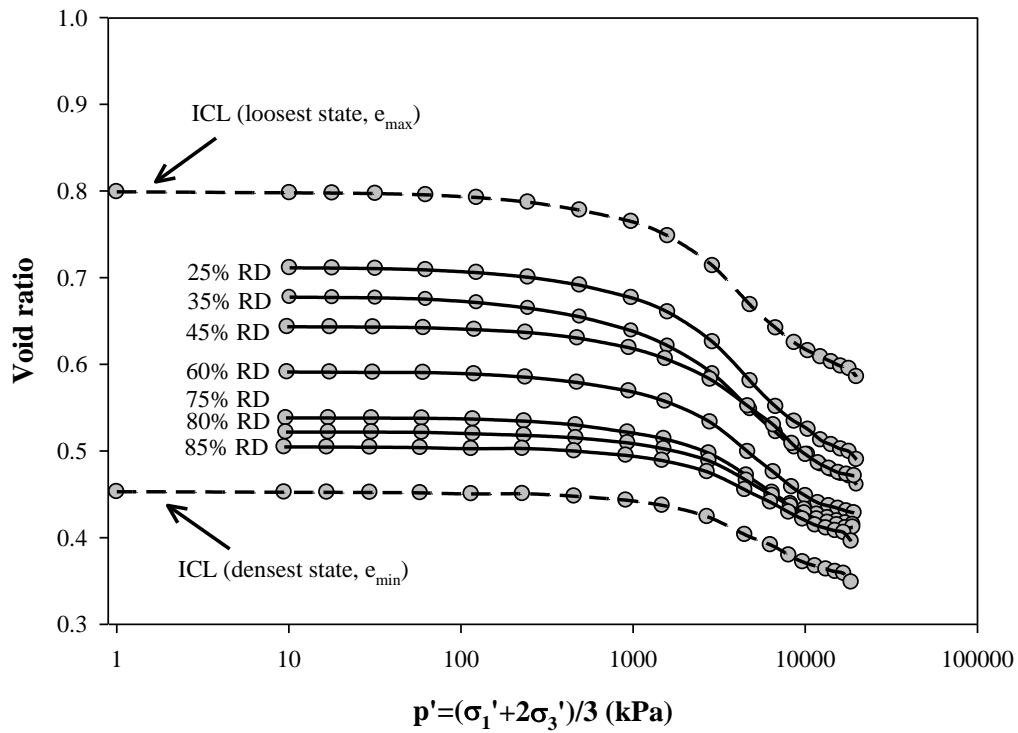
Figure 4.68. Isotropic compression lines of Kızılırmak sand
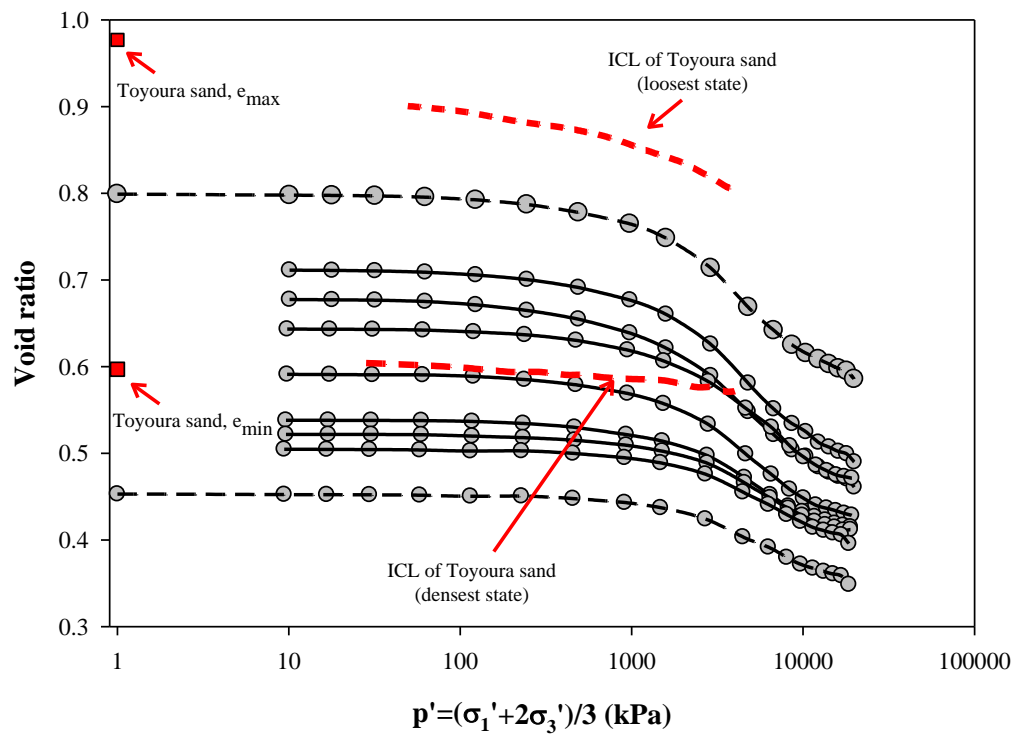
Figure 4.69. Isotropic compression lines of Kızılırmak and Toyoura sand

164

For specimens of Kızılırmak sand, which were prepared at 35% relative density and consolidated to 50-100-200 kPa consolidation pressures, quasi-steady state was observed in their stress-strain plot. Based on this observation and considering limited data points, a possible range for the initial dividing line (IDL) of Kızılırmak sand was suggested, as shown in Figure 4.70. In Figure 4.71, isotropic compression lines and initial dividing line are presented together. From this figure, it is understood that the specimen, which has a relative density equals and looser than ~45% RD, has a possibility of experiencing quasi-steady-state at which shear strength of the specimen is smaller than the steady-state shear strength.
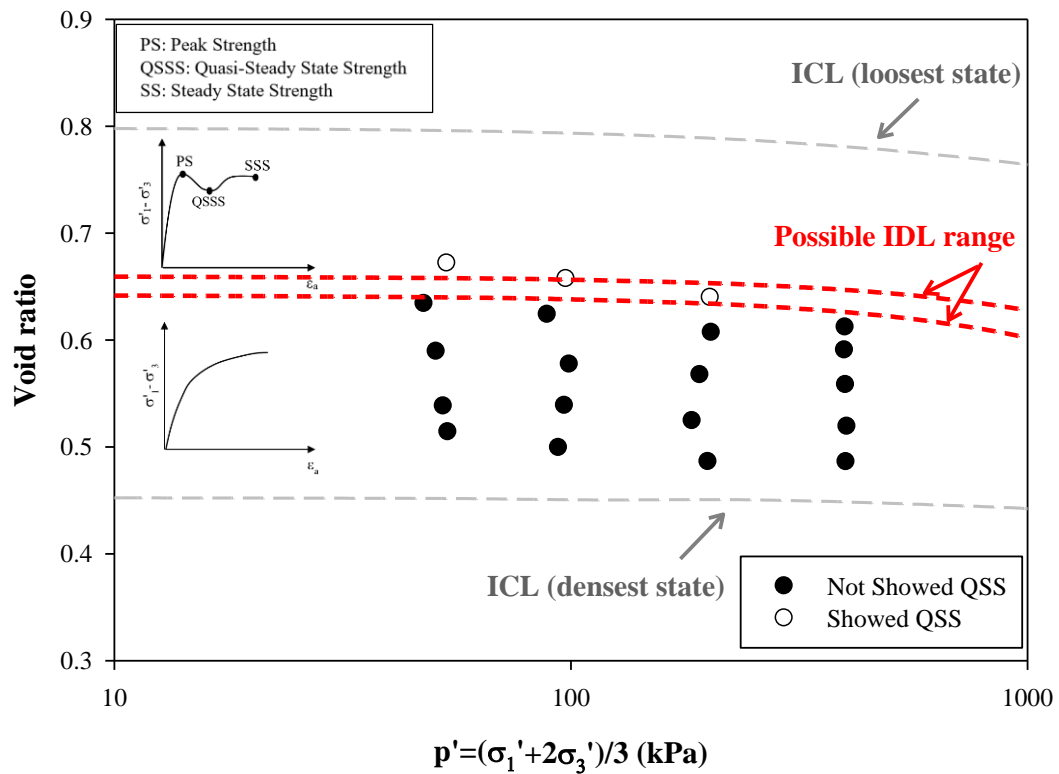
Figure 4.70. Initial dividing line of Kızılırmak sand
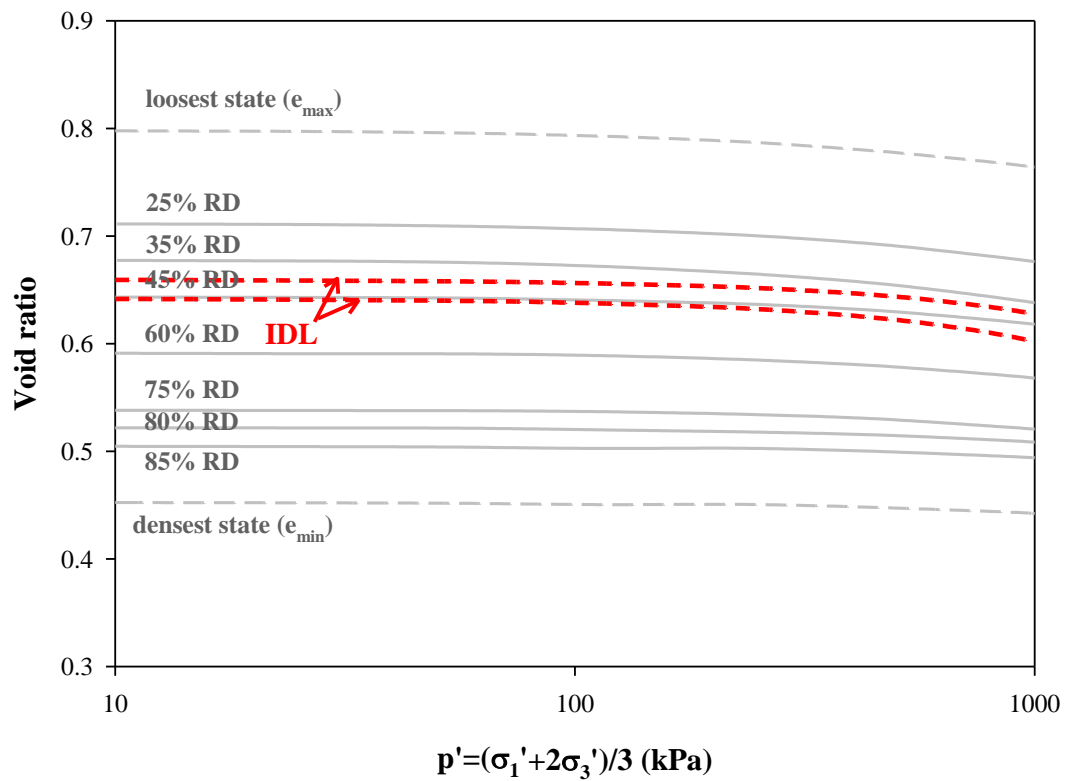
Figure 4.71. Isotropic compression lines and initial dividing line of Kızılırmak sand

Deviatoric stress vs. mean effective stress at steady state was plotted and presented in Figure 4.72. The slope of this relation was used to estimate M=1.61, and from this value, the steady-state friction angle of Kızılırmak sand was calculated as 39.4˚.
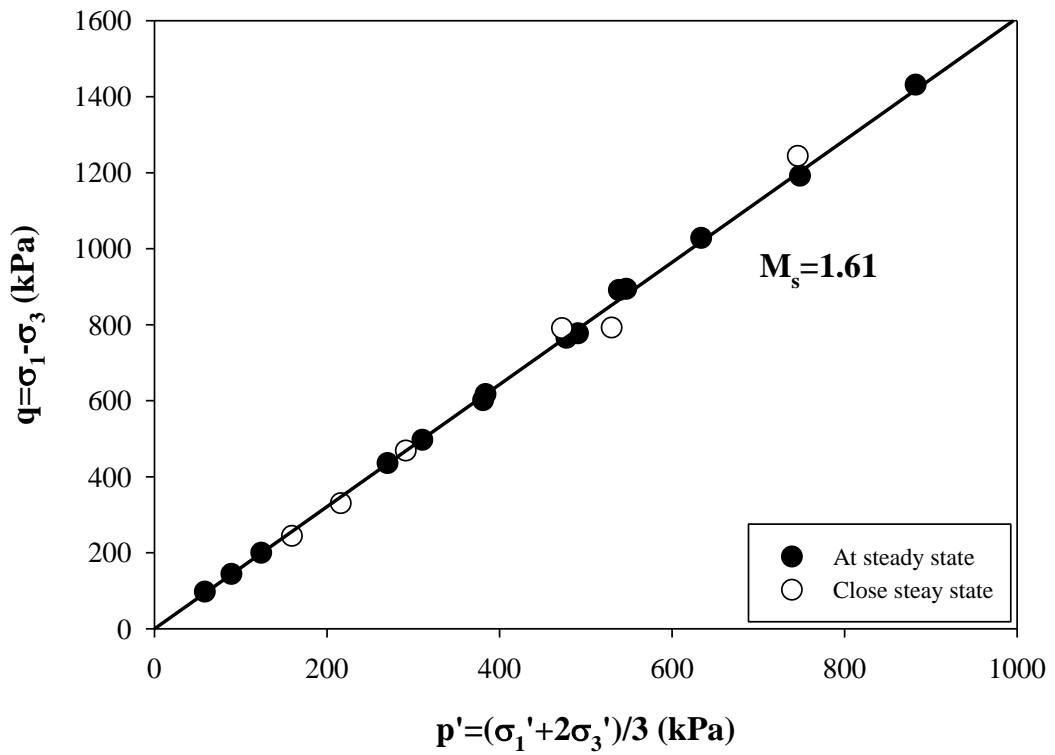
Figure 4.72. Deviatoric stress vs. mean effective stress of Kızılırmak sand at steady state

Steady-state line (SSL) was estimated from the triaxial tests as given in Figure 4.73. Steady state line parameters, λ and Γ, were estimated as 0.070 and 0.975, respectively.
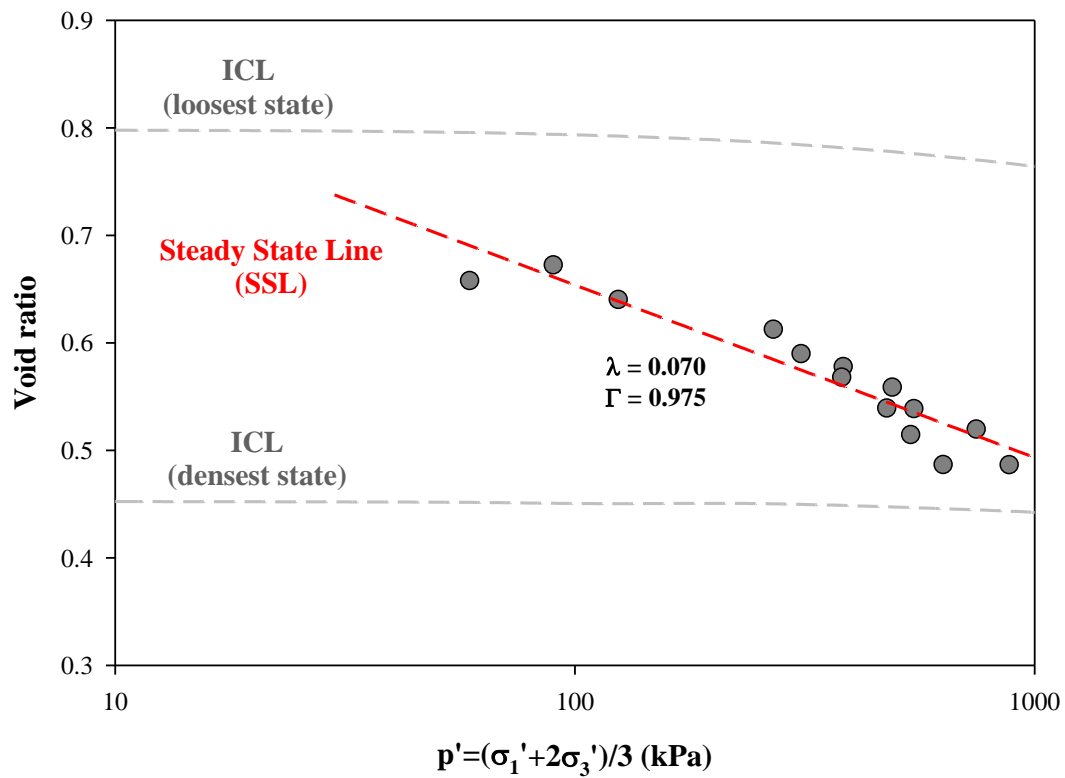
Figure 4.73. Steady-state line of Kızılırmak sand

Isotropic compression lines for loosest and densest states, steady state line, and a possible range of initial dividing line are presented jointly in Figure 4.74.
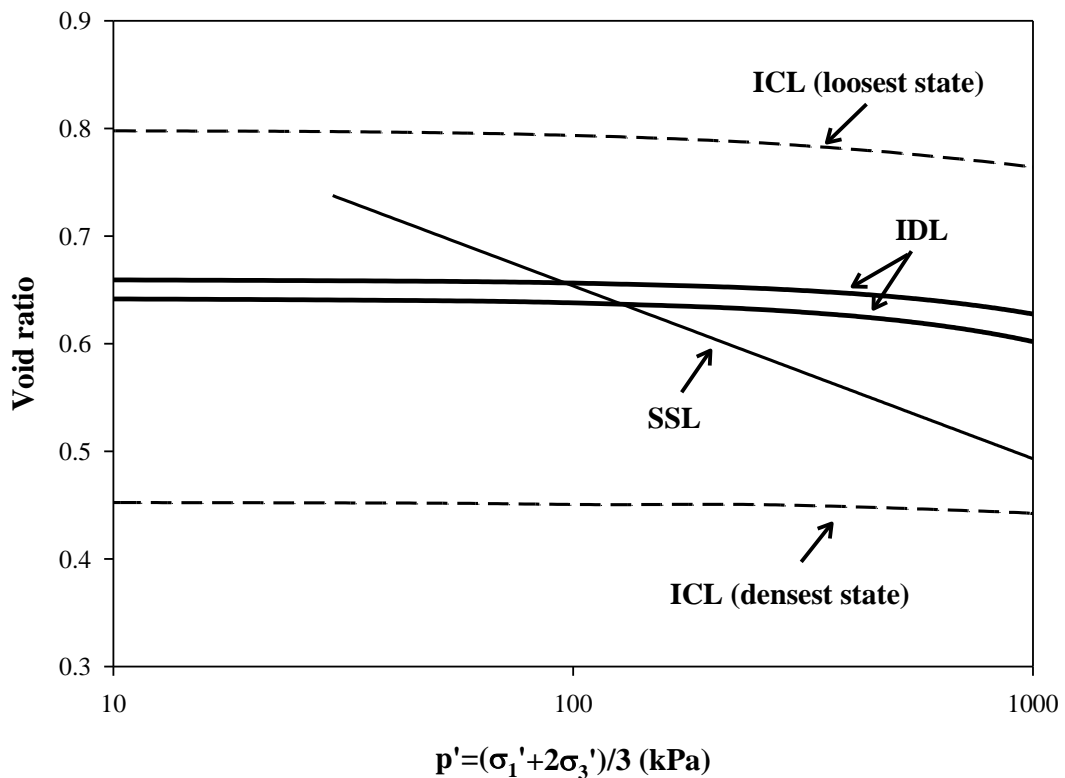
Figure 4.74. ICL, IDL, and SSL of Kızılırmak sand specimens

Researchers like Been and Jefferies (1985), Cubrinovski and Ishihara (1998), and Ishihara (1993) introduce a state parameter definition to express the response of soil by using critical state concept. State parameter comprises both density and stress state effects on the response. It is related to the distance between specimen's current position and the steady-state line. State parameters were calculated for Kızılırmak sand by using the Been and Jefferies (1985) definition. Stress ratio at failure vs. the state parameter and undrained effective peak friction angle vs. state parameter graphs were plotted and given in Figure 4.75 and Figure 4.76. Linear relations given in Eqn. 4-1 and Eqn. 4-2 were developed.

$$q/p' = 0.771 - 0.763 * \psi \qquad \text{Eqn. 4-1}$$

$$\phi' = 37.8 - 35.3 * \psi \qquad \text{Eqn. 4-2}$$

169
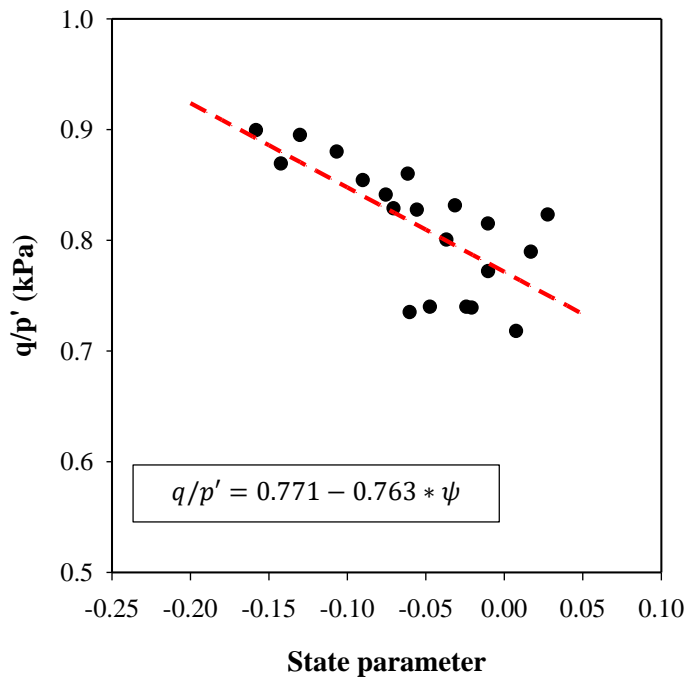
Figure 4.75. Relationship between stress ratio at failure and state parameter

$$q/p' = 0.771 - 0.763 * \psi$$
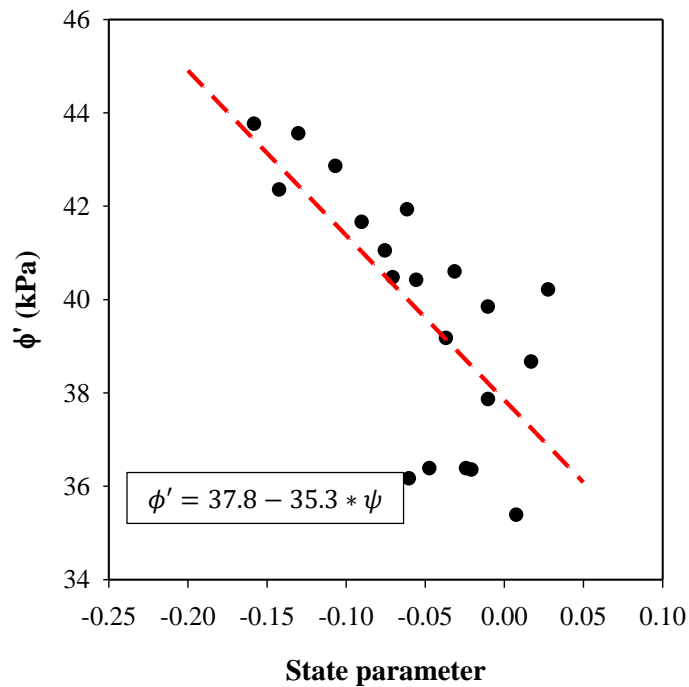
Figure 4.76. Relationship between undrained effective peak friction angle and state parameter

$$\phi' = 37.8 - 35.3 * \psi$$

From this figure, steady-state friction angle of Kızılırmak sand (where state parameter equals to zero) was estimated as 37.8°. Please do not forget that, in the previous chapter, steady-state friction angle of Kızılırmak sand was estimated as 37.5° from the angularity and sphericity relation proposed by Cho *et al.* (2006).

Been and Jefferies (1985) give the relationship between friction angle and state parameter for different sands as shown in Figure 4.77.
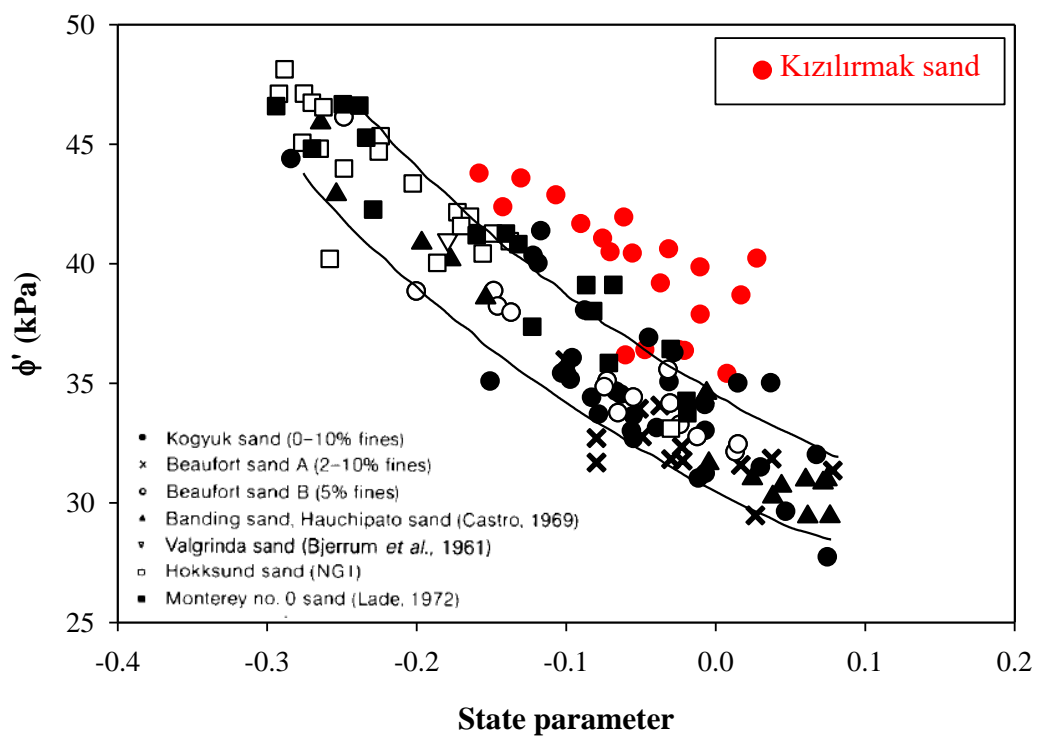
Figure 4.77. Relationship between peak friction angle and state parameter for different sands adapted from Been and Jefferies (1985) as compared with the findings of this study for Kızılırmak sand

CHAPTER 5

CONSTITUTIVE MODELING PARAMETERS FOR KIZILIRMAK SAND

5.1. Introduction

The need to model soil behavior is sourcing with the intent to develop a tool to solve engineering problems or analyze the soil behavior to fulfill pure scientific curiosity. For engineering applications, simple models are preferred, whereas, for scientific curiosity, complex models are developed to assess soil response.

Based on the results of experimental studies, which are presented in previous chapters, the constitutive modeling input parameters for elasto-plastic models, i) linear elastic-perfectly plastic, and ii) nonlinear elastic-perfectly plastic, were estimated for Kızılırmak sands' undrained shearing response. These models and some of their input parameters will be presented in this chapter.

5.2. Linear Elastic-Perfectly Plastic Model and It's Parameters

Linear elastic-perfectly plastic model for the behavior of the soil has been used widely due to ease in its use. Especially before the development of numerical analysis methods or even computers, it was not feasible to perform complicated analysis. Besides, it is easy to get model parameters (cohesion, c; friction angle, ϕ; and stiffness, E) from conventional triaxial tests. These are the reasons why linear elastic soil model is preferred, although there exist other sophisticated material models.

Linear elastic-perfectly plastic model was fitted to the stress-strain plots of Kızılırmak sand, which were obtained from triaxial tests. Mohr-Coulomb failure criterion, given in Eqn. 5-1, was used as a failure criterion.

$$F(\sigma) = \frac{\sigma_1 - \sigma_3}{2} - \frac{\sigma_1 + \sigma_3}{2} \, sin\phi - \frac{2ccos\phi}{2} \qquad \text{Eqn. 5-1}$$

where σ_1 and σ_3 are the major and minor principal stresses at failure, ϕ is the angle of shearing resistance, and c is the cohesion.

The initial, relatively linear part of the stress-strain graph is linearly extended until the failure stress (strength). The slope of this line is defined as the elastic modulus estimated from the triaxial test, E_{TRX}. Note that E is not identical with Young's Modulus and the failure stress is estimated by using obliquity concepts. Stress-strain plots, along with the linear elastic-perfectly plastic model fits are presented in Figure 5.1 through Figure 5.5. In these figures, the red dots show the failure stresses.
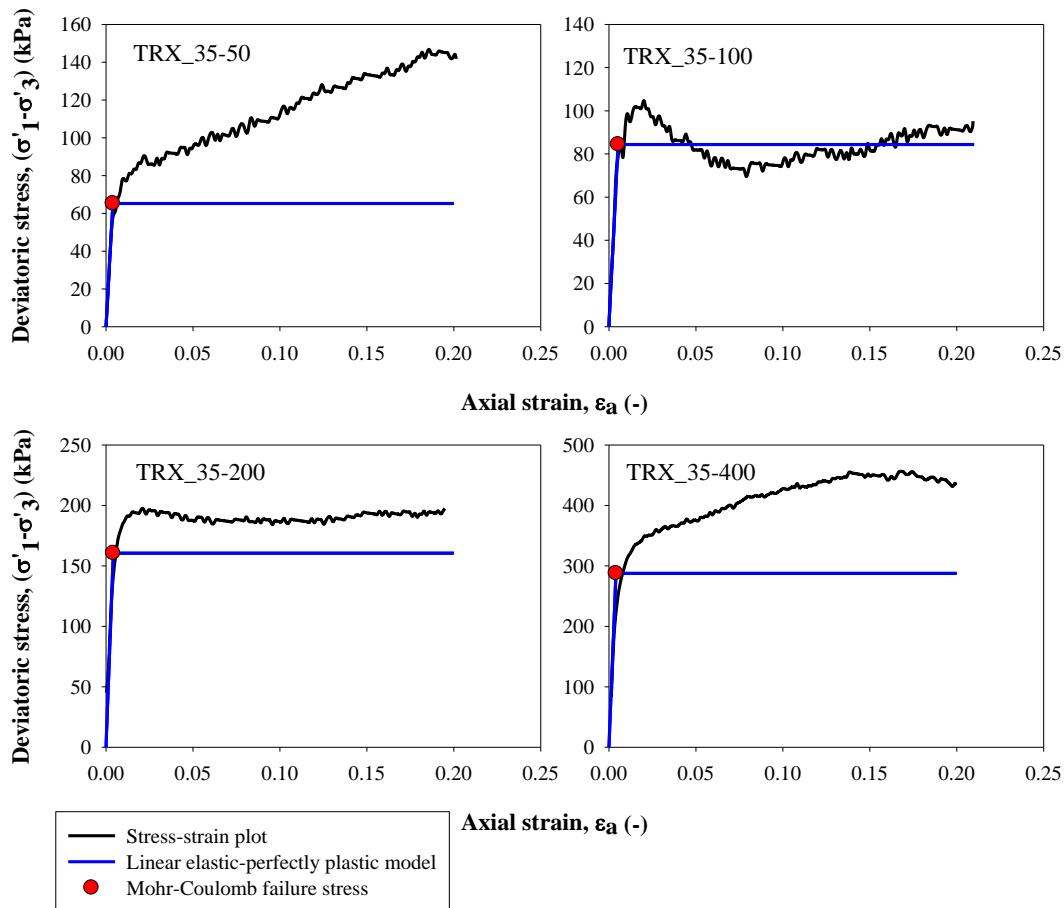
Figure 5.1. Stress-strain plots of the specimens prepared at ~35% relative density along with the linear-elastic perfectly-plastic model fit

174
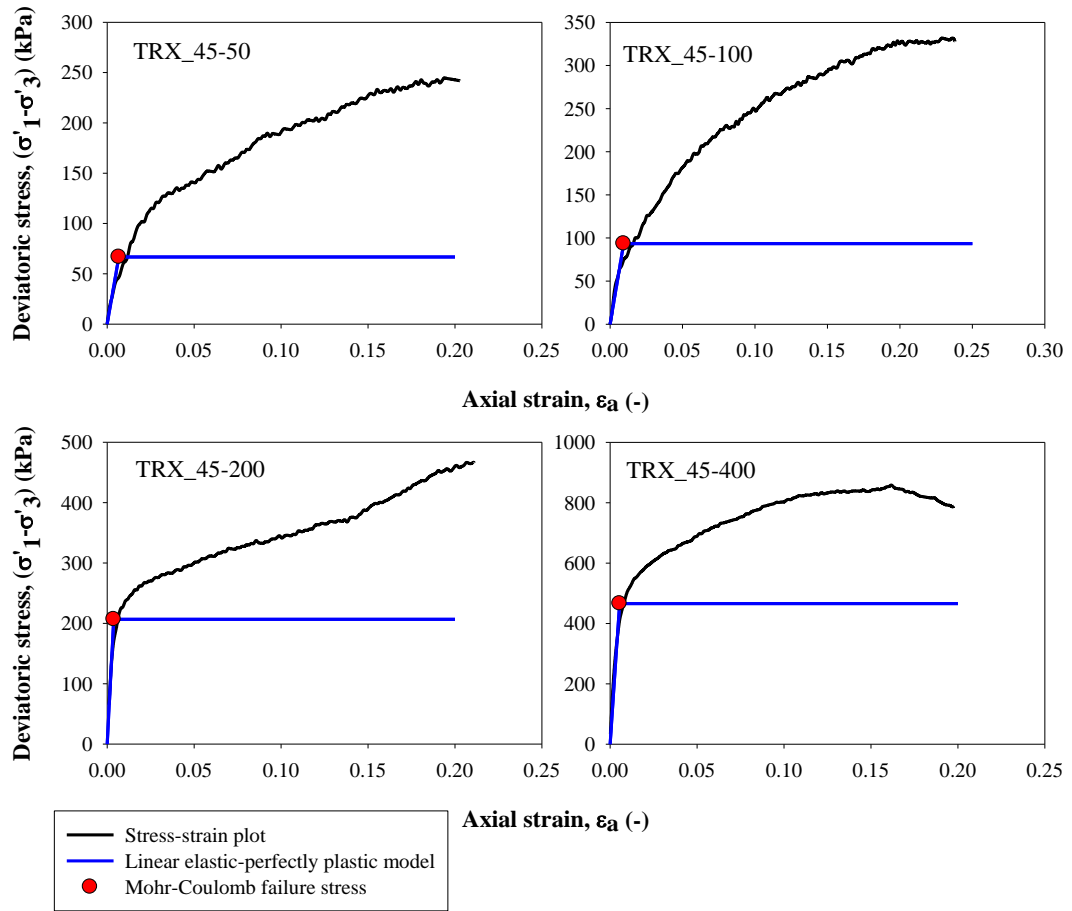
Figure 5.2. Stress-strain plots of the specimens prepared at ~45% relative density along with the linear-elastic perfectly-plastic model fit
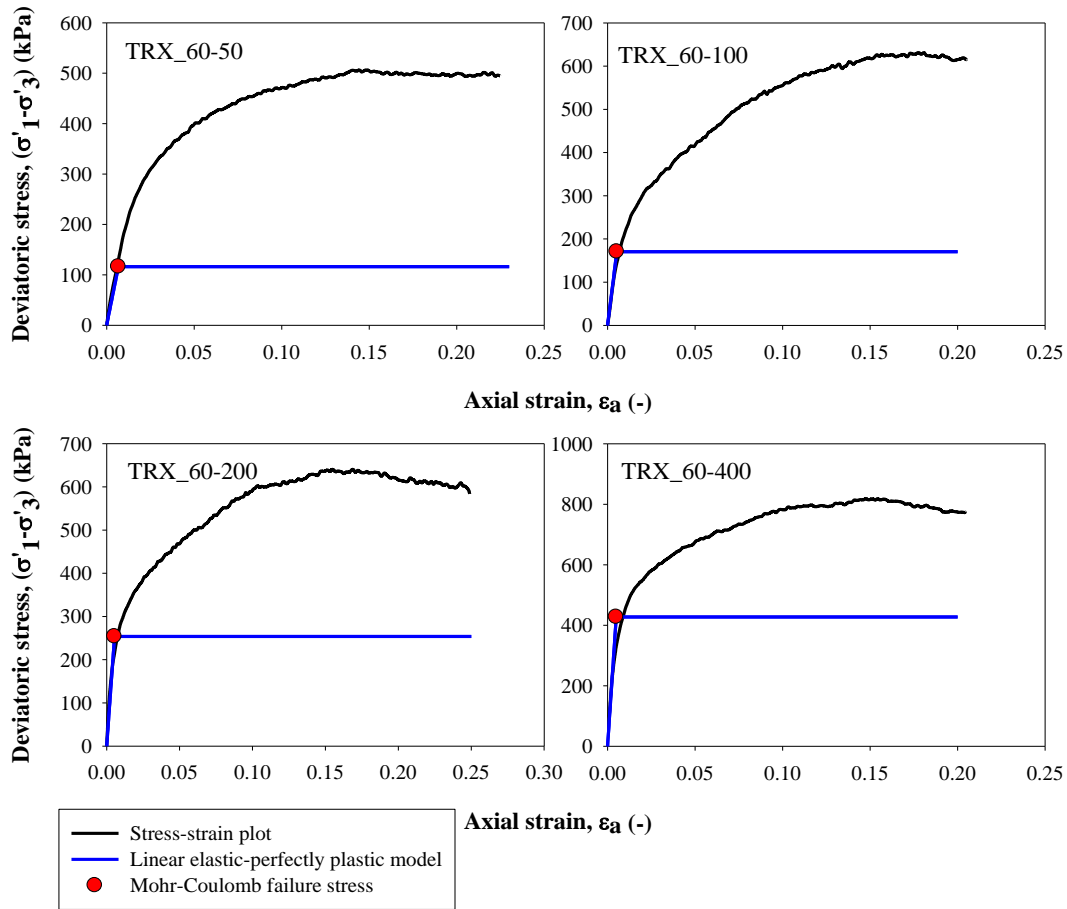
Figure 5.3. Stress-strain plots of the specimens prepared at ~60% relative density along with the linear-elastic perfectly-plastic model fit
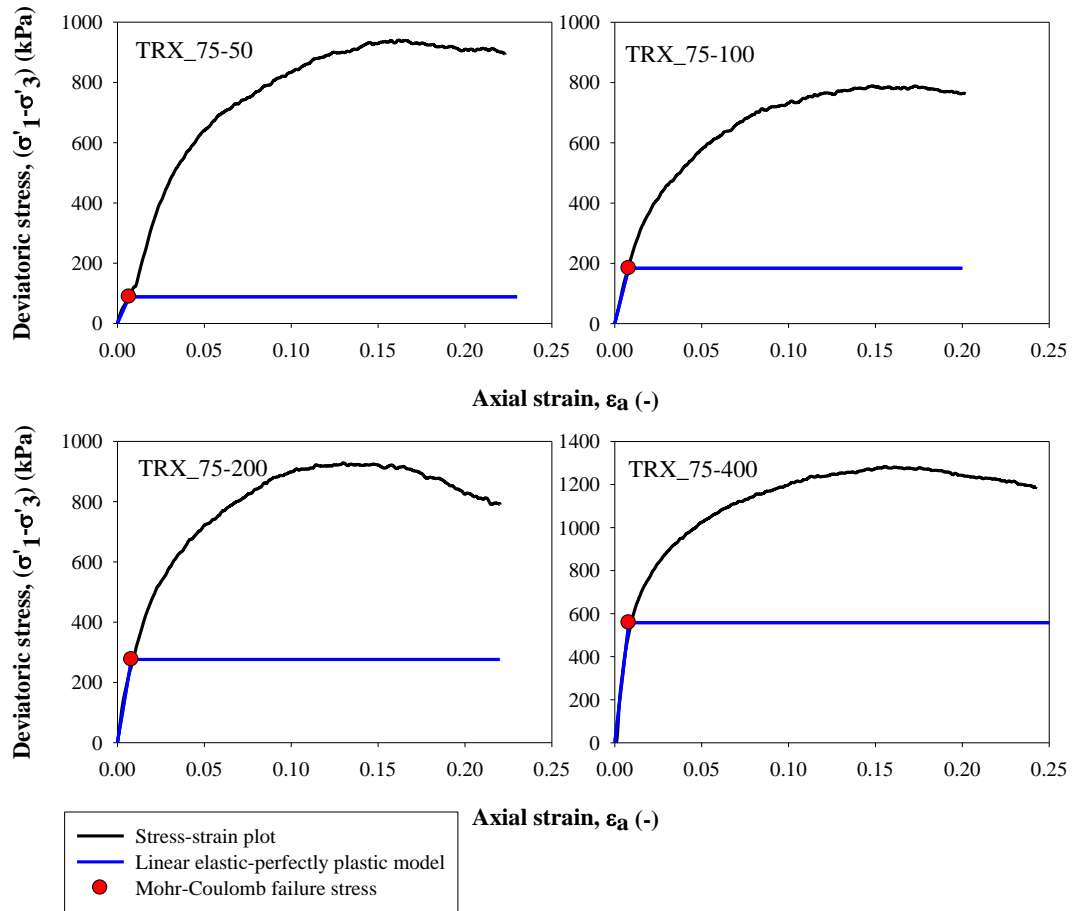
Figure 5.4. Stress-strain plots of the specimens prepared at ~75% relative density along with the linear-elastic perfectly-plastic model fit
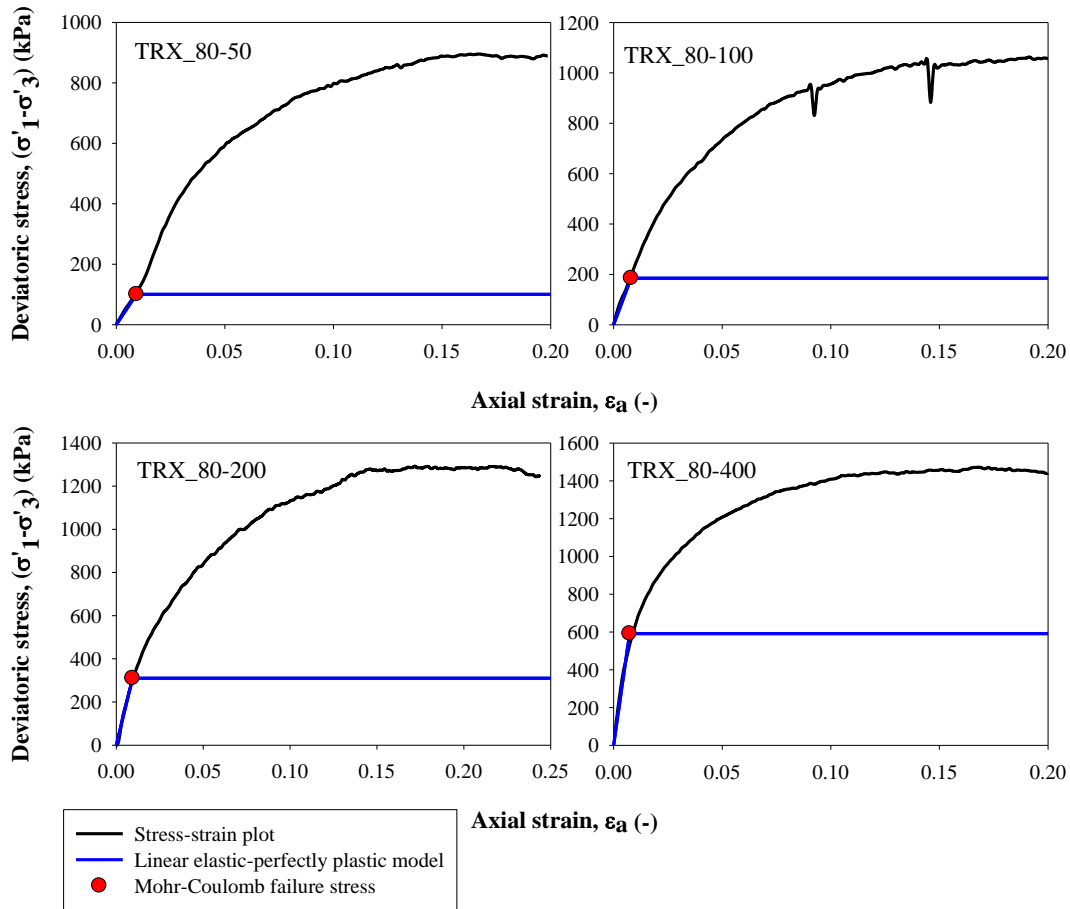
Figure 5.5. Stress-strain plots of the specimens prepared at ~80% relative density along with the linear-elastic perfectly-plastic model fit

From the stress-strain plots, it is understood that linear elastic-perfectly plastic model predictions provide a good fit to data until failure stresses; however, beyond failure the model is observed to be significantly conservative. This is due to dilative nature of Kızılırmak sand under studied stress and density states. For the purpose of assessing post failure performances, perfectly plastic model is judged to be not adequate. Next, the literature regarding the assessment of elastic modulus will be presented, followed by the introduction of specific models for Kızılırmak sand.

Janbu (1963) proposed an experimentally-based relation for elastic modulus of soils. This well-known power function is given as follows:

$$E_i = K_i p_a \left(\frac{\sigma_3'}{p_a}\right)^n \qquad \text{Eqn. 5-2}$$

where E_i is the initial tangent modulus, K_i is the modulus number, n is the exponent which controls the change in E_i with σ_3', σ_3' is the minor principal stress, p_a is the atmospheric pressure.

In order to give an elastic modulus relation for Kızılırmak sand, the power function formulation given in Eqn. 5-2 was used. Variations of the relationship, such as E_{TRX} is a function of confining stress or mean effective stress was studied. Also, the effect of the void ratio on the elastic modulus was studied by using void ratio formulations given in Eqn. 5-9 and Eqn. 5-10. Combinations of different stress parameters and different void ratio functions are listed in Eqn. 5-3 through Eqn. 5-8.

$$E = K p_a \left(\frac{\sigma_3'}{p_a}\right)^n \qquad \text{Eqn. 5-3} \qquad E = K p_a \left(\frac{p'}{p_a}\right)^n \qquad \text{Eqn. 5-4}$$

$$E = f^1(e_0) K p_a \left(\frac{\sigma_3'}{p_a}\right)^n \qquad \text{Eqn. 5-5} \qquad E = f^1(e_c) K p_a \left(\frac{p'}{p_a}\right)^n \qquad \text{Eqn. 5-6}$$

$$E = f^2(e_0) K p_a \left(\frac{\sigma_3'}{p_a}\right)^n \qquad \text{Eqn. 5-7} \qquad E = f^2(e_c) K p_a \left(\frac{p'}{p_a}\right)^n \qquad \text{Eqn. 5-8}$$

where,

$$f^1(e) = (2.17 - e)^2/(1 + e) \quad \text{(Hardin and Richart, 1963)} \qquad \text{Eqn. 5-9}$$

$$f^2(e) = e^{-1.3} \quad \text{(Lo Presti, 1990)} \qquad \text{Eqn. 5-10}$$

e_0: initial void ratio of the specimen

e_c: void ratio of the specimen after consolidation stage

p': mean effective stress $((\sigma_1' + 2\sigma_3')/3)$

Elastic moduli, which were estimated from the experiments and calculated by the proposed relations, are comparatively presented in Figure 5.6 - Figure 5.11.
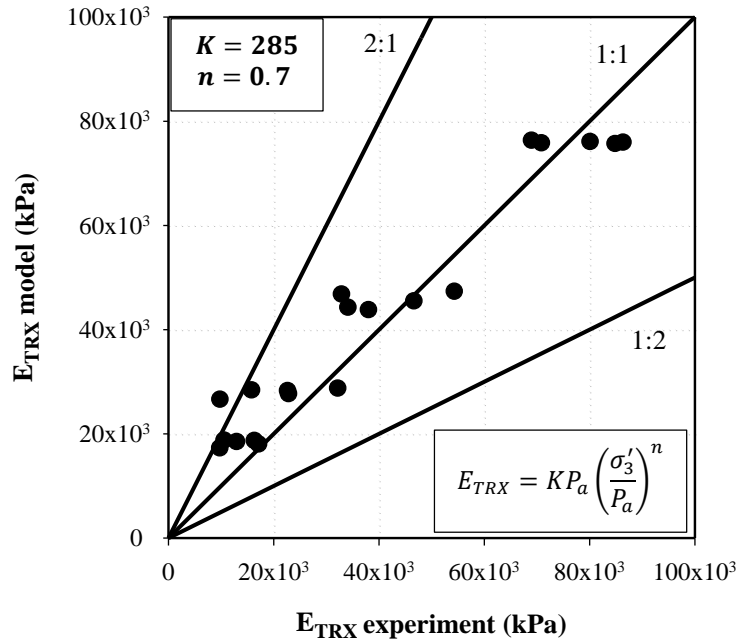
Figure 5.6. Model prediction vs. experimental results of $E_{TRX} = f(\sigma'_3)$
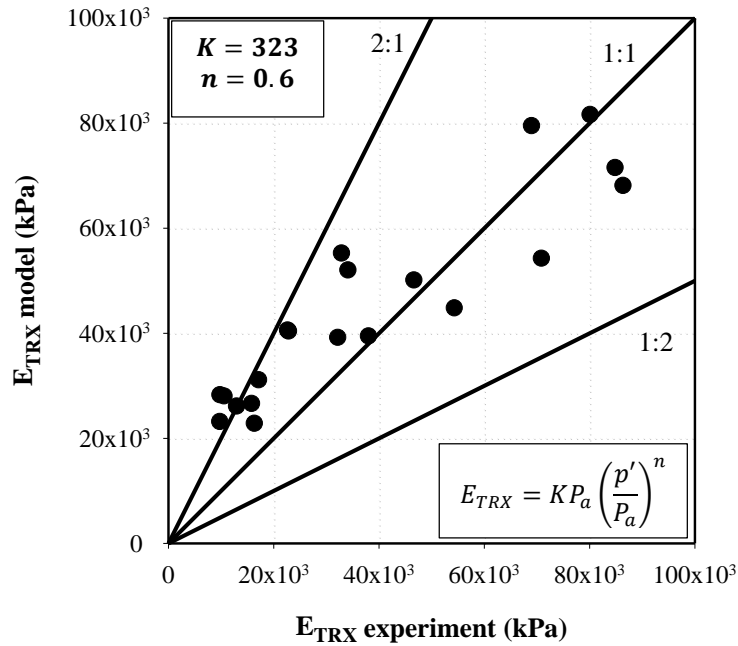
Figure 5.7. Model prediction vs. experimental results of $E_{TRX} = f(p')$
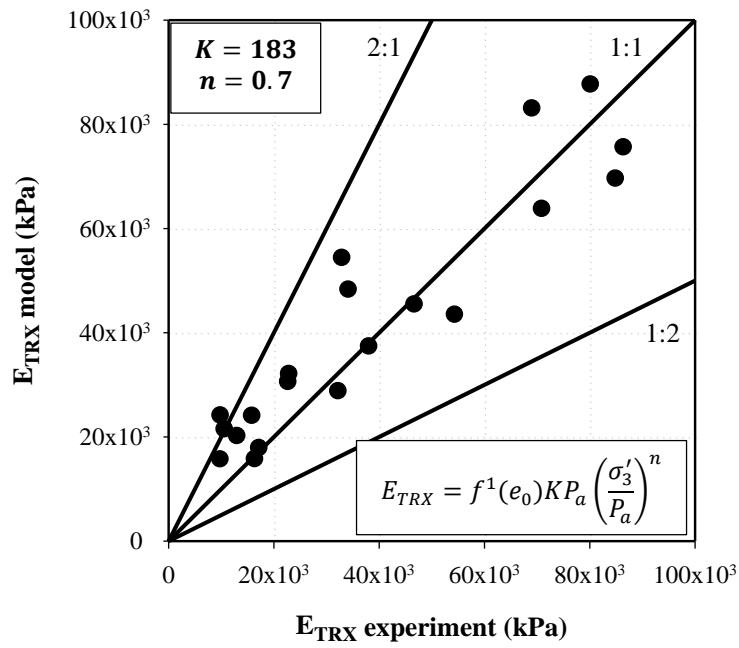
Figure 5.8. Model prediction vs. experimental results of $E_{TRX} = f\ (\sigma'_3, f^1(e_0))$
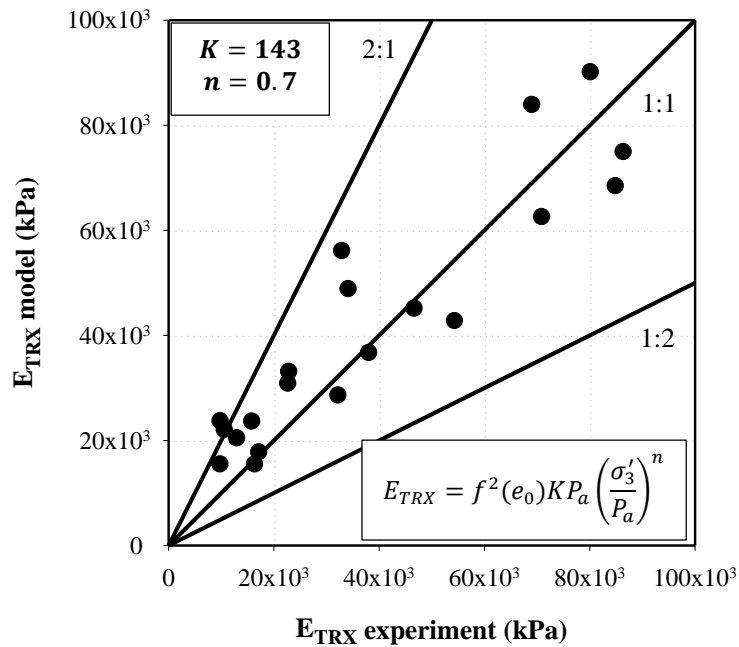
Figure 5.9. Model prediction vs. experimental results of $E_{TRX} = f\ (\sigma'_3, f^2(e_0))$
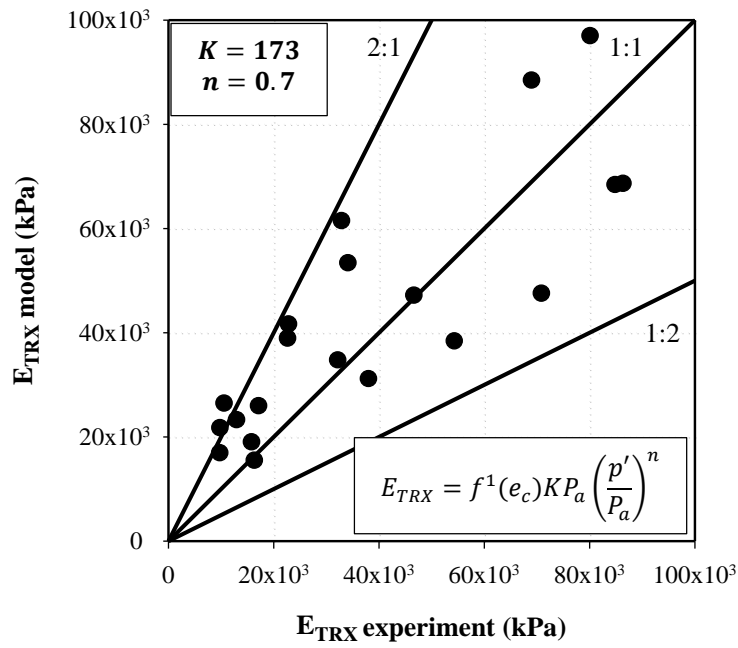
Figure 5.10. Model prediction vs. experimental results of $E_{TRX} = f(p', f^1(e_c))$

$$E_{TRX} = f^1(e_c)KP_a\left(\frac{p'}{P_a}\right)^n$$

($K = 173$, $n = 0.7$)
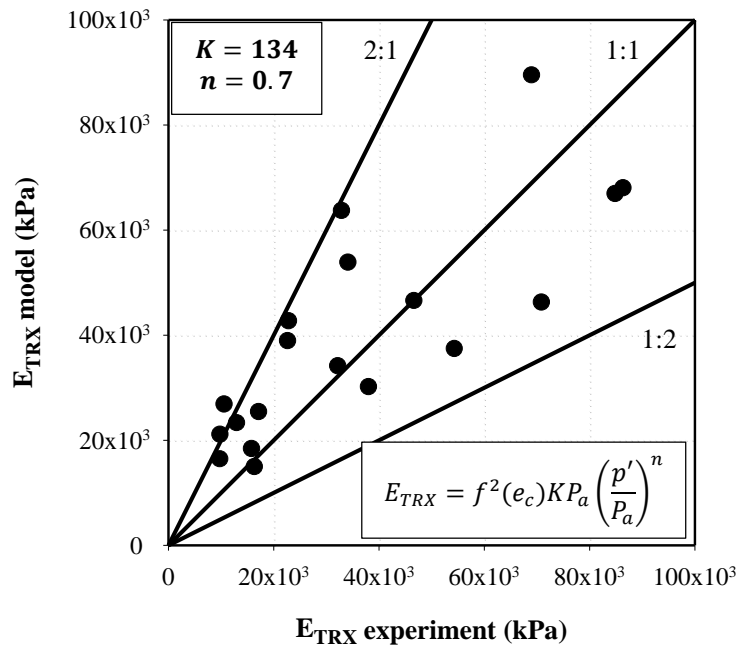
Figure 5.11. Model prediction vs. experimental results of $E_{TRX} = f(p', f^2(e_c))$

$$E_{TRX} = f^2(e_c)KP_a\left(\frac{p'}{P_a}\right)^n$$

($K = 134$, $n = 0.7$)

182

Table 5.1 Summary of the elastic modulus parameters for Kızılırmak sand

	K	n	R^2
$E_{TRX} = KP_a \left(\dfrac{\sigma_3'}{P_a} \right)^n$	285	0.7	0.86
$E_{TRX} = KP_a \left(\dfrac{p'}{P_a} \right)^n$	323	0.6	0.44
$E_{TRX} = [(2.17 - e_0)^2/(1 + e_0)]KP_a \left(\dfrac{\sigma_3'}{P_a} \right)^n$	183	0.7	0.80
$E_{TRX} = [e^{-1.3}]KP_a \left(\dfrac{\sigma_3'}{P_a} \right)^n$	143	0.7	0.78
$E_{TRX} = [(2.17 - e_c)^2/(1 + e_c)]KP_a \left(\dfrac{p'}{P_a} \right)^n$	173	0.7	0.58
$E_{TRX} = [e^{-1.3}]KP_a \left(\dfrac{p'}{P_a} \right)^n$	134	0.7	0.55

The summary of the elastic constants of Kızılırmak sand is presented in Table 5.1. Modulus constant K and n are varying in the range of 134-323 and 0.6-0.7 respectively.

Janbu (1963) recommendations for K and n values are presented in Figure 5.12. Modulus constant and the exponent values for sands are in the range of 60-600 and 0.3-0.75, as highlighted in Figure 5.12. Therefore, constants of Kızılırmak sand are concluded to fall in the range of sand specimens.
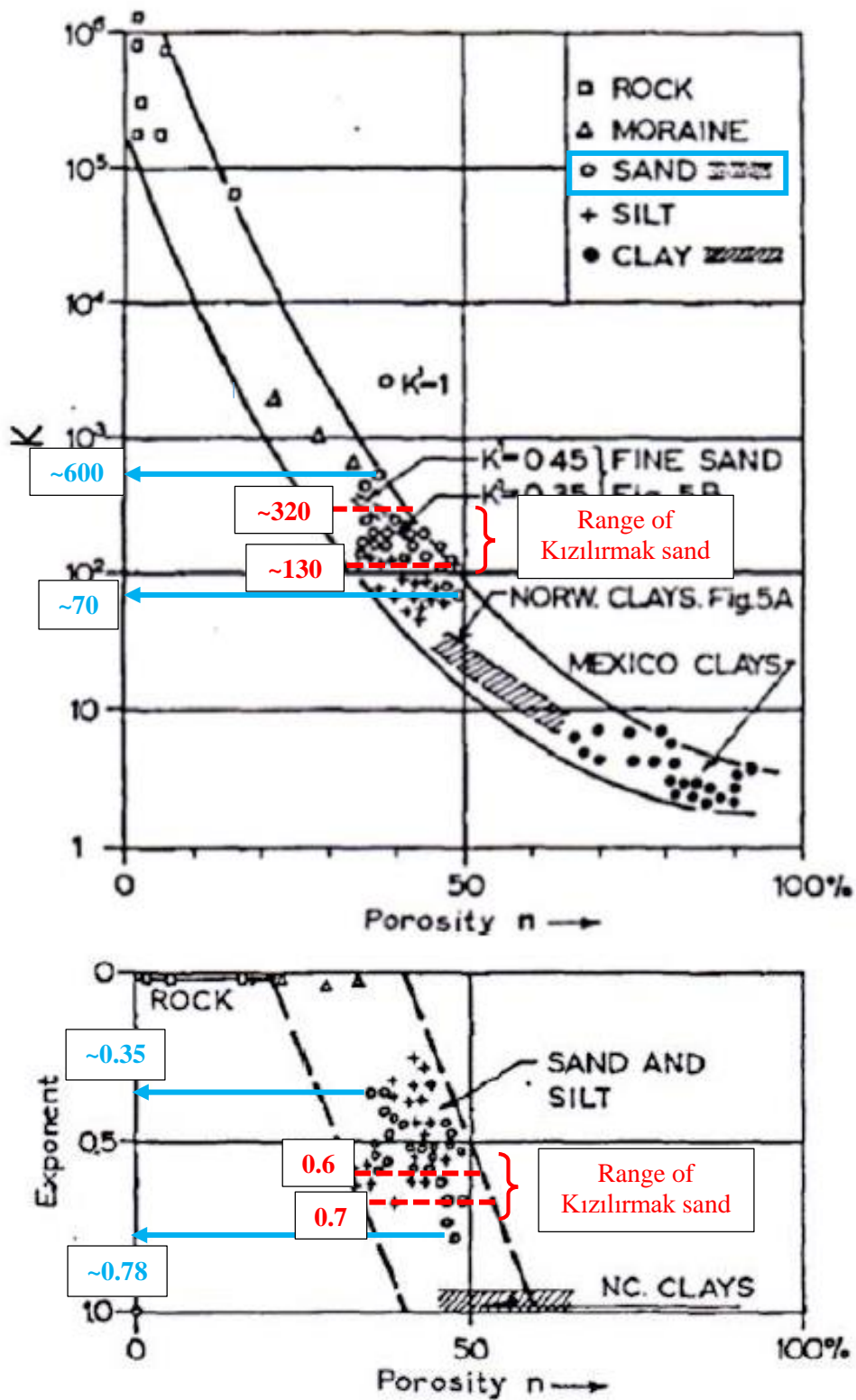
Figure 5.12. Modulus constant and exponent data for different soils (Janbu, 1963)

5.3. Nonlinear Elastic-Perfectly Plastic Model and It's Parameters

In this section, a nonlinear elastic-perfectly plastic constitutive model was attempted to be calibrated with triaxial test response of Kızılırmak sand. Kondner (1963) modeled the nonlinearity in stress-strain behavior by using a hyperbolic function as given in Eqn. 5-11.

$$(\sigma_1 - \sigma_3) = \frac{\varepsilon}{\dfrac{1}{E_i} + \dfrac{\varepsilon}{(\sigma_1 - \sigma_3)_{ult}}} \qquad \text{Eqn. 5-11}$$

where σ_1 and σ_3 are the major and minor principal stresses, ε is the axial strain, E_i is the initial tangent modulus.

Parameters which are used in this hyperbolic function have physical meanings, so that the hyperbolic approximation is suitable for modeling purposes. E_i is the initial tangent modulus or the slope of the initial part of the stress-strain plot. $(\sigma_1 - \sigma_3)_{ult}$ is the asymptotic stress. It is related to failure stress with a ratio of R_f (Duncan and Chang, 1970). The relation between deviatoric stress at failure and ultimate stress is given in Eqn. 5-12.

$$(\sigma_1 - \sigma_3)_f = R_f(\sigma_1 - \sigma_3)_{ult} \qquad \text{Eqn. 5-12}$$

Failure stress can be estimated by using the Mohr-Coulomb failure criterion, and all the other parameters can be obtained easily from conventional triaxial tests.

Nonlinear elastic-perfectly plastic model was fitted to the stress-strain plots obtained from triaxial test results performed on Kızılırmak sand. E_i was estimated from the linear part of the stress-strain graph. Mohr-Coulomb failure criterion was used as a failure criterion. R_f values were chosen as 0.7 for all experiments due to its good fit.

Stress-strain plots, along with nonlinear elastic-perfectly plastic model predictions, are presented in Figure 5.13 through Figure 5.17.
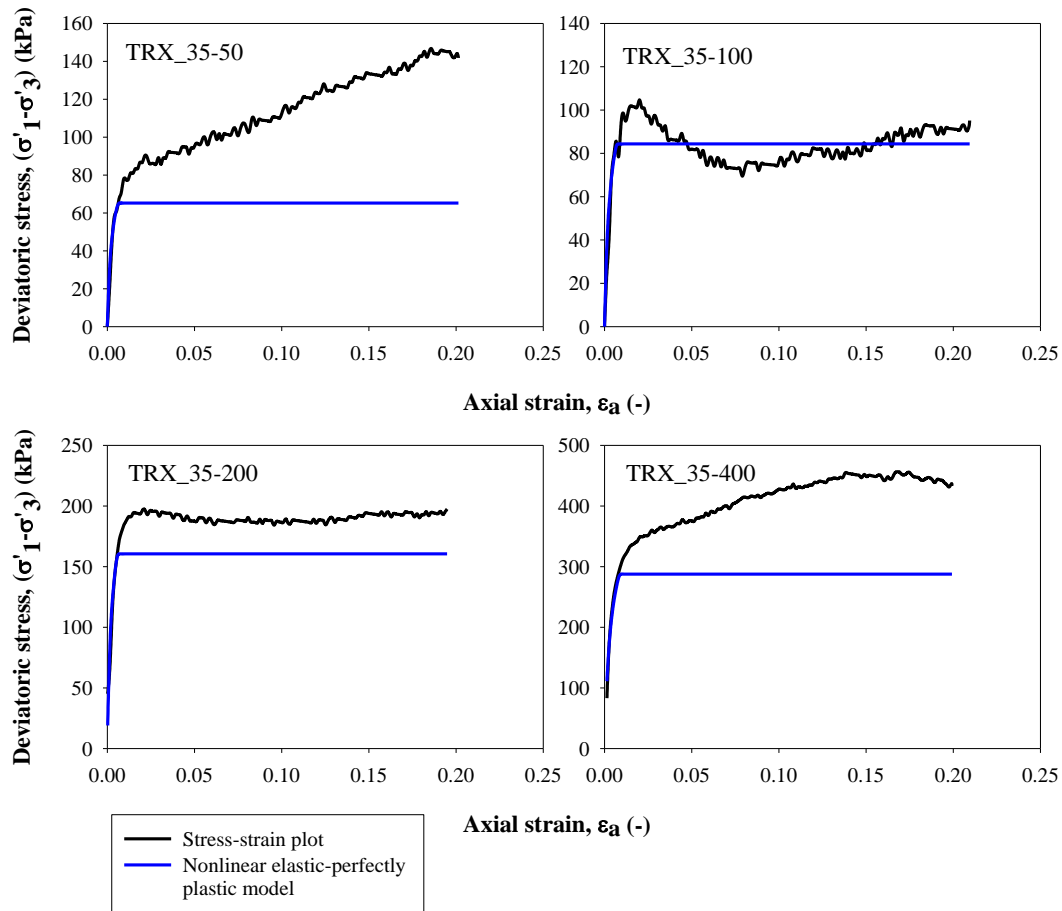
Figure 5.13. Stress-strain plots of the specimens prepared at ~35% relative density along with the nonlinear elastic-perfectly plastic model fit
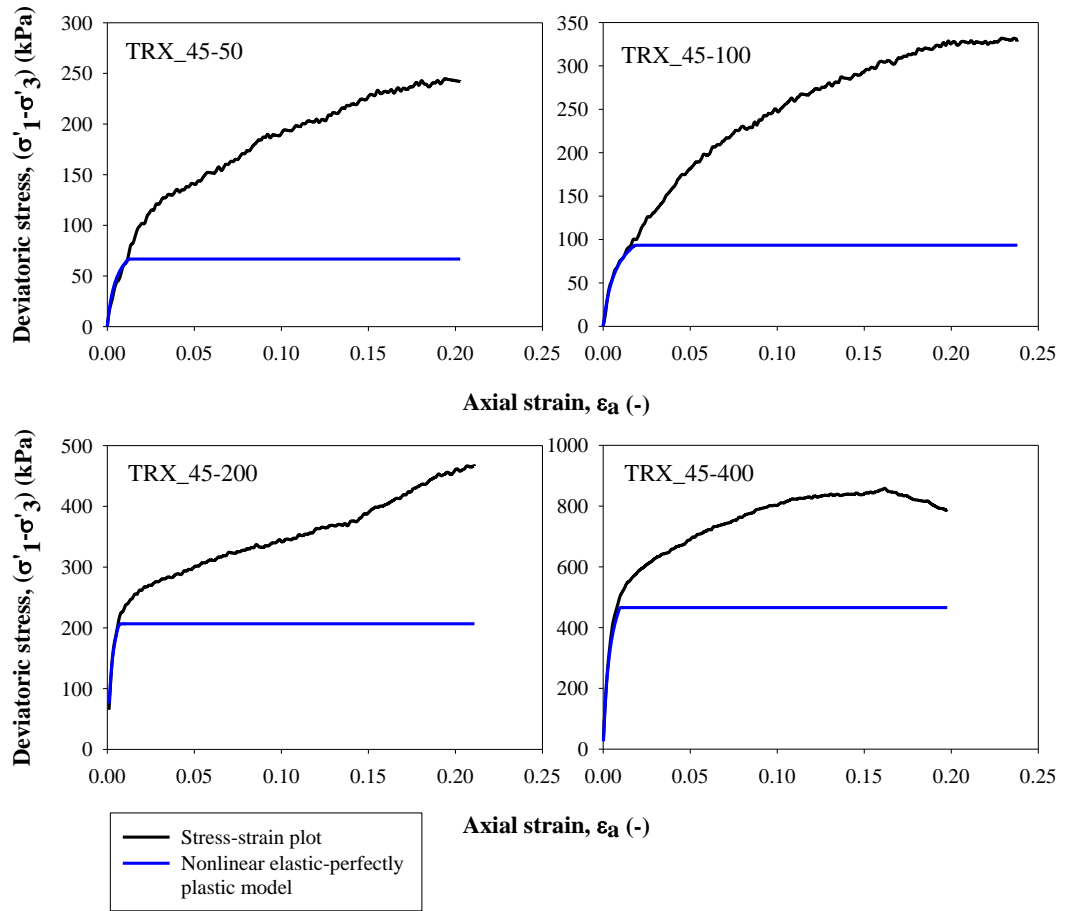
Figure 5.14. Stress-strain plots of the specimens prepared at ~45% relative density along with the nonlinear elastic-perfectly plastic model fit
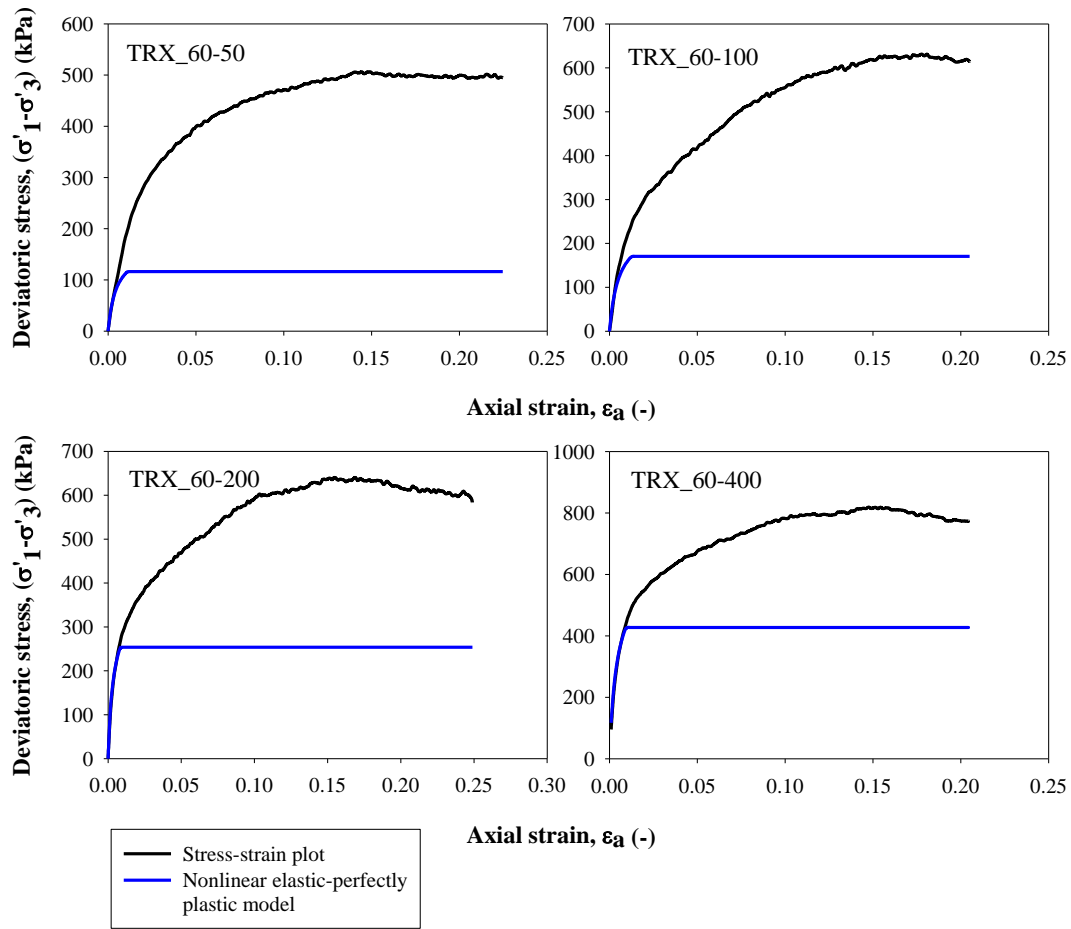
Figure 5.15. Stress-strain plots of the specimens prepared at ~60% relative density along with the nonlinear elastic-perfectly plastic model fit
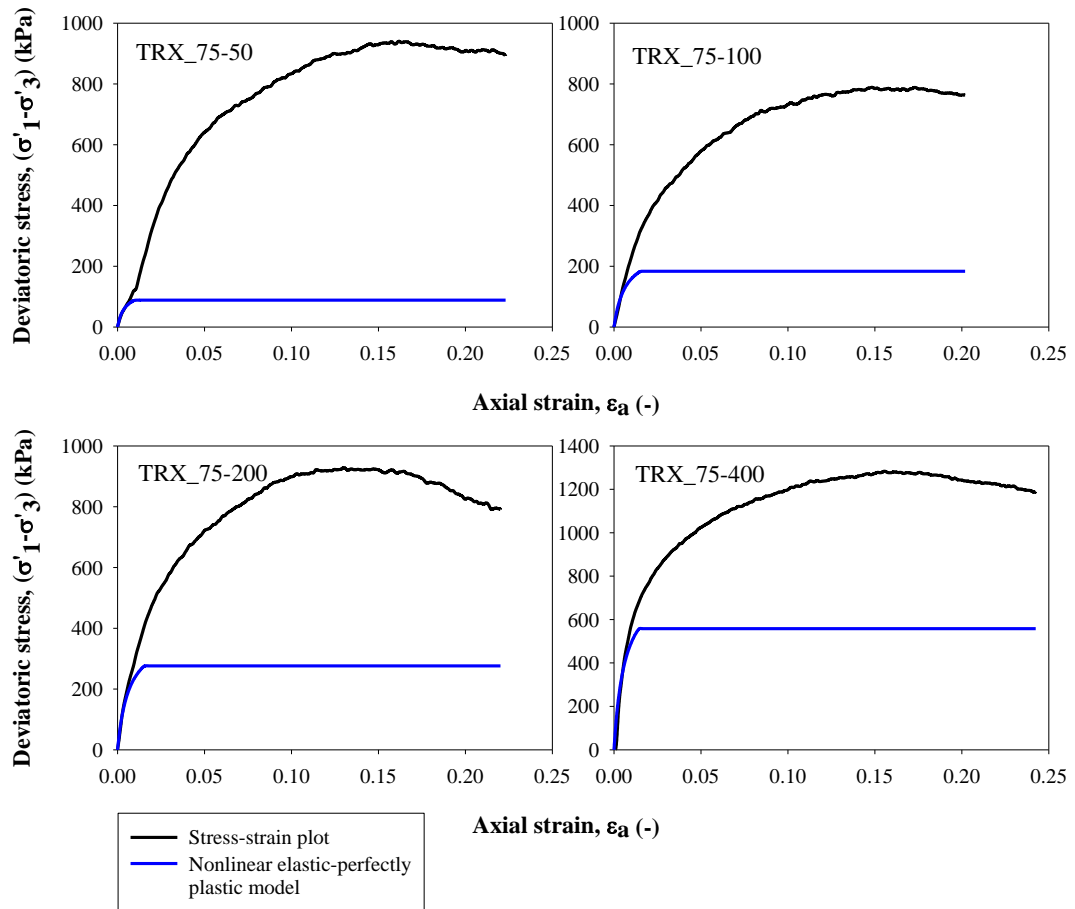
Figure 5.16. Stress-strain plots of the specimens prepared at ~75% relative density along with the nonlinear elastic-perfectly plastic model fit
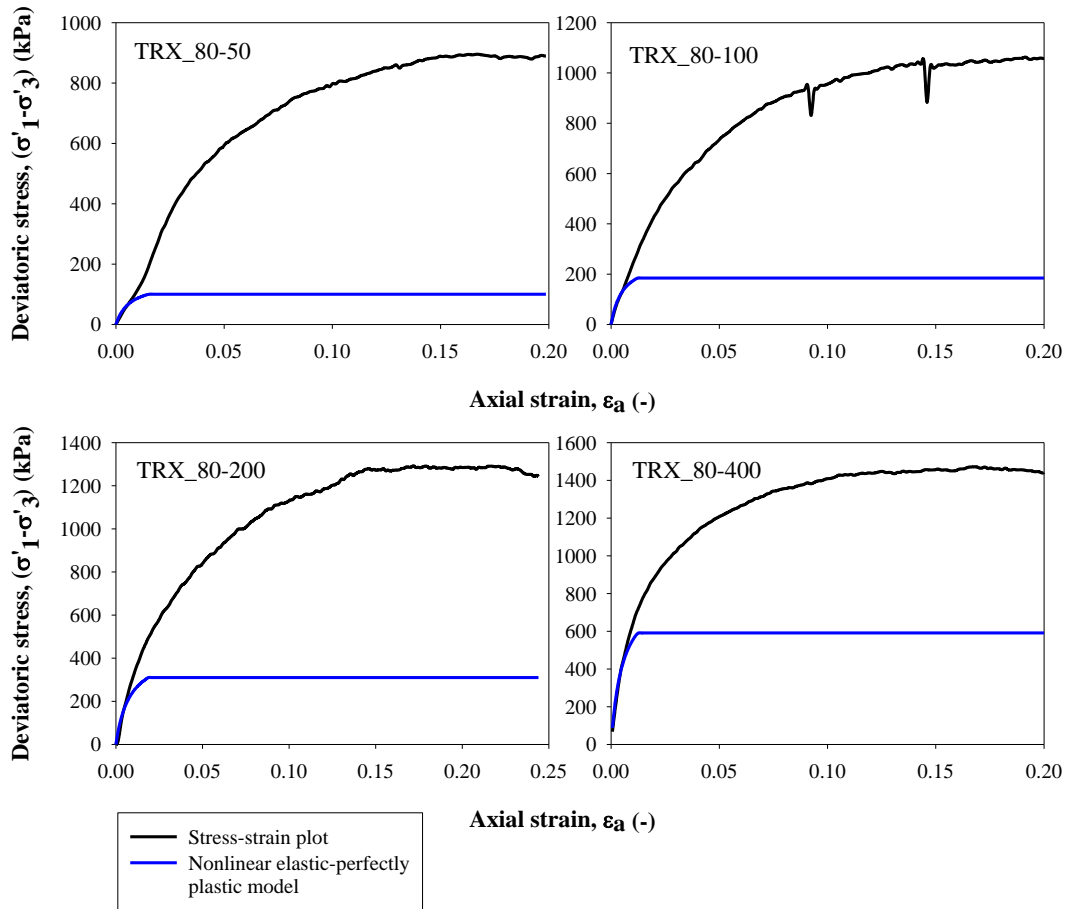
Figure 5.17. Stress-strain plots of the specimens prepared at ~80% relative density along with the nonlinear elastic-perfectly plastic model fit

On the basis of these stress-strain plots, it is understood that nonlinear elastic-perfectly plastic model mimics the response until failure in an unbiased manner. Unfortunately, due to dilative nature of Kızılırmak sand under studied stress and density states, perfectly plastic model is judged to be overly conservative to model post failure, valid for the stress and density states studied.

Similar to the implementation in the linear elastic modeling section, the power function was used for expressing a general $E_{TRX,H}$ modulus relation for Kızılırmak sand. The functional form consists of both void ratio and confining stress, as given in Eqn. 5-13.

$$E_{TRX;H} = (2.17 - e_0)^2/(1 + e_0)\, K p_a \left(\frac{\sigma_3'}{p_a}\right)^n \qquad \text{Eqn. 5-13}$$

where e_0 is the initial void ratio of the specimen, K is the modulus constant, n is the modulus exponent, p_a is the atmospheric pressure, σ_3' confining pressure.

K and n values were estimated as 340 and 0.7, respectively, for Kızılırmak sand. Initial modulus values, which were estimated from triaxial tests and the predictions by the proposed models are comparatively presented in Figure 5.18.
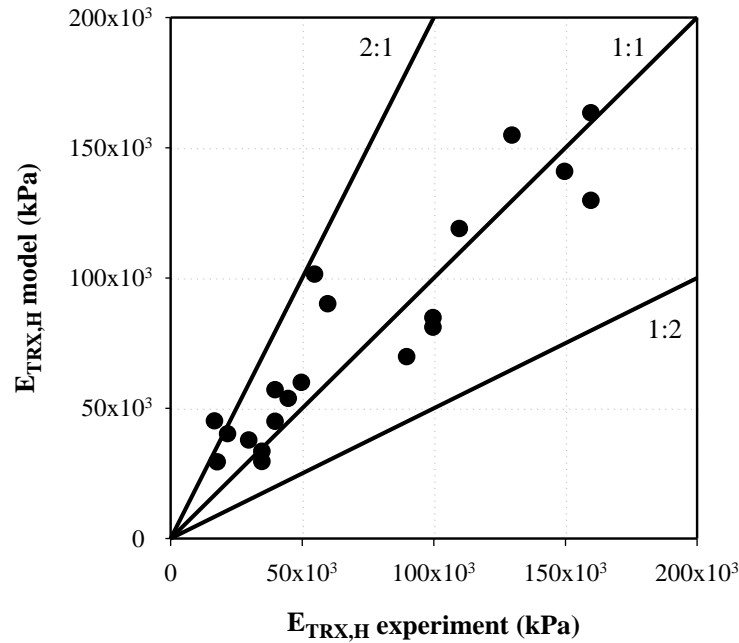
Figure 5.18. Model prediction vs. experimental results of $E_{TRX,H}$

Proposing a relation for the peak friction angle of Kızılırmak sand was attempted. While doing this, the functional form proposed by Wong and Duncan (1974) was used (Eqn. 5-14).

$$\phi = \phi_0 - \Delta\phi \log_{10}\left(\frac{\sigma_3}{p_a}\right) \qquad \text{Eqn. 5-14}$$

where ϕ_0 is the value of ϕ for σ_3 equal to p_a, $\Delta\phi$ is the reduction in ϕ for a 10-fold increase in σ_3, σ_3 is the confining pressure, p_a is the atmospheric pressure.

ϕ_0 was estimated from the relation between ϕ and relative density by using test results with σ_3=100 kPa. A power function for Kızılırmak sand was estimated for ϕ_0 as follows;

$$\phi_0 = 45.17 * RD^{0.224} \qquad \text{Eqn. 5-15}$$

where RD is the relative density.

$\Delta\phi$ value was determined as 1.5 by trial & error fitting procedure. Then the relation between friction angle and the confining pressure for Kızılırmak sand is as follows;

$$\phi = (45.17 * RD^{0.224}) - \Delta\phi \log_{10}\left(\frac{\sigma_3}{p_a}\right) \qquad \text{Eqn. 5-16}$$

where RD is the relative density, $\Delta\phi$ is the reduction in ϕ for a 10-fold increase in σ_3 (equals 1.5° for this study), σ_3 is the confining pressure, p_a is the atmospheric pressure.

Friction angle values, which were estimated from triaxial tests and calculated from the proposed relation are comparatively presented in Figure 5.19.
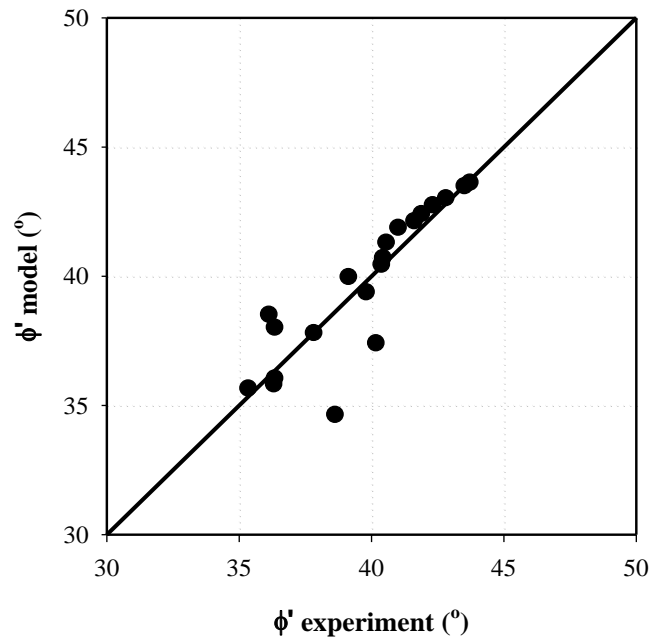
Figure 5.19. Model prediction vs. experimental results of ϕ'

A summary of the input parameters for nonlinear elastic-perfectly plastic constitutive model specific for Kızılırmak sand is presented in Table 5.2.

Table 5.2 Duncan and Chang (1970) hyperbolic model constants for Kızılırmak sand

K	340
n	0.7
c*	0
$\boldsymbol{\phi'}$	$(45.17 * RD^{0.224}) - \Delta\phi \log_{10}\left(\dfrac{\sigma_3}{p_a}\right)$
$\boldsymbol{\Delta\phi'}(°)$	1.5
R$_f$	0.7

*c=0 for clean sand

Wong and Duncan (1974) compiled modulus parameter data from literature and presented them in their study. This dataset shows that for sands K values are expected to vary in between 100-3100. Also, n and R$_f$ values fall in the rage of 0.23-0.77, and

0.62-0.96, respectively. Kızılırmak sand K and n values are judged to fall in the expected reasonable range suggested by Wong and Duncan (1974).

CHAPTER 6

SUMMARY AND CONCLUSIONS

6.1. Summary

Shearing and volumetric straining responses of local, Kızılırmak sand, were investigated with the intent to introduce a new "standard sand" to the literature from Turkey. Index, shear strength and stiffness parameters were studied and estimated.

Kızılırmak sand was classified as a poorly graded sand (SP) according to USCS, and its specific gravity was estimated as 2.65. Similarly, the minimum and the maximum void ratios were estimated as 0.45 and 0.80, respectively.

20 consolidated undrained triaxial tests were performed to assess shearing response of Kızılırmak sand. In these triaxial tests, reconstituted specimens were prepared at 35-45-60-75-80 % relative densities, and consolidated to 50-100-200-400 kPa cell pressures.

7 oedometer tests were performed to examine one-dimensional response of Kızılırmak sand. In these tests, reconstituted specimens were prepared at 25-35-45-60-75-80-85 % relative densities and they were loaded up to an axial stress of ~33.5 MPa. It was observed that yield stresses of specimens varied in the range of 2.1-4.0 MPa.

Linear elastic and nonlinear elastic-perfectly plastic constitutive modeling parameters were developed based on triaxial test results. Additionally, other constitutive modeling and critical state parameters were determined specifically for Kızılırmak sand. These and major conclusions of the study will be discussed next.

6.2. Conclusions

The major findings of this study are listed in Table 6.1 through Table 6.5.

Table 6.1 Index properties, particle morphology and mineralogy of Kızılırmak sand

Specific Gravity, G_s	2.65
e_{min}	0.45
e_{max}	0.80
D_{50}	1.20
Coefficient of uniformity, C_u	6.87
Coefficient of curvature, C_c	0.86
Sphericity, S	0.60
Roundness, R	0.26
Dominant mineral	Quartz

Table 6.2 Critical / Steady state characteristics of Kızılırmak sand

Steady state / Critical state friction angle, ϕ' (˚)	*Angularity calculations (Cho et al., 2006)*	*TRX Steady state calculations*	*State parameter approach*
	37.0˚-38.0˚	39.4˚	37.8˚
λ	0.070		
Γ	0.975		

Table 6.3 Mechanical properties of Kızılırmak sand

	~35% RD (N_{1,60}≈5*)	~45% RD (N_{1,60}≈8*)	~60% RD (N_{1,60}≈15*)	~75% RD (N_{1,60}≈23*)	~80% RD (N_{1,60}≈26*)
Peak friction angle, ϕ' (°)	36.5° - 39.0°	36.0° - 40.0°	39.5° - 40.5°	40.5° - 42.5°	42.0° - 44.0°
Yield stress, σ'_y (MPa)	~2.15	~2.70	~3.40	~3.80	~3.95
σ'_v ($C_{C,max}$) (MPa)	~8.1	~14.6	~14.6	~14.6	~14.6
$C_{C,max}$	~0.190-0.206	~0.200	~0.162	~0.123	~0.111-0.113
C_α/C_C	~0.027-0.030	~0.031	~0.032	~0.035	~0.033-0.037

Normalized SPTN values to σ'_v=100 kPa (Meyerhof, 1957)

Table 6.4 Triaxial modulus relationships proposed for linear elastic-perfectly plastic models

	K	n	R^2
$E_{TRX} = KP_a\left(\dfrac{\sigma'_3}{P_a}\right)^n$	285	0.7	0.86
$E_{TRX} = KP_a\left(\dfrac{p'}{P_a}\right)^n$	323	0.6	0.44
$E_{TRX} = [(2.17 - e_0)^2/(1 + e_0)]KP_a\left(\dfrac{\sigma'_3}{P_a}\right)^n$	183	0.7	0.80
$E_{TRX} = [e^{-1.3}]KP_a\left(\dfrac{\sigma'_3}{P_a}\right)^n$	143	0.7	0.78
$E_{TRX} = [(2.17 - e_c)^2/(1 + e_c)]KP_a\left(\dfrac{p'}{P_a}\right)^n$	173	0.7	0.58
$E_{TRX} = [e^{-1.3}]KP_a\left(\dfrac{p'}{P_a}\right)^n$	134	0.7	0.55

Table 6.5 Duncan and Chang (1970) nonlinear elastic-perfectly plastic model's parameters

K	340
n	0.7
c^*	0
ϕ'	$(45.17 * RD^{0.224}) - \Delta\phi \log_{10}\left(\dfrac{\sigma_3}{p_a}\right)$
$\Delta\phi'(°)$	1.5
R_f	0.7

*c=0 for clean sand

Due to the dilative nature of Kızılırmak sand under studied stress and density states, perfectly plastic models are judged to be overly conservative to model post failure. Hence, they are not recommended to assess the response of Kızılırmak sand in an unbiased manner.

At low stress levels, the stiffness of Kızılırmak sand increases with increasing confining stresses. After ~6.5-8.0 MPa vertical stress levels, stiffness stays constant with increasing effective vertical stress. This constant stiffness range ended up at ~8.0-14.5 MPa stress levels. Then, the stiffness starts to increase with increasing stresses. Therefore, Kızılırmak sand is classified as a soil, which exhibits Type B volumetric straining response. As a reminder Type B volumetric straining illustration is given in Figure 6.1.
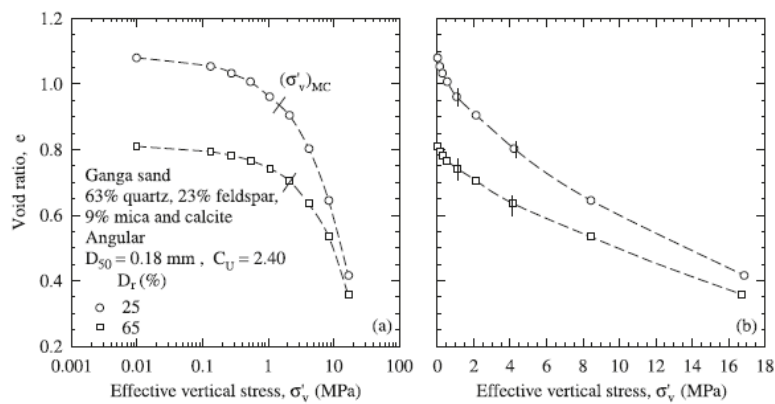
Figure 6.1. Type B volumetric straining response (Mesri and Vardhanabhuti, 2009)

The gradation of Kızılırmak sand changes with increasing vertical stresses due to particle crushing. Table 6.6 summarizes this change. As a reminder, note that the first three rows in Table 6.6 simply designates the vertical shift in the particle size gradation curves at 33.5 MPa. The last row, however presents the ratio of D_{15} before and after testing.

Table 6.6 Grain size distribution shift after particle breakage

	OED_25	OED_35	OED_45	OED_60	OED_75	OED_80	OED_85	average
Leslie, 1963 (%)	3.1	3.3	3.1	2.9	2.5	2.1	1.9	2.7
Leslie, 1975 (%)	4.3	5.9	5.9	8.3	5.3	5.1	1.4	5.2
Marsal, 1965 (%)	3.7	5.2	5.2	8.7	5.1	4.6	1.9	4.9
Lee and Farhoomand, 1967 (-)	1.180	1.307	1.297	1.450	1.251	1.242	0.991	1.246

Similarly in Table 6.7, the shifts in grain size distributions are presented for the sample with relative density 35 % and subjected to 4.5, 17.1 and 33.5 MPa vertical stresses. This table also illustrates Kızılırmak sand becoming finer with increasing vertical stresses and more pronounced particle crushing.

Table 6.7 Grain size distribution shift for the specimen prepared at 35% relative density and subjected to vertical stresses of 4.5, 17.1 and 33.5 MPa

	4.5 MPa	17.1 MPa	33.5 MPa
Leslie, 1963 (%)	0.1	1.3	3.3
Leslie, 1975 (%)	1.2	1.6	5.9
Marsal, 1965 (%)	1.3	1.3	5.2
Lee and Farhoomand, 1967 (-)	1.019	1.025	1.307

Figure 6.2 presents the increase in compression index with increasing effective vertical stresses up to 8-14 MPa. Beyond these stresses, an increase in stiffness (also a decrease in C_c values) response is observed, which is consistent with similar sands

studied in the literature (Mesri and Vardhanabhuti, 2009). In Figure 6.2, the test results for compression pressures less than 100 kPa were filtered out.
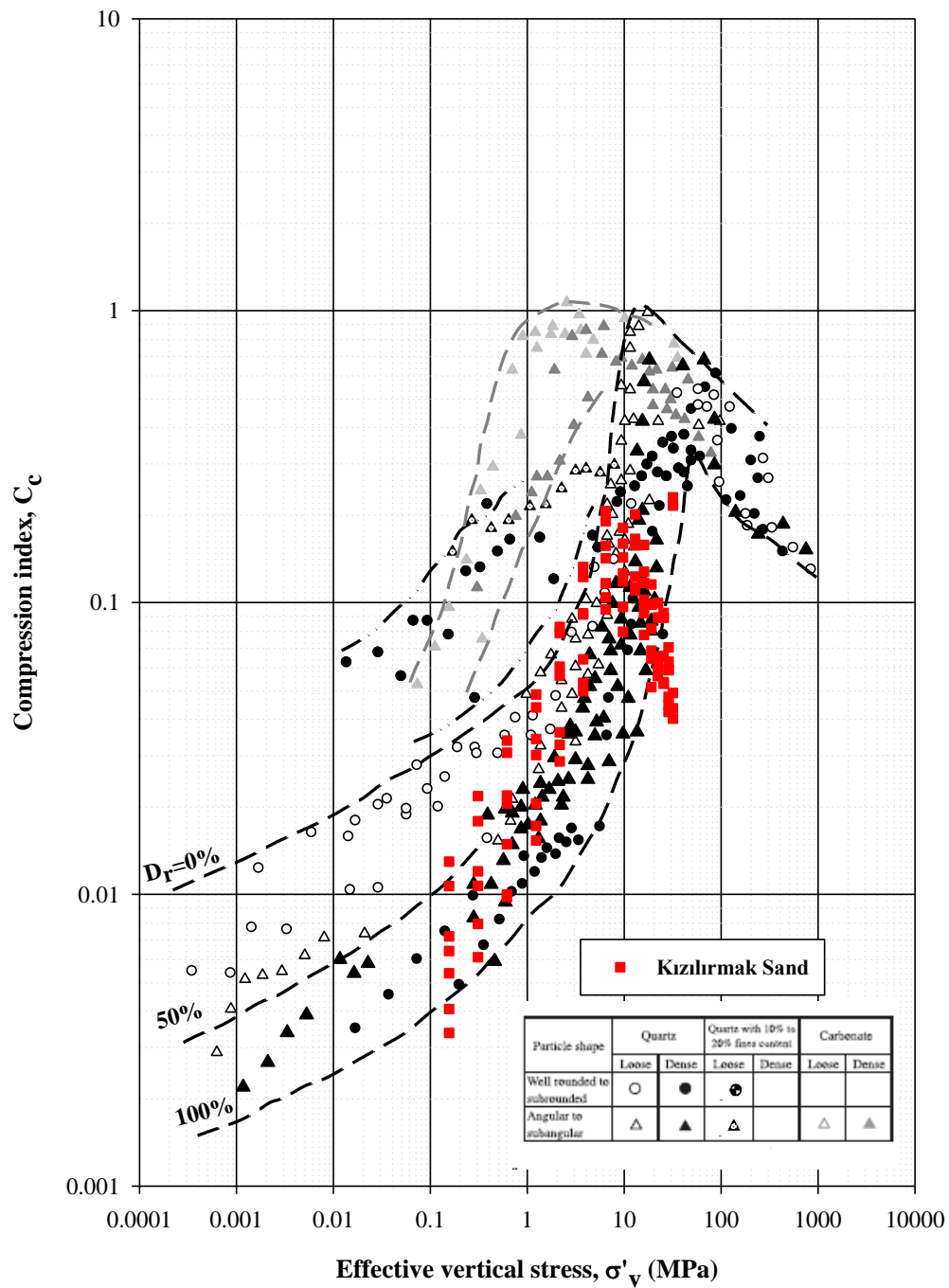
Figure 6.2. Comparison of the compression index of Kızılırmak sand with Mesri and Vardhanabhuti (2009) database

In Figure 6.3, characteristic curves useful for critical state-based assessments of Kızılırmak sand are presented. Isotropic compression lines corresponding to the loosest and the densest states are shown. Additionally, the initial dividing line, which differentiates the strain hardening and softening responses, are also illustrated. These curves are useful to assess the pore pressure and volumetric straining compression during drained and undrained loading, which in turn governs overall stress-strain responses. Additionally, in Figure 6.4, comparison of characteristic curves of Kızılırmak sand and Toyoura sand is presented.
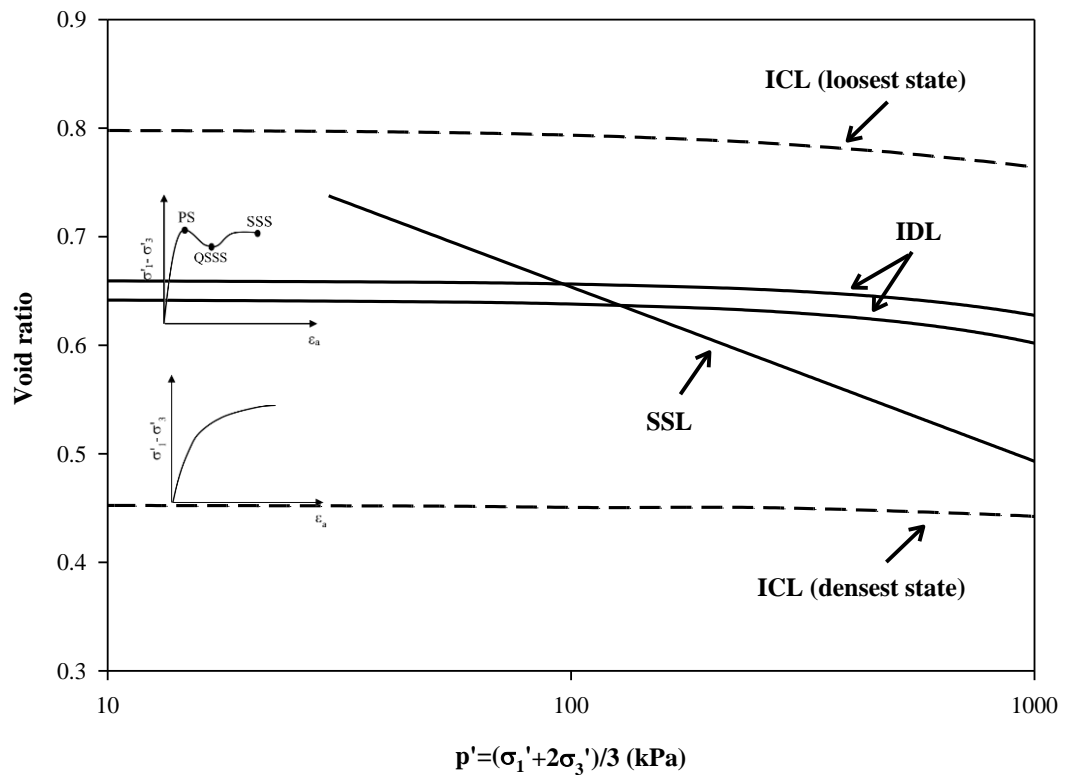
Figure 6.3. ICL, IDL, and SSL of Kızılırmak sand specimens
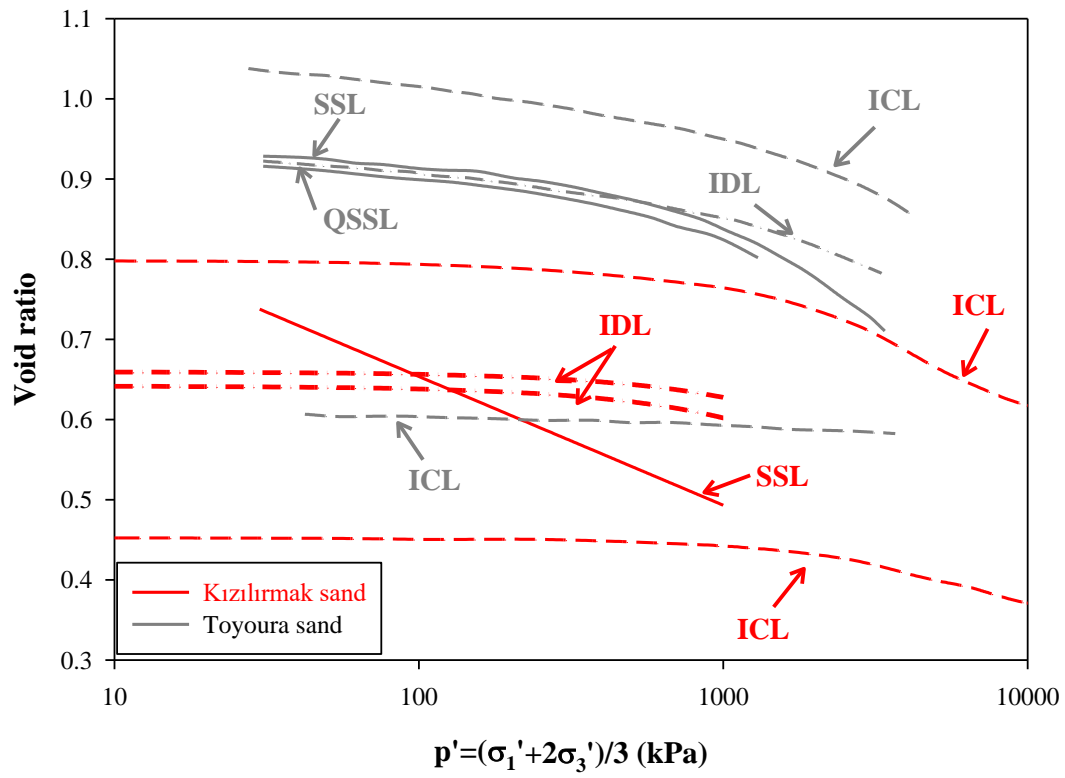
Figure 6.4. Comparison of characteristic curves of Kızlırmak sand and Toyoura sand

6.3. Future Works

In this study, the conclusions were listed based on consolidated undrained triaxial and one-dimensional oedometer tests, which were loaded up to a maximum stress level of ~33.5 MPa. Experiments with different failure modes and boundary conditions, using simple shear or torsional shear apparatus, and compression or extension loading schemes are recommended to be performed on Kızılırmak sand to test the uniqueness of the parameters presented herein. Additionally, one-dimensional compression tests may be repeated under higher stress levels.

Angularity calculations were performed in 2-D space. 3-D assessments may be performed to improve the accuracy of results. Besides, a more detailed assessment can be performed regarding the mineralogy of Kızılırmak sand.

Since Kızılırmak sand is angular, and shows dilative response, it hardens with shear straining. Therefore, linear-elastic and nonlinear elastic perfectly plastic models are not adequate to model Kızılırmak sand's post failure shearing behavior. Alternatively, strain hardening/softening constitutive models can be considered for an improved modeling of Kızılırmak sand's shearing response.

Last but not least, a Kızılırmak sand specific constitutive model, addressing particle yielding at larger stress levels for the assessment of shear and volumetric straining responses, are recommended to be developed.

REFERENCES

Alarcon-Guzman, A., Leonards, G. A. and Chameau, J. L. (1988) 'Undrained monotonic and cyclic strength of sands', *Journal of Geotechnical Engineering*, 114(10). doi: 10.1061/(ASCE)0733-9410(1988)114:10(1089).

Alshibli, K. A. and Alsaleh, M. I. (2004) 'Characterizing surface roughness and shape of sands using digital microscopy', *Journal of Computing in Civil Engineering*, 18(1). doi: 10.1061/(ASCE)0887-3801(2004)18:1(36).

Alshibli, K. A. and Cil, M. B. (2018) 'Influence of particle morphology on the friction and dilatancy of sand', *Journal of Geotechnical and Geoenvironmental Engineering*, 144(3). doi: 10.1061/(ASCE)GT.1943-5606.0001841.

Altomare, A. *et al.* (2015) 'QUALX2.0: A qualitative phase analysis software using the freely available database POW-COD', *Journal of Applied Crystallography*. International Union of Crystallography, 48, pp. 598–603. doi: 10.1107/S1600576715002319.

Altuhafi, F. N. and Coop, M. R. (2011) 'The effect of mode of loading on particle-scale damage', *Soils and Foundations*, 51(5). doi: 10.3208/sandf.51.849.

Andersen, K. H. and Schjetne, K. (2013) 'Database of friction angles of sand and consolidation characteristics of sand, silt, and clay', *Journal of Geotechnical and Geoenvironmental Engineering*, 139(7). doi: 10.1061/(ASCE)GT.1943-5606.0000839.

ASTM International (2011a) 'D2435/D2435M − 11 Standard one-dimensional consolidation properties of soils using incremental loading', *ASTM Standards*. doi: 10.1520/D2435.

ASTM International (2011b) 'D4767−11 Standard test method for consolidated undrained triaxial compression test for cohesive soils', *ASTM Standards*. doi: 10.1520/D4767-11.2.

ASTM International (2014) 'D854-14 Standard test methods for specific gravity of soil solids by water pycnometer', *ASTM Standards*. doi: 10.1520/D0854-10.2.

ASTM International (2016) 'D4254−16 Standard test methods for minimum index density and unit weight of soils and calculation of relative density', *ASTM Standards*. doi: https://doi.org/10.1520/D4253-16E01.

ASTM International (2017) 'D6913-D6913M-17 Standard test methods for particle-size distribution (gradation) of soils using sieve analysis', *ASTM Standards*. doi: 10.1520/D6913-04R09.2.

Atkinson, J. (2007) *The mechanics of soils and foundations*. Available at: https://books.google.com/books?hl=en&lr=&id=KRR34SOOUNAC&oi=fnd&pg=PP1&dq=The+Mechanics+of+Soils+and+Foundations+atkinson&ots=y3KMX_JHjB&sig=m5-QvqW6i8EZH--4lhO1YKA4YUI (Accessed: 5 September 2020).

Atkinson, J. H. (2000) 'Non-linear soil stiffness in routine design', *Geotechnique*, 50(5). doi: 10.1680/geot.2000.50.5.487.

Atkinson, J. H. and Sallfors, G. (1991) 'Experimental determination of stress-strain-time characteristics in laboratory and in situ tests', in *Proceedings of the International Conference on Soil Mechanics and Foundation Engineering*.

Baldi, G. *et al.* (1990) 'Modulus of sands from CPT's and DMT's', *Proc. 12th international conference on soil mechanics and foundation engineering, Rio de Janeiro, 1989. Vol. 1*. doi: 10.1016/0148-9062(91)93491-n.

Barden, L., Ismail, H. and Tong, P. (1969) 'Plane strain deformation of granular material at low and high pressures', *Geotechnique*, 19(4). doi: 10.1680/geot.1969.19.4.441.

Been, K., Hachey, J. and Jefferies, M. G. (1991) 'The critical state of sands', *Geotechnique*, 41(3). doi: 10.1680/geot.1991.41.3.365.

Been, K. and Jefferies, M. G. (1985) 'A state parameter for sands', *Geotechnique*, 35(2). doi: 10.1680/geot.1985.35.2.99.

De Beer, E. E. (1963) 'The scale effect in the transposition of the results of deep-sounding tests on the ultimate bearing capacity of piles and caisson foundations', *Geotechnique*, 13(1). doi: 10.1680/geot.1963.13.1.39.

Benz, T. (2007) 'Small-strain stiffness of soils and its numerical consequences'.

Biarez, J. and Hicher, P. (1994) *Elementary mechanics of soil behaviour: saturated remoulded soils.* Available at: https://www.cabdirect.org/cabdirect/abstract/19951904796 (Accessed: 1 October 2020).

Bilge, H. (2005) 'Volumetric and deviatoric strain behavior of cohesionless soils under cyclic loading'.

Bishop, A. W. (1966) 'The strength of soils as engineering materials', *Géotechnique*, 16(2). doi: 10.1680/geot.1966.16.2.91.

Bishop, A. W. (1972) 'Shear strength parameters for undisturbed and remolded soil specimens', in *Roscoe Memorial Symp.*, pp. 3–58.

Bolton, M. D. (1986) 'The strength and dilatancy of sands', *Geotechnique*, 36(1). doi: 10.1680/geot.1986.36.1.65.

Casagrande, A. (1963) 'The determination of pre-consolidation load and it's practical significance', in *Proc. Int. Conf. Soil Mech. Found. Eng. Cambridge, Mass.* Available at: https://ci.nii.ac.jp/naid/10018165483/ (Accessed: 5 September 2020).

Castro, G. (1975) 'Liquefaction and cyclic mobility of saturated sands', *ASCE J Geotech Eng Div*, 101(6).

Castro, G. and Poulos, S. J. (1977) 'Factors affecting liquefaction and cyclic mobility', *ASCE J Geotech Eng Div*, 103(6).

Cho, G. C., Dodds, J. and Santamarina, J. C. (2006) 'Particle shape effects on packing density, stiffness, and strength: Natural and crushed sands', *Journal of Geotechnical and Geoenvironmental Engineering*, 132(5). doi: 10.1061/(ASCE)1090-0241(2006)132:5(591).

Chuhan, F. A. *et al.* (2002) 'Porosity loss in sand by grain crushing - Experimental evidence and relevance to reservoir quality', *Marine and Petroleum Geology*, 19(1). doi: 10.1016/S0264-8172(01)00049-6.

Chuhan, F. A. *et al.* (2003) 'Experimental compression of loose sands: Relevance to porosity reduction during burial in sedimentary basins', *Canadian Geotechnical Journal*, 40(5). doi: 10.1139/t03-050.

Coop, M. R. (1990) 'The mechanics of uncemented carbonate sands', *Geotechnique*, 40(4). doi: 10.1680/geot.1990.40.4.607.

Coop, M. R. (1993) 'The behaviour of granular soils at elevated stresses', *Predictive soil mechanics. Proc. of the Wroth memorial symposium, Oxford, 1992*.

Cornforth, D. H. (1973) *Prediction of Drained Strength of Sands from Relative Density Measurements*. Available at: www.astm.org (Accessed: 4 September 2020).

Cubrinovski, M. and Ishihara, K. (1998) 'State concept and modified elastoplasticity for sand modelling', *Soils and Foundations*, 38(4). doi: 10.3208/sandf.38.4_213.

Cundall, P. A. and Strack, O. D. L. (1979) 'A discrete numerical model for granular assemblies', *Geotechnique*, 29(1). doi: 10.1680/geot.1979.29.1.47.

Duncan, J. M. and Chang, C. Y. (1970) 'Nonlinear analysis of stress and strain in soils', *Journal of Soil Mechanics & Foundations Div*.

Hagerty, M. M. *et al.* (1993) 'One-dimensional high-pressure compression of granular media', *Journal of Geotechnical Engineering*, 119(1). doi: 10.1061/(ASCE)0733-9410(1993)119:1(1).

Hardin, B. O. (1985) 'Crushing of soil particles', *Journal of Geotechnical Engineering*, 111(10). doi: 10.1061/(ASCE)0733-9410(1985)111:10(1177).

Hardin, B. O. and Black, W. L. (1969) 'Closure to: Vibration modulus of normally consolidated clays', *J. Journal of Soil Mechanics and Foundation Division, ASCE,* 95(6). doi: 10.1186/s13287-017-0683-2.

Hardin, B. and Richart, F. (1963) 'Elastic wave velocities in granular soils', *Journal of the Soil Mechanics and Foundations Division*, 89(1).

Houlsby, G. T. (1991) 'How the dilatancy of soils affects their behaviour -done', *International Proceedings of the 10th European Conference on Soil Mechanics and Foundation Engineering*.

Ishihara, K. (1993) 'Liquefaction and flow failure during earthquakes', *Geotechnique*, 43(3). doi: 10.1680/geot.1993.43.3.351.

Ishihara, K. (1996) *Soil behaviour in earthquake geotechnics*. New York: Oxford University Press Inc.

Janbu, N. (1963) 'Soil compressibility as determined by odometer and triaxial tests', in *Proc. Europ. Conf. SMFE*, pp. 19–25.

Jefferies, M. and Been, K. (2006) *Soil Liquefaction*. Abingdon, UK: Taylor & Francis. doi: 10.4324/9780203301968.

Kang, X. *et al.* (2019) 'The critical state and steady state of sand: A literature review', *Marine Georesources and Geotechnology*, 37(9). doi: 10.1080/1064119X.2018.1534294.

Koener, R. (1968) ''The behavior of cohesionless materials formed from various materials'.

Kondner, R. L. (1963) 'A hyperbolic stress-strain formulation for sands', in *Proc. 2 nd Pan Am. Conf. on Soil Mech. and Found. Eng.* Brazil, pp. 289–324.

Krumbein, W. C. and Sloss, L. L. (1963) *Stratigraphy and sedimentation*. San Francisco: H Freeman and Company.

Kwag, J. M., Ochiai, H. and Yasufuku, N. (1999) 'Yield stress characteristics of carbonate sand in relation to individual particle fragmentation strength', in *Engineering for Calcareous Sediments*.

Ladd, R. S. (1978) 'Preparing test specimens using undercompaction', *Geotechnical Testing Journal*, 1(1), pp. 16–23.

Lade, P. V. and Liu, C. T. (1998) 'Experimental study of drained creep behavior of sand', *Journal of Engineering Mechanics*, 124(8). doi: 10.1061/(ASCE)0733-9399(1998)124:8(912).

Lade, P. V. and Nelson, R. B. (1987) 'Modelling the elastic behaviour of granular materials', *International Journal for Numerical and Analytical Methods in Geomechanics*, 11(5). doi: 10.1002/nag.1610110507.

Lade, P. V., Yamamuro, J. A. and Bopp, P. A. (1996) 'Significance of particle crushing in granular materials', *Journal of Geotechnical Engineering*, 122(4). doi: 10.1061/(asce)0733-9410(1996)122:4(309).

Lambe, T. W. and Whitman, R. V. (1969) *Soil mechanics*. New York: John Willey & Sons. Inc.

Lee, K. L. and Farhoomand, I. (1967) 'Compressibility and crushing of granular soil in anisotropic triaxial compression', *Canadian Geotechnical Journal*, 4(1). doi: 10.1139/t67-012.

Leslie, D. D. (1963) 'Large scale triaxial tests on gravelly soils', in *Proceedings of the 2nd Panamerican Conference on Soil Mechanics and Foundation Engineering*. Brazil, pp. 181–202.

Leslie, D. D. (1975) *Shear strength of rockfill*. California.

Mair, R. J. (1993) 'Developments in geotechnical engineering research: application to tunnels and deep excavations', in *Proceedings of Institution of Civil Engineers: Civil Engineering*, pp. 27–41.

Marsal, R. J. (1965) 'Discussion of Shear Strength', in *Proceedings of the 6th International Conference on Soil Mechanics and Foundaiton Engineering*. Montreal, pp. 310–316.

Marsal, R. J. (1967) 'Large scale testing of rockfill materials', *Journal of Soil Mechanics and Foundations Division, ASCE*, 93(SM2).

McDowell, G. R. and Bolton, M. D. (1998) 'On the micromechanics of crushable aggregates', *Geotechnique*, 48(5). doi: 10.1680/geot.1998.48.5.667.

McDowell, G. R., Bolton, M. D. and Robertson, D. (1996) 'The fractal crushing of granular materials', *Journal of the Mechanics and Physics of Solids*, 44(12). doi: 10.1016/S0022-5096(96)00058-0.

McDowell, G. R. and Harireche, O. (2002) 'Discrete element modelling of yielding and normal compression of sand', *Geotechnique*, 52(4). doi: 10.1680/geot.2002.52.4.299.

Mesri, G. *et al.* (1981) 'Shear stress-strain-time behaviour of clays', *Géotechnique*. Thomas Telford Ltd , 31(4), pp. 537–552. doi: 10.1680/geot.1981.31.4.537.

Mesri, G. and Vardhanabhuti, B. (2009) 'Compression of granular materials', *Canadian Geotechnical Journal*, 46(4). doi: 10.1139/T08-123.

Meyerhof, G. G. (1957) 'Discussion on research on determining the density of sands by penetration testing', in *Proc. 4th Int. Conf. on Soil Mech. And Found. Engrg.*

Miao, G. and Airey, D. (2013) 'Breakage and ultimate states for a carbonate sand', *Geotechnique*, 63(14). doi: 10.1680/geot.12.P.111.

211

Murayama, S. (1983) 'Formulation of stress-strain-time behavior of soils under deviatoric stress condition', *Soils and Foundations*, 23(2). doi: 10.3208/sandf1972.23.2_43.

Murayama, S., Michihiro, K. and Sakagami, T. (1984) 'Creep characteristics of sands', *Soils and Foundations*, 24(2). doi: 10.3208/sandf1972.24.2_1.

Nakata, Y., Hyodo, M., *et al.* (2001) 'Microscopic particle crushing of sand subjected to high pressure one-dimensional compression', *Soils and Foundations*, 41(1). doi: 10.3208/sandf.41.69.

Nakata, Y., Kato, Y., *et al.* (2001) 'One-dimensional compression behaviour of uniformly graded sand related to single particle crushing strength', *Soils and Foundations*, 41(2). doi: 10.3208/sandf.41.2_39.

Pestana, J. M. and Whittle, A. J. (1995) 'Compression model for cohesionless soils', *Geotechnique*, 45(4). doi: 10.1680/geot.1995.45.4.611.

Poulos, S. J. (1981) 'The steady state of deformation.', *Journal of the Geotechnical Engineering Division, ASCE*, 107(GT5, Proc. Paper, 16241).

Rahim, A. (1989) 'Effect of morphology and mineralogy on compressibility of sands'.

Roberts, J. (1965) 'Sand compression as a factor in oil field subsidence.' Available at: https://dspace.mit.edu/bitstream/handle/1721.1/13626/24228445-MIT.pdf?sequence=2 (Accessed: 5 September 2020).

Roberts, J. E. and de Souza, J. M. (1958) 'The compressibility of sands', *Proceedings of the American Society of Testing and Materials*, 58.

Roscoe, K. H., Schofield, A. N. and Wroth, C. P. (1958) 'On the yielding of soils', *Geotechnique*, 8(1). doi: 10.1680/geot.1958.8.1.22.

Rowe, P. W. (1962) 'The stress-dilatancy relation for static equilibrium of an assembly of particles in contact', *Proceedings of the Royal Society of London. Series A. Mathematical and Physical Sciences*, 269(1339). doi: 10.1098/rspa.1962.0193.

Schofield, A. and Wroth, P. (1968) *Critical state soil mechanics*, *Engineer*.

Stroud, M. (1971) 'The behaviour of sand at low stress levels in the simple-shear apparatus'. Available at: https://www.repository.cam.ac.uk/handle/1810/265294 (Accessed: 4 September 2020).

Takei, M., Kusakabe, O. and Hayashi, T. (2001) 'Time-dependent behavior of crushable materials in one-dimensional compression tests', *Soils and Foundations*, 41(1). doi: 10.3208/sandf.41.97.

Tatar, H. M. (2018) *Consolidated undrained shearing response of hydrophobic sands*.

Taylor, D. (1948) *Fundamentals of soil mechanics*. Available at: https://journals.lww.com/soilsci/Citation/1948/08000/Fundamentals_of_Soil_Mechanics.8.aspx (Accessed: 4 September 2020).

Vaid, Y. P., Chern, J. C. and Tumi, H. (1985) 'Confining pressure, grain angularity, and liquefaction', *Journal of Geotechnical Engineering*, 111(10). doi: 10.1061/(ASCE)0733-9410(1985)111:10(1229).

Vaid, Y. P., Chung, E. K. F. and Kuerbis, R. H. (1990) 'Stress path and steady state', *Canadian Geotechnical Journal*, 27(1). doi: 10.1139/t90-001.

Vesic, A. S. and Clough, G. W. (1968) 'Behavior of granular materials under high stresses', *Journal of Terramechanics*, 5(3). doi: 10.1016/0022-4898(68)90104-3.

Wong, K. S. and Duncan, J. M. (1974) *Hyperbolic stress-strain parameters for nonlinear finite element analyses of stresses and movements in soil masses*.

Wroth, C. P. and Houlsby, G. T. (1985) 'Soil mechanics - property characterization and analysis procedures.', *Proc. 11th international conference on soil mechanics and foundation engineering, San Francisco, August 1985. Vol. 1, (Balkema).*

Wu, Y., Yamamoto, H. and Izumi, A. (2016) 'Experimental investigation on crushing of granular material in one-dimensional test', *Periodica Polytechnica Civil Engineering*, 60(1). doi: 10.3311/PPci.8028.

Yudhbir and Rahim, A. (1987) 'Compressibility characteristics of sands', in *Proceedings of the 9th Southeast Asian Geotechnical Conference*, pp. 483–494.

APPENDICES

A. Appendix A

Table A-1: Details of specific gravity tests

Experiment No.	1		2	
Temperature (°C)	20.6		23.1	
Trial No.	1	2	1	2
Mass of empty bottle, M_b (g)	125.552	122.737	122.803	115.089
Mass of bottle filled with water only, M_{b+w} (g)	386.002	390.628	390.427	377.542
Mass of bottle with dry soil, M_{b+s} (g)	165.53	162.713	185.684	175.568
Mass of solids, $M_{b+s} - M_b$ $(= M_s)$ (g)	39.978	39.976	62.881	60.479
Mass of bottle with soil, filled with deaired water, M_{b+s+w} (g)	410.923	415.499	429.665	415.15
Mass of water with volume equal to the volume of solids, $M_{b+w} + M_s - M_{b+s+w}$ (g)	15.057	15.105	23.643	22.871
Specific gravity of solids at this temperature, G_s	2.655	2.647	2.660	2.644
Specific gravity of solids at 20°C, $G_s@20°C$	2.655	2.646	2.653	2.638
Mean value of Gs	2.650		2.645	
Standard Deviation	0.006		0.011	

Table B-1: Details of maximum void ratio calculations

Experiment No.	1	2	3
Diameter of mold (mm)	152.01	152.01	152.01
Height of mold (mm)	116.57	116.57	116.57
Volume of mould (cm^3)	2114.62	2114.62	2114.62
Mass of mold (g)	5544.7	5544.7	5544.7
Specific gravity of soil	2.65	2.65	2.65
Mass of Soil + Mould (g)	8675.2	8640.1	8664
Mass of Soil (g)	3130.5	3095.4	3119.3
Volume of Soil Particles (cm^3)	1181.321	1168.075	1177.094
Volume of Voids (cm^3)	933.299	946.544	937.525
Maximum void ratio	0.790	0.810	0.796

Table B-2: Details of minimum void ratio calculations

Experiment No.	1	2
Diameter of the mold (mm)	152.05	152.01
Height of the mold (mm)	116.51	116.51
Volume of the mould (cm^3)	2114.583	2113.471
Mass of the mold (g)	5563.6	5545.2
Specific gravity of the soil samples	2.65	2.65
Mass of Soil + Mould (g)	9391.1	9428.2
Mass of Soil (g)	3827.5	3883
Volume of Soil Particles (cm^3)	1444.34	1465.283
Volume of Voids (cm^3)	670.243	648.188
Maximum void ratio	0.464	0.442